Title
Supramolecular Nanoparticles for Molecular Diagnostics and Therapeutics

Author
Chen, Kuan-Ju

Publication Date
2012

Peer reviewed|Thesis/dissertation

UNIVERSITY OF CALIFORNIA

Los Angeles

Supramolecular Nanoparticles for Molecular Diagnostics and Therapeutics

A dissertation submitted in partial satisfaction of the
requirements for the degree Doctor of Philosophy
in Biomedical Engineering

by

Kuan-Ju Chen

2012

ABSTRACT OF THE DISSERTATION

Supramolecular Nanoparticles for Molecular Diagnostics and Therapeutics

by

Kuan-Ju Chen

Doctor of Philosophy in Biomedical Engineering

University of California, Los Angeles, 2012

Professor Hsian-Rong Tseng, Chair

Over the past decades, significant efforts have been devoted to explore the use of various nanoparticle-based systems in the field of nanomedicine, including molecular imaging and therapy. Supramolecular synthetic approaches have attracted lots of attention due to their flexibility, convenience, and modularity for producing nanoparticles. In this dissertation, the developmental story of our size-controllable supramolecular nanoparticles (SNPs) will be discussed, as well as their use in specific biomedical applications. To achieve the self-assembly of SNPs, the well-characterized molecular recognition system (*i.e.*, cyclodextrin/adamantane recognition) was employed. The resulting SNPs, which were assembled from three molecular building blocks, possess incredible stability in various physiological conditions, reversible size-controllability and dynamic disassembly that were exploited for various *in vitro* and *in vivo* applications. An advantage of using the supramolecular approach is that it enables the convenient incorporation of functional ligands onto SNP surface that confers functionality (*e.g.*, targeting, cell penetration) to SNPs. We utilized SNPs for molecular imaging such as magnetic resonance imaging (MRI) and positron emission tomography (PET) by introducing reporter systems (*i.e.*,

radio-isotopes, MR contrast agents, and fluorophores) into SNPs. On the other hand, the incorporation of various payloads, including drugs, genes and proteins, into SNPs showed improved delivery performance and enhanced therapeutic efficacy for these therapeutic agents. Leveraging the powers of (i) a combinatorial synthetic approach based on supramolecular assembly and (ii) a digital microreactor, a rapid developmental pathway was developed that is capable of screening SNP candidates for the ideal structural and functional properties that deliver optimal performance. Moreover, SNP-based theranostic delivery systems that combine reporter systems and therapeutic payloads into a single SNP for both diagnosis and therapy were generated. The results show that this type of theranostic SNPs may have a great contribution in the optimization of therapeutic efficacy for individual patients in clinical translation in the near future. It is anticipated that our supramolecular synthetic approach could be adopted to assemble various SNP-based delivery agents for molecular diagnostics and therapeutics that pave the way toward personalized medicine.

The dissertation of Kuan-Ju Chen is approved.

Pei-Yu Chiou

Yunfeng Lu

Benjamin M. Wu

Hsian-Rong Tseng, Committee Chair

University of California, Los Angeles

2012

To My Dear Family

Dad, Mom, Hung-Che, and Yi-Hsuan

Table of Contents:

Acknowledgments

My graduate study at UCLA was a precious, unique and memorable experience. All the challenges and experiences had happened made me grow stronger and wiser. Moreover, the acquired experiences and professional skills help me prepare myself to face any future challenges in my life and the next career.

I could not have completed my Ph.D. journey at UCLA without the guidance, support, and encouragement of many people. Especially, I would like to thank my advisor, Prof. Hsian-Rong Tseng, for his great mentorship. I will never forget the lessons he taught me throughout the course of my research. His insight, guidance, inspiration, and support not only trained me to become an independent research scientist but also helped me to develop my own strength. Dr. Tseng is not just an advisor but a father figure to me. Just like a father, knowing that I could be better, he always has higher expectations on me. I am particularly grateful to the way he mentors me, which make me to accomplish lots of fruitful results and motivate me to achieve many ambitious goals.

I have been fortunate to be surrounding by extremely hardworking, super friendly, and remarkably talented group members in Dr. Tseng's lab. In my first year of graduate training, I was assigned to work with two outstanding postdoc fellows (now are professors in China), Dr. Hao Wang and Dr. Shutao Wang, on several exciting projects. I sincerely appreciate that Dr. Hao Wang taught me all the synthetic skills unconditionally with patience and have advised me throughout lots of projects ever since. Also, I would like to thank Dr. Shutao Wang for all the characteristic techniques he taught me. We spent lots of time together, not just doing research or discussing science; they also taught me how to prepare myself to become a scientist and provided many suggestions in both research and life. To me, they are not just lab-members, but

my family. I also want to thank every former and current group members in Dr. Tseng's research group. I would never forget the joyful lunchtimes we had and the nights we spent together in order to get data done. Without their company, assistance, and support, my graduate journey won't be completed. Here, I specifically would like to thank to Dr. Mitch Garcia, who is both a knowledgeable colleague and a sincere friend. With his joining in nanoparticle team, we not only work closely together in several promising project as a great team but often times challenge each other in order to make sure from our experimental plans to manuscript writings are logical, clear, flawless, and have great scientific values. I really appreciate his enthusiasm and persistence that help me improve myself and motivate me to devote myself to science. Moreover, I am grateful to his guidance and support in both research and daily life that make my Ph.D. journey enjoyable.

Through my graduate study, I have had a good fortune of working in collaboration with various scientists from different disciplines nationwide, and without their expertise none of these interdisciplinary works could have been possibly done. I acknowledge the contribution of all co-authors of publications that are discussed in this dissertation. Chapter 2.1. and Chapter 3.2. are versions of H. Wang, S. Wang, H. Su, K.-J. Chen, A. L. Armijo, W.-Y. Lin, Y. Wang, J. Sun, K. Kamei, J. Czernin, C. G. Radu, H.-R. Tseng, "A Supramolecular Approach for Preparation of Size-Controlled Nanoparticles." *Angew. Chem. Int. Ed.* **2009**, 48: 4344-4348. Chapter 2.2.2. is a version of S. Wang, K.-J. Chen, T.-H. Wu, H. Wang, W.-Y. Lin, E. P.-Y. Chiou, H.-R. Tseng, "Photothermal Effects of Supramolecular Assembled Gold Colloids for Targeted Treatment of Cancer Cells." *Angew. Chem. Int. Ed.* **2010***,* 49: 3777-3781. Chapter 3.3.is a version of K.-J. Chen, S. M. Wolahan, H. Wang, C.-H. Hsu, H.-W. Chang, L.-P. Hwang, M. A. Garcia, Z. K. Jiang, L. Wu, Y.-Y. Lin and H.-R. Tseng, "A Small MRI Contrast Agent Library of Gadolinium(III)-Encapsulated Supramolecular Nanoparticles for Improved Relaxivity

and Sensitivity." *Biomaterials* **2011** 32: 2160-2165. Chapter 4.2. is a version of H. Wang, K.-J. Chen, S. Wang, M. Ohashi, K. Kamei, J. Sun, H.-R. Tseng, "A Small Library of DNA-Encapsulated Supramolecular Nanoparticles for Targeted Gene Delivery." *Chem. Commun.* **2010** 46: 1851-1853. Chapter 4.3. is a version of Y. Liu, H. Wang, K. Kamei, M. Yan, K.-J. Chen, L. Shi, Y. Lu, H.-R. Tseng, "Delivery of Intact Transcription Factor Using Self-Assembled Supramolecular Nanoparticles." *Angew. Chem. Int. Ed.* **2011**, 50: 3058-3062. Chapter 4.4. is a version of H. Wang, K. Liu, K.-J. Chen, Y. Lu, S. Wang, F. Guo, W.-Y. Lin, K. Kamei, Y.-C. Chen, X.-Z. Zhao, C. K.-F. Shen, H.-R. Tseng, "A Rapid Pathway Toward a Superb Gene Delivery System: Programming Structural and Functional Diversity into a Supramolecular Nanoparticle Library." *ACS Nano* **2010**, 4: 6235-6243. Chapter 6.2. is a version of K.-J. Chen, L. Tang, M. A. Garcia, H. Wang, H. Lu, W.-Y. Lin, S. Hou, Q. Yin, C. K.-F. Shen, J. Cheng, H.-R. Tseng, "The Therapeutic Efficacy of Camptothecin-Encapsulated Supramolecular Nanoparticles." *Biomaterials* **2012**, 33: 1162-1169.

I also like to thank Prof. Pei-Yu Chiou, Prof. Yunfeng Lu, and Prof. Benjamin Wu for serving on my doctoral committee and participating in the review process of this dissertation. Very importantly, I would like to acknowledge my family and friends for their unconditional support and love that have helped me and given me the courage to finish my doctoral study.

VITA

June 2008 — B.S., Materials Science and Engineering
National Tsing Hua University
Hsinchu, Taiwan

PUBLICATIONS AND PRESENTATIONS

1) H. Wang, S. Wang, H. Su, **K.-J. Chen**, A. L. Armijo, W.-Y. Lin, Y. Wang, J. Sun, K. Kamei, J. Czernin, C. G. Radu, H.-R. Tseng (2009) A Supramolecular Approach for Preparation of Size-Controlled Nanoparticles. *Angew. Chem. Int. Ed.* 48: 4344-4348.

2) S. Wang, H. Wang, J. Jiao, **K.-J. Chen**, G. E. Owens, K. Kamei, J. Sun, D. J. Sherman, C. P. Behrenbruch, H. Wu, H.-R. Tseng (2009) Three-Dimensional Nanostructured Substrates toward Efficient Capture of Circulating Tumor Cells. *Angew. Chem. Int. Ed.* 48: 8970-8973.

3) **K.-J. Chen**, H. Wang, H.-R. Tseng. A Supramolecular Approach for Synthesizing Size-Controllable Nanoparticles. Poster presentation at Nanotechnology Systems Biology Cancer Center, Annual Retreat, Ventura, CA, USA, April 2009.

4) **K.-J. Chen**, S. Wang, H.-R. Tseng. "Fly Paper" to Capture Circulating Cancer Cells. Poster presentation at Nanotechnology Systems Biology Cancer Center, Annual Retreat, Ventura, CA, USA, April 2009.

5) **K.-J. Chen**, H. Wang, S. Wang, H.-R. Tseng. Size-Controllable Nanoparticles Prepared by A Supramolecular Approach. Oral presentation at Material Research Society Fall Meeting, Boston, MA, USA, November 2009.

6) H. Wang, **K.-J. Chen**, S. Wang, M. Ohashi, K. Kamei, J. Sun, H.-R. Tseng (2010) A Small Library of DNA-Encapsulated Supramolecular Nanoparticles for Targeted Gene Delivery. *Chem. Commun.* 46: 1851-1853.

7) S. Wang, **K.-J. Chen**, T.-H. Wu, H. Wang, W.-Y. Lin, E. P.-Y. Chiou, H.-R. Tseng (2010) Photothermal Effects of Supramolecular Assembled Gold Colloids for Targeted Treatment of Cancer Cells. *Angew. Chem. Int. Ed.* 49: 3777-3781.

8) H. Wang, K. Liu, **K.-J. Chen**, Y. Lu, S. Wang, F. Guo, W.-Y. Lin, K. Kamei, Y.-C. Chen, X.-Z. Zhao, C. K.-F. Shen, H.-R. Tseng (2010) A Rapid Pathway Toward a Superb Gene Delivery System: Programming Structural and Functional Diversity into a Supramolecular Nanoparticle Library. *ACS Nano* 4: 6235-6243.

9) K. Liu, H. Wang, **K.-J. Chen**, F. Guo, W.-Y. Lin , Y.-C. Chen, D. L. Phung, H.-R. Tseng, C. K.-F. Shen (2010) A Digital Microfluidic Droplet Generator Produces Self-assembled Supramolecular Nanoparticles for Targeted Cell Imaging.
Nanotechnology 21: 445603-445610.

10) **K.-J. Chen**, H. Wang, M. A. Garcia, H.-R. Tseng. Supramolecular Nanoparticles for Molecular Therapeutics and Diagnostics. Poster presentation at Novel Nano-delivery of siRNA/miRNA Symposium, Los Angeles, CA, USA, June 2010.

11) **K.-J. Chen**, H. Wang, M. A. Garcia, H.-R. Tseng. Supramolecular Nanoparticles for Molecular Therapeutics and Diagnostics. Poster presentation at Physical Sciences in Oncology Center Symposium, Los Angeles, CA, USA, June 2010.

12) Y. Liu, H. Wang, K. Kamei, M. Yan, **K.-J. Chen**, L. Shi, Y. Lu, H.-R. Tseng (2011) Delivery of Intact Transcription Factor Using Self-Assembled Supramolecular Nanoparticles. *Angew. Chem. Int. Ed.* 50: 3058-3062.

13) **K.-J. Chen**, M. A. Garcia, H. Wang, H.-R. Tseng. Drug(s)-Encapsulate Supramolecular Nanoparticles for Cancer Treatment. Poster presentation at Nanomedicine and Drug Delivery Research Conference, Los Angeles, CA, USA, March 2011.

14) **K.-J. Chen**, Y. Liu, H. Wang, Y. Lu, H.-R. Tseng. Supramolecular Nanoparticles for Delivering Intact Transcription Factor. Poster presentation at Nanohealth Symposyium. Seoul, Korea, November 2011.

15) **K.-J. Chen**, M. A. Garcia, H. Wang, H.-R. Tseng (2012) Supramolecular Nanoparticles for Molecular Diagnostics and Therapeutics. *Supramolecular Chemistry: From Molecules to Nanomaterials* (John Wiley & Sons, Ltd.).

16) **K.-J. Chen**, S. M. Wolahan, H. Wang, C.-H. Hsu, H.-W. Chang, L.-P. Hwang, M. A. Garcia, Z. K. Jiang, L. Wu, Y.-Y. Lin and H.-R. Tseng (2011) A Small MRI Contrast Agent Library of Gadolinium(III)-Encapsulated Supramolecular Nanoparticles for Improved Relaxivity and Sensitivity. *Biomaterials* 32: 2160-2165.

17) **K.-J. Chen**, L. Tang, M. A. Garcia, H. Wang, H. Lu, W.-Y. Lin, S. Hou, Q. Yin, C. K.-F. Shen, J. Cheng, H.-R. Tseng (2012) The Therapeutic Efficacy of Camptothecin-Encapsulated Supramolecular Nanoparticles. *Biomaterials* 33: 1162-1169.

Chapter 1. BACKGROUND

Nanoparticles (NPs), particles in the size range from 1 to 100 nm, are emerging as a new class of diagnostics and therapeutics in the field of medicine. The applications of NPs offer many advantages over traditional methods, such as, providing more effective or more convenient routes of administration, lowering toxicity and extending the product life cycle, and as a result they have attracted diverse communities from chemistry, engineering, and biology to explore the use of NPs for solving clinically relevant problems. For diagnostic applications, NPs allow molecular level detection for improved sensitivity and specificity of imaging. As therapeutic delivery systems, they allow targeted delivery and controlled release of therapeutic agents. NP-based diagnostics focuses on *in vitro* specific marker detection and/or *in vivo* imaging that encompasses magnetic resonance imaging (MRI), positron emission tomography (PET), and computed tomography (CT), while NP-based therapeutics is concerned with the delivery of biologically relevant molecules such as small-molecule drugs, peptides, proteins, and nucleic acids into cells. Currently, both NP-based diagnostics and therapeutics are actively being applied to cancer therapy,[1] drug delivery,[2] cancer imaging,[3] and immunology.[4] Moreover, a new approach that combines diagnosis and therapy has been developed. Theranostics, which integrates both imaging motifs and therapeutic agents in a single NP, have been considered promising delivery agents against various diseases to achieve personalized medicine.

Complexity in biology

The main challenge for researchers is to design a platform that is compatible with the complexity of living systems. Living organisms are hierarchical structures that comprise of individual molecules, *e.g.*, DNA, protein and lipids, and integrate these smallest constituent components across multiple levels of organization, from organelles, to cells, tissues, organs, and the

organism. Different molecular parts can interact and affect each other, and self-organize into a whole system that exhibits synergetic properties are the reasons for the complexity of living systems. NPs must survive in the dynamic *in vivo* environment long enough to be applied as a diagnostic and therapeutic tool. Besides, when NPs travel through the body, they need to bypass healthy tissues and accumulate at a tumor site or a specific organ of interest. Therefore, how to control the interactions between NPs and bio-systems is essential for the effective utilization of these materials in biomedicine.

Size, surface chemistry, charge, and shape affect the properties of NPs

It is well known that a NP's biological activity is a function of size, surface chemistry, charge, and shape.[5] The upper size limit of NPs (~few hundred nm) is bounded by the *in vivo* formation of granulomas due to the non-specific phagocytosis by hepatic and splenic reticuloendothelial cells.[6] The lower limit (~10 nm) is determined by the sieving coefficient of the renal capillary walls along the glomerulus.[7] The surface chemistry can also be modified by incorporating passivation, targeting ligands or other functional ligands onto the surface of the NPs that alleviates non-specific trapping in tissues and confers delivery specificity. The passivation ligands, *i.e.*, poly ethyleneglycol (PEG), can suppress protein adsorption and prolong retention time. The incorporation of targeting ligands such as small molecules, peptides, proteins, or antibodies, offers specificity by targeting an over-expressed receptor along the tumor cell's surface. As a NP's surface charge changes from neutral, either in a positive or negative direction, the NPs will become a target for macrophage scavenging and will result in increased clearance by the lymph nodes and the spleen. In addition, the shape of the NPs has been found to influence the mechanism of endocytosis uptake into cells.[8] Taken together, the delivery performance of

NPs will be determined by its chemical and physical properties, which would be the parameters for researchers to fine-tune in order to achieve optimal delivery performance.

Supramolecular chemistry

Supramolecular chemistry, "chemistry beyond the molecule", is an extensively explored and actively investigated field that is capable of designing self-assembled systems that utilize non-covalent interactions to achieve controllable assembly of molecular building blocks.[9] These supramolecular complexes are inherently dynamic in nature and highly selective with their complementary guest molecules via various weak and reversible non-covalent interactions, including ion-ion, π-π stacking, hydrogen bonding, hydrophobic interactions and van der Waals interactions. Due to their inherent modularity and reversibility, supramolecular systems can be engineered to assemble and disassemble in response to external triggers.

While conventional chemical synthesis is capable of forming/breaking covalent bonds, supramolecular chemistry combines the twin concepts of self-assembly and molecular recognition to easily generate unique nanostructured materials from the non-covalent bonding of a small set of molecular building blocks.[10] The concept of self assembly has been extensively used to prepare organic NPs such as liposomes and nano-scaled vesicles (self-assembly from phospholipids)[11]. These self-assembled NP systems have been considered key platforms to innovate on existing methodologies for clinical diagnosis and therapy, drug development, and also primary life science researches.

Different types of self-assembled NP system

Liposomes are spherical lipid vesicles with a bilayer structure of natural amphiphilic lipid molecules that can form via the accumulation of lipids interacting with one another in an energetically favorable manner. These liposomes are not rigid formations but are versatile

supramolecular assemblies. The unique advantages of liposomes are their diverse range of morphologies, compositions, ability to envelop and protect many types of therapeutic biomolecules, and their differential release characteristics.[12] Thus, liposomes have been used widely for drug and gene delivery.[13]

Similar to liposomes, which are composed of natural amphiphiles derived from cell membranes, polymer vesicles are made of materials that are synthetic.[14] Polymer vesicles can deliver both hydrophilic and hydrophobic agents encapsulated in their aqueous segment and hydrophobic membrane, respectively. For example, the multifunctional stable polymer vesicles that combined superparamagnetic iron oxide for molecular imaging and chemo-drug for cancer therapy are prepared by self-assembly of heterofunctional amphiphilic triblock copolymers with two different PEG segment lengths.[15] However, compared with liposomes, polymer vesicles offer many more possibilities to control their physical, chemical, and biological properties by engineering their polymeric building blocks.[16]

Polymer micelles, which are self-assembled from amphiphilic block copolymers in aqueous solution, have received a great attention for drug delivery applications.[17] The core of the polymer micelle is a hydrophobic domain that can physically entrap hydrophobic drugs and the hydrophilic blocks, which are often composed of poly(ethylene oxide) (PEO), can form hydrogen bonds with the outer aqueous surroundings and form a “stealth” shell around the micelle core. The resulting polymer micelles, which exhibit prolong blood circulation and enhance accumulation in tumors, can be used as drug carriers. Moreover, positive charged polymer micelles are suitable for gene delivery. Cationic amphiphilic ABC type triblock copolymers consisting of (i) hydrophilic PEG, which acts as shell forming, (ii) a polyester block like poly-ε-caprolactone (PCL), which arranges as a hydrophobic core that is ideal for

encapsulating hydrophobic drugs, and (iii) a cationic linear poly(ethylene imine) (PEI) that can condense nucleic acids or anionic charged drugs have emerged as promising carriers for co−deliver drugs and nucleic acids.[18]

Polycationic dendrimers, such as poly(amidoamine) (PAMAM), are considered as promising DNA delivery systems.[19] The primary amine groups on their surface can bind with DNA via electrostatic interactions and compact DNA into nanoscale particles; meanwhile their tertiary amine groups inside can act as proton sponge in endosomes and enhance the release of DNA. The practicability of these dendrimers is under critical investigation, as these nanocarriers can carry various cargoes for the delivery of both therapeutic and imaging agents. PAMAM dendrimers, in particular, are being highly investigated due to their nontoxiticity feature makes them more biocompatible compared to many other nanomaterials.[20]

Limitation

Various approaches in controlling the size and surface chemistry of NPs have employed the use of liposomes,[21] polymers,[22] and inorganic particles.[23] However, the synthesis of these NPs are often time consuming and tedious, limiting the ease of generating a diverse set of sizes and unique surface chemistry. Moreover, the formation of liposomes and inorganic compounds are sometimes not compatible with biomolecules, which adds additional synthetic steps in order to attach proteins or DNA to the NPs. These researchers synthesize and modify their NPs by a semi-empirical approach. Each generation of NPs is a refined and more optimized version of their previous generation. Ideally, a NP platform should provide a quick method of generating structural diversity in tandem with functional diversity in order to easily find the optimal formulation that offers the best biological performance.

Molecular recognition system

Among all the self-assembled synthetic approaches for the formation of NPs, molecular recognition systems or host-guest interactions have been regarded as an important class of non-covalent interactions for inducing self-assembly due to their specific molecular recognition, reversibility and precise size controllability. In host-guest systems, molecular recognition units combine/bind in a one to one ratio, where one component, the "host", is known to spatially accommodate a "guest" molecule. A number of synthetic receptors act as host molecules that possess a cage-like supramolecular structure including cucurbit[n]uril (CB[n]),[24] cyclodextrins,[25] cyclophanes,[26] calixarenes,[27] and crown ethers[28] have been investigated. The cucurbit[n]uril (CB[n]) family of macrocyclic receptors can form stable host-guest inclusion complexes with a wide variety of guest molecules (especially polyamines) due to their well defined structure and recognition properties. For example, CB[6] binds spermidine or spermine with a binding constant up to 10^{11} M^{-1}[29] or 10^{12} M^{-1},[30] respectively, which is almost comparable to that of biotin-streptavidin, showing exceptionally high selectivity and stability. Crown ethers, for instance, have been shown to be excellent receptors for ammonium ions forming inclusion complexes. The most commonly investigated host-guest interactions are based on the cyclodextrins (CDs) owing to their extremely low toxicity, excellent biocompatibility and flexible capacity with lipophilic molecules. Furthermore, inclusion complexes with various types of guest molecules can be reversibly dissociated by external stimuli.[25] One of the most typical model systems is the CD and adamantane (Ad) recognition.[31] For example, supramolecular labeling strategy that utilized CD-modified antibodies as a primary target binding to targeted cells and subsequently non-covalent coupling with Ad-modified NPs for achieving higher labeling efficiency in biomarker detection.[32] CD-grafted cationic polyethylenimine (CD-PEI) delivery systems have been regarded as promising carriers for gene and drug delivery.[33] The

Ad-conjugated groups (*i.e.*, chemotherapeutic agent carriers) act as the guest component that self-assembles with the host CD-PEI into supramolecular NPs for drug delivery. Besides, these cationic NPs can readily complex with anionic plasmid DNA into gene/drug-loaded NPs for co-delivery of gene and drugs.[31a, 34] Charge-tunable supramolecular dendritic polymers prepared from different cationic β-CD derivative hosts and Ad-modified hyperbranched polyglycerol guest via host-guest interaction as efficient gene delivery agents.[35] Moreover, due to the hydrophobic cavity of CD, a large number of scientists have demonstrated the incorporation of hydrophobic drugs into various CD derivatives that enhance the solubility and activity of the drugs.[36]

Along the idea of Ad/CD recognition, we construct our supramolecular nanoparticles (SNPs) via self-assembled synthetic approach from three molecular building blocks, including Ad-grafted first-generation polyamidoamine dendrimer, Ad-PAMAM, β-CD-grafted branched polyethylenimine, CD-PEI, and Ad-functionalized PEG, Ad-PEG. The host molecule, CD-PEI, interacts with the 2-nm Ad-PAMAM guest molecule to form an intraparticular cationic hydrogel network; while, Ad-PEG serves as a capping/solvation group that competes with the propagation of the cross-linked hydrogel network and also confers water-solubility to the SNPs. By fine-tuning the different mixing ratios of the three components, SNPs of different sizes can be obtained. The dynamic nature of our supramolecular approach engenders size reversibility and controllable disassembly to the SNPs. Moreover, our self-assembled synthetic approach allows the incorporation of various reporter systems (*i.e.*, fluorophores, radio-isotopes, contrast agents and their combinations) and payloads (*i.e.*, genes, proteins, drugs and their combinations) into the SNPs for molecular diagnosis and therapy applications. In summary, our three-component supramolecular approach offers synthetic convenience, flexibility and modularity to alter the

sizes and surface chemistry of the SNPs. The resulting SNPs with structural and functional diversity can be considered as a new generation NP-based delivery system that is compatible with the complexity of living systems. In the following chapters, I will introduce both organic (see **Chapter 2.1.**) and inorganic (see **Chapter 2.2.**) SNP-based delivery systems and their applications in molecular imaging (see **Chapter 3.**), gene/protein delivery (see **Chapter 4.**), drug delivery (see **Chapter 5.**) and theranostics (see **Chapter 6.**).

Chapter 2. SUPRAMOLECULAR NANOPARTICLES (SNPs)

2.1. Organic SNPs

2.1.1. Introduction

Over the past decades, significant efforts have been devoted to explore the use of nanoparticles in the fields of biology and medicine.[37] For example, gold nanoshells,[38] quantum dots,[39] and super-paramagnetic nanoparticles[40] that carry target-specific ligands have been employed for *in vivo* imaging of cancerous cells; drug molecules have been packaged into polymer-based nanoparticles and/or liposomes to achieve controlled release at the disease sites;[11] and positively charged nanoparticles have served as non-viral delivery systems for both *in vitro* and *in vivo* genetic manipulation and programming.[41] However, there remains an imperious desire to develop novel synthetic approaches to produce a new generation of nanoparticles (NPs) that have 1) controllable sizes and morphologies, 2) low toxicity, compatible immunogenicity and *in vivo* degradability, and 3) proper surface charges and chemistry for improved physiological stability and longer circulation time. Moreover, multiple functions,[42] such as reporter systems for real-time monitoring with imaging techniques (*i.e.*, optical imaging, magnetic resonance imaging (MRI), and positron emission tomography (PET)), targeting ligands for disease-specific delivery, and a controllable mechanism for packaging and releasing drugs and genes, will be conferred to individual nanoparticles for conducting multiple applications in parallel.

2.1.2. Molecular design of organic SNPs

To meet the requirements of producing new generation of NPs, we report a convenient, flexible, and modular synthetic approach (**Figure 2.1.**) for the preparation of size-controllable supramolecular nanoparticles (SNPs).[43] CD/Ad recognition was employed to achieve self-assembly of SNPs from three different molecular building blocks, namely 1) Ad-grafted first-

generation polyamidoamine dendrimer, n-Ad-PAMAM, 2) β-CD-grafted branched polyethylenimine (MW=10 kD), CD-PEI, and 3) Ad-functionalized PEG compound (MW=5 kD), Ad-PEG. The uniqueness of our design is the use of a capping/solvation group. This solvation group Ad-PEG on the one hand competes with the dendrimer block n-Ad-PAMAM to constrain the continuous propagation of the cross-linked network, and on the other hand confers water solubility to the SNPs. By tuning mixing ratios among the three molecular building blocks in phosphate-buffered saline (PBS) aqueous buffer solution (pH 7.2, containing 1.5 mm KH_2PO_4, 155 mm NaCl, and 2.7 mm Na_2HPO_4), the equilibrium between the propagation/aggregation and capping/solvation of the cross-linked network fragments can be altered, allowing arbitrary control over the sizes of the water-soluble SNPs. In contrast to the production of polymer based nanoparticles,[44] where significant synthetic endeavors are required to prepare specific types of polymeric building blocks to achieve the desired level of control over the size, our three-component supramolecular approach offers synthetic convenience, flexibility, and modularity to alter the sizes and surface chemistry of the SNPs. By using such a supramolecular approach we were able to obtain a collection of SNPs with controllable sizes ranging from 30 to 450 nm. Further studies were carried out to unveil the unique properties of these SNPs, including 1) their stability at different temperatures and pH values, as well as in physiological ionic strength media, 2) their competitive disassembly in the presence of Ad molecules, and 3) reversible control over the size using in situ alteration of the mixing ratios of the molecular building blocks.

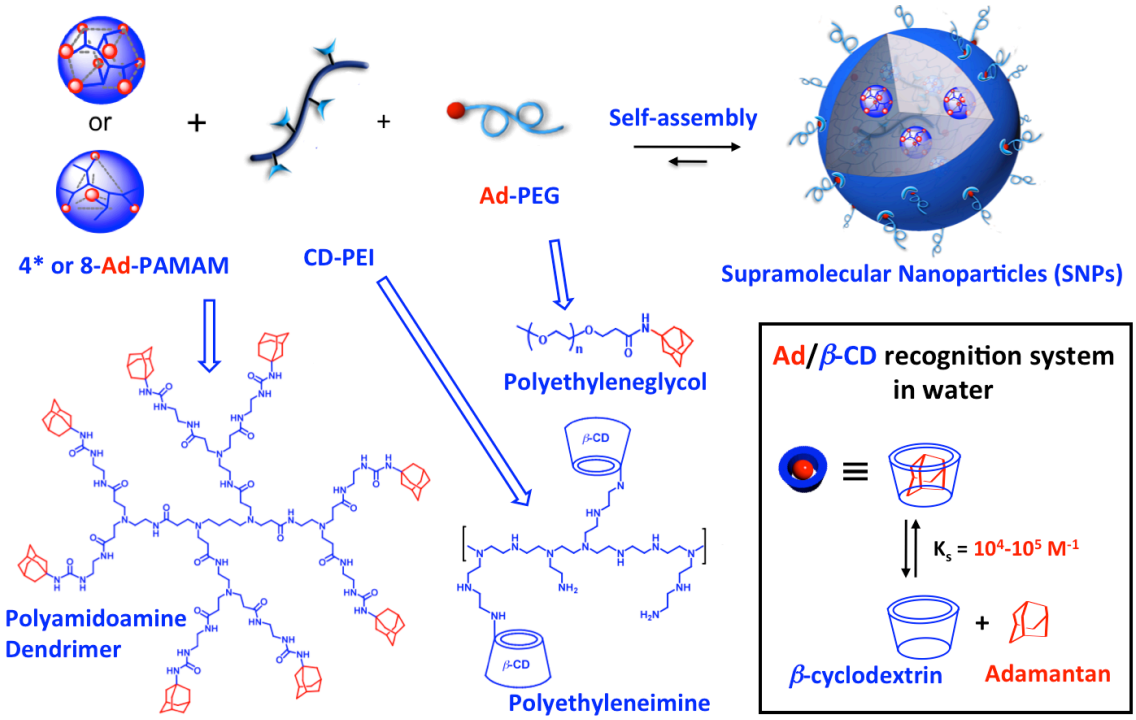

Figure 2.1. A convenient, flexible, and modular synthetic approach for preparation of size-controlled supramolecular nanoparticles (SNPs). A molecular recognition system based on adamantane (Ad) and β-cyclodextrin (CD) was employed to assemble three molecular building blocks 1) *n*-Ad-PAMAM (*n*=4* or 8), 2) CD-PEI, and 3) Ad-PEG.

2.1.3. Size controllability of organic SNPs

The three molecular building blocks n-Ad-PAMAM, CD-PEI, and Ad-PEG were prepared and characterized (see **Supporting Information 1.1., 1.3., 1.4. and 1.5.**). According to the ^{1}H NMR spectrum, in the polymer building block CD-PEI, there are about 7 to 8 CD recognition units grafted on a branched PEI backbone. It is known that the CD modification can increase biocompatibility and reduce toxicity of PEI compounds.[45] Two different dendrimer building blocks, 8-Ad-PAMAM with eight substituted Ad motifs and 4*-Ad-PAMAM with four Ad motifs (on average, based on its ^{1}H NMR spectrum), were examined in parallel. To analyze how the mixing ratios between Ad-PAMAM and CD-PEI affect the sizes of the resulting SNPs, we utilized dynamic light scattering (DLS) measurements to analyze the freshly prepared SNPs. To ensure sufficient supply of the capping/solvation group, an excess amount of Ad-PEG was added

to each mixture. The octasubstituted dendrimer 8-Ad-PAMAM was first tested. In this case, CD-PEI (168 μM) in PBS buffer was slowly added into the mixtures containing Ad-PEG (840 μM) and a variable amount (84 to 672 μM) of 8-Ad-PAMAM. A collection of water-soluble SNPs with variable sizes ranging between 30 and 450 nm were obtained (**Figure 2.2.a**). To ascertain the influence of the number of the Ad-substitution groups in a dendrimer core on the sizes of the respective SNPs, the tetra-substituted dendrimer 4*-Ad-PAMAM was also examined. SNPs with relative smaller sizes (30–120 nm) were obtained under similar self-assembly conditions. The morphology and size of the SNPs were also examined by using transmission electron microscopy (TEM). The TEM images show that the SNPs exhibit spherical shapes and narrow size distributions (**Figure 2.2.b–e**), which are consistent with those results from DLS.

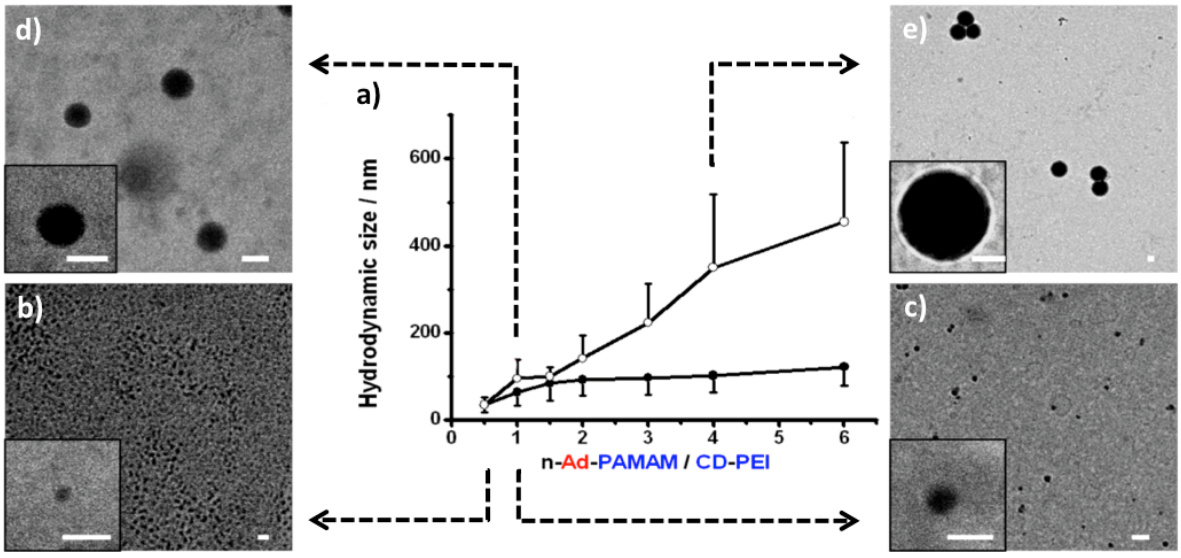

Figure 2.2. a) Titration plots summarize the relationship between SNP sizes and the mixing ratios of the two molecular building blocks (*n*-Ad-PAMAM/CD-PEI). Dynamic light scattering (DLS) was employed to measure SNP sizes. The titration plot for an octa-substituted dendrimer building block 8-Ad-PAMAM (○) and for a tetra-substituted dendrimer building block 4*-Ad-PAMAM (•). The standard deviation of each data point was contained from, at least, three repeats. Transmission electron microscopy (TEM) images of the resulting SNPs with different sizes of b) (32±7) nm from 8-Ad-PAMAM, c) (61±17) nm from 4*-Ad-PAMAM, d) (104±16) nm from 8-Ad-PAMAM, and e) (340±46) nm from 8-Ad-PAMAM. Scale bars: 100 nm

2.1.4. Stability of organic SNPs

The use of the supramolecular approach conferred dynamic characteristics to the self-assembled SNPs. To understand the dynamic stability of the SNPs, we employed real-time DLS measurements to monitor the size variation of the 30 and 100 nm SNPs (composed of the 8-Ad-PAMAM based dendrimer) at different temperatures, pH values, and in physiological ionic strength media. First, temperature-dependent DLS measurements indicate that the SNPs are stable over a wide range of temperatures (7 to 50 °C; **Figure 2.3.a**). Second, we observed negligible size variation of the resulting SNPs at different pH values (pH 3.8–8.3; **Figure 2.3.b**) and physiological ionic strength (**Figure 2.3.c**). We note that the stability of these SNPs can be attributed to the multivalent CD/Ad recognition, which holds individual molecular building blocks in each SNP. Two sets of experiments were carried out to examine the dynamic characteristics (*i.e.* control of competitive disassembly and reversible alteration of the size) of these SNPs, which further validate the molecular mechanism of this supramolecular approach. First, we introduced 100 equivalents of a competitive reagent (*i.e.*, 1-adamantamine hydrochloride) into a solution containing either 30 or 100 nm SNPs. After 10 minutes of sonication, disassembly of the SNPs was observed by DLS as a result of competitive inclusion of the free 1-adamantamine hydrochloride into CD-PEI. As a control, without the addition of 1-adamantamine hydrochloride, sonication alone could not disassemble the SNPs (**Figure 2.3.d**).

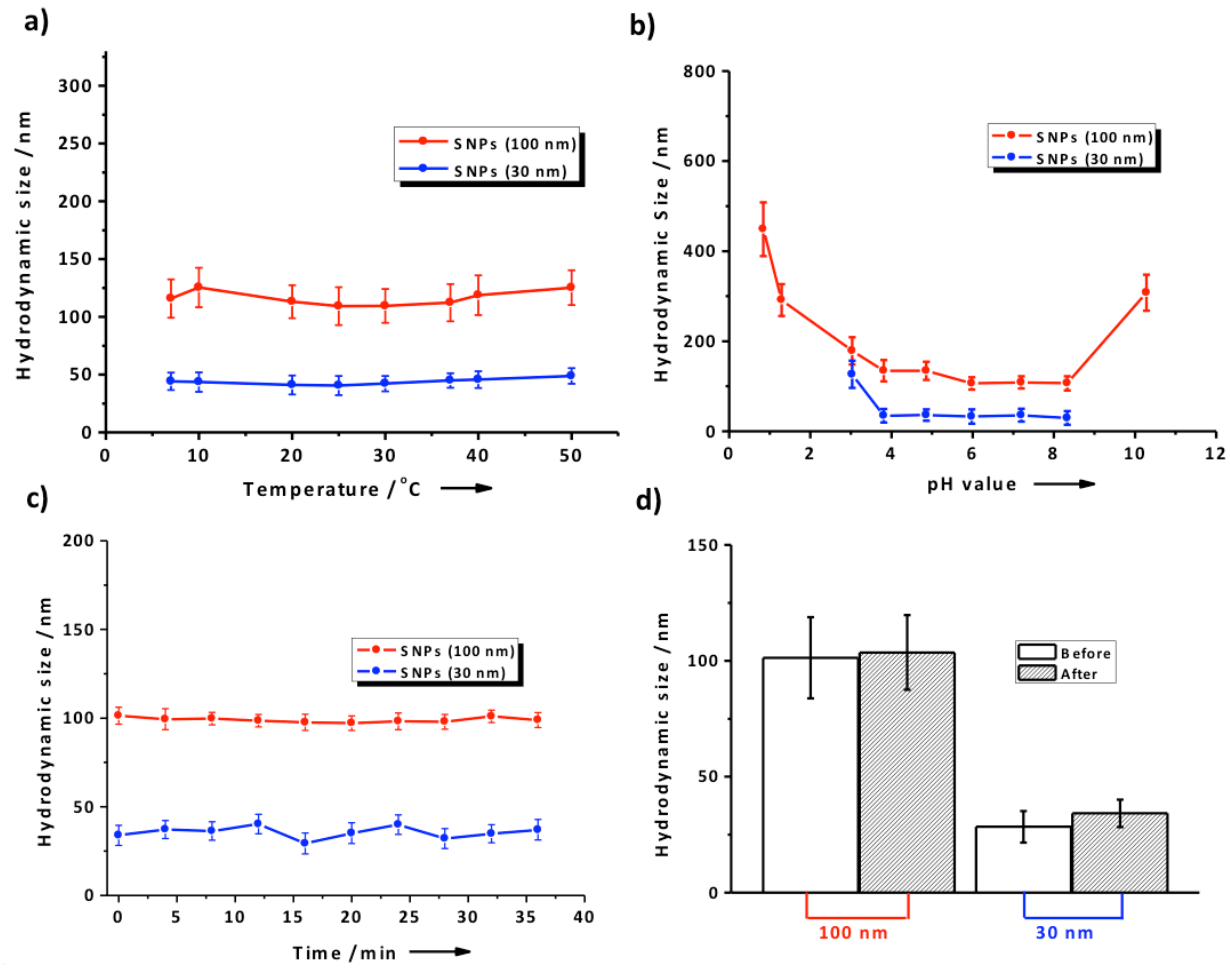

Figure 2.3. a) Temperature-dependent size variation of both of the 30- and 100-nm SNPs in PBS buffer with different temperatures at 7, 10, 20, 25, 30, 37, 40 and 50 °C. b) pH-dependent size variations of both 30- and 100-nm SNPs in the respective buffer solutions with pH values ranging from 0.84 ± 0.03 to 10.28 ± 0.03. Error bars are obtained from three measurements. c) Time-dependent size variation of the 30- and 100-nm SNPs in in physiological ionic strength media. d) Sonication effect on size variation of 30- and 100-nm SNPs.

Second, starting from 100 nm SNPs (8-Ad-PAMAM/CD-PEI=1:1, mol/mol), we were able to reduce the size of the SNPs to 30 nm by adding the polymer component CD-PEI in situ (8-Ad-PAMAM/CD-PEI=1:2, mol/mol), or increase the size of the SNPs to 140 nm by adding the dendrimer component 8-Ad-PAMAM in situ (8-Ad-PAMAM/CD-PEI=2:1, mol/mol). In these studies, 10 minutes of sonication was employed to facilitate the conversion among the three sizes of the SNPs (**Figure 2.4.**).

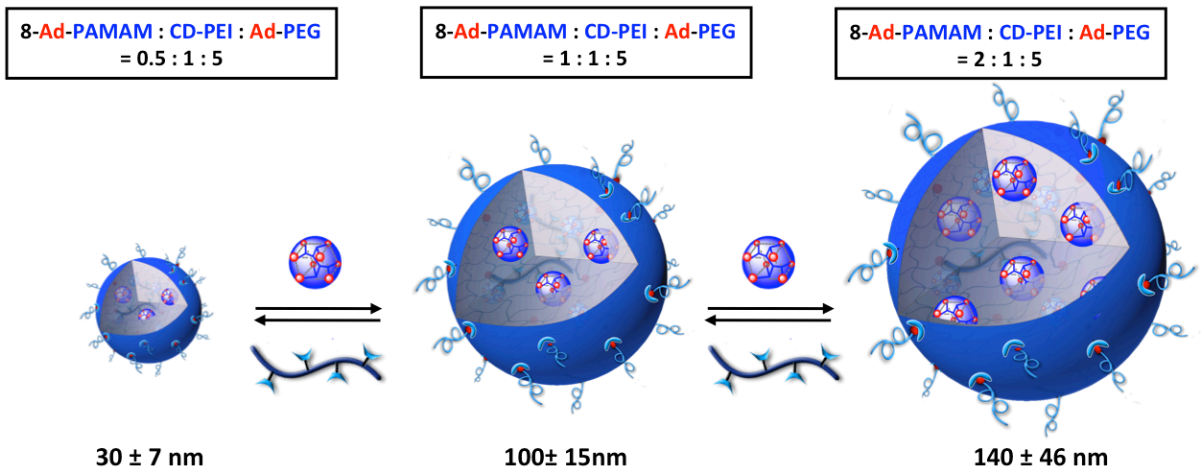

Figure 2.4. Reversible size controllability of SNPs

2.1.5. Conclusion

In conclusion, we have developed a convenient, flexible, and modular synthetic approach for the preparation of size-controllable SNPs (see **Appendix** for reference[43]). The resulting SNPs can incorporate reporter systems for real-time imaging; for example, the incorporation of a radioisotope, *i.e.*, ^{64}Cu for PET imaging studies, which will be discussed in **Chapter 3**. Besides the imaging studies, we also explored the use of the size controllable SNPs for other biomedical applications. More extensive and in-depth studies in the following chapters will show the potentials of these SNPs.

2.2. Inorganic SNPs

2.2.1. Introduction

When introducing inorganic NPs into biological systems, their unique nanoscale size-dependent physical and chemical properties make them useful probes or delivery systems for a wide range of biological diagnostic or therapeutic applications.[46] For example, gold nanoparticles with surface plasmon behavior have been used as unique optical probes for sensing.[47] Moreover, their photophysical properties make them strong candidates for the use in photothermal treatments.[48] Magnetic nanoparticles, on the other hand, have been utilized for controllable drug delivery driven by magnetic field, hyperthermia and MRI contrast agents.[49] However, most of conventional synthetic approaches for producing inorganic NPs are cumbersome and incapable of rapidly and ideally controlling their structural properties in order to achieve desired functions and performances.[50] Therefore, there is a need to have a convenient, easy, and flexible approach for the preparation of inorganic NPs. In this chapter, I will discuss the utilization of our supramolecular synthetic approach by introducing 1) gold NPs as one of our molecular building blocks to give gold supramolecular NPs for the application of photothermal treatments (**Chapter 2.2.2.**) and 2) superparamagnetic nanoparticles to give supramolecular magnetic NPs as powerful MRI contrast agents (**Chapter 2.2.3.**).

2.2.2. Gold Supramolecular Nanoparticles (Au-SNPs)

2.2.2.1. Metal nanomaterials for the application of photothermal treatments

Noble-metal nanostructures with unique photophysical properties have been considered as prime candidate agents for the photothermal treatment of cancer.[48] Normally, the photothermal properties of these nanostructures can be controlled by manipulating their sizes and shapes.[50a] Many significant endeavors have been devoted to the production of a variety of gold

nanostructures, such as nanoparticles[51], nanoshells,[52] nanorods,[53] and nanocages,[54] which are able to overcome limitations of organic-dye-based photothermal agents,[55] such as low light absorption and undesired photobleaching. In order to harvest/generate enough of energy to damage tumor cells, the sizes of these nanostructure-based agents are required to be in the range of tens to hundreds nm.[56] However, the relatively "large" size of the agents often leads to poor bio-clearance (*i.e.*, accumulation in the liver, spleen, and kidneys), which is a major obstacle to their *in vivo* application.[57] Alternatively, the photophysical properties of noble-metal nanostructures can be altered systematically by the formation of aggregates through self-assembly.[58] The antibody-assisted aggregation of Au nanoparticles on cell membranes or in intracellular environments led to the enhancement of photothermal performance[59] as a result of the collective effects[60] associated with the assembled structures. Therefore, the self-assembly of small noble-metal building blocks, that is, noble-metal colloids with diameters of less than 8 nm[57] (compatible with renal clearance) would be a promising approach toward a new class of noble-metal photothermal agents.

2.2.2.2. Design of molecular building blocks

The convenience, flexibility, and modularity of supramolecular synthetic approach can be further explored to assemble inorganic building blocks (*i.e.*, 2 nm Au colloids) into Au supramolecular nanoparticles (Au-SNPs) with defined sizes. We adopted the supramolecular approach employed for organic SNP (see **Chapter 2.1.**) to prepare size-controlled Au-SNPs as a new type of photothermal agent from three building blocks: Ad-grafted 2-nm Au colloids, CD-PEI, and Ad-PEG (**Figure 2.5.**). The characterization of Au-SNPs was carried out by TEM. Other studies, including 1) stability at different temperatures and pH values, 2) size-dependent photophysical properties, and 3) thermally induced disassembly, also been investigated in order to unveil the

unique physical properties of the Au-SNPs. Moreover, laser-induced microbubble-generation experiments performed by 118-nm Au-SNPs demonstrate significantly enhanced photothermal effects compared with 2-nm Au colloids. The use of a supramolecular approach enables[61] the convenient incorporation of targeting ligands to provide target-specific Au-SNPs. In this case, we used arginine–glycine–aspartic acid (RGD) peptide as a targeting ligand and $\alpha_v\beta_3$-positive/negative cells as corresponding biological system to test the specificity and selectivity of RGD-Au-SNPs.

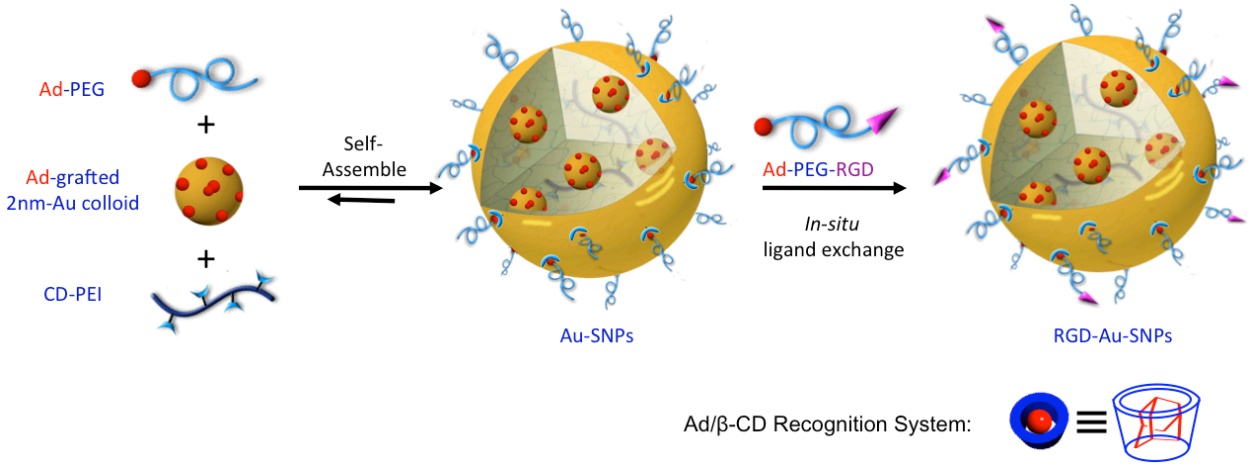

Figure 2.5. Supramolecular synthetic approach for the preparation of size-controlled gold supramolecular nanoparticles (Au-SNPs). A molecular-recognition system based on adamantane (Ad) and β-cyclodextrin (CD) was employed to assemble three building blocks: Ad-grafted 2 nm Au colloids, CD-PEI, and Ad-PEG. Ad-PEG-RGD was introduced onto Au-SNPs by in situ ligand exchange to give RGD-Au-SNPs that could recognize a certain type of tumor cell with membrane $\alpha_v\beta_3$ integrin receptors.

2.2.2.3. Size controllability and Stability of Au-SNPs

Size-controllable Au-SNPs can be generated (**Figure 2.6.**) by slowly adding PBS with Ad-grafted 2-nm Au colloids (0.0213 $mgmL^{-1}$) to PBS solutions with variable amounts of CD-PEI (0.0725–5.73 $mgmL^{-1}$) and Ad-PEG (4.2 $mgmL^{-1}$), followed by incubating the resulting solution at room temperature overnight. By simply tuning the ratio between the Ad-grafted 2-nm Au colloids and CD-PEI, we were able to obtain a collection of Au-SNPs with variable sizes ranging

between 40 and 118 nm (**Figure 2.6.a**). TEM images and histograms in **Figure 2.6.b-f** show the Au-SNPs have spherical shapes with a narrow size distribution.

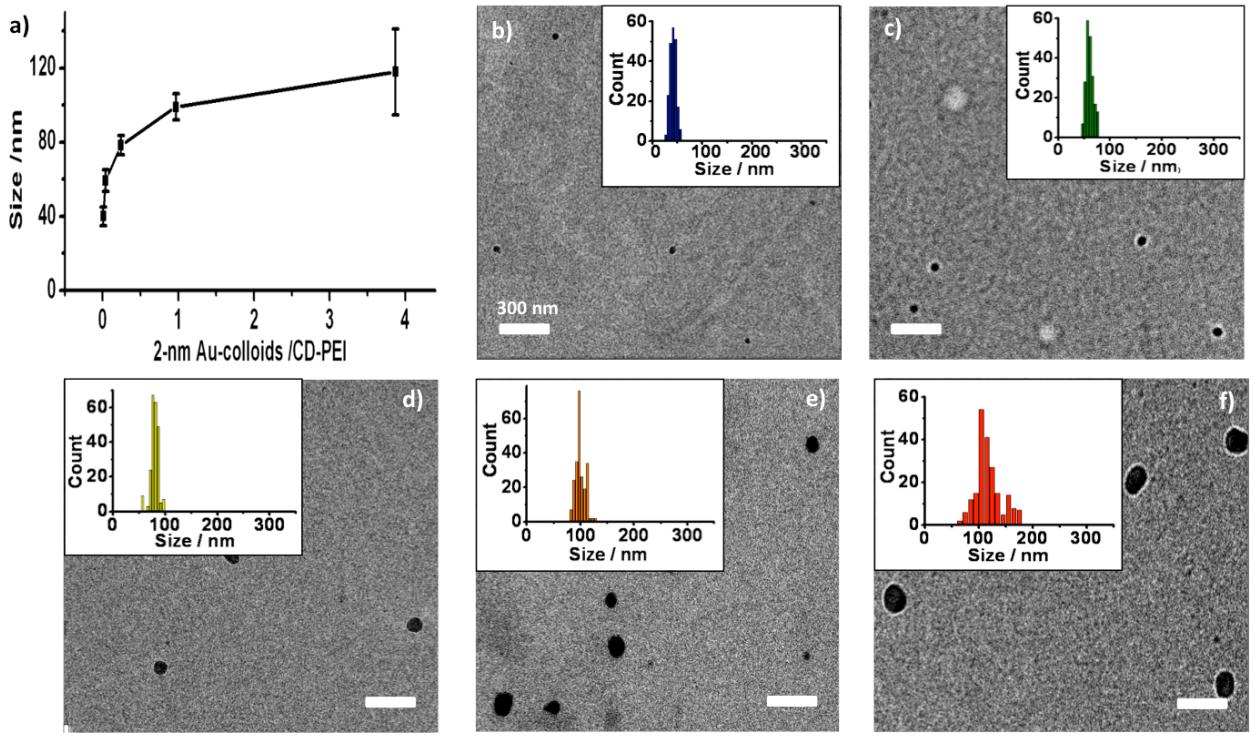

Figure 2.6. a) Titration plot showing the relationship between the size of Au-SNPs and the mixing ratio of the Au colloids and CD-PEI. The TEM images and histograms of different sizes of Au-SNPs range from (b) 40 ± 5 nm, (c) 59 ± 6 nm, (d) 78 ± 5 nm, (e) 99 ± 7 nm, (f) 118 ± 23 nm. Scale bars: 300 nm

Since the Au-SNPs were prepared by supramolecular assembly, we characterized their dynamic stability under different environmental conditions. We monitored size variations of 118-nm Au-SNPs in PBS at temperatures ranging from 7 to 100 °C (**Figure 2.7.a**) and at pH values from 3 to 10 (**Figure 2.7.b**) by TEM. The results indicate 118-nm Au-SNPs are stable in PBS at 7–40 °C and pH 5–10. Also, Au-SNPs maintain their size and morphology in PBS and in 10% serum, most likely because the "stealth" effect imparted by PEG grafted on the outside of Au-SNPs that could lower further agglomeration of the particles.[62] These results suggest that 118-nm Au-SNPs can be used under physiological conditions. At higher temperatures (>50 °C), 118-nm Au-SNPs dissociated into small fragments, and a broader size distribution was observed by

TEM. Complete disassembly of the 118-nm Au-SNPs into 2-nm Au colloids was observed when the temperature was increased to 100 °C. The thermal disassembly of 118-nm Au-SNPs can be attributed to the weakened Ad/CD supramolecular interactions at elevated temperatures.[63]

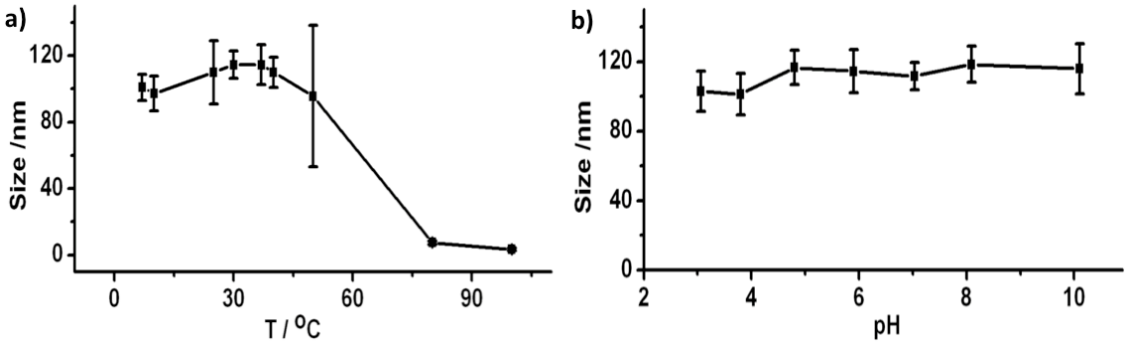

Figure 2.7. Analysis by TEM on effects of temperature (a) and the pH value (b) on the stability of 118 nm Au-SNPs

2.2.2.4. Photothermal effect observed for Au-SNPs

To test the feasibility of the application of Au-SNPs as photothermal agents, we chose 118-nm Au-SNPs as our model system. For comparison, 2-nm Au colloids were employed as a control. First, we investigated photophysical properties of the 118-nm Au-SNPs and 2-nm Au colloids by UV/Vis spectroscopy (**Figure 2.8.a**). Given the characteristic surface plasmon resonance absorption of Au-SNPs and Au colloids (between 500 and 530 nm),[58a] we chose a 532 nm green pulsed laser to test their photothermal effects and performed laser induced micro-bubble generation studies to monitor the locally accumulated heat of individual Au-SNPs. We tested a broad range of energy densities (3–265 $mJcm^{-2}$) of a 532 nm pulsed laser with a 6 ns pulse duration. Au-SNPs and Au colloid suspensions in PBS (with a normalized Au concentration of 4.67 $mgmL^{-1}$) were irradiated with the laser at different energies. For the 118-nm Au-SNPs, a laser threshold of 32 $mJcm^{-2}$ was sufficient for the generation of micro-bubbles upon laser irradiation (**Figure 2.8.b**). In contrast, no micro-bubbles were observed for 2-nm Au colloids

even at the maximum laser energy tested (265 mJcm^{-2}; **Figure 2.8.c**). The significant enhancement of the photothermal effects in 118-nm Au-SNPs can be attributed to the collective heating effect[60] in Au-SNPs. Interestingly, we also found that the efficiency of the collective heating effect was size-dependent: 40-nm Au-SNPs exhibited a threshold of 61 mJcm^{-2}. The formation of explosive vapor bubbles on individual Au-SNPs requires an elevated local temperature higher than critical temperature of the liquid medium (374 °C for water).[64] We hypothesize that upon the formation of micro-bubbles, the localized accumulated heat could facilitate the thermal disassembly of Au-SNPs into smaller fragments, which is in a process similar to that observed for 118 nm Au-SNPs when temperature was above 100 °C. To monitor laser-induced Au-SNPs disassembly, we used a pulsed laser (with a 6 ns pulse duration) to irradiate Au-SNPs at a repetition rate of 1 Hz. Micro-bubble formation was captured by the time-resolved imaging setup 70 ns after the arrival of the laser pulse. We observed a dramatic decrease in the number of laser-induced micro-bubbles after irradiation with several laser pulses. The attenuation of their photothermal effect might due to thermally disassembly of Au-SNPs in the solution.[58a] In the following studies on photothermal treatment, a fixed laser power of 120 mJcm^{-2} was used to ensure micro-bubble formation on the 118-nm Au-SNPs.

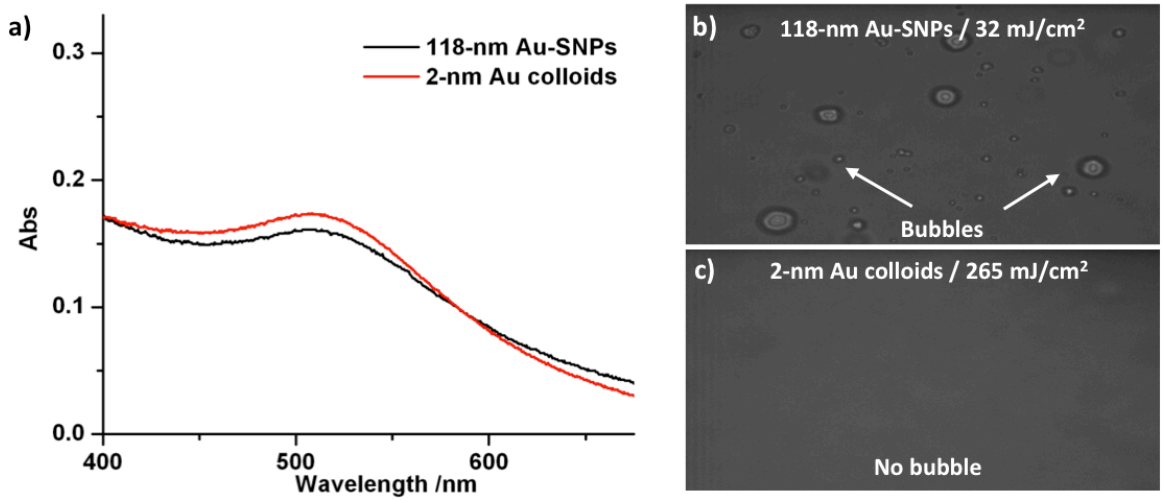

Figure 2.8. a) UV/Vis absorption spectra of 2 nm Au colloids and 118 nm Au-SNPs. Time-resolved bright-field micrographs of suspensions of 118 nm Au-SNPs (b) and Ad-grafted 2 nm Au colloids (c) during the scanning of a pulsed laser (6 ns, 532 nm; 32 mJ cm^{-2} for 118 nm Au-SNPs and 265 mJ cm^{-2} for Ad-grafted 2 nm Au colloids).

2.2.2.5. Application for single-cell surgery

The incorporation of targeting ligands, photothermal agents based on Au nanostructures can be utilized for targeted photothermal treatment of certain types of cancer cells.[65] In our study, RGD-Au-SNPs that recognize tumor cells with membrane $\alpha_v\beta_3$ integrin receptors were produced by dynamic ligand exchange.[61] The 118-nm RGD-Au-SNPs were used along with the controls (RGD-grafted 2-nm Au colloids and nontargeting 118-nm Au-SNPs) for targeted photothermal treatments in four-well chamber slides containing both $\alpha_v\beta_3$-positive U87 glioblastoma cells and $\alpha_v\beta_3$-negative MCF7 breast cancer cells. To visually differentiate the two types of cells, we labeled the U87 and MCF7 cells with green and red fluorescent dyes (DiO and DiD cell-labeling solution, Invitrogen), respectively. After incubation for 20 min with the three agents and subsequent replacement of the culture media, the cells in the culture chambers were exposed to pulsed laser irradiation (6 ns, 120 $mJcm^{-2}$) with a beam diameter of 1 mm (a photomask was used). The irradiated cells were kept in an incubator (5% CO_2, 37 °C) for 2 h, during which time the cells damaged by micro-bubble formation could detach from the substrates. An inverted fluorescence microscope (Nikon TE2000) was employed to examine the cells within the irradiated regions. Cell detachment was observed for the U87 cells treated with RGD-Au-SNPs (**Figure 2.9.a**). In contrast, negligible cell detachment was observed for MCF7 cells treated with RGD-Au-SNPs (**Figure 2.9.b**) as well as for both types of cells treated with nontargeted Au-SNPs. These results suggest that 1) RGD peptide confers target specificity to the Au-SNPs to enable the photothermal treatment of $\alpha_v\beta_3$-positive U87 cells, and 2) nontargeting Au-SNPs have no significant effect on cancer cells, as their surface-grafted PEG chains are capable of reducing

nonspecific binding to cells.[66] Furthermore, no cell detachment was detected for the U87 cells treated with 2-nm Au colloids (**Figure 2.9.c**); this result validated our previous observation that 2-nm Au colloids exhibit minute photothermal effects at this given pulsed laser irradiation. To demonstrate the selectivity of RGD-Au-SNPs for target-specific photothermal treatment, we investigated the targeted depletion of $\alpha_v\beta_3$-positive cells in a cell mixture containing both $\alpha_v\beta_3$-positive U87 and $\alpha_v\beta_3$-negative MCF7 cells. We treated a 1:1 cell mixture (**Figure 2.9.d**, middle) containing U87 cells (green) and MCF7 cells (red) with RGD-Au-SNPs (4.67 $mgmL^{-1}$). After the removal of free RGD-Au-SNPs, the cell mixture was irradiated with a pulsed laser. In the irradiated region, U87 cells (green) were depleted, and the remaining MCF7 cells (red) were able to be continuously cultured on the substrates (**Figure 2.9.d**, right). In the region outside the laser footprint, both types of cells remained. These results suggest that the photothermal treatment of RGD-Au-SNPs is highly selective for targeted cells. Besides the specific targeting effects of RGD-Au-SNPs, the use of a pulsed laser led to effective photothermal effects in a defined location within a nanosecond time frame and thus enabled localized cell damage in a spatially confined fashion.

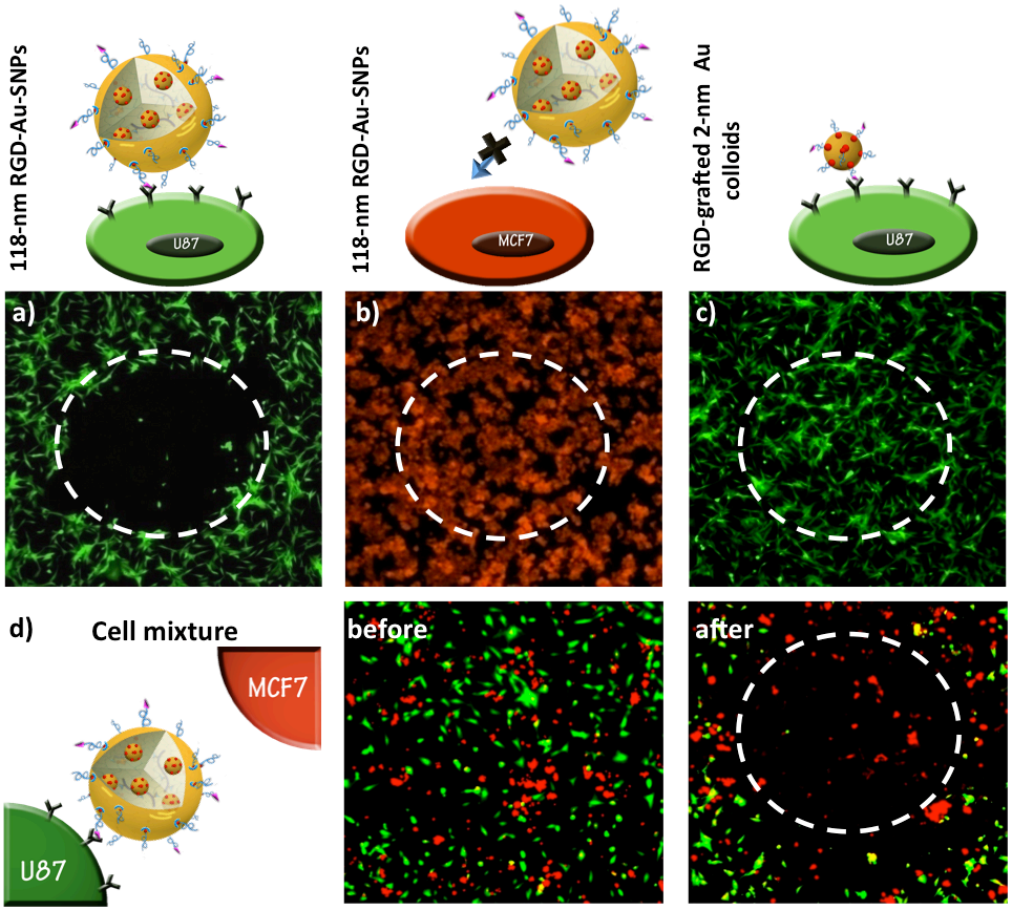

Figure 2.9. a–c) Fluorescence micrographs of U87 cells ($\alpha_v\beta_3$+, labeled green) treated with 118 nm RGD-Au-SNPs (a), MCF7 cells ($\alpha_v\beta_3$-, labeled red) treated with 118 nm RGD-Au-SNPs (b), and U87 cells treated with RGD-grafted 2 nm Au colloids (c) after irradiation with a pulsed laser (6 ns, 120 mJ cm^{-2}). A mask was employed to confine the laser beam to a circular region with a diameter of 1 mm (as indicated by the white dashed circles). d) Fluorescence micrographs of a 1:1 mixture of U87 and MCF7 cells. After treatment with RGD-Au-SNPs and subsequent medium exchange, the cell mixture was irradiated with a pulsed laser. In the irradiated region after culture for 2 h, U87 cells (green) were depleted, whereas MCF7 cells (red) were left alive on the substrate.

2.2.3. Supramolecular Magnetic Nanoparticles (SMNPs)

2.2.3.1. Magnetic nanoparticles for medical diagnosis

MRI is one of the most powerful diagnosis tools for molecular and cellular imaging in the field of medicine due to the fact that it can give anatomic images of tissue with high resolution.[67] Although MRI itself can give detailed images for diagnosis, it is known that the resulting images may sometimes be not accurate due to small differences in relaxation time between the lesion

site and normal tissues. MRI contrast agents (CAs) that help to clarify images and improve contrast allow better interpretation.[68] Depends on their relaxation processes, the CAs can categorize into T_1 and T_2 CAs.[69] T_1 CAs are usually paramagnetic complexes;[70] while T_2 CAs are based on iron oxide NPs. Iron oxide NPs, which are the most representative magnetic nanoparticulate agents, have been used extensively due to their 1) suitable properties for high magnetization, 2) compatibility with biological systems, and 3) availability to attach functional ligands on the surface. [71] There have been numerous studies conducted to develop new MRI CAs based on magnetic NPs with improved magnetic properties and suitable surface characteristics.[72] A crucial step for the development of all the applications is to control the size, composition and morphology precisely in order to have the optimal impact on the final properties of the nanomaterials and their performances. Therefore, the question of how to better control size and magnetization of the NPs with reproducibility, and having simpler synthetic approach that generates large scale and time-efficient products for clinical translation are the main issues that need to be solved.[73]

2.2.3.2. Molecular design of SMNPs

It is known that the sizes of magnetic CAs would effect their magnetization.[73] Therefore, absolute control of the size and size distribution of magnetic CAs are the key parameters prior to proper investigate the correlation between the sizes and magnetic properties. To meet the requirements, we utilized supramolecular synthetic approach to generate supramolecular magnetic nanoparticles (SMNPs) with precise size control as a novel MRI CA. The SMNPs self-assembled from three molecular blocks, *i.e.*, 6 nm Ad-grafted zinc-doped iron oxide magnetic nanoparticles (Ad-ZnMNP), CD-PEI and Ad-PEG (**Figure 2.10.**). Surface modification of ZnMNP was prepared according to literature[74] to give Ad-ZnMNP, which can be recognized by

CD-PEI via Ad/CD-based molecular recognition. By simply mixing the ratio between the three molecular building blocks, a series of size-controllable SMNPs were obtained. With precise size controllability of SMNPs, we investigated the correlation between NPs' sizes and their magnetic properties. From a collection of SMNPs, we identified the optimal SMNPs with enhanced MRI performance that can serve as potential MRI CAs for numerous biomedical applications.

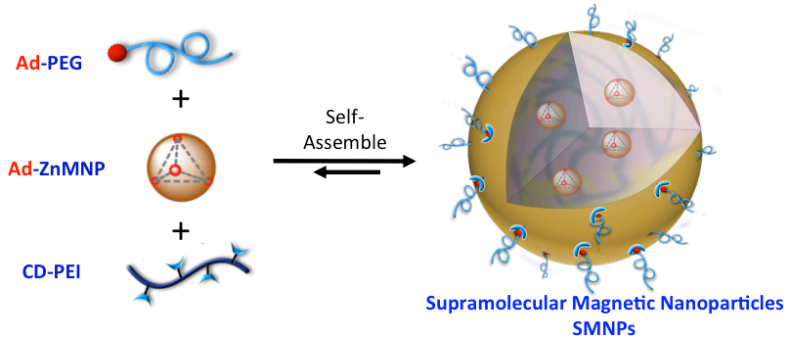

Figure 2.10. Schematic representation of self-assembly approach for preparation of supramolecular magnetic nanoparticles (SMNPs)

2.2.3.3. Size Controllability of SMNPs

A series of size-controllable SMNPs can be generated (**Figure 2.10.**) by slowly adding PBS with Ad-ZnMNP (1 μg/mL) to PBS solutions with variable amounts of CD-PEI (1.5–18 mg/mL) and Ad-PEG (4.5 mg/mL) under vigorous stirring, followed by incubating the resulting solution at room temperature for 20 min. The formation mechanism originally proposed for SNPs[43] can be applied to explain the size controllability observed for SMNPs. In short, the mixing ratios of the three molecular building blocks altered the equilibrium between the propagation/aggregation of the Ad-ZnMNP/CD-PEI hydrogel networks and the Ad-PEG induced capping/solvation of the hydrogel network and hence changes the equilibrium and led to the size changes of SMNPs. By find-tuning the ratios between the building blocks, SMNPs with sizes ranging from 20 nm to 200 nm can be obtained. TEM images of the resulting SMNPs in **Figure 2.11.** show the SMNPs

have spherical shapes with a narrow size distribution, which is a key criteria before investigating their magnetic properties.

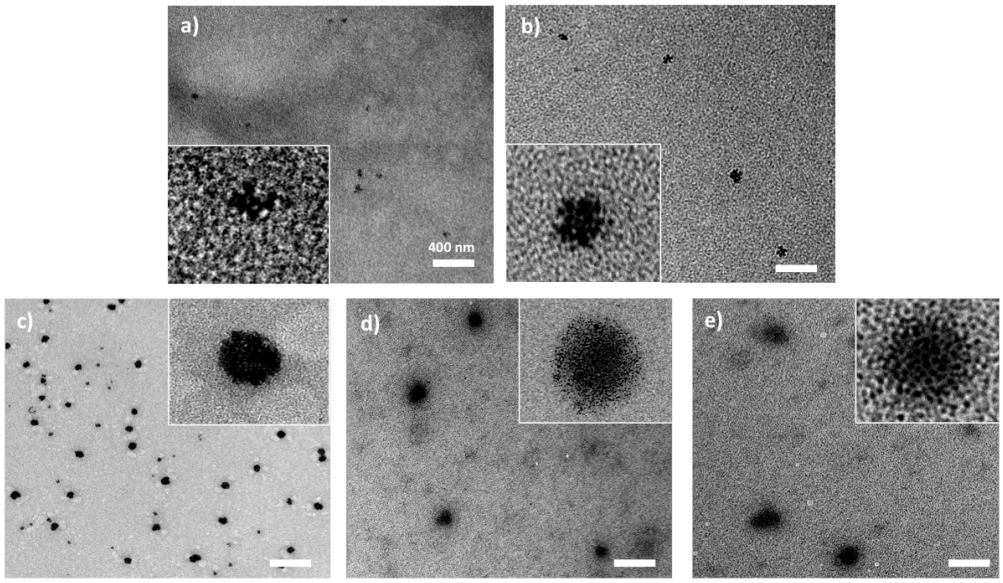

Figure 2.11. TEM images of size-controllable SMNPs ranging from (a) 20 ± 2 nm, (b) 40 ± 5 nm, (c) 80 ± 11 nm, (d) 150 ± 18 nm, and (e) 200 ± 25 nm. Scale bars: 400 nm. Inserts: Higher magnification TEM images of SMNPs for each size.

2.2.3.4. Application of SMNPs for MRI

To investigate the relationship between the sizes of SMNPs and their magnetic properties, T_2-weighted phantom images of 6 nm ZnMNP, 20 nm SMNPs and 80 nm SMNPs were acquired using a spin-echo pulse sequence (**Figure 2.12.**). We chose 20 nm and 80 nm SMNPs in this study as a proof-of-concept, which are also the proper size range relevant to clinical use.[41a] T_2-weighted images shows that 1) the assembled SMNPs enhance their magnetic properties compared to the non-assembled 6 nm ZnMNP and 2) as echo time (TE) increases, the 20 nm SMNPs have the highest contrast compared to the rest of the group. The results indicate the identified SMNPs, *i.e.*, 20 nm SMNPs, exhibit significant relaxivity improvement that can serve as powerful MRI CAs in the field of molecular imaging.

To sum up, these size-controllable SMNPs produced via self-assembly synthetic approach provide various potential applications. For example, SMNPs can be size-tailored and surface-modified[61] in order to accumulate in organs of interest for target imaging purposes. Also, their outstanding contrast improvement can lead to the potentials of detecting diseases at an earlier stage or monitoring their development that could benefit the medical field.

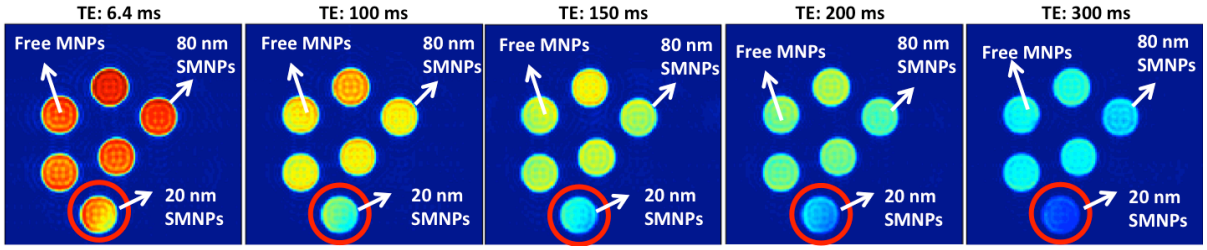

Figure 2.12. T_2-weighted phantom images acquired using a spin-echo pulse sequence. As TE increases, the 20 nm SMNPs yield better contrast compared to reference, MNPs, and 80 nm SMNPs.

2.2.4. Conclusion

In conclusion, we have successfully demonstrated the use of supramolecular self-assembly approach for synthesizing size-controllable inorganic supramolecular nanoparticles (see **Appendix** for reference[75]) from inorganic building block, *i.e.*, Au colloids or superparamagnetic iron oxide nanoparticles. We envision that 1) such a supramolecular synthetic approach could be used to assemble other "small" inorganic nanoparticles for broader applications in materials science and biomedicine; 2) diverse therapeutic loads (*e.g.*, DNA, proteins, and drugs) could be packaged into these inorganic SNPs with various functional ligands (*e.g.*, cell penetration ligand) for target delivery.

Chapter 3. MOLECULAR IMAGING

3.1. Introduction

Molecular imaging techniques are powerful tools in biomedical research for diagnosis due to the fact that they can specifically visualize, characterize and monitor biological processes at molecular level in living systems.[76] A wide variety of imaging techniques, including optical fluorescence imaging, computed tomography, positron emission tomography (PET), single photon emission computed tomography (SPECT), magnetic resonance imaging (MRI), and ultrasound imaging have been successfully employed in the field of molecular imaging.[76a, 77] To support the unmet need for *in vivo* molecular imaging, significant endeavors have been devoted to investigate the deign of highly sensitive and specific imaging probes.[78] Nanoparticle (NP)-based probes have been used extensively in molecular imaging that can enhance signal sensitivity, improve spatial resolution and better correlate the imaging information with biological systems at molecular levels.[79] NP-based probes with different modalities have their specific advantages that can acquire desired biological characteristics at different levels.[46] For example, NP-based probes conjugating radio-isotopes allow highly sensitive dynamic PET imaging that is capable of acquiring pharmacokinetic of radio-labeled NP-based delivery vectors, and can dramatically accelerate the study with minimum use of animals and consumption of samples (at pg to ng level).[77a] NP-based MRI contrast agents allow superb resolution for anatomical imaging.[46] Most importantly, the hyperthermia heating by the superparamagnetic nanoparticles can be utilized for controlling drug release from the delivery vector.[80] Noninvasiveness, high spatial resolution, three-dimension tomography, high accuracy, target specificity and real-time imaging are key requirements for the development of next-generation nanoparticle probes. In this chapter, I will introduce applications of SNPs in molecular imaging.

In **Chapter 3.2.**, SNP-based probes can be utilized for PET imaging that helps understand their 1) size-dependent lymph node trafficking and 2) whole-body biodistribution. Moreover, the incorporation of paramagnetic MRI CAs as one of molecular building blocks allows the exploration of the use of SNPs as new generation MRI CAs with improved contrast and sensitivity (see **Chapter 3.3.**).

3.2. Positron Emission Tomography (PET) Imaging

3.2.1. Nanoparticle-based PET imaging

Positron emission tomography[81] (PET) provides a noninvasive approach for imaging molecular processes in humans and animal models. Two key advantages of PET are sensitivity (due to the use of a radioisotope, probes can be detected at nM to pM levels) and tumor specificity. Cancer is highly amenable to probing by PET, since its development is based on specific genetic, molecular and functional changes (*e.g.*, leaky vasculature) in tumors. Nevertheless, developing effective PET probes that can preferentially accumulate in tumors remains one of the major challenges in oncologic PET imaging. Aside from small molecule and affinity ligand-based PET imaging probes, NPs exhibiting unique enhanced permeability and retention (EPR) effects[82] represent a new category of PET probes capable of passively targeting leaky vasculature – a universal characteristics observed for most solid tumors.[83] Over the past decades, a variety of NP PET probes[42, 79, 84] have been examined in pre-clinical setting, while challenges remain to further improve tumor uptake and reduce nonspecific distribution elsewhere. Specifically, their performance is constrained by NPs' intrinsic pharmacokinetics (PKs) – predominately affected by their sizes and surface properties.[85] Therefore, a promising solution for generating new NP PET probes with desired PK that can improve imaging performance is need. In this chapter, we utilize supramolecular synthetic approach to produce a SNP-based PET probe, which has

controllable size and proper surface properties that lead to desirable PK for improving the probe performance.

3.2.2. Self-assembled synthesis of ^{64}Cu-labeled SNPs for PET imaging

The versatility of supramolecular synthetic approach confers SNPs with multiple functions by incorporating a radioisotope, ***i.e.***, ^{64}Cu, into SNPs. DOTA-CD-PEI was synthesized as one of the molecular building blocks by introducing DOTA into the CD-PEI building block through peptide coupling reactions between the free amino groups in the CD-PEI and DOTA-NHS. The resulting DOTA-grafted SNPs were prepared by mixing the different ratios of three molecular building blocks- namely, 8-Ad-PAMAM, CD-PEI-DOTA and Ad-PEG in the respective ratios as described in the **Chapter 2**. Labeling by ^{64}Cu in consequent, ^{64}Cu-labeled SNPs can be obtained (**Figure 3.1.**).

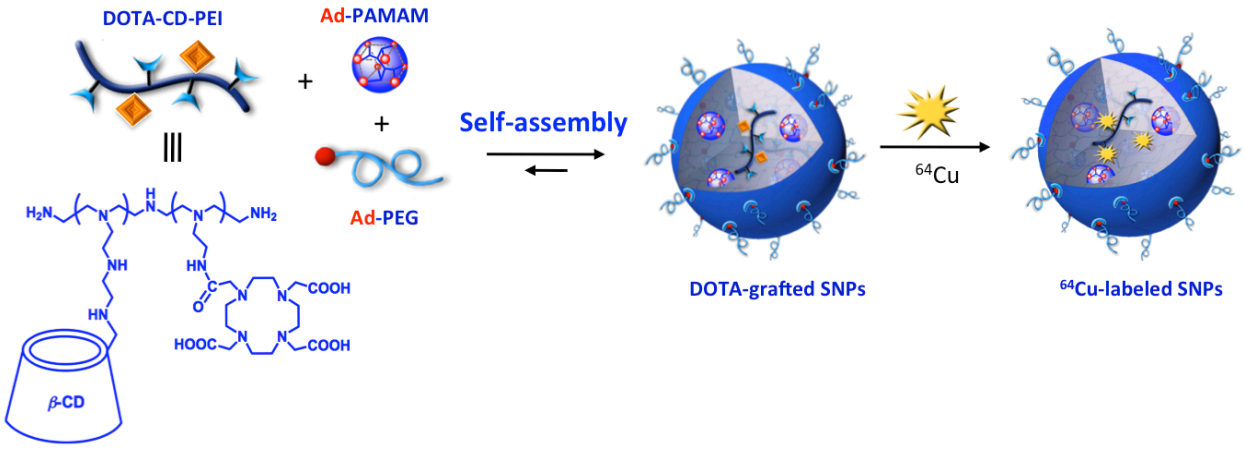

Figure 3.1. Schematic illustrating the preparation of DOTA-grafted SNPs. By incorporating a radioisotope, *i.e.*, ^{64}Cu, into SNPs, ^{64}Cu-labeled SNPs can be generated.

To explore the use of the SNPs for immune modulation, we investigated the lymph node trafficking of both 30-nm and 100-nm ^{64}Cu-labeled SNPs by using front footpad injection (**Figure 3.2.**). Due to the fact that the path of lymph drainage from footpad injections is well known, this is a common method for the delivery of immunological agents.[86] MicroPET/CT

imaging was carried out for 40 minutes (**Figure 3.2.**, left) and 20 hours (**Figure 3.2.**, right) immediately after injecting the 30-nm and 100-nm SNPs into different sides of the footpads of a mouse. We observed that the 30-nm SNPs drained into the local auxiliary lymph node and peaked at 5 minutes post injection with (58.6 ± 15.6)% ID/g of signal accumulation. This signal decreased to (26.6 ± 5.8)% ID/g at 40 minutes post injection, and further reduced to (7.0 ± 2.2)% ID/g by 20 hours post injection. On the other hand, there was no significant accumulation detected in the lymph nodes on the same side where the 100-nm SNPs were injected. The results revealed that the sizes of the SNPs are critical factors for their lymph node trafficking.

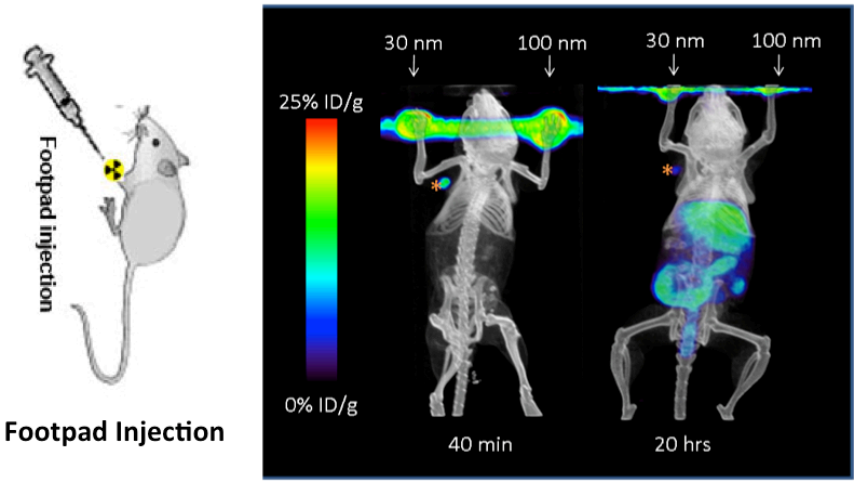

Figure 3.2. Lymph node trafficking studies of SNPs using front footpad injections. The 30-nm and 100-nm SNPs were injected on different sides of footpads of a mouse. MicroPET/CT was carried out for 40 min immediately after injection (left) and 20 h after injection (right).

We characterized the *in vivo* biodistribution (**Figure 3.3.**) of the 30-nm and 100-nm ^{64}Cu-labeled SNPs (composed of the 8-Ad-PAMAM-based dendrimer) by systemically injecting the SNPs into mice through the tail veins. MicroPET/CT studies suggested that the biodistribution patterns of the 30-nm and 100-nm SNPs were quite similar (**Figure 3.3.a** and **b**). In both cases, rapid blood clearance through liver accumulation (30–50% ID/g of the SNPs accumulated in the liver within 5 min after injection) was observed, and there was less accumulation in the kidneys

(16–20% ID/g) and lungs (8–12% ID/g). The results show that the size of SNPs is a crucial factor that affects their *in vivo* properties (see **Appendix** for reference[43]).

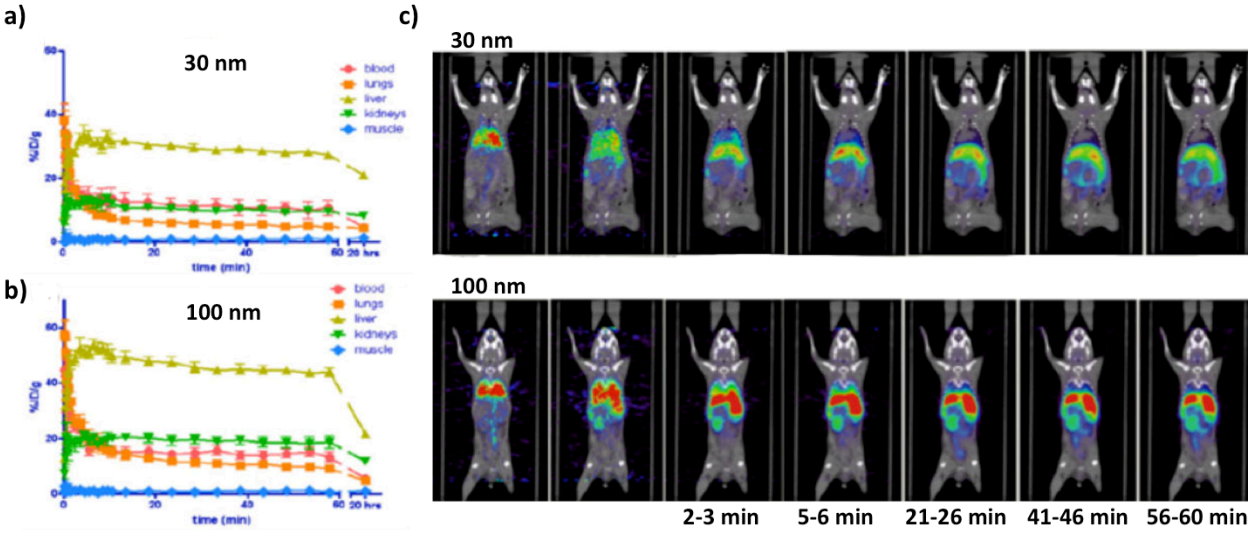

Figure 3.3. a) and b) Time-activity curves of mice that received the tail vein injection of the 30-nm and 100-nm SNPs, respectively. c) Time-resolved microPET/CT images from a 1h dynamic scan. Top panel shows the images from a mouse that received the 30-nm DOTA-grafted SNPs via tail vein injection and lower panel is from a mouse treated with 100-nm SNPs.

3.3. Magnetic Resonance Imaging (MRI)

3.3.1. Nanoparticle-based MR imaging

Magnetic resonance imaging (MRI) is a medical imaging technique capable of three-dimensional (3D), high-resolution visualization of specific tissues or organs in the body and has been extensively used in neurological, cardiovascular, and oncological diagnosis.[87] Paramagnetic MRI contrast agents (CAs), usually composed of gadolinium(III) ion (Gd^{3+}), are capable of reducing the longitudinal relaxation time (T_1) of surrounding water protons, thus increasing signal intensity in T_1-weighted MRI. In general, the performance of T_1-weighted MRI CAs is determined by the relaxivity (r1), which can be correlated to several parameters, including 1) loading capacity (Gd^{3+} quantity in the intraparticular space) and 2) water accessibility (the distance of closest approach between water and Gd^{3+}, the number of water molecules associated

with Gd^{3+}, and/or the diffusion of water) as described by relaxation theory.[88] Based on this fundamental understanding, researchers have incorporated Gd^{3+} onto or into nanoscale carriers to enhance r1 of paramagnetic CAs. Compared to small Gd^{3+} chelated complexes alone, nanocarriers (*e.g.*, dendrimers,[89] polymers,[90] liposomes,[91] and inorganic nanoparticles (NPs)[92]) allow dramatically increased Gd^{3+} loading. In some cases, poor water accessibility to the intraparticular Gd^{3+} buried inside the carriers can compromise the performance in T_1-weighted MRI[93] and this challenge can be tackled by; for example, using porous nanocarriers[94] where a water molecule can travel from the bulk water into the interior space. Nevertheless, fine-tuning the balance of the relevant parameters in a synergistic fashion is challenging due to the lack of direct correlations among the parameters, not to mention the unsatisfactory synthetic approach employed for the development of Gd^{3+}-incorporated nanocarriers that are considered to be time-consuming and cumbersome.[95] Therefore, there is a need to establish a method capable of effective optimization of all parameters to achieve high relaxivity enhancement of T_1-weighted MRI CAs.

3.3.2. Design of molecular building blocks

We set out to further explore such a self-assembled approach to develop Gd^{3+}•DOTA-encapsulated SNPs (Gd^{3+}•DOTA⊂SNPs) that can be utilized as highly efficient T_1-weighted MRI CAs (see **Appendix** for reference[96]). In our design, Gd^{3+} chelated complex (Gd^{3+}•DOTA) is covalently conjugated onto CD-PEI building block to give Gd^{3+}•DOTA-CD-PEI, which enhances r1 due to a distinct chemical environment with a high Gd^{3+} loading capacity inside the pseudo porous polymer-dendrimer hydrogel network and good water accessibility to the intraparticular space. By altering the mixing ratios among Gd^{3+}•DOTA-CD-PEI and the other two molecular building blocks, *i.e.*, Ad-PAMAM and Ad-PEG (**Figure 3.4.**), a small library of

Gd^{3+}•DOTA⊂SNPs can be produced with different sizes and cross-linking degrees of the corresponding hydrogel networks. A systematic variation of SNP sizes and cross-linking degrees results in a broad performance diversity of r1 in the Gd^{3+}•DOTA⊂SNPs library due to the respective changes in relaxation parameters. By finding the balance between the material's properties and r1 performance of the resulting library, Gd^{3+}•DOTA⊂SNPs can serve as a powerful and efficient SNP-based T_1-weighted MRI CA for dynamic imaging of biological processes *in vivo*.

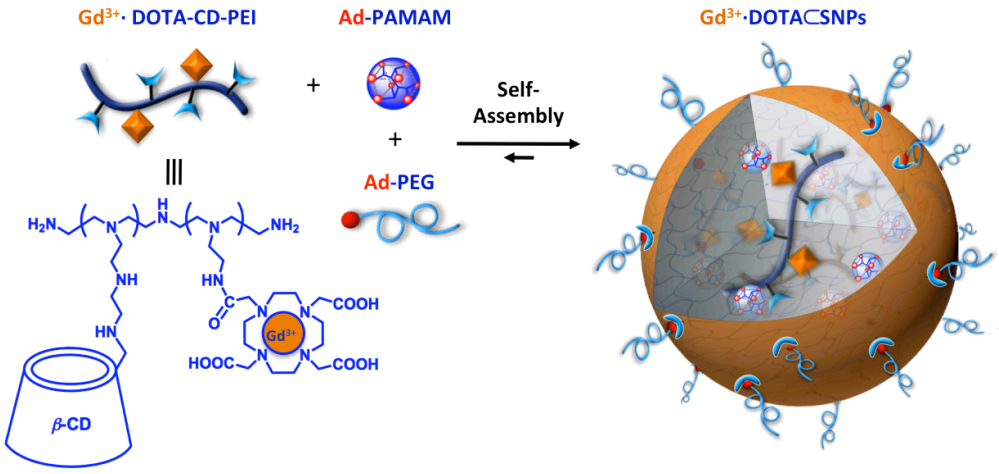

Figure 3.4. Schematic representation of self-assembly approach for preparation of Gd^{3+}·DOTA-encapsulated supramolecular nanoparticles (Gd^{3+}·DOTA⊂SNPs)

3.3.3. A combinatorial library of Gd^{3+}•DOTA⊂SNPs

By systematically changing (i) the concentration of encapsulated Gd^{3+} (0.32, 0.63, 1.61, 3.22, 3.90 and 6.44 mM) and (ii) the Ad-PAMAM/DOTA-CD-PEI ratios (1:1, 2:3, 1:2 and 1:3), a small library composed of 24 different formulations of Gd^{3+}•DOTA⊂SNPs (**Figure 3.5.**) was prepared. The size and cross-linking degree of the hydrogel core are dependent on the Ad-PAMAM/DOTA-CD-PEI ratio. The 24 different formulations of Gd^{3+}•DOTA⊂SNPs result from mixing Gd^{3+}•DOTA-CD-PEI (prepared at one of six Gd^{3+} concentrations) with solutions of Ad-

PAMAM/Ad-PEG (prepared at one of four Ad-PAMAM concentrations). The dynamic nature of the supramolecular synthetic approach leads to 80-95% of Gd^{3+} encapsulated into Gd^{3+}•DOTA⊂SNPs, which was quantified by ICP-MS. A broad spectrum of r1 emerges from the resulting Gd^{3+}•DOTA⊂SNPs library with r1 ranging from 4.19 s^{-1} mM^{-1} to 17.3 s^{-1} mM^{-1}. Measurements were performed in water on a 600 MHz NMR spectrometer and are presented in a mesh plot in **Figure 3.5.**. The results highlight an optimal synthetic formulation of $^{-1}$ (1:2 M ratio and 3.9 mM of Gd^{3+}) with a relaxivity of 17.3 s^{-1} mM^{-1}.

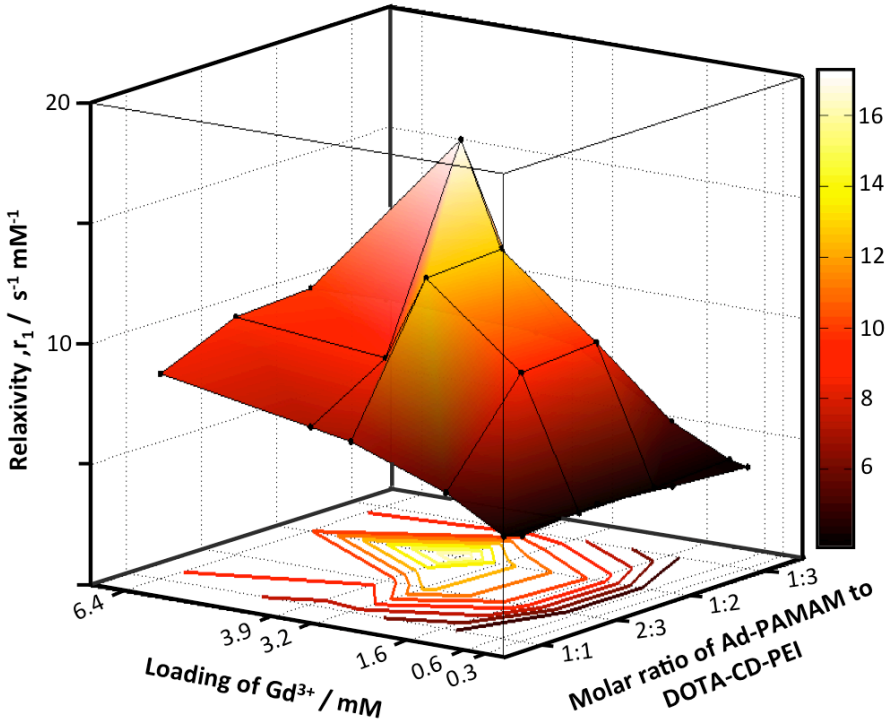

Figure 3.5. A mesh plot of r_1 relaxivity performance of Gd^{3+}·DOTA⊂SNPs with variation of (i) ratio of two molecular building blocks, *i.e.*, Ad-PAMAM and DOTA-CD-PEI, and (ii) loading of Gd^{3+} (24 data points). The peak value indicates the highest r_1 relaxivity (Gd^{3+}·DOTA⊂SNPs with a ratio of 1:2 and at a Gd^{3+} concentration of 3.9 mM).

3.3.4. Characterization of structures and stability of Gd^{3+}•DOTA⊂SNPs

We characterize the resulting optimized formulation, *i.e.*, Gd^{3+}•DOTA⊂SNPs by measuring the hydrodynamic size of Gd^{3+}•DOTA⊂SNPs with DLS, which is around 124 nm (**Figure 3.6.a**). As

shown in **Figure 3.6.b**, the TEM images indicate that Gd^{3+}•DOTA⊂SNPs in dry state have an average diameter of 103 ±10 nm with a spherical morphology and narrow size distribution. The stability tests of Gd^{3+}•DOTA⊂SNPs were carried out under two conditions: (i) 400 times dilution in water and (ii) 10% serum. The solutions were prepared from Gd^{3+}•DOTA⊂SNPs with 3.9 mM of Gd^{3+} and then incubated under the conditions for 24 h. The sizes of both solutions were characterized by TEM and summarized in **Figure 3.6.c.**. The original size of Gd^{3+}•DOTA⊂SNPs is 103 ±10nm (**Figure 3.6.c**, left). The size after 400 times dilution is 112 ±15 nm (**Figure 3.6.c**, center) and in 10% serum is 101±9 nm (**Figure 3.6.c**, right). There are no distinct changes in the average sizes of Gd^{3+}•DOTA⊂SNPs after dilution and in 10% serum; therefore, we conclude that the Gd^{3+}•DOTA⊂SNPs remain stable under these conditions.

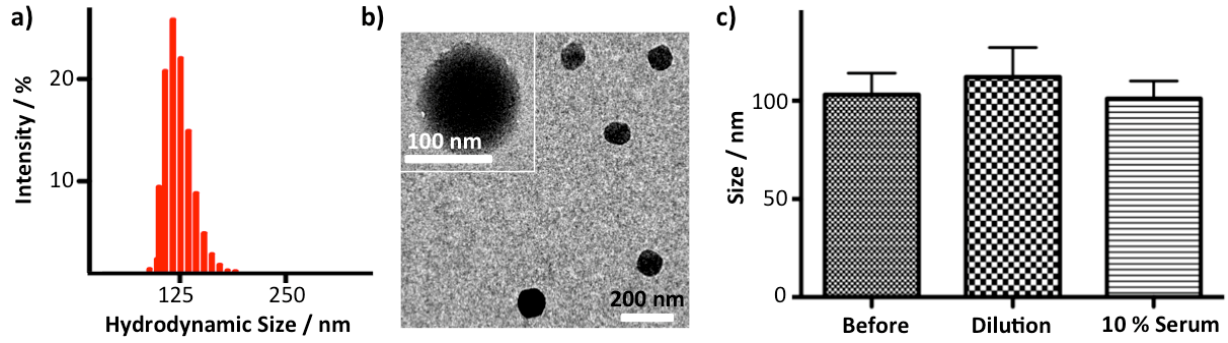

Figure 3.6. a) DLS results and b) TEM image show the narrow size distribution and spherical morphology of the resulting Gd^{3+}·DOTA⊂SNPs (formulate with a ratio of 1:2 and at a Gd^{3+} concentration of 3.9 mM). c) Stability studies of Gd^{3+}·DOTA⊂SNPs before (left) and after 24 h incubation under different conditions: 400 times dilution in water (center) and 10% serum (right). All the sizes of Gd^{3+}·DOTA⊂SNPs were characterized by TEM after 24 h incubation. (Each sample has at least 20 counts).

3.3.5. Sensitivity of Gd^{3+}•DOTA⊂SNPs as MRI CAs

To test feasibility of Gd^{3+}•DOTA⊂SNPs as a sensitive MRI CA, we performed a series dilution study of Gd^{3+}•DOTA⊂SNPs with deionized (DI) water to establish the minimum Gd^{3+} concentration detectable by MRI. **Figure 3.7.** shows T_1-weighted imaging results of the series

dilution for Gd^{3+}•DOTA⊂SNPs solution and Gd^{3+}•DTPA (**Figure 3.7.a**) at seven concentrations (from 195 to 4.88 μM) and **Figure 3.7.b** plots the C/N ratios as a function of Gd^{3+} concentration for Gd^{3+}•DOTA⊂SNPs (circles) and Gd^{3+}•DTPA (squares). The Gd^{3+}•DOTA⊂SNPs and Gd^{3+}• DTPA phantoms were imaged separately (note different scale bars) and the C/N ratio between Gd^{3+}•DOTA⊂SNPs and DI water are higher than the C/N ratio between Gd^{3+}•DTPA and DI water at all concentrations. The results indicate the significant sensitivity improvement and relaxivity enhancement of Gd^{3+}•DOTA⊂SNPs compared to Gd^{3+}•DTPA is maintained after diluting the CA solutions down to μM concentrations of Gd^{3+}.

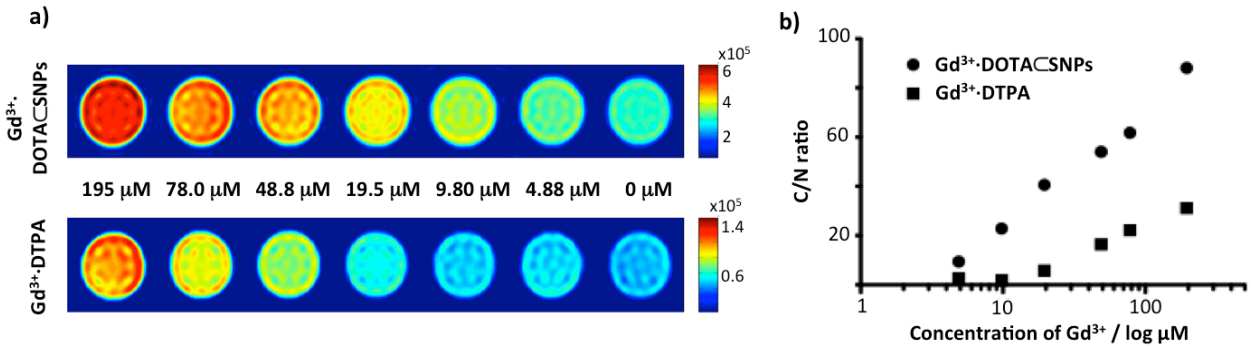

Figure 3.7. a) Phantom images for capillaries containing Gd^{3+}·DOTA⊂SNPs (formulate with a ratio of 1:2 and at a Gd^{3+} concentration of 3.9 mM, top) and Gd^{3+}·DTPA diluted with deionized water (bottom). The capillary on the right contains deionized water (labeled 0 μM) and the concentration of Gd^{3+} in the capillaries increases from 4.88 μM to 195 μM from right to left. b) Plot of contrast-to-noise (C/N) ratios as a function of Gd^{3+} concentration for Gd^{3+}·DOTA⊂SNPs (circles) and Gd^{3+}·DTPA (squares) of the phantom images. The C/N ratio between Gd^{3+}·DOTA⊂SNPs and DI water is higher than the C/N ratio between Gd^{3+}·DTPA and DI water at all concentrations.

3.3.6. Imaging Gd^{3+}•DOTA⊂SNPs in a mouse model

The lymphatic system is a common route for metastatic spread of cancer.[97] Dynamic imaging of lymphatic drainage has been regarded as a powerful diagnostic protocol for monitoring cancer metastasis. Here, we attempted to explore the use of Gd^{3+}•DOTA⊂SNPs as a new type of NPs for dynamic imaging of lymphatic drainage compared with conventional Gd^{3+} chelated

complexes. **Figure 3.8.** shows 3D maximum intensity projection (MIP) T_1-weighted *in vivo* imaging results before and after injecting Gd^{3+}•DOTA⊂SNPs into NOD/SCID mice. The yellow circles in the figure contain the right brachial lymph node of the mouse. We injected 20 μL of a 3.9 mM Gd^{3+}•DOTA⊂SNPs solution into the front right foot pad of a NOD/SCID mouse and monitored the changes with MRI. The draining of the lymph nodes was clearly visualized with the Gd^{3+}•DOTA⊂SNPs. The average voxel signal intensity increases in the right brachial lymph node after injecting Gd^{3+}•DOTA⊂SNPs but not after injecting Gd^{3+}•DTPA. Meanwhile, the average signal intensity in the left brachial lymph node remains around 20% less than the right lymph node. After 12 h, the average signal intensity in both lymph nodes decreases close to the values before injecting the Gd^{3+}•DOTA⊂SNPs.

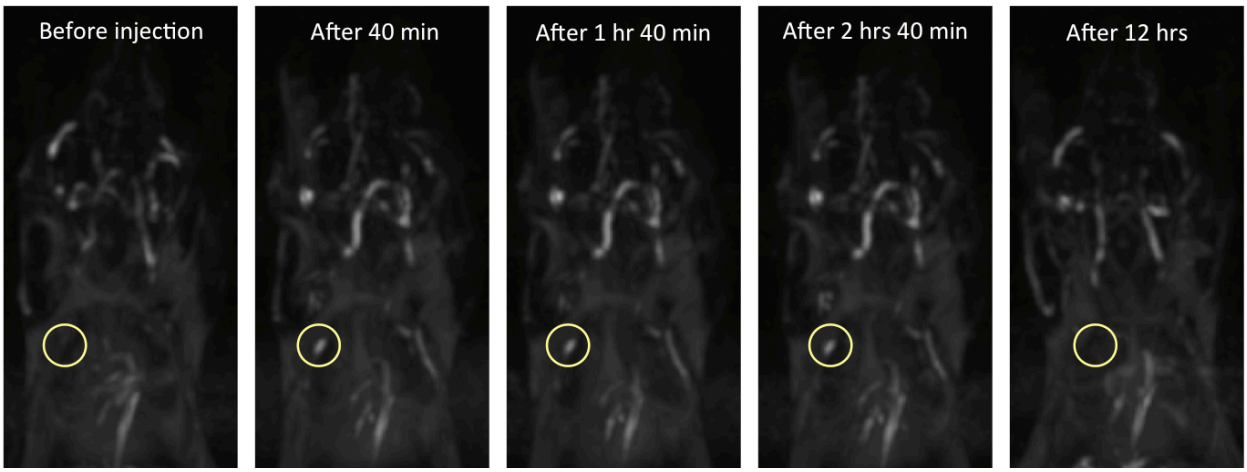

Figure 3.8. Three-dimensional (3D) T_1-weighted MR images show dynamic lymphatic drainage of Gd^{3+}·DOTA⊂SNPs. The yellow circle contains the right brachial lymph node. The five images were acquired before injecting and at four times after injecting 20 μL of Gd^{3+}·DOTA⊂SNPs (formulate with a ratio of 1:2 and at a Gd^{3+} concentration of 3.9 mM) as labeled.

3.3.7. Validation by *ex vivo* quantification

To support the detection of Gd^{3+}•DOTA⊂SNPs drainage in the brachial lymph node with MRI, we carried out ICP-MS analysis on *ex vivo* tissues removed at two time points after injecting MRI CA, *i.e.*, Gd^{3+}•DOTA⊂SNPs and Gd^{3+}•DTPA, into the front foot pad of the mice following

the same procedure used for *in vivo* imaging. We removed the brachial lymph nodes of mice after 30 min and 2.5 h. The brachial lymph nodes were dissected and underwent ICP-MS measurements. The ICP-MS analysis in **Figure 3.9.b** reveals that Gd^{3+} concentration decreased by approximately 6% after 2.5 h. As a comparison, the Gd^{3+} concentration from mice treated with Gd^{3+}•DTPA was negligible and close to the baseline measurement on untreated brachial lymph node tissue. The results show that the ICP-MS measurements are in good agreement and validate the *in vivo* T_1-weighted MRI results. These results show that Gd^{3+}•DOTA⊂SNPs not only exhibits enhanced relaxivity and high sensitivity but also can serve as a potential tool for diagnosis of cancer metastasis.

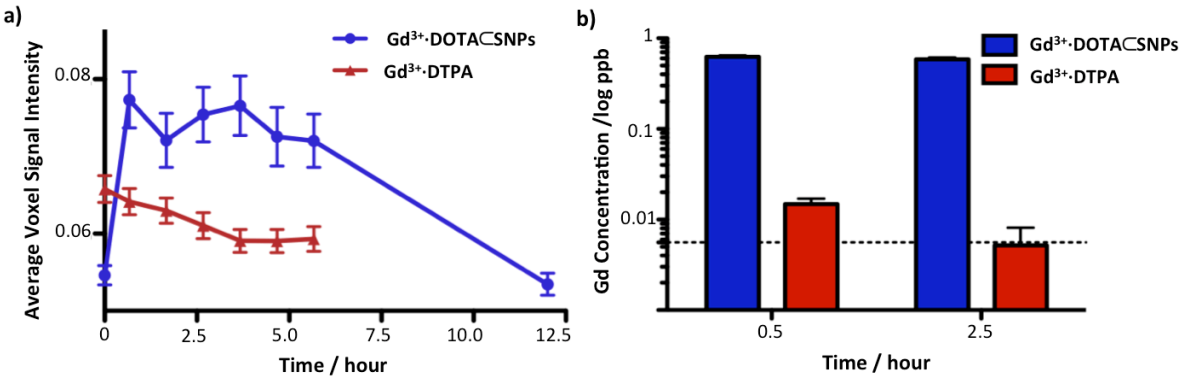

Figure 3.9. a) Average voxel signal intensity plotted as a function of image acquisition time (0 h represents data acquired before injecting the MRI contrast agents). b) Gd^{3+} concentration from ICP-MS measurements on lymph node tissue removed 30 min and 2.5 h after injecting the MRI contrast agents. Dashed line represents the baseline measurement on untreated brachial lymph node tissue. Note the log scale for the Gd^{3+} concentration axis.

Chapter 4. GENE/PROTEIN DELIVERY

4.1. Introduction

Among the existing delivery systems, NPs have been regarded as promising non-viral vectors for delivering either a gene[41a, 98]or a protein[99] into specific types of cells[100] or tissues.[101] NPs with favorable delivery characteristics usually possess sizes ranging between ten to a few hundred nanometers.[102] Gene or protein payloads can be encapsulated inside their intraparticular spaces,[103] avoiding potential degradation over the delivery process. It is conceivable that the ample intraparticular capacity[104] of NPs allows simultaneously incorporation of multiple payloads, *e.g.*, gene and protein molecules. In addition, NPs have sufficient surface area to accommodate multiple functional ligands that enable specific recognition of target cells and/or foster cellular internalization.[79, 102a, 105] Therefore, NPs could serve as a prime delivery vector with superb efficiency and specificity. In this chapter, we present a novel SNPs delivery system for gene and protein delivery. Also, in conjunction with miniaturized high throughput screening platform, a combinatorial library of SNPs with diverse structural (sizes and shapes) and functional (surfaces chemistry and charges) properties can be rapidly programmed, which can lead to ground-breaking breakthroughs in NP-based delivery systems.

4.2. Gene Delivery

4.2.1. NP-based gene delivery

Gene therapy generally requires delivery vehicles that are capable of (i) carrying/protecting genetic materials, *e.g.*, DNA and siRNA, and (ii) target-specific delivery to desired tissues or subsets of cells.[106] Over the past decades, significant endeavors have been devoted to develop

non-viral gene delivery vehicles as alternatives to their viral counterparts, whose applications are restricted due to the potential safety issues and complex processes of preparing. Among the existing non-viral gene delivery systems,[107] nanoparticle-based gene delivery vehicles[108] have received extensive attention.

4.2.2. Molecular design of DNA-encapsulated SNPs (DNA⊂SNPs)

Given the fact that the interior of SNPs is composed of a cationic Ad-PAMAM/CD-PEI hydrogel network, it is conceivable that SNPs can encapsulate anionic plasmid DNA via electrostatic interactions. This new type of gene delivery system can provide significant protection of the encapsulated DNA from degradation in an extracellular context. Besides, the advantages of supramolecular synthetic approach allow the incorporation of targeting ligands onto DNA-encapsulated SNPs in order to have specific delivery to target cells. Therefore, we adopted our supramolecular assembly approach to prepare a small library of DNA-encapsulated SNPs (DNA⊂SNPs and RGD-DNA⊂SNPs) with controllable sizes and tunable surface coverage of a targeting ligand, *i.e.*, arginine-glycine-aspartic (RGD) peptide (**Figure 4.1.**). A two-step preparation process has been developed to first generate both 100-nm and 300-nm DNA⊂SNPs from Ad-PAMAM, CD-PEI, Ad-PEG and DNA, followed by in situ RGD ligand exchange of DNA⊂SNPs to give six different RGD-DNA⊂SNPs with ligand coverage of 1, 5 and 10 mol% (based on Ad-PEG). Here, a plasmid DNA encoded with an enhanced green fluorescent protein (EGFP) driven by a CMV promoter was used as a reporter system, and the RGD ligand[109] was employed to recognize the $\alpha_v\beta_3$ integrin receptor on the membranes of certain types of tumor cells (see **Appendix** for reference[61]).

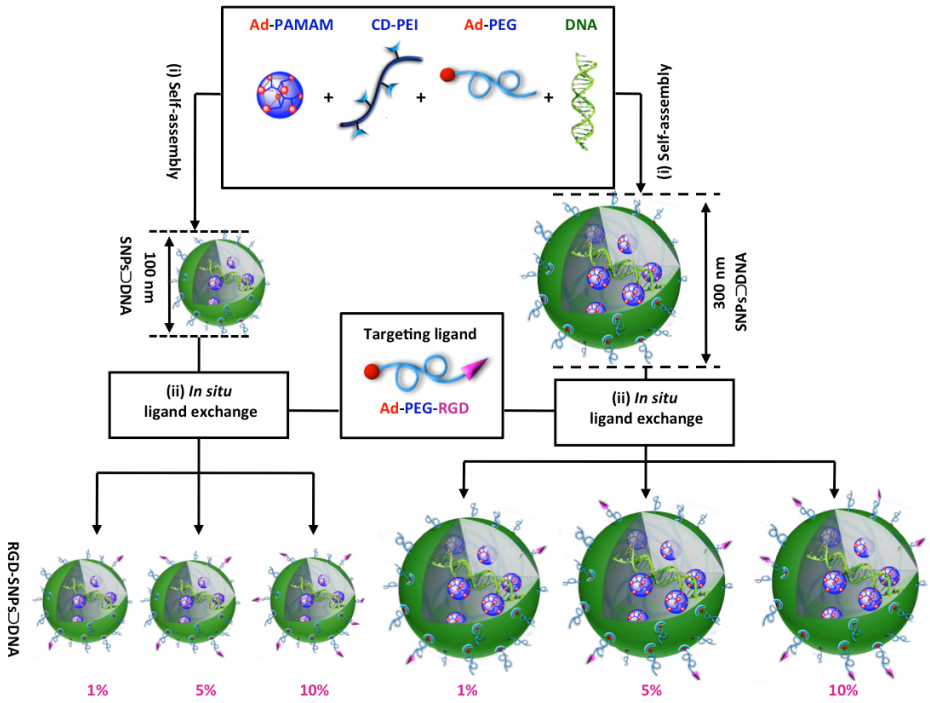

Figure 4.1. A two-step modular assembly approach for preparation of a small library of DNA-encapsulated supramolecular nanoparticles (DNA⊂SNPs and RGD-DNA⊂SNPs) with controllable sizes and tunable RGD ligand coverage.

4.2.3. Size controllability of DNA⊂SNPs

We first determined the DNA loading capacity to be used for preparation of DNA⊂SNPs and RGD-DNA⊂SNPs. The DNA loading capacity of SNPs depends on the net cationic charges embedded in the interior Ad-PAMAM/CD-PEI hydrogel network. We utilized both electrophoresis analysis[110] and ethidium bromide exclusion assay[111] to measure the DNA loading capacity of the Ad-PAMAM/CD-PEI hydrogel, resulting in the respective nitrogen/phosphate (N/P) ratios of 2.6 and 5.0. The N/P ratio of 5.0 was chosen to ensure complete DNA encapsulation in our studies. Next, DNA⊂SNPs with 100 and 300 nm diameters were prepared separately by slowly adding a PBS solution of CD-PEI (600 nM) into PBS solution containing Ad-PAMAM (300 nM for 100-nm DNA⊂SNPs and 600 nM for 300-nm DNA⊂SNPs), Ad-PEG (3 μM) and DNA (2.2 nM), followed by incubation at room temperature

for 20 min. The DLS measurements indicated that the hydrodynamic sizes of the 100 and 300 nm DNA⊂SNPs were 106±14 and 312 ±47 nm, respectively. Subsequently, the samples of each size of DNA⊂SNPs were split into four aliquots, and three of them were subjected to the in situ ligand exchange by adding 30, 150 or 300 nM of Ad-PEG-RGD (**Figure 4.1.**). A collection of RGD-DNA⊂SNPs with different RGD coverage, namely 100-1%, 100-5%, 100-10%, 300-1%, 300-5% and 300-10%, were obtained accordingly. After in situ ligand exchange, the hydrodynamic sizes of RGD-SNPs*DNA exhibited negligible changes (<5%). The morphologies of DNA⊂SNPs and RGD-DNA⊂SNPs were then examined by using TEM. The TEM images (**Figure 4.2.**) showed smaller sizes (62±8 for 100 nm DNA⊂SNPs and 210 ±24 nm for 300 nm DNA⊂SNPs), spherical shapes and narrow size distributions of DNA⊂SNPs and RGD-DNA⊂SNPs.

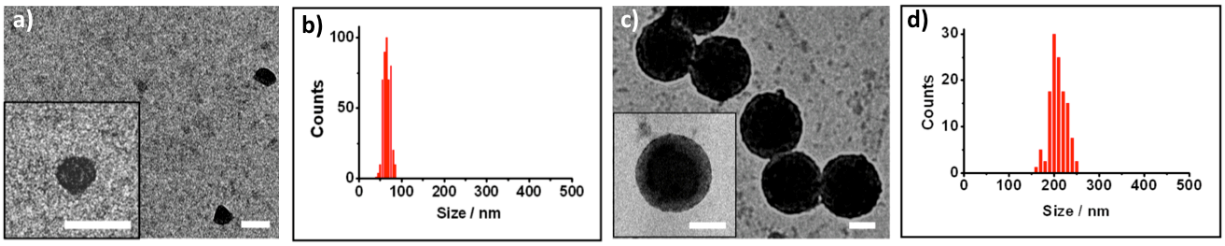

Figure 4.2. TEM images and histograms of 100 nm DNA⊂SNPs (a and b, respectively) and 300 nm DNA⊂SNPs (c and d, respectively). Insets: the respective higher magnification TEM images. Scale bars: 100 nm

4.2.4. Gene delivery performance of DNA⊂SNPs

We carried out an *in vitro* EGFP transfection study of a collection of DNA⊂SNPs and RGD-DNA⊂SNPs along with the controls, *i.e.*, DNA, DNA complexes of CD-PEI, CD-PEI/Ad-PEG and RGD-jet-PEI, in 8-well chamber slides containing two $\alpha_v\beta_3$ high-expressed cells (*i.e.*, U87 and scraping-collected 3T3 cells)[112] and two $\alpha_v\beta_3$ low-expressed cells (*i.e.*, MCF7 and 0.25% trypsin-treated 3T3 cells).[113] For the purpose of comparison, an equal amount of EGFP-encoded

plasmid DNA (100 ng) was added to individual cell culture chambers in the transfection study. The resulting 48 individual EGFP transfection experiments were incubated at 37 °C (5% CO_2) for 24 h. After paraformaldehyde fixation and DAPI nuclear staining, a fluorescence microscope was used to quantify the EGFP expression levels in individual cells. These levels were then used to determine the transfection efficiency for each vehicle. The transfection study was repeated three times, and the results of average transfection efficiency of gene delivery vehicles for different cell lines were summarized in **Figure 4.3.a.**. First, DNA complexes based on each of the molecular building blocks (CD-PEI and CD-PEI/Ad-PEG) gave very poor transfection performance similar to free plasmid DNA, indicating that the formation of supramolecular nanoparticles is crucial for achieving enhanced transfection efficiency. Second, 100-nm RGD-DNA⊂SNPs appeared to exhibit higher transfection efficiency than those of 300-nm analogues. This observation is consistent with the results from the reported polymer-based gene delivery systems,[41a, 105b, 114] in which vehicles with 10–100 nm size range display better gene transfection efficiency. Third, 100-5% RGD-DNA⊂SNPs gave the highest transfection efficiency compared to those observed for DNA⊂SNPs and other targeted RGD-DNA⊂SNPs. The reduced transfection efficiency observed for 100-10% RGD-DNA⊂SNPs can be attributed to the excess amount of free RGD ligand in the culture medium, which compromised the targeted binding of RGD-DNA⊂SNPs as a result of a competition effect.[115] Overall, 100-5% RGD-DNA⊂SNPs demonstrated the best transfection efficiencies (57 ±11% and 31 ±8% for $\alpha_v\beta_3$ high-expressed 3T3 (**Figure 4.3.b**) and U87, respectively). These results are comparable to those observed for the commercially available RGD-jet-PEI (64 ±15% and 38 ±9% for $\alpha_v\beta_3$ high expressed 3T3 and U87, respectively), which is a well-known selective and efficient transfection reagent for integrin-expressing cell lines.[116] Fourth, in addition to high transfection efficiency, 100-5%

RGD-DNA⊂SNPs also exhibited outstanding delivery specificity to the $\alpha_v\beta_3$ high expressed cells, U87 (31 ±8%) and 3T3 (57 ±11%), over the $\alpha_v\beta_3$ low expressed cells, MCF7 (21 ±6%) and trypsin-treated 3T3 (15 ±4%). Four-fold difference in transfection efficiencies were observed for 100-5% RGD-DNA⊂SNPs between $\alpha_v\beta_3$ high expressed and $\alpha_v\beta_3$ low expressed 3T3 cells, while only 1.2-fold difference was observed for RGD-jet-PEI. In contrast to non-target-specific transfection performance of RGD-jet-PEI, 100-5% RGD-DNA⊂SNPs had higher transfection efficiency for the U87 cell line with respect to the MCF7 cell line, which indicated good transfection specificity of RGD-DNA⊂SNPs for the $\alpha_v\beta_3$ high expressed cell lines. Moreover, we tested the toxicity of DNA⊂SNPs and RGD-DNA⊂SNPs by using cell viability assay. The cells transfected by DNA⊂SNPs and RGD-DNA⊂SNPs were compared with the cells cultured in normal medium. There were no significant differences in viability (97 ±2%), which suggested that the toxicity of DNA⊂SNPs and RGD-DNA⊂SNPs is negligible for *in vitro* transfection studies.

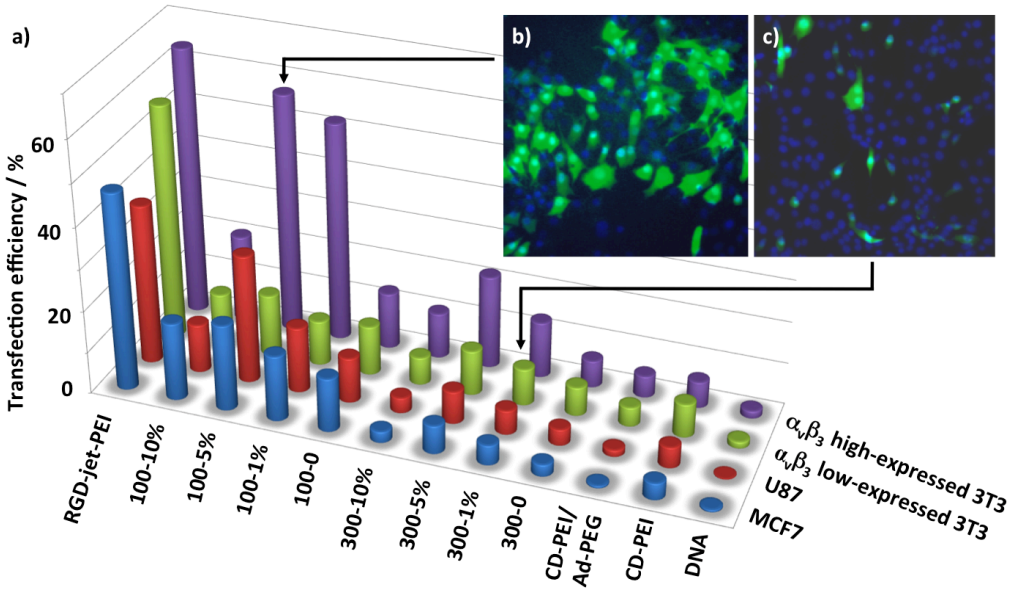

Figure 4.3. a) EGFP transfection efficiency of a collection of DNA⊂SNPs and RGD-DNA⊂SNPs along with control delivery systems for two $\alpha_v\beta_3$ high-expressed cells (U87 and scraping-collected 3T3 cells)

and two $\alpha_v\beta_3$ low-expressed cells (MCF7 and 0.25% trypsin-treated 3T3 cells). The representative fluorescence micrographs of 57 ± 11% and 9 ± 4% transfection efficiencies observed for b) 5 mol% RGD-grafted 100 nm RGD-DNA⊂SNPs (100-5%)-treated $\alpha_v\beta_3$ high-expressed 3T3 cells and c) 1 mol% RGD-grafted 300 nm RGD-DNA⊂SNPs (300-1%)-treated $\alpha_v\beta_3$ low-expressed 3T3 cells.

In conclusion, these results revealed that the size and target ligand coverage of RGD-DNA⊂SNPs played a critical role in the target-specific gene delivery. In conjunction with the use of a miniaturized high throughput screening platform[117] (see **Chapter 4.3**) and molecular imaging technology,[43] we will dramatically accelerate the discovery processes of SNPs-based gene delivery vehicles toward *in vivo* application.

4.3. Protein Delivery

4.3.1. NP-based protein delivery

Protein delivery[118] has been considered as the most straightforward strategy for modulating cellular behavior without the safety concerns and expression performance issues associated with gene deliver approaches. Two major challenges remain to be overcome in order to enable practical applications in biology and medicine 1) how to foster cellular uptake of protein molecules and 2) how to retain their stabilities and functions[119] over the delivery process. Recently, attempts have been made to develop a variety of delivery vectors, including liposomes,[120] polymer micelles,[121] and nanoparticle,[99a, 122] to enhance the uptake of protein molecules in target cells, and at the same time, to stabilize the encapsulated proteins. Owing to the time-consuming procedures employed in optimization of delivery materials, there has been limited progress in the field to date in order to in search of better delivery systems. Alternatively, recombinant technology[123] can be utilized to conjugate cell-penetrating peptides (CPPs)[124] onto protein molecules, which is consider the most commonly used protein delivery system with improved delivery efficiency. However, in this case, the major bottlenecks associated with the

complicated procedure of generating recombinant proteins and the lack of protection mechanism against protein denature need to be solved.

Transcription factor (TF) is a protein responsible for regulating gene transcription in cellular circuitry.[125] In general, TFs contain one or more DNA-binding domains (DBDs), which recognize matching DNA sequences adjacent to the genes they regulate. Apparently, highly efficient delivery of TFs can provide a powerful technology for modulating cellular behavior. One of the most important *in vitro* applications that required highly efficient TF delivery is generation of human induced pluripotent stem cells (hiPSCs), which has recently been demonstrated by introducing CPPs fused reprogramming TFs (*i.e.*, OCT4, SOX2, KLF4, and c-MYC)[126] into human somatic cells. The resulting hiPSCs have the potential to revolutionize regenerative medicine.[127] However, the high costs of the four reprogramming TFs in their recombinant forms makes the approach unlikely to be used for large-scale hiPSCs generation without further improvement in the delivery performance of the reprogramming proteins. Therefore, it is crucial to develop a new type of vector capable of delivering intact (unmodified) TFs in a highly efficient manner.

4.3.2. Molecular design of TF·DNA⊂SNPs

Considering the unique role of TF, we attempted to explore the use of SNPs as a new type of nanoscale vector for delivering intact (unmodified) TFs with an efficiency superior to that of existing approaches (see **Appendix** for reference[128]). Our idea is to achieve the encapsulation of a TF into cationic SNP vectors by introducing anionic characteristics to the TF. A DNA plasmid with a matching recognition sequence specific to a TF can be employed to form an anionic TF·DNA complex, which can be subsequently encapsulated into SNPs, resulting in TF encapsulated SNPs (TF·DNA⊂SNPs). In this proof-of-concept work, a mammalian orthogonal

fusion TF, GAL4-VP16 was chosen to serve as a model TF. Since GAL4-VP16 is an artificial transcription factor, there should be no background concentration in the mammalian cells employed in the delivery studies. To facilitate the encapsulation of the model TF into the SNP vectors, a DNA plasmid (*i.e.*, pG5E4T-Fluc) that contains five tandem copies of GAL4-VP16 matching recognition sequences and a conjugated luciferase reporter was designed. The incorporation of multivalent recognition sequences enhances dynamic binding between GAL4-VP16 and pG5E4T-Fluc, allowing improved encapsulation and dynamic releasing of the intact TF. In addition, the conjugated luciferase reporter can be specifically activated by GAL4-VP16, providing a real-time readout reflecting the activities of the TF after its intracellular delivery. As shown in **Figure 4.4.**, three types of molecular recognition mechanisms were employed to facilitate the preparation of TF·DNA⊂SNPs, including 1) specific binding between TF and matching DNA plasmid for formation of an anionic TF·DNA complex, 2) the Ad/CD-based molecular recognition for generation of SNP vectors with cationic hydrogel cores, and 3) electrostatic interactions that facilitate encapsulation of anionic TF·DNA into SNPs.

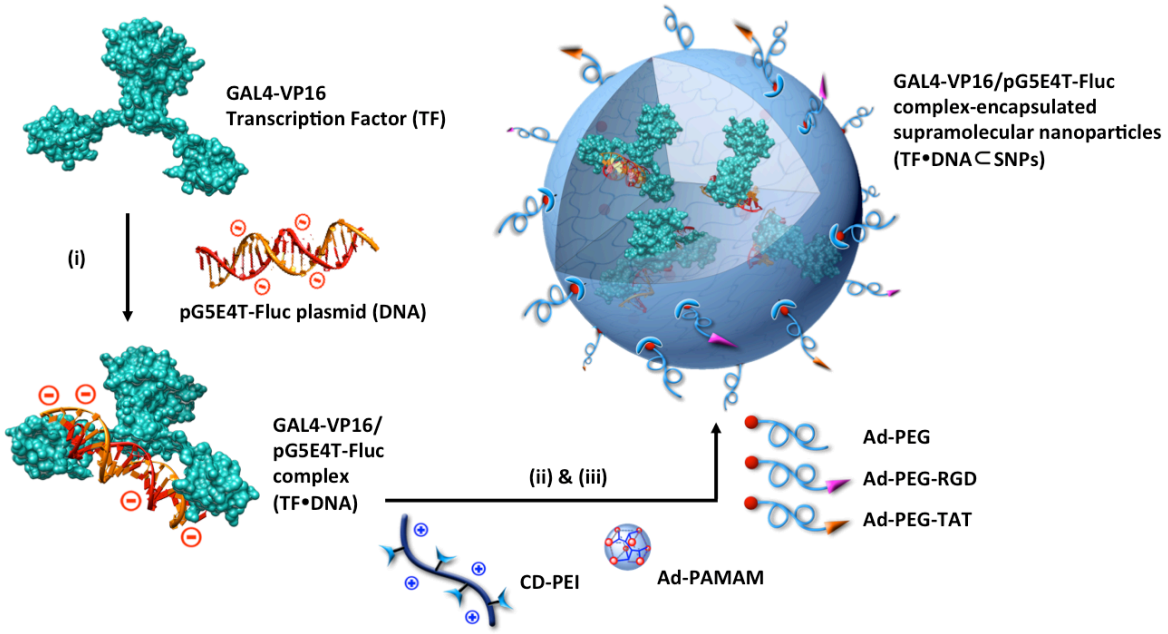

Figure 4.4. Schematic representation of self-assembly approach for the preparation of transcription factor-incorporated supramolecular nanoparticles (TF·DNA⊂SNPs). Three types of molecular recognition mechanisms, including i) specific binding between GAL4-VP16 (a mammalian-orthogonal fusion TF) and pG5E4T-Fluc vector (with five tandem copies of GAL4-VP16 matching recognition sequences and a conjugated luciferase reporter) for formation of an anionic TF·DNA complex, ii) the Ad/CD-based molecular recognition for generation of SNP vectors with cationic PEI/PAMAM hydrogel cores, and iii) electrostatic interactions that facilitate incorporation of anionic TF·DNA into SNPs, were harnessed for the self-assembly of TF·DNA⊂SNPs by simply mixing TF·DNA with five functional molecular building blocks: CD-PEI, Ad-PAMAM, Ad-PEG, Ad-PEG-RGD, and Ad-PEG-TAT.

4.3.3. Size controllability of TF·DNA⊂SNPs

The preparation of TF·DNA⊂SNPs can be accomplished by simply mixing TF·DNA complex with other five functional building blocks (*i.e.*, CD-PEI, Ad-PAMAM, Ad-PEG, Ad-PEG-RGD, and Ad-PEG-TAT). Among the three ligand compounds, Ad-PEG plays a role of a capping/solvation reagent that can not only confine continuous propagation of the TF·DNA-encapsulated PEI/PAMAM hydrogel networks, but also impart desired water solubility, structural stability, and passivation performance to the resulting TF·DNA⊂SNPs. In addition, Ad-PEG-RGD and Ad-PEG-TAT, which were incorporated onto the surfaces of TF·DNA⊂SNPs during the one-pot mixing process,[61, 129] enable delivery specificity (to recognize a certain population of cells with $\alpha_v\beta_3$-integrin receptors) and cell transfusion capability (to foster internalization through membrane and releasing from endosome trapping), respectively, of TF·DNA⊂SNPs. The previous study revealed a set of optimal synthetic parameters[129] that produce DNA-encapsulated SNPs, which have good gene transfection performance. Additionally, the results suggested that the presence of both 5% RGD and 9% TAT ligands is a crucial factor in the enhanced efficiency.[129] In this study, we took the advantage of these optimal synthetic parameters for the preparation of TF·DNA⊂SNPs.

Prior to the preparation of TF·DNA⊂SNPs, GAL4-VP16 was incubated with a slight excess amount of pG5E4T-Fluc (GAL4-VP16/pG5E4T-Fluc=1: 0.35 n/n, each pG5E4T-Fluc contains

five tandem copies of GAL4-VP16 recognition sequences thus might accommodate more than one TF) for 30 min at 48 °C to generate TF·DNA. Subsequently, TF·DNA⊂SNPs were prepared by slowly adding CD-PEI (4.32 μg) in 1 μL PBS into a 19 μL of PBS solution containing TF·DNA complex (200 ng GAL4-VP16 and 2 μg pG5E4T-Fluc), Ad-PEG (5.94 μg), Ad-PEG-RGD (0.297 μg), Ad-PEG-TAT (0.535 μg), and Ad-PAMAM (0.528 μg). After a brief stirring, the mixture was incubated at 48 °C for another 30 min. To determine hydrodynamic size of the resulting TF·DNA⊂SNPs, we performed DLS measurements (**Figure 4.5.b**), indicating a uniform size of 50 ±3 nm. In parallel, the morphology of TF·DNA⊂SNPs was characterized by TEM, suggesting homogeneous, narrow size distributed spherical nanoparticles with size of 40 ±3 nm (**Figure 4.5.a**). Finally, the encapsulation rate of TF in TF·DNA⊂SNPs was characterized by quantifying the SNP-encapsulated TF. For the convenience of using a florescence spectroscopy, Cy5-labeled GAL4-VP16 was prepared and employed. The result indicated that more than 81 ±12 % of the TFs were successfully encapsulated into SNPs.

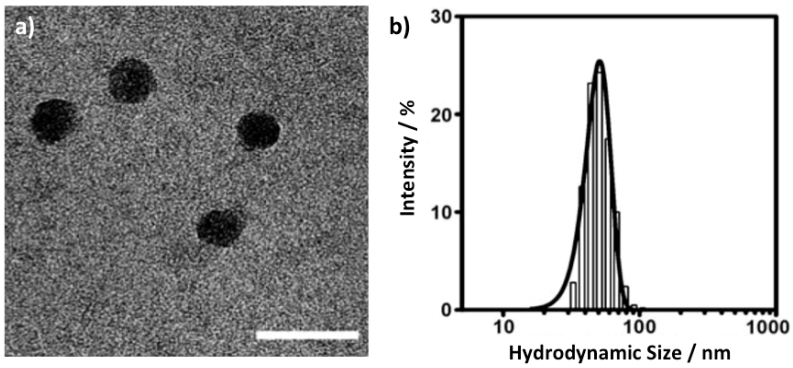

Figure 4.5. a) TEM image of TF·DNA⊂SNPs. Scale bar: 80 nm. b) Histogram summarizes the hydrodynamic size distribution obtained from DLS measurement.

4.3.4. Protein delivery performance of TF·DNA⊂SNPs

To examine the delivery performance of TF·DNA⊂SNPs, we perform the cell uptake studies using by incubating TF·DNA⊂SNPs (10 ng TF per well) with HeLa cells in a 96-well plate (10^4

cells per well). Again, GAL4-VP16 was labeled by Cy5 dye to allow quantitative monitoring of the delivery performance of TF·DNA⊂SNPs. Control experiments based on Cy5-labeled-TF alone (TF), Cy5-labeled-TF·DNA complex, and Cy5-labeled-TF with TAT-conjugation (TAT-TF) were carried out in parallel under the same experimental conditions. After incubation for various periods (*i.e.*, 0.5, 1, 2, 6, 12, and 24 h) and removal of non-uptake reagents in the media, the delivery performances of individual studies were quantified by measuring their fluorescence intensities in a plate reader. As shown in **Figure 4.6.b**, Cy5-labeled TF·DNA⊂SNPs exhibited dramatically enhanced delivery performance in contrast to those observed in the control studies. It is noteworthy that the delivery efficiency of TF·DNA⊂SNPs was approximately five times greater than that of TAT-TF, which is commonly used as a standard method for TF delivery. The time-dependent uptake studies (**Figure 4.6.c**) of TF·DNA⊂SNPs revealed that accumulation of the fluorescence signals increased with the incubation time and reached saturation at 12 h. Fluorescence micrograph (**Figure 4.6.c insert**) indicated that localization of Cy5-labeled TF in the cell nuclei, suggesting that the TF molecules were delivered to cell nuclei, where TF functioned as a regulator by controlling the translation of specific gene(s).

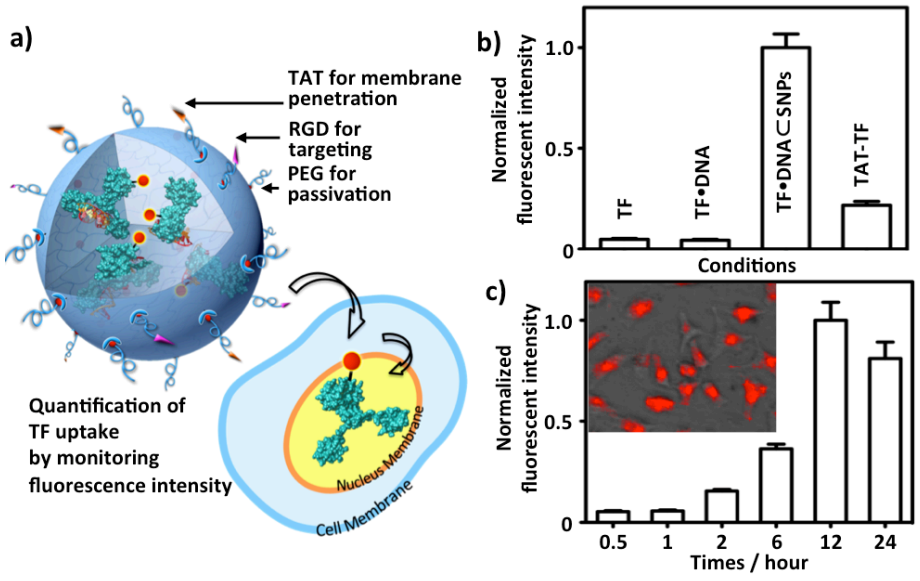

Figure 4.6. a) Quantification studies on the delivery performance of TF·DNA⊂SNPs. b) Delivery efficiency of Cy5-labeled TF·DNA⊂SNPs, Cy5-labeled-TF alone (TF), Cy5-labeled-TF·DNA complex, and Cy5-labeled-TF with TAT-conjugation (TAT-TF). c) Time-dependent uptake studies of TF·DNA⊂SNPs. Insert: Fluorescence micrographs of HeLa cells after incubating with TF·DNA⊂SNPs for 12 h. Cy5-labeled TF was localized in the cell nuclei, where TF functioned as a regulator to control the translation of a specific gene.

To confirm that the GAL4-VP16 (TF) retained its activity after delivery, we quantified the luciferase expression by measuring the bioluminescence intensity of TF·DNA⊂SNPs treated cells (**Figure 4.7.**). Again, the pG5E4T-Fluc (DNA) used in our study contains a luciferase reporter that can be specifically activated by GAL4-VP16. Therefore, the activity of GAL4-VP16 is reflected in the bioluminescence intensity of TF·DNA⊂SNPs-treated cells as a result of luciferase expression. After the incubation of HeLa cells with TF·DNA⊂SNPs and the control reagents (including SNP vector, TF·DNA, and DNA⊂SNPs), the cells were lysed for quantification of bioluminescence. After incubation with luciferin for 2 min, bioluminescence intensities were recorded by both a plate reader (**Figure 4.7.b**) and a cooled charge-coupled device (CCD) camera (**Figure 4.7.c**). Compared to the background-level bioluminescence intensities observed from the control experiments, the signal from TF·DNA⊂SNPs-treated cells is significantly higher, suggesting that the GAL4-VP16 retains its activity to trigger the luciferase expression after intracellular delivery. Moreover, the cell viability assays carried out at different doses of TF·DNA⊂SNPs indicated that the TF·DNA⊂SNPs exhibit negligible toxicity.

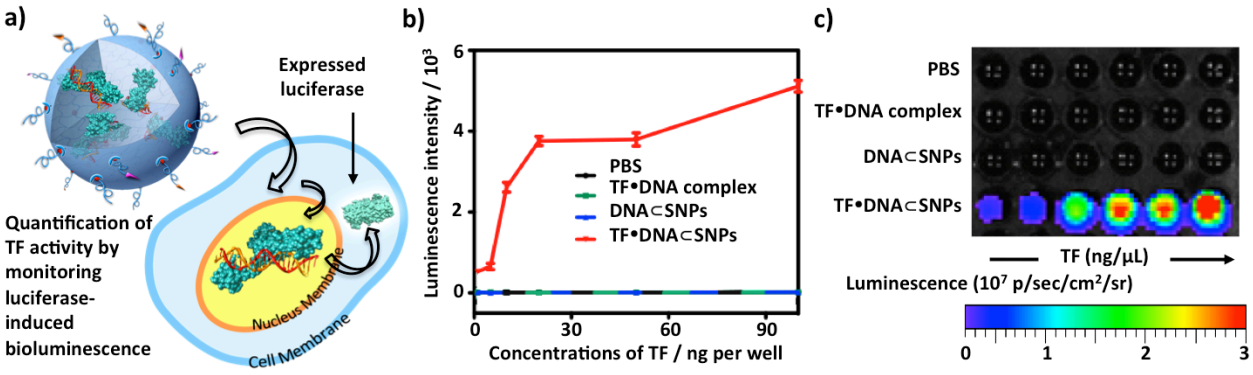

Figure 4.7. a) Bioluminescence study on TF·DNA⊂SNPs-treated cells. The activity of GAL4-VP16 can be reflected in the bioluminescence intensity as a result of luciferase expression. b) Dose-dependent profile and c) bioluminescence imaging of TF·DNA⊂SNPs-treated cells along with the controlled experiments based on TF·DNA complex and DNA⊂SNPs. Error bars in (b) were obtained from three independent experiments.

In conclusion, we believe such a TF delivery approach provides a powerful method for manipulating cellular behaviors. A potential application is for generating hiPSCs, which required the delivery of four reprogramming TFs. We note that, in conjunction with the use of a miniaturized highthroughput screening platform[117a, 129] (see **Chapter 4.3.**) and biological assays,[130] to achieve hiPSCs generation in a highly efficient manner, it is feasible to optimize the ratios of the four reprogramming TFs.

4.4. A Rapid Pathway Toward a Superb Gene Delivery System

4.4.1. Current challenges of NP-based delivery vectors

Gene delivery constitutes one of the most critical steps in gene manipulation and therapy.[131] By mimicking the size and function of viral vectors, numerous non-viral gene delivery systems based on biocompatible nanostructured materials;[41a, 132] for example, inorganic nanoparticles,[98a, 105a] carbon nanotubes,[109] liposomes,[133] cationic polymers[105b, 107b] and dendrimers,[134] have been developed to provide an alternative approach to the problems in viral gene delivery. However, an emerging challenge of nanoparticle-based delivery reagents is their low transfection performance.[41a] To overcome this problem, researchers have attempted to modulate[57a] the structural (sizes[135] and shapes) and functional (surfaces chemistry and charges) properties of nanoparticles,[57a] often requiring multiple optimization cycles to gradually improve the performance of nanoparticle-based delivery reagents. Such procedures have proven to be time intensive and have demonstrated limited diversity over the past decades. Alternatively, it is

believed that exploration of a new developmental pathway capable of rapid and parallel programming of a combinatorial library of NP-based delivery systems could lead to revolutionary breakthroughs in NP-based delivery systems (see **Appendix** for reference[136]).

4.4.2. Design of molecular building blocks

We developed a rapid developmental pathway (**Figure 4.8.**) that leverages the powers of (i) a combinatorial synthetic approach (**Figure 4.8.a**) based on supramolecular assembly[43, 137] and (ii) a digital microreactor[117a, 138] (**Figure 4.8.b-e**), toward the generation of a highly efficient nanoparticle-based gene delivery system. Unlike the slow, multistep syntheses employed for producing existing gene-delivery materials,[41a] our supramolecular method (**Figure 4.8.a**) enables a convenient, flexible, and modular method[61] for generating a combinatorial library of DNA⊂SNPs, in which a broad structural/functional diversity covering size variation, surface chemistry, and DNA loading capacity was programmed into individual DNA⊂SNPs by systematically altering the mixing ratios of five functional molecular building blocks (2-6), DNA plasmid (7a, enhanced green fluorescent protein (EGFP), and 7b, firefly luciferase (FLuc)). To reduce human operational errors, accelerate handling procedures, enhance experimental fidelity, and achieve economical use of reagents, a digital Dual-Core Microreactor (DCM, **Figure 4.8.b-e**) was designed and implemented to allow automated sampling, dilution, metering, and mixing of 2-7, resulting in a combinatorial library composed of 648 different DNA⊂SNPs within 2.5 h. The structural/functional diversity of the DNA⊂SNPs library can be translated into diversity in performance by conducting transfection studies of individual DNA⊂SNPs in 96 well plates containing mouse fibroblast cells. A small group of DNA⊂SNPs that facilitates high levels of delivery performance was identified. We then carried out comprehensive characterizations on these DNA⊂SNPs revealing that improved transfection performance can be attributed to the

defined size, surface chemistry, zeta potential, uniformity, and dynamic stability. Compared to the leading gene transfection reagents, such as lipofectamine 2000 and RGD-jet-PEI, the identified 40-nm TAT/RGD-DNA⊂SNPs (1) with defined surface chemistry exhibited significantly improved gene transfection efficiency and low toxicity in a number of cancer cell lines and fibroblast cells.

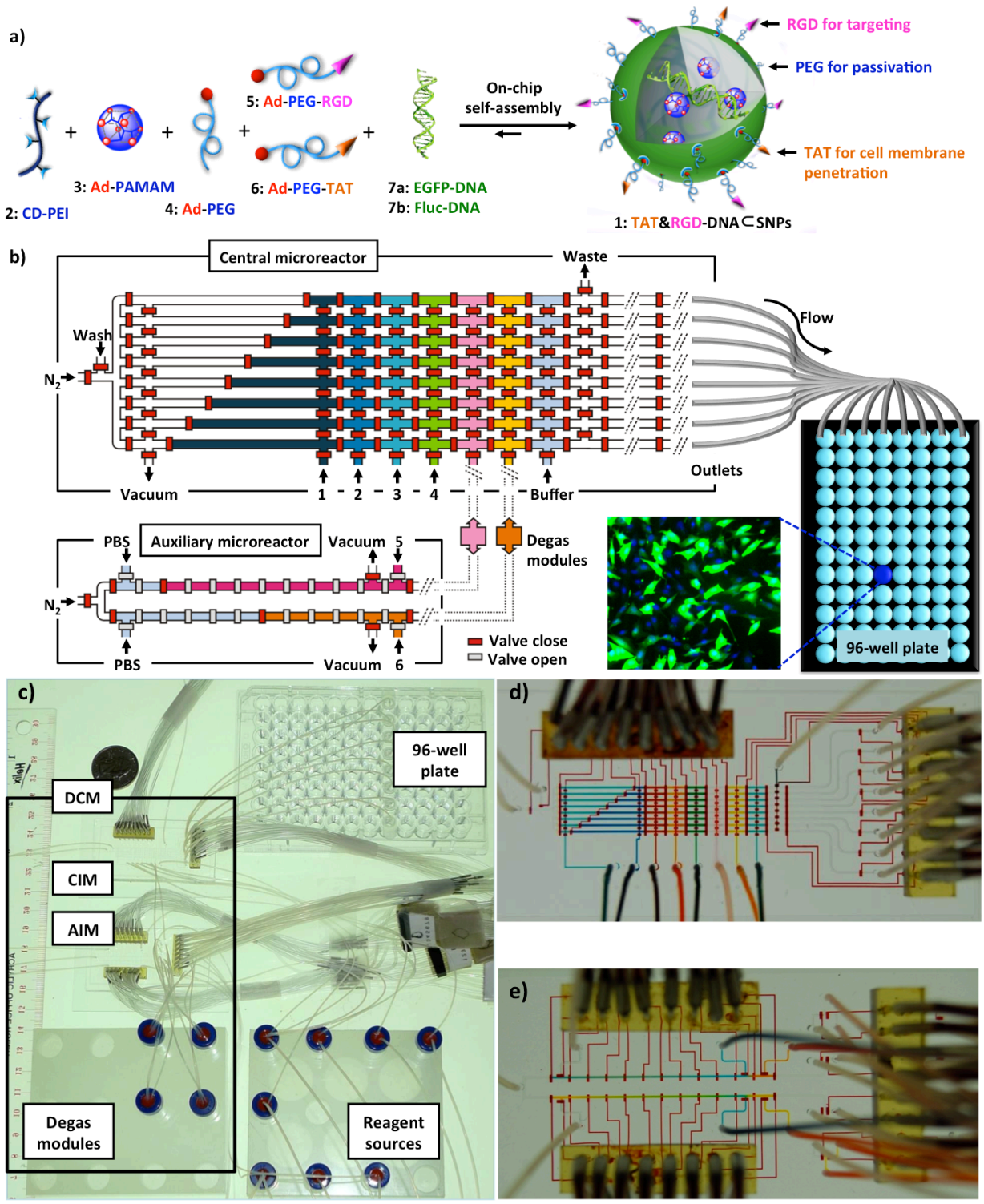

Figure 4.8. a) Graphical schematic representations of the self-assembly approach for producing a combinatorial library of DNA encapsulated supramolecular nanoparticles (DNA⊂SNPs), in which a broad structural/functional diversity can be programmed into individual DNA⊂SNPs (**1**) by systematically altering the mixing ratios of the five functional molecular building blocks, *i.e.*, CD-PEI (**2**), Ad-PAMAM(**3**), Ad-PEG (**4**), Ad-PEG-RGD (**5**), and Ad-PEG-TAT (**6**), as well as DNA plasmid ((**7a**)

enhanced green fluorescent protein (EGFP) and (**7b**) firefly luciferase (FLuc)). b) Graphical illustration of a digital Dual-Core Microreactor (DCM). The device settings are composed of a central integrated mixer (CIM), an auxiliary integrated mixer (AIM), and degas modules bridges. The operation of the circuit was computer controlled using color-coded pressure-driven valves: red, positive pressure, off/on; yellow, peristaltic pumping; green, vacuum. Eight slugs containing eight different formulated DNA-encapsulated DNA⊂SNPs were generated in parallel and transferred to a 96-well plate through PTFE tubes. The gene transfection performance for each combination was evaluated by a plate reader. c) The picture of the whole set of actual instrument. d) and e) show optical images of the CIM and AIM, respectively. The various channels were loaded with dyes to visualize the different components.

4.4.3. Formulating a combinatorial library of DNA⊂SNPs in Dual-Core Microreactor (DCM)

By systematically altering the mixing ratios among the five molecular building blocks (*i.e.*, CD-PEI (**2**), Ad-PAMAM (**3**), Ad-PEG (**4**), Ad-PEG-RGD (**5**), and Ad-PEG-TAT (**6**)) and DNA (7), distinct structural/functional properties (*i.e.*, sizes and surface chemistry) can be programmed into individual DNA⊂SNPs in the combinatorial library. It is important to point out that, in contrast to the lipid-like gene delivery system where the diversity was built upon the binary combination of a plethora of molecular precursors,[41b, 139] the diversity of our DNA⊂SNPs library was generated by ratiometric combination of only the five molecular building blocks and DNA loading. It is feasible to manually prepare the DNA⊂SNPs library by pipetting and mixing individual molecular building blocks and DNA plasmid at different ratios, while potential operation errors, slow handling speed, and a significant amount of sample consumption might compromise the throughput, fidelity, and efficiency of the study. Digital microfluidic reactors[140] are promising platforms to overcome these challenges. In our case, an oil-free, digital DCM (**Figure 4.8.b-e**) composed of (i) a central integrated mixer (CIM) and (ii) an auxiliary integrated mixer (AIM), was designed and implemented to systematically program the structural/functional diversity into the DNA⊂SNPs libraries. As illustrated in **Figure 4.8.b**, there are eight parallel microchannels in CIM, capable of parallel generation of eight slugs with different mixing ratios of 2-7. Each microchannel was partitioned by hydraulic-actuated microvalves into nine confined

plug regions, which were assigned for precise metering of five molecular building blocks (2-6), a DNA plasmid, (7a, EGFP or 7b, FLuc) and phosphate buffered saline (PBS). AIM incorporates a pair of fractionally partitioned microchannels, capable of synchronized supply of functional ligands (5 and 6) at different concentrations. CIM and AIM were coupled together by a pair of degas that remove gas through liquid transferring processes. By using the digital DCM, the automated preparation of DNA⊂SNPs library was achieved by systematically modulating the mixing ratios of CD-PEI (2), Ad-PEG-RGD (5), and Ad-PEG-TAT (6), against fixed amounts of Ad-PAMAM (3), Ad-PEG (4), and plasmid DNA (7). In CIM, constant concentrations of 3 (3.0 μM), 4 (60.0 μM), and 7 (100 ng/μL) were assigned to fill into plug regions (ca. 20 nL per region). To adjust the quantities of CD-PEI (2), the eight uneven partitioned plug regions on the west side of CIM were utilized to accommodate different volumes of 2 (4.0 μM, 10-80 nL). The concentration modulation of the two functional ligands (5 and 6) was accomplished in AIM, where each fractionally partitioned microchannel is responsible for ratiometric mixing of the respective ligand (5, 0-9.6 μM; 6, 0-12.0 μM) with PBS. In each operation cycle, CIM generate eight 200-nL slugs containing different precursor mixtures, which were introduced into 96-well plates by nitrogen through eight poly(tetrafluoroethylene) (PTFE) tubes attached at the east side of CIM. To produce sufficient quantity of DNA⊂SNPs for subsequent transfection studies, 50 cycles were performed continuously in CIM within 90 s, affording eight different DNA⊂SNPs solutions (ca. 10 μL each, 100 ng DNA). The resulting DNA⊂SNPs libraries were incubated in the 96-well plates for 20 min at room temperature prior to transferring to the 96-well plates containing NIH 3T3 cells (ca. 8000 cells/well) for transfection studies in parallel. The gene transfection efficiency was evaluated by a plate reader after culturing the cells at 37 °C (5% CO_2) for 24 h.

In proof-of-concept trials a CMV promoter-driven EGFP-encoded plasmid DNA was encapsulated into the DNA⊂SNPs. Before a full-scale screening with three variables (*i.e.*, CD-PEI (2), Ad-PEG-RGD (5), and Ad-PEG-TAT (6)), simplified studies on two pairs of variables (*i.e.*, CD-PEI (2) vs. Ad-PEG-RGD (5) and CD-PEI (2) vs. Ad-PEG-TAT (6)) were conducted in search of the optimal transfection performance of RGD-DNA⊂SNPs and TAT-DNA⊂SNPs, respectively. The transfection outcomes (96 data points in each case) were fitted into two 3-dimensional (3D) profiles (**Figure 4.9.a and b**). The full-scale screening was accomplished by systematically programming the three variables, including eight different concentrations for CD-PEI (2), nine for Ad-PEG-RGD (5), and nine for Ad-PEG-TAT (6). Using the digital DCM, a combinatory library composed of 648 different DNA⊂SNPs was generated within 2.5 h to fill up seven 96-well plates. To ensure the operation fidelity, all the experiments were conducted in triplicate. A 4D gene expression plot shown in **Figure 4.9.c** was employed to summarize the results from the full-scale screening of the combinatorial library. The results reveal that the optimal transfection performance of DNA⊂SNPs was achieved at CD-PEI (2) concentration of 0.6-0.8 μM, Ad-PEG-RGD (5) of 0.24-0.48 μM, and Ad-PEG-TAT (6) of 0.4-0.8 μM. We also note the transfection performance of the TAT/RGD-DNA⊂SNPs (1a) is significantly improved compared with those observed for RGD-DNA⊂SNPs and TAT-DNA⊂SNPs. To validate the general applicability of this developmental pathway, we performed a relatively smaller screening to identify DNA⊂SNPs capable of highly efficient delivery of FLuc-encoded plasmid DNA. We manipulated three variables (5 × 5 × 5 concentrations) resulting in a combinatorial library of 125 different TAT/RGD-DNA⊂SNPs (1b). All four sets of screening studies show that the TAT/RGD-DNA⊂SNPs (1) composed of CD-PEI (2, 0.7 ±0.1 μM), Ad-PEG-RGD (5, 0.28 ±0.04 μM), and Ad-PEG-TAT (6, 0.60 ±0.20 μM) exhibit the best transfection performance.

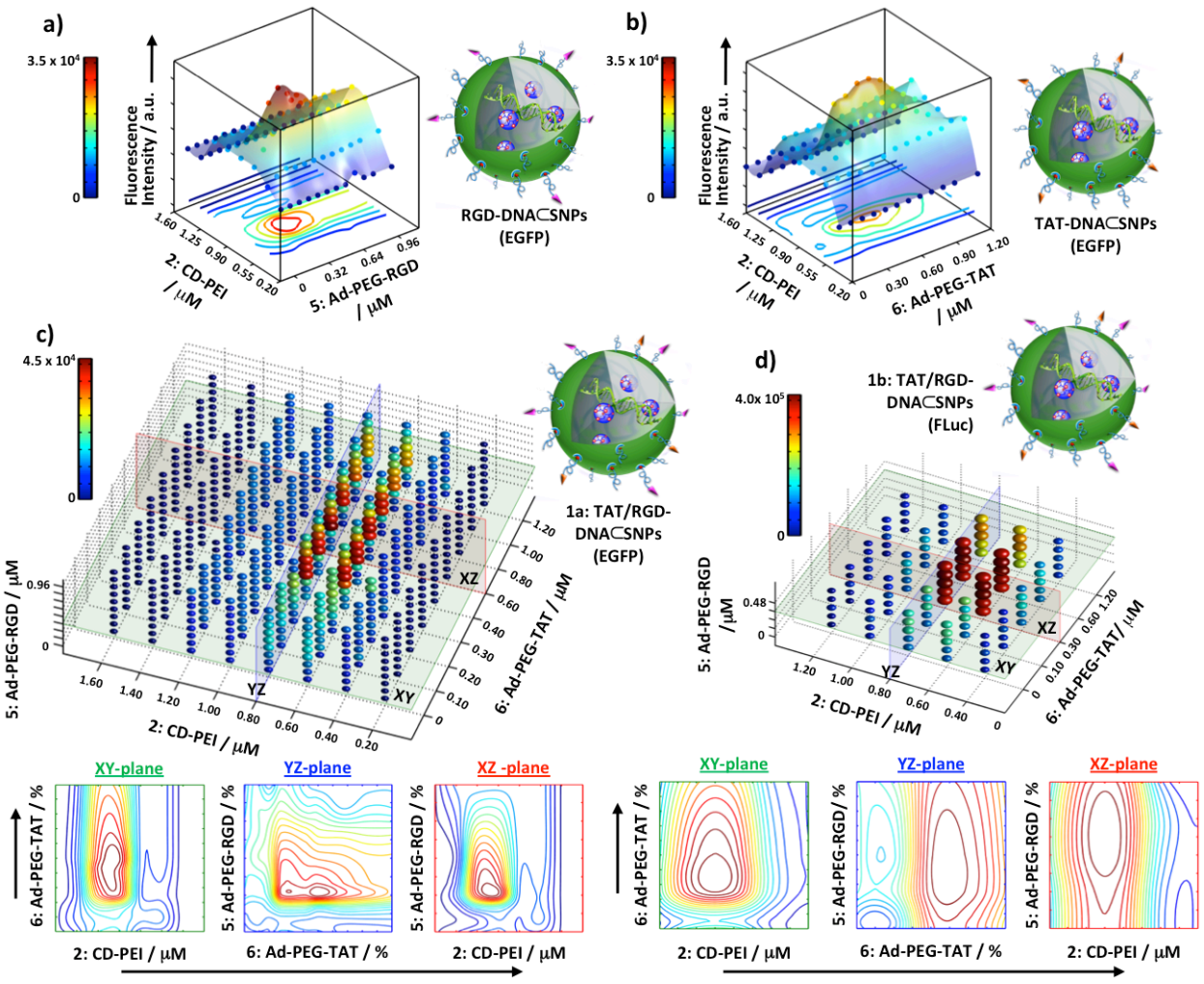

Figure 4.9. a) A 3D profile of gene transfection performance of RGD-DNA⊂SNPs (EGFP) with variation of CD-PEI (2) and RGD coverage (96 data points). b) A 3D profile of gene transfection performance of TAT-DNA⊂SNPs (EGFP) with variation of CD-PEI (2) and TAT coverage (96 data points). c) A 4D profile of gene transfection performance of TAT/RGD-DNA⊂SNPs (EGFP) with variation of CD-PEI (2), TAT and RGD coverages (648 data points). The XY, YZ, and XZ plates across the best performance were simplified and denoted 2D contour images. d) A 4D profile of gene transfection performance of TAT/RGD-DNA⊂SNPs (FLuc) with variation of CD-PEI (2), TAT, and RGD coverages (125 data points). The XY, YZ, and XZ plates across the best performance were simplified and denoted 2D contour images.

4.4.4. Characterization and Stability of TAT/RGD-DNA⊂SNPs

In order to understand how the identified synthetic variables contribute to the optimal transfection performance, we scaled up the production of TAT/RGD-DNA⊂SNPs (1a) under three sets of synthetic variables for characterization at three CD-PEI (2) concentrations (0.6, 0.8,

and 1.2 μM) while keeping concentrations of Ad-PEG-RGD (0.28 μM) and Ad-PEG-TAT (0.6 μM) constant. We realize that CD-PEI (2) concentration affects the cross-linking degrees of the CD-PEI/Ad-PAMAM hydrogel cores in TAT/RGD-DNA⊂SNPs (1), leading to the size variation. Both TEM (**Figure 4.10.a**) and scanning electron microscopy (SEM, **Figure 4.10.b**) were employed to examine the morphology and sizes of the resulting TAT/RGD-DNA⊂SNPs (1). Three distinct sizes of 42 ±4, 86 ±9, and 160 ±13 nm were observed for those produced at CD-PEI (2) concentrations of 0.6, 0.8, and 1.2 μM, respectively. Interestingly, we also noticed that the size distributions of the DCM-produced DNA⊂SNPs are much narrower than those prepared manually, and these results were confirmed by DLS measurements (**Figure 4.10.c**). We attribute the greater control upon DNA⊂SNPs size distribution to the precision and reproducibility of the sampling, metering, and mixing processes in the digital DCM. In addition, no significant size variations were observed by introducing different concentrations ranging from 0 to 1.2 μM of ligands (5 and/or 6). We also characterized the surface potentials of these TAT/RGD-DNA⊂SNPs (**Figure 4.10.d**), which are at a range of 3.7 ±0.2 to 6.8 ±0.3 mV. In addition, the actual surface coverages of Ad-PEG-RGD (5) and Ad-PEG-TAT (6) were estimated by measuring absorption intensity of a FITC-labeled analogue (*i.e.*, Ad-PEG-FITC)[61] on the DNA⊂SNPs prepared by the respective synthetic parameters. The results indicated that 0.28 and 0.60 μM of Ad-PEG-RGD (5) and Ad-PEG-TAT (6) reflect 5 and 9% of surface coverage on the resulting DNA⊂SNPs, respectively. In short, TAT/RGD-DNA⊂SNPs (1) with sizes of 40 and 80 nm, as well as 5% Ad-PEG-RGD (5) and 9% Ad-PEG-TAT (6) coverages exhibited optimal cell transfection performance.

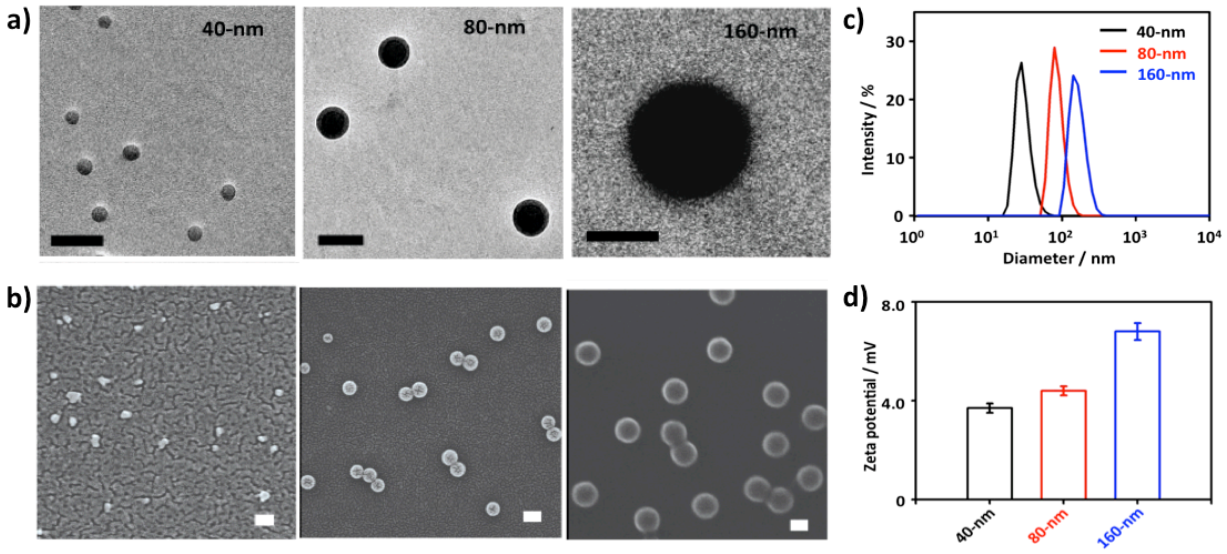

Figure 4.10. a) and b) TEM and SEM images of the resulting TAT/RGD-DNA⊂SNPs with different sizes of 42 ± 4, 86 ± 9, and 160 ± 13 nm. Scale bars: 100 nm. c) DLS was employed to measure hydrodynamic size of DNA⊂SNPs in PBS buffer. (d) Zeta potentials variations of DNA⊂SNPs in PBS buffer.

Finally, to understand the dynamic stability of 40- and 80-nm TAT/RGD-DNA⊂SNPs (1) we employed real-time DLS measurements to monitor their size variation (i) at different pH values (pH 3.8-9.2) and temperatures (25, 37, and 60 °C), (ii) in the presence of 10% serum, and (iii) at different storage times in the presence of physiological salt concentrations (**Figure 4.11.a-f**). The stability of the TAT/RGD-DNA⊂SNPs (1) can be attributed to the multivalent CD/Ad recognition and electrostatic interactions between Ad-PAMAM/CD-PEI hydrogel and DNA. To study the role of Ad-PEG (4) for dynamic stability of DNA⊂SNPs, we monitored the size variation of DNA⊂SNPs (**Figure 4.11.e and f**) by removing the excess amount of Ad-PEG (4) in the mixture through membrane dialysis (MWCO 10kD) under pH 5.5 and 7.2. It was found that the 40- and 80-nm TAT/RGD-DNA⊂SNPs (1) were disassembled gradually within 6 h at both pH conditions. However, the TAT/RGD-DNA⊂SNPs (1) exhibited faster disassembly

behavior at pH 5.5 (<2 h) than at pH 7.2, which allows the TAT/RGD-DNA⊂SNPs (1) efficiently degraded inside the endosomes and released the DNA intracelluarly.[141]

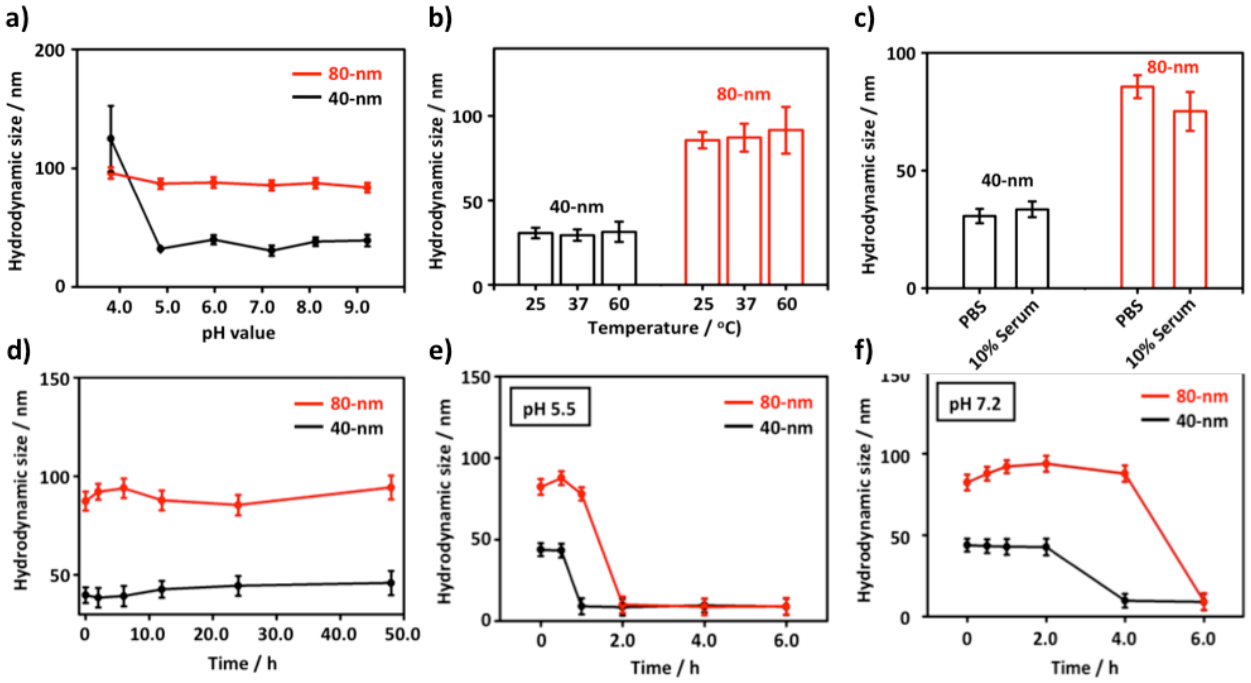

Figure 4.11. Stability studies of 40- and 80-nm DNA⊂SNPs under different conditions: a) pH-dependent size variations of DNA⊂SNPs in the respective buffer solutions with pH values ranging from 3.8 to 9.2. b) Temperature-dependent size variation of DNA⊂SNPs in PBS buffer (pH = 7.2) with different temperatures at 25, 37, and 60 °C. c) Size variations of DNA⊂SNPs in presence and absence of 10% serum containing PBS buffer after 4 h incubation. (d) Time-dependent size variation of DNA⊂SNPs from 0−48 h in PBS. e) and f) Time-dependent dynamic stability of DNA⊂SNPs under dialysis at pH 5.5 and 7.2, respectively. Error bars are obtained from three measurements.

4.4.5. Gene delivery performance of TAT/RGD-DNA⊂SNPs

To compare the transfection performance of the optimal 40-nm TAT/RGD-DNA⊂SNPs (1) with the leading transfection reagents (*i.e.*, RGD-jet-PEI and lipofectamine 2000), we carried out the dose-dependent gene transfection studies in 24-well plates with encapsulated-DNA (50 and 1000 ng per well) by using a collection of cells, including NIH 3T3 (mouse fibroblast cell line), HeLa (human cervix epithelial carcinoma cell line), A549 (human lung cancer cell line), U87 (human glioblastoma cell line), MCF7 (human breast adenocarcinoma cell line), PC3 (human prostate

cancer cell line), and IMR-90 (human fibroblast cell line). The gene transfection studies results (**Figure 4.12.a and b**) indicate the 40-nm TAT/RGD-DNA⊂SNPs (1) exhibit significant improved transfection performance compared to those observed for RGD-jet-PEI and lipofectamine 2000 across the different cancer and fibroblast cell lines at high dosage of DNA (1000 ng DNA per well). Higher than 70% transfection efficiencies were observed across various cancer cell lines we tested, even for the PC3 cell line, which is difficult to be transfected by those two commercial reagents. IMR-90, one of the hard-to-transfect human fibroblast cell lines, was tested and the transfection efficiency of DNA⊂SNPs toward IMR-90 cells reached to 17 ±7%, which can be visualized by the fluorescence micrographs (**Figure 4.12.c**). The transfection efficiency of 40-nm TAT/RGD-DNA⊂SNPs (1) for IMR-90 cells is 11-fold and 5-fold higher than that of RGD-jet-PEI and lipofectamine 2000, respectively. It is important to note that 40-nm TAT/RGD-DNA⊂SNPs (1) still achieved high transfection efficiency at low dosage of DNA (50 ng per well), indicating the outstanding gene delivery ability of DNA⊂SNPs. Moreover, the cell viability assay results indicate that the 40-nm TAT/ RGD-DNA⊂SNPs (1) exhibit negligible cytotoxicity. More than 96 ±3% of DNA⊂SNPs-transfected cells showed normal viability even in the presence of high dosage of reagent (1000 ng DNA per well). In contrast, at a high DNA dose, more than 34% and 22% NIH 3T3 cells died after treatment by RGD-jet-PEI and lipofectamine 2000 for 48 h, respectively (**Figure 4.12.d**).

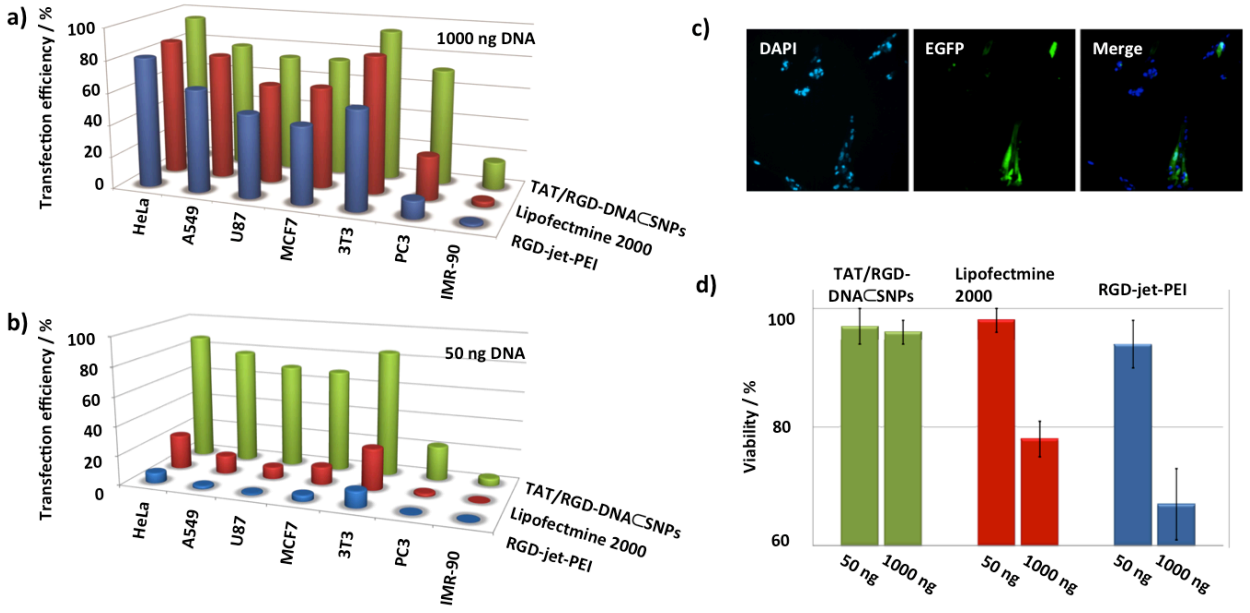

Figure 4.12. a and b) Transfection efficiencies of the optimal 40-nm TAT/RGD-DNA⊂SNPs at high (1000 ng DNA per well) and low (50 ng DNA per well) DNA dosage along with control delivery reagents (lipofectamine 2000 and RGD-jet-PEI) for a collection of cell lines, including NIH 3T3 (mouse fibroblast cell line), HeLa (human cervix epithelial carcinoma cell line), A549 (human lung cancer cell line), U87 (human glioblastoma cell line), MCF7 (human breast adenocarcinoma cell line), PC3 (human prostate cancer cell line), and IMR-90 (human fibroblast cell line) in 24-well plates. c) The representative fluorescence micrographs of IMR-90 cells transfected by 40-nm TAT/RGD-DNA⊂SNPs at high dosage of DNA (1000 ng DNA/well). d) Cytotoxicity of RGD-jet-PEI, lipofectamine 2000 and 40-nm TAT/RGD-DNA⊂SNPs at high and low dosage of DNA transfected NIH 3T3 cells determined by cell viability assay after 48 h of transfection.

In conclusion, we have demonstrated a rapid developmental pathway toward generation of a highly efficient gene delivery system by leveraging the powers of a supramolecular synthetic approach and a custom designed digital microreactor. This pathway can be adopted for the development of nanoparticle-based vectors capable of delivering a variety of loads, such as gene, drugs, and proteins. Moreover, the approach can be adopted for generating SNPs-based co-delivery vectors for simultaneous delivery of a wide range loads and their combinations in immunotherapy and stem cell reprogramming.

Chapter 5. DRUG DELIVERY

5.1. Doxorubicin-Encapsulated Supramolecular Nanoparticles (Dox⊂SNPs)

5.1.1. Introduction

Nanoparticles (NPs) have been regarded as promising non-viral vectors, capable of delivering various payloads (*e.g.*, genes, proteins and drugs) to sub-populations of cells with great efficiency and specificity, thus creating new opportunities in crucial biomedical applications,[142] including diagnostics and therapeutics.[143] Therefore, significant endeavors have been devoted to exploit the use of NPs for delivery of anti-cancer drugs with the expectation of achieving targeted delivery and reducing systemic toxicity.[144] Over the past decades, a diversity of synthetic and formulation approaches have been established to introduce anti-cancer drugs onto or into various NP vectors, resulting in new-generation cancer therapeutics that exhibit dramatically improved treatment outcomes. For example, one approach has been demonstrated to improve therapeutic outcomes by covalently conjugating hydrophobic anti-cancer drugs to water-soluble polymers, via degradable linkers, and these polymer-drug conjugates can then self-organize to form NP vectors for improved water-solubility, bioavailability,[145] and for longer circulation times in the body. However, the polymer-drug conjugation approach is limited by its inefficient drug release mechanism, which requires complete cleavage of the drug-polymer bonds;[146] thus, non-covalent approaches to incorporate drugs into NP vectors have been established in order to overcome this limitation. Such non-covalent approaches possess advantages of dynamic release of active drugs[147] and enhanced drug loading capacities, which have been exploited in copolymer micelles for rapid controlled release of drugs[148] and higher drug loading capacity.[149]

Along the idea of non-covalent formulation approaches, we have previously demonstrated a convenient, flexible, and modular self-assembly approach for the preparation of supramolecular nanoparticle (SNP) vectors from a small collection of molecular building blocks through a multivalent molecular recognition based on adamantane (Ad) and β-cyclodextrin (CD) motifs (see **Chapter 2.1.**).[150] In order to further expand the utility of SNP vectors for delivery of an active anti-cancer drug (*i.e.*, doxorubicin, Dox), we test the feasibility of producing Dox-encapsulated SNPs (Dox⊂SNPs) through self-assembly of SNP molecular building blocks in the presence of free Dox molecules. It is well-known that Dox is an intrinsically fluorescent compound whose photophysical properties are highly susceptible to its surrounding environment.[151] We envision that the cores of SNP vectors offer a unique nano-environment that could induce self-organization of encapsulated Dox molecules, leading to their fluorescence quenching. According to this molecular design, Dox can serve as both a chemotherapeutic agent and a reporter system for monitoring drug delivery kinetics of Dox⊂SNPs. Given the dual roles of Dox molecule; Dox⊂SNPs can be regarded as new type of theranostics for cancer treatment.

5.1.2. Molecular design of Dox⊂SNPs

In this chapter, we introduce a unique theranostic system, Dox⊂SNPs prepared by ratiometric mixing (**Figure 5.1.**) of free Dox molecules with three SNP building blocks, including Ad-grafted polyamidoamine dendrimer (Ad-PAMAM), β-CD-grafted branched polyethylenimine (CD-PEI) and Ad-functionalized polyethylene glycol (Ad-PEG). Two dimensions of supramolecular mechanisms are responsible for the formation of Dox⊂SNPs. The first dimension has to deal with the self-assembly of Ad-PAMAM, CD-PEI and Ad-PEG that generates size-controllable SNP vectors with intraparticular cationic hydrogel networks. Consequently, such hydrogel networks constitute a unique nano-environment that induces the

second level of self-organization of Dox molecules driven by their intermolecular π–π stacking interactions. As a result, the fluorescent signal of encapsulated Dox molecules is quenched remarkably. Upon internalization of Dox⊂SNPs into cells, the dynamic disassembly[61] of Dox⊂SNPs leads to release of encapsulated Dox molecules, restoring their fluorescent signals. Such an environmentally sensitive fluorescent property of Dox molecule constitutes a reporter system that enables monitoring the dynamic Dox release behavior from Dox⊂SNPs. We therefore adopted fluorescent microscopy, in conjunction with single-cell image cytometry technique,[152] to study Dox delivery kinetics of Dox⊂SNPs in U87 glioblastoma cells. The results were compared with those observed for free Dox and Dox⊂SNPs grafted with arginine-glycine-aspartic (RGD) ligand (RGD–Dox⊂SNPs).

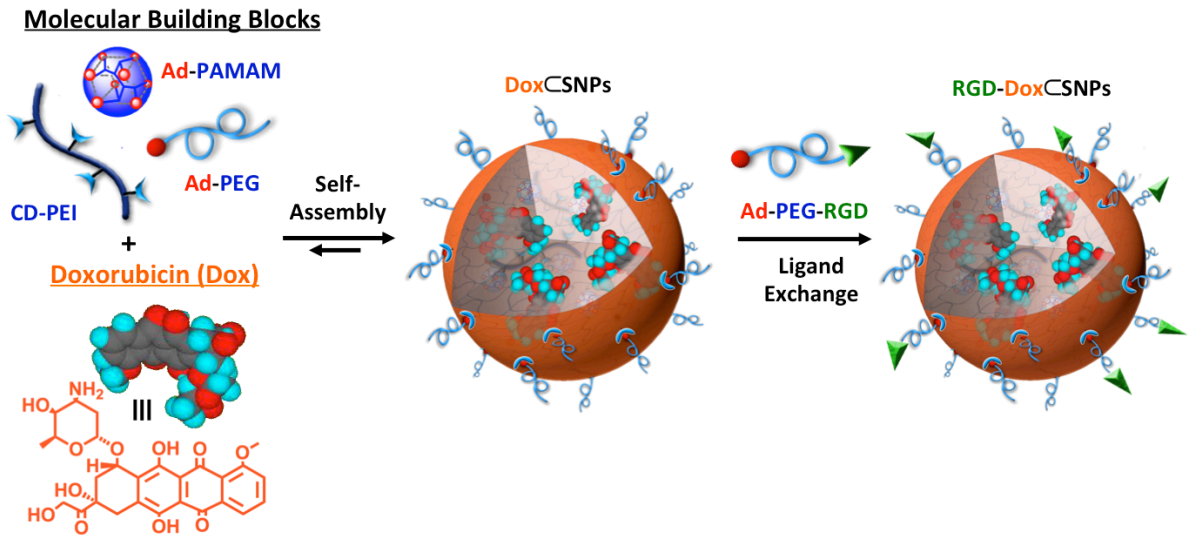

Figure 5.1. Schematic representation of a self-assembled approach utilized for preparing doxorubicin (Dox)-encapsulated supramolecular nanoparticles, Dox⊂SNPs from three molecular building blocks (*i.e.*, Ad-PAMAM, CD-PEI and Ad-PEG) in the presence of free Dox molecule. Through the dynamic exchange of a targeting ligand (*i.e.*, Ad-PEG-RGD), RGD-grafted Dox⊂SNPs, RGD-Dox⊂SNPs capable of targeted delivery were obtained.

5.1.3. Characterization of Dox⊂SNPs

80-nm Dox⊂SNPs are prepared by adding 10-μL DMSO solution of Ad-PAMAM (0.22 mg) into a 500-μL DMSO/PBS mixture (1:50, v/v) containing Dox (0.16 mg), Ad-PEG (6 mg) and CD-PEI (4 mg). The mixture was kept at 70 ^{o}C for 30 min, followed by annealing at room temperature for 2 h, affording 80-nm Dox⊂SNPs as a dark purple solution. The encapsulation efficiency (95%) of the resultant 80-nm Dox⊂SNPs was determined by quantifying free Dox molecules (collected via filtration through Amicon ultra-centrifugal filter) in the solution. Similarly, the Dox loading capacity can be calculated as ca. 2% (Dox:SNPs, w/w). Both transmission electron microscopy (TEM) (**Figure 5.2.a and b**) and dynamic light scattering (DLS) (**Figure 5.2.c**) were employed to measure the size and to characterize morphologies of the resulting Dox⊂SNPs. TEM images reveal that Dox⊂SNPs exhibit a spherical shape and uniform size distribution, consistent with results obtained from DLS measurements. Under a less stringent staining condition applied for TEM sample preparation, the TEM image of bundle-like Dox structures inside of SNPs can be visualized as shown in **Figure 5.2.b.** The photophysical properties of Dox⊂SNPs were studied by UV-Visible and fluorescence spectroscopies. As illustrated in **Figure 5.2.d**, the presence of a bathochromic shift in the absorption peak of Dox⊂SNPs (575 nm) compared to free Dox (490 nm) indicates the π–π stacking interaction[153] of encapsulated Dox molecules. The fluorescence intensity of Dox⊂SNPs is lowered by a factor of 14 when compared to free Dox with the same concentration (**Figure 5.2.e**), strongly suggesting that Dox molecules are self-organized inside SNP vectors and resulted in their fluorescence quenching.[154] This quenching phenomenon can be restored upon release the free Dox from the SNP vectors. Together, this environmentally sensitive fluorescent property of Dox can be exploited for visualization and quantitation of drug release kinetics inside of cells.

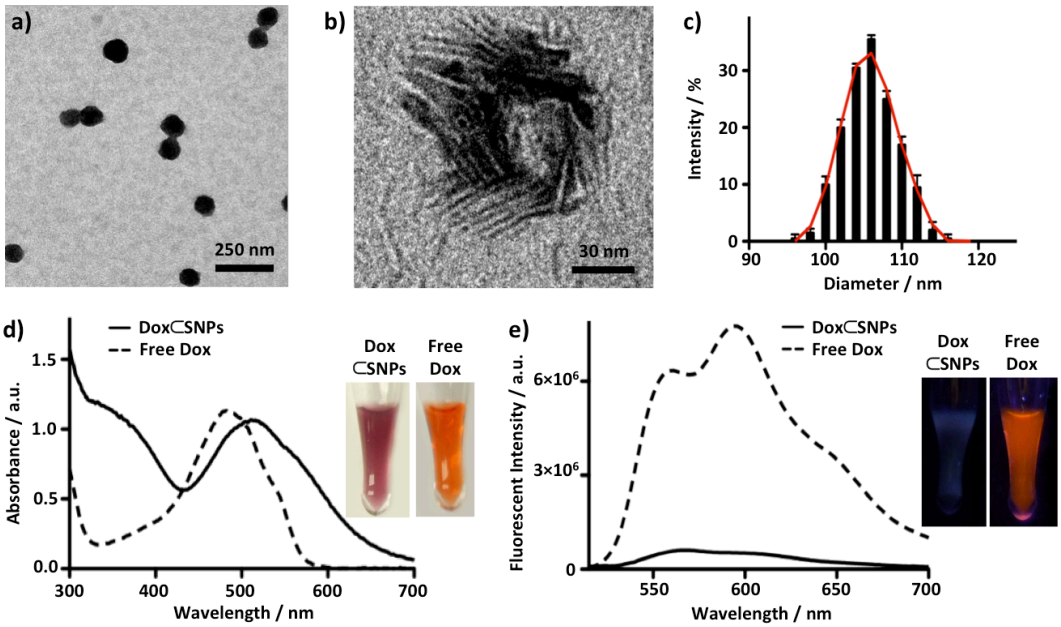

Figure 5.2. a) TEM image reveals that DoxCSNPs exhibit uniform sizes of ca. 80 nm. b) Under less stringent staining condition, TEM image of buddle-like structures were observed inside the intraparticular spaces of DoxCSNPs. c) DLS data of the resultant DoxCSNPs. d) UV−Vis spectra of both free Dox and DoxCSNPs. A red shift was observed for the absorption peak of DoxCSNPs (575 nm) in contrast to that observed for free Dox (490 nm). Concentrations of Dox in both cases were normalized to 0.4mg/mL in water. Inset photographs show the aqueous solutions containing free Dox and DoxCSNPs. e) Fluorescence spectra of free Dox and DoxCSNPs. Dramatically quenched fluorescence were observed (λ ex.= 490 nm, λ em. = 560 and 595 nm for Dox and DoxCSNPs, respectively). Inset: photographs show the free Dox and DoxCSNPs solutions under irradiation of UV light (365 nm).

5.1.4. Target specificity and drug delivery kinetics of DoxCSNPs

RGD targeting ligand was incorporated, via dynamic exchange,[61] onto DoxCSNPs yielding RGD−DoxCSNPs, which can specifically target the $\alpha_v\beta_3$ integrin on U87 cells.[155] Sequential microscopic imaging was employed to study how the RDG targeting ligand affects Dox delivery performance in a 24-well plate containing U87 cells (10^5 cells/well) between RGD−DoxCSNPs and DoxCSNPs. Here, free Dox system was used as a control. The first set of data was acquired at 15 min post treatment; the differences of Dox fluorescent signals for the three groups can be visualized with fluorescent microscopy (**Figure 5.3.a-c**). The most intense Dox fluorescence was observed in the cells treated with RGD−DoxCSNPs (**Figure 5.3.c**). We employed fluorescent

microscopy together with single-cell image cytometry to quantify the Dox fluorescence intensity in single cell. Dox fluorescence intensity histograms of the three systems were plotted and summarized in **Figure 5.3.d**. The Dox fluorescence intensity of RGD–DoxCSNPs is 1.8 and 6.0 times higher than that of DoxCSNPs and free Dox, respectively. The results show that an incubation time of 15 min is sufficient to distinguish differential Dox delivery outcomes for RGD–DoxCSNPs and DoxCSNPs. We attribute the enhanced targeted delivery kinetics of RGD–DoxCSNPs to the RGD targeting ligand, which expedited the binding of RGD–DoxCSNPs to U87 cells in a short period of time compared to the DoxCSNPs control. In our experiments, we continuously monitored the Dox fluorescence intensity inside individual cells at various time points in order to study the different drug delivery kinetics for free Dox, DoxCSNPs and RGD-DoxCSNPs.

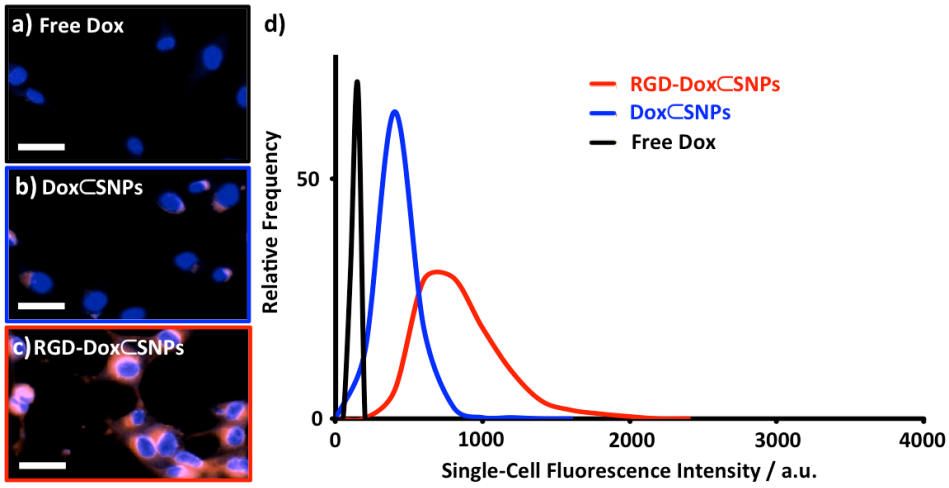

Figure 5.3. Fluorescent microscopy was employed to quantify differential Dox fluorescent signal in U87 cells. Each group received 15-min treatment of a) free Dox, b) DoxCSNPs, or c) RGD-DoxCSNPs. Cells were fixed in 4% paraformaldehyde and treated with DAPI for nuclei staining. Red: Dox. Blue: DAPI. Scale bars = 50 μm. d) Image cytometry technique was utilized to quantify single-cell fluorescence intensity that reflects differential Dox fluorescent signal in the treated cells. The resulting histograms suggest that RGD-DoxCSNPs exhibit the best delivery performance. Each histogram was generated from more than 1000 individual cells.

In **Figure 5.4.a**, we present time-lapse three serial histograms quantifying Dox fluorescence for single cells at four different incubation time points (*i.e.*, 1 min, 15 min, 1 h and 5 h). After incubation for 1 min, all cells in the three groups had low signal intensity near background. By the 15 min time point, cells treated with RGD–Dox⊂SNPs show higher Dox fluorescent signal than cells treated with Dox⊂SNPs or free Dox. However, at 1 h incubation time point, both SNP groups show similar Dox fluorescent signal. We then assess the relative delivery outcomes for the three groups, shown in **Figure 5.4.b**, by normalizing the average Dox fluorescent signal of each group to the average Dox fluorescent signal of RGD–Dox⊂SNPs at the 5 h time point in **Figure 5.4.a**. Again, we note that cells treated with RGD–Dox⊂SNPs showed increased Dox fluorescent signal after 15 min incubation and their Dox fluorescent signal intensities were 20% higher than the cells treated with Dox⊂SNPs, indicating that the Dox delivery kinetic profile of RGD–Dox⊂SNPs is faster than both controls. These types of differential Dox delivery kinetics can be distinguished with our theranostic delivery system. However, after 1 h incubation, the Dox fluorescent signal for RGD–Dox⊂SNPs and Dox⊂SNPs plateaued to a statistically similar amount of released Dox for both groups, thus indicating that longer incubation times overcome the kinetic advantages of using a targeting ligand. In contrast, there was significantly lower Dox fluorescent signal for the free Dox group. Although, as expected, the Dox uptake of free Dox group did slightly increase with longer incubation times. The evaluation of *in vitro* therapeutic efficacy of free Dox, Dox⊂SNPs and RGD–Dox⊂SNPs was assessed by MTT assay after 48 h incubation. The result in **Figure 5.4.c** shows that both Dox⊂SNPs and RGD–Dox⊂SNPs outperform free Dox; however, there are negligible differences between Dox⊂SNPs and RGD–Dox⊂SNPs, likely due to utilizing a long treatment time, which is consistent with what observed from **Figure 5.4.a and b**.

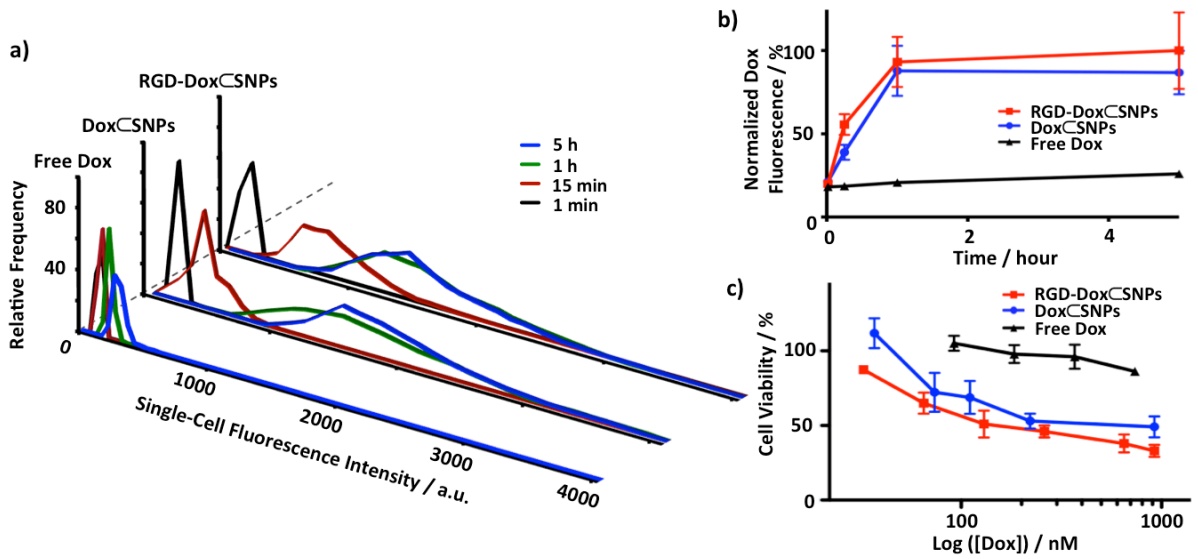

Figure 5.4. a) Dox fluorescent signal histograms observed for U87 cells treated with free Dox, DoxCSNPs and RGD-DoxCSNPs at various post-administration time points of 1 min, 15 min, 1 h and 5 h. Each histogram was generated from quantitative fluorescence image cytometry of more than 1000 cells. b) Average Dox signal intensity of each group is derived from histograms shown in a). By normalizing the average signal intensity for each group to the RGD-DoxCSNPs signal intensity at the 5 h time point, relative Dox delivery performance for each group at different time points can be generated. c) Viability of U87 cells treated with free Dox, DoxCSNPs or RGD-DoxCSNPs. The MTT assay was conducted at 48 h post treatments.

5.1.5. Conclusion

In conclusion, we demonstrate a unique drug delivery system, DoxCSNPs that utilized self-assembled synthetic strategy to incorporate an active anti-cancer drug, *i.e.*, Dox, into SNPs via non-covalent drug encapsulation. In our molecular design, Dox can serve as both a therapeutic agent and a fluorescent reporter system. Together with fluorescent microscopy and single-cell image cytometry, the Dox delivery kinetics of DoxCSNPs can be monitored and studied *in vitro*. We foresee this promising theranostic system can be utilized *in vivo* to generate drug delivery kinetic profiles as a preclinical tool that can direct future optimization strategies toward ideal therapeutic efficacy.

Chapter 6. COMPANION DELIVERY (THERANOSTICS)

6.1. Introduction

Nanoparticles (NPs) have been regarded as promising vectors[41a, 102a, 156] for controlled delivery of anti-cancer drug(s) to tumors, providing a powerful therapeutic strategy with enhanced anti-tumor efficacy and reduced systemic side effects.[157] However, there are only a few successful examples[102a, 158] that have reached clinical usage over the past decades due to several major challenges encountered in the development of drug(s)-encapsulated nanoparticles, drug(s)⊂NPs.[159] These challenges include the following: (1) the commonly-used multistep synthetic approaches are cumbersome and incapable of controlling the sizes, charges and surface chemistry of drug(s)⊂NPs that affect their pharmacokinetic (PK) and pharmacodynamic (PD) properties[160] and therapeutic efficacies;[161] (2) lack of companion reporter systems for quantitatively measuring PK/PD characteristics and detecting therapeutic efficacy of drug(s)⊂NPs in the tissues after administration; and (3) it is difficult to establish how the structural-property relationship that concludes how drug(s)⊂NPs' sizes and surface affect their PK/PD characteristics and therapeutic efficacy.[162] As a result, crucial feedback information about synthetic optimization of the NPs has been missing. Therefore, there is a need to develop a new kind of drug(s)⊂NPs with companion reporter systems that can be employed to evaluate PK/PD properties of drug(s)⊂NPs at cellular, tumor and whole body levels. The resulting PK/PD data will be correlated with the therapeutic efficacy of a variety of drug(s)⊂NPs, providing crucial feedback information for guiding synthetic optimization of drug(s)⊂NPs.

6.2. Camptothecin-Encapsulated SNPs with Built-in Companion Diagnostic Utilities

6.2.1. Current challenges for searching optimal therapeutics

There have been two main challenges in developing optimized NP-based drug delivery systems: (i) the existing synthetic approaches are cumbersome and incapable of achieving precise control of their structural properties, which will affect their biodistribution and therapeutic efficacies,[161, 163] and (ii) lack of an early checkpoint to quickly predict which drug(s)-incorporated NPs exhibit optimal therapeutic outcomes. Therefore, there is a need to develop a novel approach to quickly screen NP-based cancer therapeutic agents with optimal therapeutic efficacy in clinic.

6.2.2. Molecular design of CPT-PGA encapsulated SNPs (CPT-PGA⊂SNPs)

We utilize a new rational developmental approach to rapidly screen NP-based cancer therapeutic agents containing a built-in companion diagnostic utility for optimal therapeutic efficacy (see **Appendix** for reference[164]). The approach leverages the advantages of a self-assembly synthetic method for preparation of supramolecular nanoparticles (SNPs), and a positron emission tomography (PET) imaging-based biodistribution study to quickly evaluate the accumulation of SNPs at a tumor site *in vivo*. The self-assembly synthetic method enables a convenient, flexible and modular production of a small collection of drug-incorporated NPs with precisely controlled sizes ranging from 37 to 104 nm, below the threshold of NP size that allows the efficient extravasation of NPs into the leaky tumor vasculatures and accumulation of the NPs in the tumor tissues via enhanced permeability and retention (EPR) effect[165] (see **Chapter 3.2.1.**). Subsequently, PET imaging-based biodistribution studies are employed to correlate the sizes of drug-incorporated NPs with their delivery performances. Thus, a specific size of drug-incorporated NPs that exhibit optimal accumulation and prolonged retention in tumor tissue can

be readily identified, resulting in potentially the lead modality with improved therapeutic efficacy and reduced side effect that is subject to comprehensive pre-clinical studies.

6.2.3. Size controllability, stability and *in vitro* therapeutic performance of CPT−PGA⊂SNPs

Given the versatile utility of such a self-assembly synthetic method, we attempted to explore the use of SNP-based vectors for delivering an anti-cancer drug. In this case, camptothecin (CPT), a cytotoxic quinoline alkaloid that inhibits the topoisomerase I, was selected for the proof-of-concept demonstration. Similar to the self-assembly preparation of DNA encapsulated SNPs,[61, 129] which used the coulombic interactions between the negatively charged DNA plasmid with the positively charged SNP vector, 5 KD anionic poly(l-glutamic acid) (PGA)[166] was employed as a carrier to covalently link with CPT molecules, enabling encapsulation into SNP vectors. Approximately five CPT molecules were conjugated to each PGA polymer chain (via ester bond formation) to give CPT-grafted PGA, denoted as CPT-PGA.[167] It is noteworthy that the connecting ester bonds can be degraded via esterase-mediated hydrolysis, which allows controlled release of CPT under physiological conditions. The encapsulation of CPT-PGA into SNP vectors to generate CPT-PGA encapsulated SNPs (CPT-PGA⊂SNPs) can be accomplished (**Figure 6.1.**) by simply mixing the drug conjugated polymer, CPT-PGA, with the other two SNP building blocks (CD-PEI and Ad-PAMAM), as well as a solvation ligand (Ad-PEG).

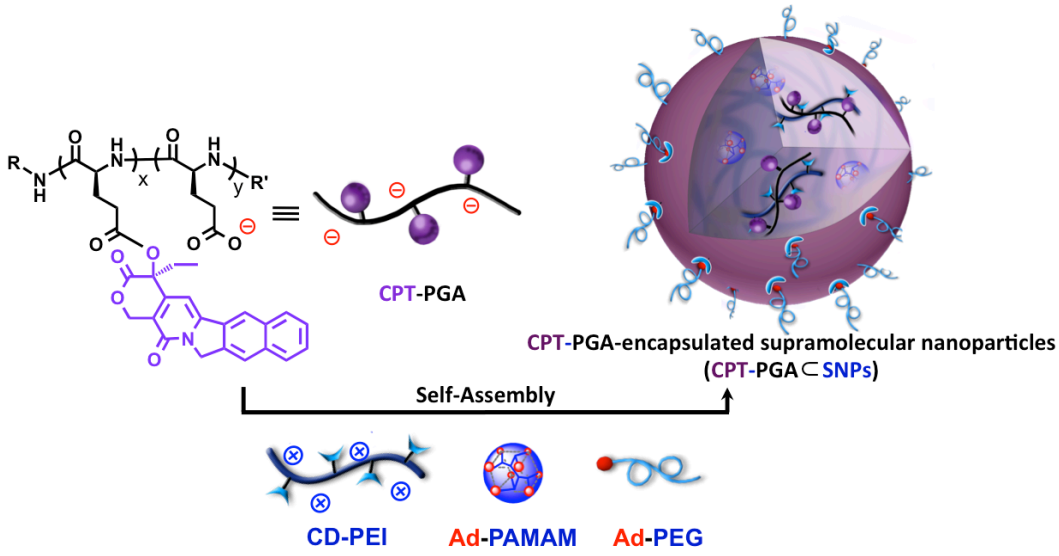

Figure 6.1. Schematic representations of the self-assembly synthetic method for the production of CPT-grafted PGA encapsulated Supramolecular NanoParticles (CPT-PGA⊂SNPs) from the respective molecular building blocks and CPT-PGA (camptothecin-grafted poly(l-glutamic acid)).

By altering the mixing ratios between the two SNP building blocks (Ad-PAMAM/CD-PEI = 0.125 and 0.25), two different sizes (37 and 104 nm) of CPT-PGA⊂SNPs can be obtained with narrow size distributions after annealing at 50 °C for 20 min. Both TEM and DLS measurements were performed to characterize the sizes and morphologies of the resulting CPT-PGA⊂SNPs and the results are summarized in **Figure 6.2.a**. TEM images show that the resulting CPT-PGA⊂SNPs possessed homogeneous size distributions (**Figure 6.2.b and c**).

a)

Formulation	TEM	DLS	Zeta potential
37-nm CPT-PGA⊂SNPs	37 ± 8 nm	56 ± 4 nm	-11 ± 0.7 mV
104-nm CPT-PGA⊂SNPs	104 ± 12 nm	180 ± 11 nm	-4 ± 0.2 mV

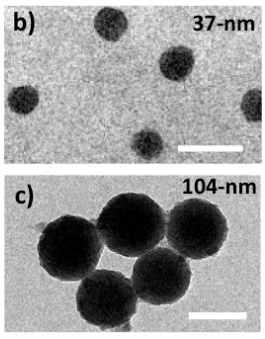

Figure 6.2. Two different sizes of CPT-PGA⊂SNPs were obtained by altering the mixing ratio between two building blocks (Ad-PAMAM and CD-PEI). a) The characterizations of the resulting CPT-

PGA⊂SNPs. b) and c) TEM images of 37-nm and 104-nm CPT-PGA⊂SNPs, respectively. Scale bars: 100 nm

Moreover, other studies, including zeta potential (The zeta potentials of the resulting 37-nm CPT-PGA⊂SNPs and 104-nm CPT-PGA⊂SNPs are -11 ± 0.7 and -4 ± 0.2 mV, respectively), drug encapsulation efficiency (The drug encapsulation efficiency for 37-nm and 104-nm CPT-PGA⊂SNPs are $90 \pm 3\%$ and $95 \pm 2\%$, respectively.), stability (The results in **Figure 6.3.a** indicate that the resulting CPT-PGA⊂SNPs exhibit good stability in PBS solution under a physiological ionic strength up to 6 days.), drug release kinetics (The accumulative release of free CPT from CPT-PGA⊂SNPs was quantified by HPLC. The data in **Figure 6.3.b** point out that CPT-PGA⊂SNPs release 20% of CPT after 6 days without any associated burst release.) and *in vitro* viability (The IC_{50} values, the concentration at which 50% inhibition of cellular growth occurs, were around 100 nM for free CPT and approximately 400 nM for CPT-PGA⊂SNPs and CPT-PGA. There were negligible difference among CPT-PGA and the two other sizes of CPT-PGA⊂SNPs, which is probably due to the slow release of the drug from polymer (**Figure 6.4.**). Note that the cells treated with PGA⊂SNPs present high viability, indicating low cytotoxicity attributed to our SNPs.), of the resulting CPT-PGA⊂SNPs were also carried out.

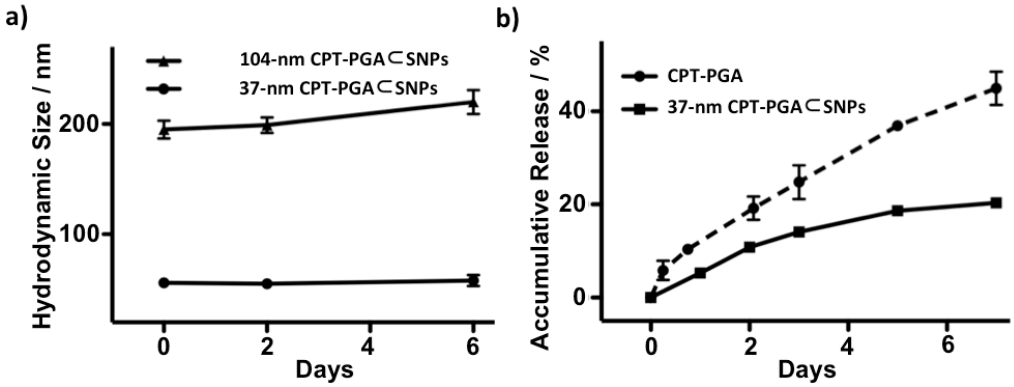

Figure 6.3. a) Time-dependent studies on the stability of 37-nm and 104-nm CPT-PGA⊂SNPs in 1 × PBS. b) Release kinetics of CPT-PGA and 37-nm CPT-PGA⊂SNPs in 50% human serum (human serum:1 × PBS = 1:1, v/v). Released CPT was quantified by HPLC.

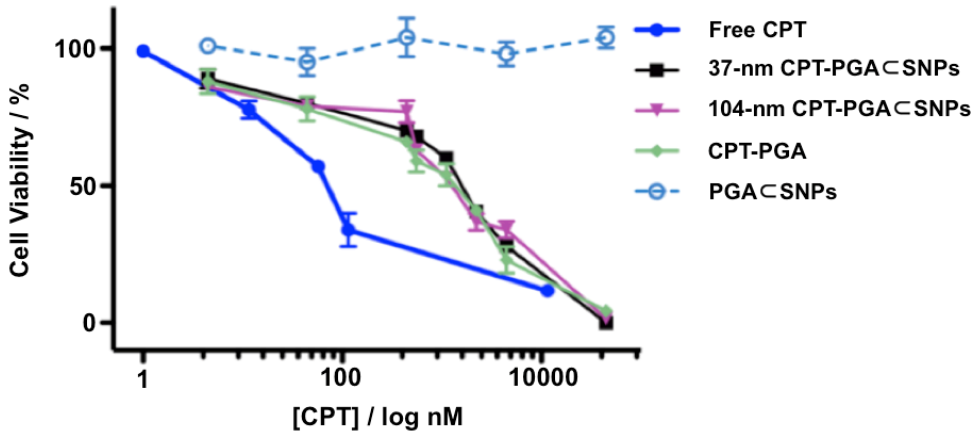

Figure 6.4. Dose-dependent cell viability studies of two different sizes of CPT-PGA⊂SNPs along with controls.

6.2.4. Rapid screening in search of an optimal therapeutic agent

Different sizes of CPT-PGA⊂SNPs will have distinctive biodistribution patterns and varying therapeutic performances due to their differential EPR.[168] Instead of directly performing the *in vivo* efficacy studies of all of the two sizes of CPT-PGA⊂SNPs, which would require a significant quantity of CPT-PGA⊂SNPs and a large cohort of animals, we utilized micro-PET imaging technology (see **Chapter 3.2.**) to understand the biodistribution properties of the 37-nm and 104-nm CPT-PGA⊂SNPs. We anticipated that the resulting biodistribution data would correlate the sizes of CPT-PGA⊂SNPs with their delivery performances. Thus, the specific size of drug-incorporated NPs that exhibit preferential accumulation in the tumor can be identified for subsequent pre-clinical studies. Similar to our previous strategy,[43] ^{64}Cu-labeled CPT-PGA⊂SNPs (with the sizes of 37 and 104 nm) can be prepared (**Figure 6.5.a**) by incorporating

DOTA-CD-PEI as one of the precursors (along with CD-PEI, Ad-PAMAM, Ad-PEG and CPT-PGA), followed by ratiometric mixing and labeling by ^{64}Cu. The 37-nm and 104-nm ^{64}Cu-labeled CPT-PGA⊂SNPs were instantaneously injected into LLC tumor-bearing C57Bl/6 mice via tail vein intravenous (*i.v.*) administration. The respective biodistribution data (**Figure 6.5.b-d**) were acquired by micro-PET imaging technology 24 h post injection. Static micro-PET images of the two sizes of ^{64}Cu-labeled CPT-PGA⊂SNPs (**Figure 6.5.b and c**, respectively) revealed that 37-nm ^{64}Cu-labeled CPT-PGA⊂SNPs exhibited significantly enhanced tumor accumulation. Semi-quantitative biodistribution data (**Figure 6.5.d and insert therein**) of ^{64}Cu-labeled CPT-PGA⊂SNPs in major organs were obtained by taking the average signal per voxel in the organ of interest and multiplying that value by the total volume of the organ via Amide software (see **Supporting Information 5.2.**). The PET imaging-based biodistribution studies revealed that the 37-nm ^{64}Cu-labeled CPT-PGA⊂SNPs exhibited 100% more accumulation in the tumor than that observed for the 104-nm ^{64}Cu-labeled CPT-PGA⊂SNPs. We suggest that the preferential accumulation of 37-nm ^{64}Cu-labeled CPT-PGA⊂SNPs in xenografted LLC tumors CPT-PGA⊂SNPs is due to their higher blood retention concentrations that facilitated the EPR effect[169]-mediated accumulation of the SNPs in tumors.

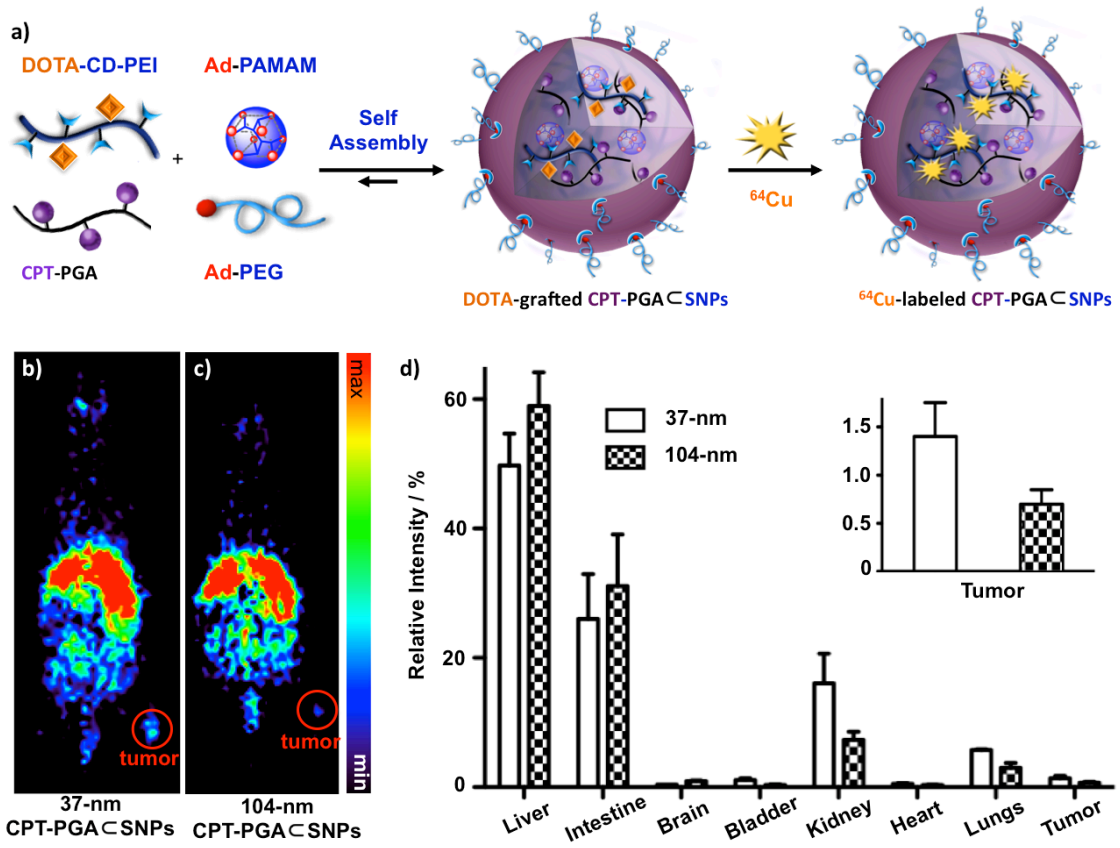

Figure 6.5. a) Schematic illustration of the incorporation of a radioisotope, *i.e.*, ^{64}Cu, into SNPs, resulting in ^{64}Cu-labeled CPT-PGA⊂SNPs. Static micro-PET images of C57Bl/6 mice bearing Lewis lung carcinoma (LLC) tumor at 24 h post injection of b) 37-nm and c) 104-nm ^{64}Cu-labeled CPT-PGA⊂SNPs. Tumor volumes are approximately 245 mm^3. d) *In vivo* biodistribution of 37-nm and 104-nm ^{64}Cu-labeled CPT-PGA⊂SNPs after 24 h intravenous injection. 37-nm ^{64}Cu-labeled CPT-PGA⊂SNPs had higher tumor-specific uptake than 104-nm ^{64}Cu-labeled CPT-PGA⊂SNPs. The error bar corresponds to the standard deviation calculated by the Amide software.

6.2.5. *In vivo* therapeutic performance of CPT-PGA⊂SNPs

Given the preferential tumor accumulation of the 37-nm ^{64}Cu-labeled CPT-PGA⊂SNPs as compared to the larger SNPs, we next performed tumor reduction/inhibition studies using the 37-nm CPT-PGA⊂SNPs in C57/BL6 mice bearing subcutaneously implanted LLC tumors on the right flank. After the tumors developed to approximately 60–90 mm^3, we performed comparative efficacy studies by dividing animals into four groups ($N = 5$) in a way to minimize weight and tumor size differences. The following regimens were administrated three times via *i.v.* injection

on day 1, 6 and 11 including PBS, PGA⊂SNPs (equivalent to the amount of SNPs in the CPT-PGA⊂SNPs group), 37-nm CPT-PGA⊂SNPs at 13.6 mg CPT equivalent/kg, while another group received a single dose of emulsified CPT at 13.6 mg CPT/kg through intraperitoneal injection (*i.p.*). CPT is very insoluble in aqueous solution and is acutely lethal when given to mice at such a high dose via *i.v.* due to embolization induced by the particulate matter in the drug suspension.[170] **Figure 6.6.a** depicts the median tumor size for each group as a function of time, and clearly shows that the 37-nm CPT-PGA⊂SNPs had the best anti-tumor efficacy among all groups tested. As compared with PGA⊂SNPs (drug-free vectors), 37-nm CPT-PGA⊂SNPs started to show statistically significant efficacy in delaying tumor growth from day 6 ($*p < 0.05$ at day 6 and 8, Student's *t*-test) and even higher significant inhibition effect at day 10 and 12 ($**p < 0.01$ at day 10 and 12). However, there was no statistical significance between the data points of PGA⊂SNPs group and PBS group indicating that the efficacy of the 37-nm CPT-PGA⊂SNPs was ascribed to the released CPT. The 37-nm CPT-PGA⊂SNPs also significantly outperformed CPT in this study with statistical significance from day 6 to day 12 ($*p < 0.05$). It is noteworthy that one of the five mice treated with 37-nm CPT-PGA⊂SNPs experienced complete tumor reduction on day 10. The final mean tumor burden of the 37-nm CPT-PGA⊂SNPs group was 265.5 ± 101.3 mm^3 (mean ± SEM), which was smaller than any other group ($*p < 0.05$). On the other hand, no obvious body weight loss was observed for the group treated with the 37-nm CPT-PGA⊂SNPs at the tested dosage throughout the study (**Figure 6.6.b**), indicating there is no acute toxicity of the 37-nm CPT-PGA⊂SNPs. As a comparison, the CPT group showed emerging toxicity after a single dose with around 9% body weight loss at day 5 (data not shown). The results demonstrate that 37-nm CPT-PGA⊂SNPs group is the most efficacious group among all the groups with reduced toxicity compared to free drug. Presumably,

the reason for the enhanced efficacy of 37-nm CPT-PGA⊂SNPs may be the preferential tumor accumulation due to EPR effect as demonstrated. After the SNPs reached the tumor tissues, the sustained release of CPT from CPT-PGA⊂SNPs (**Figure 6.3.b**) was ascribed to the extended inhibition on tumor growth.

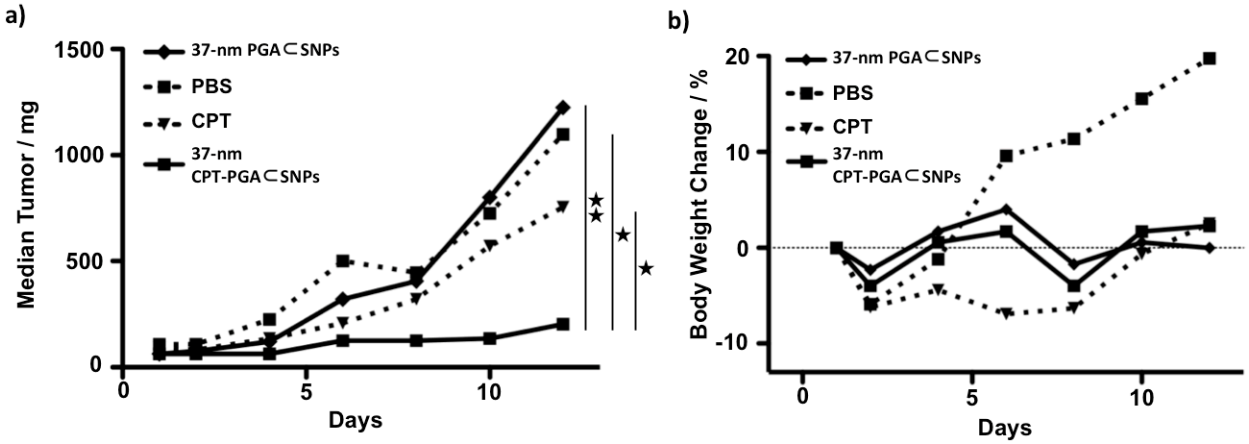

Figure 6.6. a) *In vivo* anti-tumor efficacy studies of 37-nm CPT-PGA⊂SNPs (13.6 mg CPT equivalent/kg) along with controls, *i.e.*, free CPT (13.6 mg/kg), PBS and PGA⊂SNPs (equivalent to the amount of SNPs in the CPT-PGA⊂SNPs group). LLC tumor-bearing C57Bl/6 mice were treated with different groups via intravenous injection at day 1, 6 and 11 (except for CPT group, which was only treated once at day 1 via intraperitoneal injection). 37-nm CPT-PGA⊂SNPs showed delayed tumor growth from day 6 compared to PGA⊂SNPs group and also significantly outperformed CPT group from day 4 (*$p < 0.05$; **$p < 0.01$; Student's *t*-test). b) Body weight changes of the four groups over the course of treatments.

In conclusion, the integration of the two technologies can lead to a breakthrough in the development of a new generation of cancer therapeutic agents. We foresee our work providing a general strategy in the search of optimal therapeutic agents among the diversity of NP-based therapeutic agents by utilizing imaging technology as a fast and early checkpoint prior to performing large-scale pre-clinical studies. In principle, this work can also be adopted for discovery of other NP-based vectors for delivery of various payloads (*e.g.*, DNAs, RNAs, proteins or their combinations).

6.3. Doxorubicin-Encapsulated Supramolecular Magnetic Nanoparticles (Dox⊂SMNPs) for Controllable Drug Release

6.3.1. Theranostics with controlled drug release

Nanoparticle (NP)-based theranostics, which contain imaging probes for molecular diagnosis and therapeutic compounds for therapy in a single NP, have been considered promising delivery agents against various diseases to achieve personalized medicine.[171] In both diagnosis and therapy, one of the key factors is to deliver imaging agents and drugs to target sites efficiently. In order to investigate disease sites, the contrast intensity between the target site and surrounding area should be as high as possible, thus it requires efficient amount of imaging agents to the target sites.[172] On the other hand, in the case of delivering drugs, delivery agents should carry sufficient drugs to the target sites in order to have favorable therapeutic efficacy meanwhile avoiding the nonspecific delivery to normal tissues.[173] A wide range of NP-based theranostics have been developed for the improvement of diagnosis and therapy.[54a, 80, 143f, 174] However, the delivery of these NPs in animal models and patients remains a problem even if they have promising outcomes *in vitro*.[171] Alternatively, the combination of controlled-release properties and efficient delivery to the target sites should enable the development of safer and more effective theranostic NPs in clinical translation.[156, 172, 175] In this chapter, we introduce doxorubicin-encapsulated supramolecular nanoparticles (Dox⊂SMNPs) as powerful theranostic delivery agents. By introducing radio-isotopes, *i.e.*, ^{64}Cu, into Dox⊂SMNPs, ^{64}Cu-labeled Dox⊂SMNPs serve as multimodal diagnostics for both PET and MR imaging. We screened out the optimized Dox⊂SMNPs with the most tumor accumulation percentage using PET imaging-based biodistribution studies, which guarantees that the identified Dox⊂SMNPs can carry the most contrast agents and drugs to the target tumor site. Moreover, the dynamic PET imaging-based biodistribution data show the highest tumor accumulation time point, which is a key

parameter for *in vivo* controlled-release therapeutic treatments. We then demonstrated 1) the potential of using Dox⊂SMNPs as promising contrast agents for MRI and 2) the successful results of controlled drug release *in vitro* triggered by external magnetic filed. Finally, we are now investigating the controlled-release therapeutic efficacy of identified Dox⊂SMNPs in a mouse model.

6.3.2. Molecular design of Dox⊂SMNPs

Previously, we demonstrated the feasibility of using supramolecular synthetic approach to 1) encapsulate Dox molecular into SNP vector (see **Chapter 5.1.**) for drug delivery and 2) introduce magnetic nanoparticles, *i.e.*, ZnMNP, as one of our molecular building blocks to give SMNPs for MRI applications (see **Chapter 2.2.3.**). In this chapter, we incorporate both chemotherapeutic and magnetic nanoparticles into our SNP vector as a new generation theranostic delivery agent (Dox⊂SMNPs). The Dox⊂SMNPs are generated from four molecular building blocks and Dox molecule (**Figure 6.7.**). The four molecular building blocks, *i.e.*, Ad-PEG, CD-PEI, Ad-PAMAM, and Ad-ZnMNP, were prepared and characterized according to literature.[43, 74] By find-tuning the ratios between the building blocks, Dox⊂SMNPs with various sizes can be obtained.

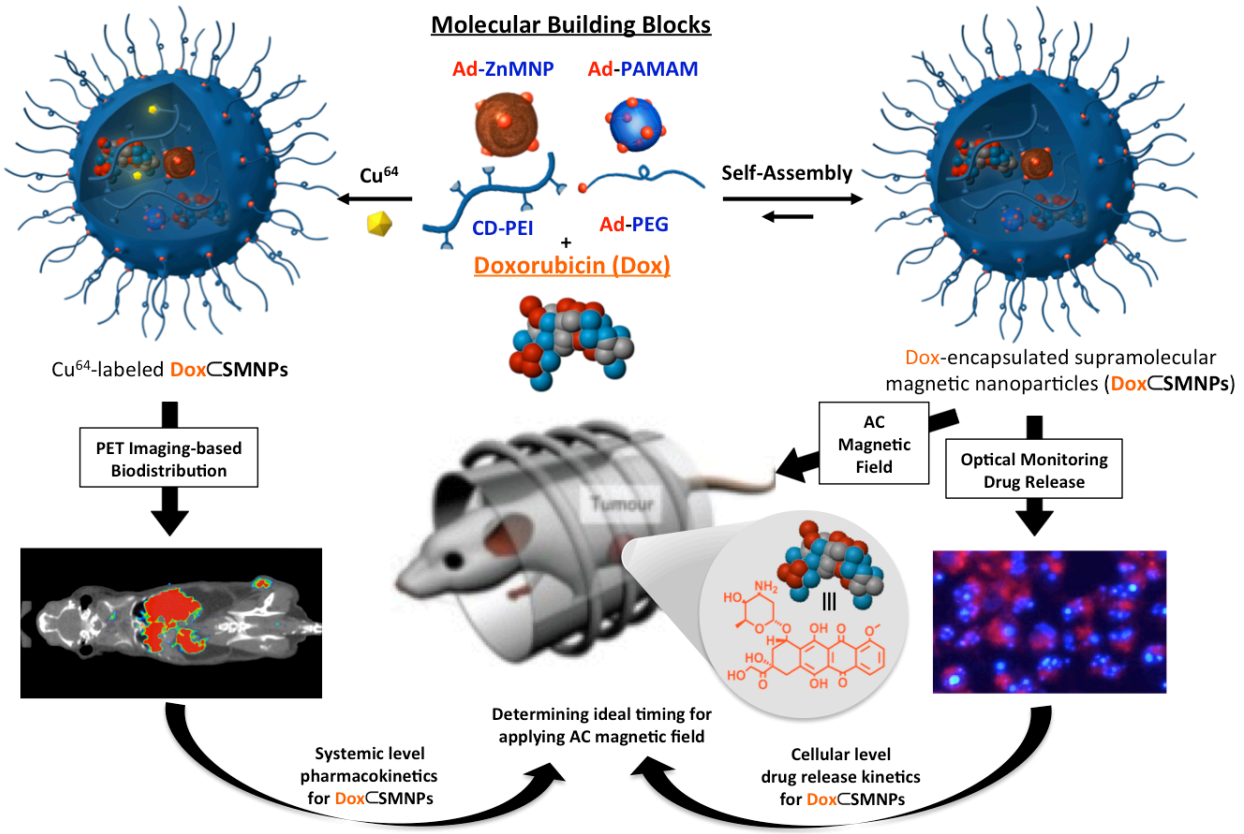

Figure 6.7. Schematic representation of a self-assembled approach employed for the preparation of a multi-modality theranostics system, doxorubicin (Dox)-encapsulated supramolecular magnetic nanoparticles (Dox⊂SMNPs), from four molecular building blocks (*i.e.*, Ad-PAMAM, Ad-ZnMNP, CD-PEI and Ad-PEG) and free Dox molecule. The synthetic modularity of such a supramolecular synthetic approach allows incorporation of radioisotope (*i.e.*, ^{64}Cu). The resulting ^{64}Cu-labeled Dox⊂SMNPs can be subjected to PET imaging biodistribution studies, resulting in systemic level of pharmacokinetics for Dox⊂SMNPs. On the other hand, in our molecular design, Dox can serve as both a chemotherapeutic agent and a fluorescent reporter system for monitoring in vitro drug releasing, providing cellular level of drug release kinetics for Dox⊂SMNPs. Thus, taken together, ideal timing for applying the AC magnetic field can be determined for on-demand burst drug release at tumor site for improved therapeutic efficacy *in vivo*.

6.3.3. Size controllability and characterization of Dox⊂SMNPs

Size-controllable Dox⊂SMNPs are prepared by adding 12-μL DMSO solution containing various amount of Ad-PAMAM (0.06, 0.13, and 0.26 mg) and Dox (0.1 mg) into a 500-μL PBS mixture of Ad-ZnMNP (0.1 mg), Ad-PEG (3.15 mg) and CD-PEI (2 mg). The mixture was kept at 70 ^{o}C for 30 min, followed by annealing at room temperature for 2 h, affording three different sizes of Dox⊂SMNPs as a dark purple solution. The encapsulation efficiency was determined to

be 95%. By tuning the ratios between the four molecular building blocks, three different sizes of Dox⊂SMNPs can be obtained. TEM images in **Figure 6.8.** show narrow size distribution and spherical morphology of the resulting Dox⊂SMNPs (70, 100, 160 nm). DLS analysis (150, 188, and 280 nm) and zeta potential measurements (18, 22, 28 mV) were also carried out to characterize the three different sizes of Dox⊂SMNPs.

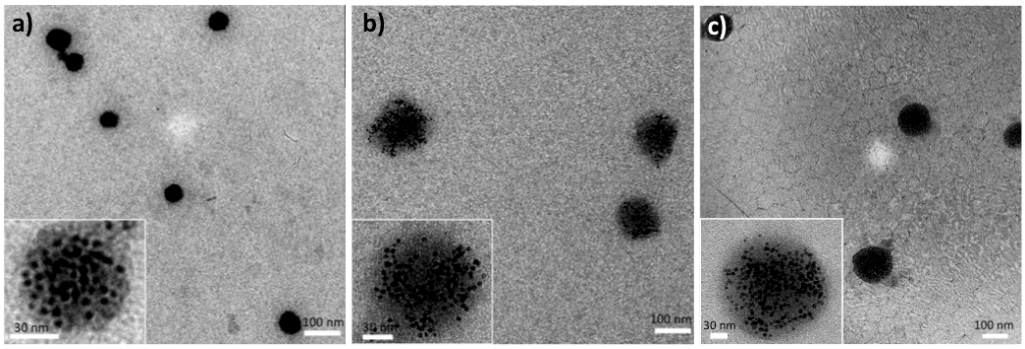

Figure 6.8. TEM images of size-controllable Dox⊂SMNPs with various sizes: a) 70 ± 9, b) 96 ± 7 and 161 ± 8 nm. Scale bars: 100 nm. Inserts: Higher magnification TEM images of Dox⊂SMNPs with different sizes. Scale bars: 30 nm

6.3.4. Size dependent biodistribution study of Dox⊂SMNPs

Nanoparticles' size is a key parameter for their biodistribution patterns and therapeutic performances due to their differential EPR effects.[165] In order to have the most tumor accumulation for further *in vivo* studies, we screened out the optimal size of Dox⊂SMNPs among the three different sizes. Similar to previous approach (see **Chapter 6.2.4.**), we utilized micro-PET imaging technology (see **Chapter 3.2.**) to understand the biodistribution properties of the 70-nm, 100-nm and 160-nm Dox⊂SMNPs. The resulting biodistribution data can thus correlate the sizes of Dox⊂SMNPs with their tumor accumulation performances. According to previous strategy,[43] ^{64}Cu-labeled Dox⊂SMNPs with three different sizes can be prepared by incorporating DOTA-CD-PEI as one of the precursors (along with CD-PEI, Ad-PAMAM, Ad-ZnMNP, Ad-PEG and Dox), followed by ratiometric mixing and labeling by ^{64}Cu. The three

different sizes of ^{64}Cu-labeled Dox⊂SMNPs were immediately injected into DLD-1 tumor-bearing C57Bl/6 mice via intravenous (*i.v.*) administration. Their respective biodistribution data (**Figure 6.9.**) for each size were acquired by micro-PET imaging technology 48 h post injection. Static micro-PET images of the three different sizes of ^{64}Cu-labeled Dox⊂SMNPs reveal that 70-nm ^{64}Cu-labeled Dox⊂SMNPs exhibited significantly enhanced tumor accumulation (**Figure 6.9.a**) compared to the other two sizes (**Figure 6.9.b and c**). We also did the time dependent biodistribution study of the three Dox⊂SMNPs and the results show that the Dox⊂SMNPs accumulate the most at 36 h post-injection, which is a key time-point for *in vivo* controlled-release therapeutic study. We quantified their individual *ex vivo* biodistribution data 48 h post-injection (data not shown) and divided the signal of specified organ from the signal of tumor. Tumor to organ signal ratios in **Figure 6.10.** indicate that 70-nm Dox⊂SMNPs have the highest tumor to organ ratio in each case, which also suggest that the 70-nm Dox⊂SMNPs can specifically accumulate at the tumor site while minimizing the non-specific accumulation at other organs compared to 100-nm Dox⊂SMNPs and 160-nm Dox⊂SMNPs.

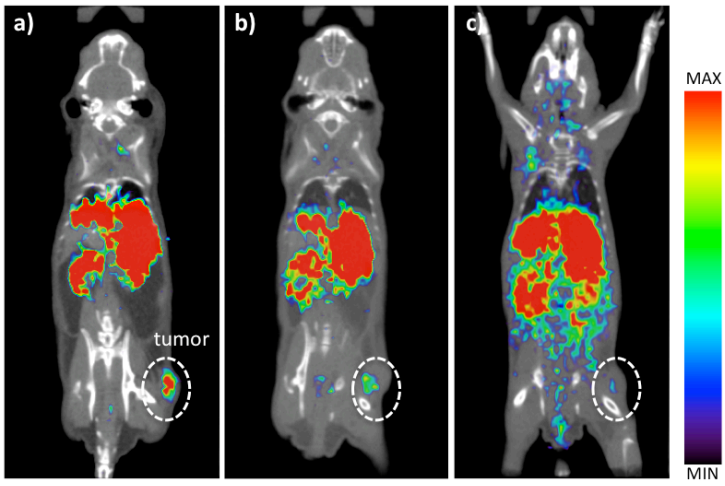

Figure 6.9. Static filtered back-projection micro-PET images of NU/NU mice bearing DLD-1 tumor at 48 h post injection of a) 70-nm, b) 100-nm and c) 160-nm ^{64}Cu-labeled Dox⊂SMNPs. 70-nm ^{64}Cu-labeled Dox⊂SMNPs had higher tumor-specific uptake than the other two groups.

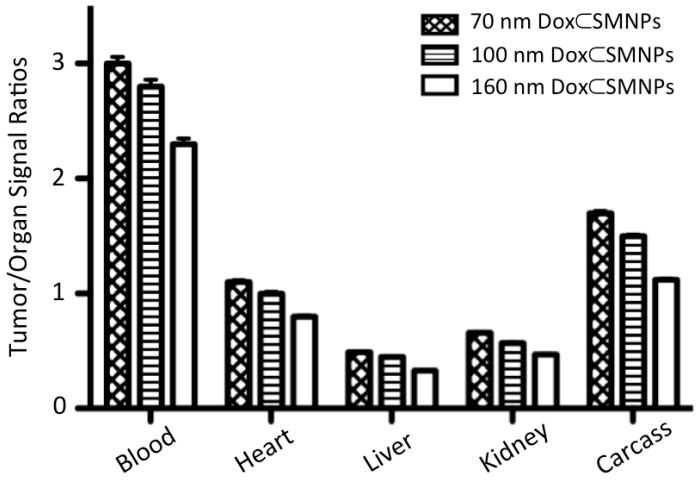

Figure 6.10. Tumor to organ signal ratios quantifying from *ex vivo* biodistribution data of mice treated with 70-nm, 100-nm, or 160-nm DoxCSMNPs after 48 h intravenous injection

6.3.5. Control release profile of DoxCSMNPs

Given the fact that the 70-nm DoxCSMNPs exhibit preferential tumor accumulation as compared to the larger SMNPs, *i.e.*, 100-nm DoxCSMNPs and 160-nm DoxCSMNPs, we then studied the magnetic properties and magnetic activated drug release performances of 70-nm DoxCSMNPs. T_2 relaxation time plot and phantom images of 70-nm DoxCSMNPs and 6 nm ZnMNP are shown in **Figure 6.11.**. The results indicate 70-nm DoxCSMNPs improve their relaxivity (**Figure 6.11.a**) compared to 6 nm ZnMNP; also, across the various concentrations of nanoparticle probes, DoxCSMNPs indeed show better contrast effects (**Figure 6.11.b**).

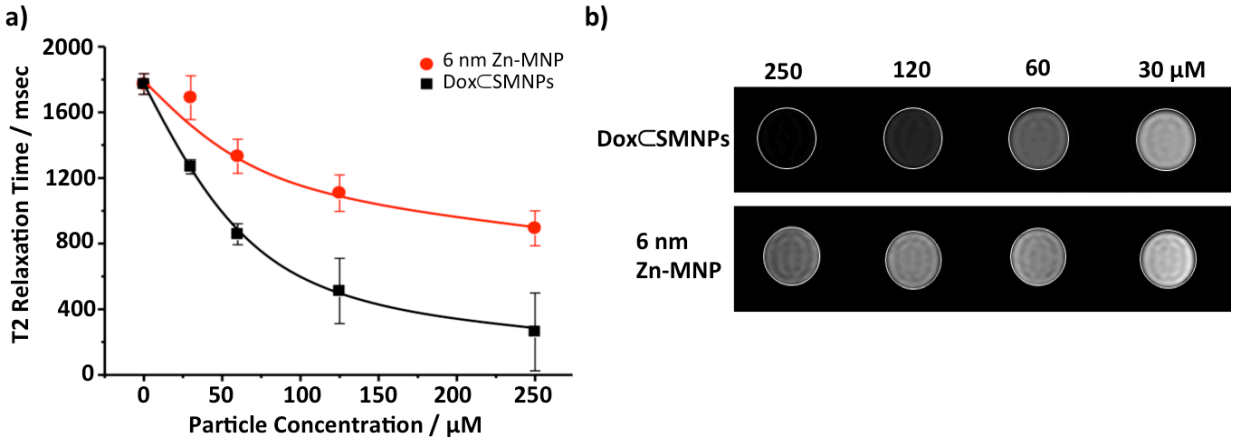

Figure 6.11. a) Plot of T_2 relaxation time of Dox⊂SMNPs and 6 nm ZnMNP with various particle concentrations. b) Phantom images for capillaries containing Dox⊂SMNPs (top) and 6 nm ZnMNP (bottom) with various concentrations increasing from 30 μM to 250 μM from right to left.

We used an oscillating magnetic field (AMF) as an external control to trigger the release of the drug from Dox⊂SMNPs. The release of Dox molecule can act as a built-in reporter that allows real-time monitoring of drug release (see **Chapter 5.1.**). In this study, we first investigated drug release performance of Dox⊂SMNPs as a function of AFM duration (**Figure 6.12.a**). The sample at a concentration of 3 mg/mL was placed inside a water-cooled copper coil producing an AMF having a frequency of 500 kHz and a current amplitude of 37.4 kAm−1 (Taeyang Instrument Company, Korea). After applying AMF to the sample for various duration times, we measures its fluorescent intensity change in order to monitor its drug release performance. From the fluorescence spectra in **Figure 6.12.a** for each group, we plot the drug release profile based on their maximum intensity, which is at 593 nm (**Figure 6.12.b**). The result shows the amount of drug releases from Dox⊂SMNPs reaches to a plateau after applying AMF for 10 min. We then explored the effect of applying pulsed AMF to Dox⊂SMNPs on their drug release performance. Dox release profiles after exposure a single pulsed AMF (red) and multiple pulsed AMF (black) are summarized in **Figure 6.12.c**. Dox⊂SMNPs exposed to a single AMF (red line) exhibited 17% cargo release after an initial 2 min pulse; meanwhile, the sample exposed to multiple AMF pulses (every 10 min) increases its fluorescent intensity even more until the 7^{th} pulse (black line), which indicates multiple pulsed AMF enabled more drug release.

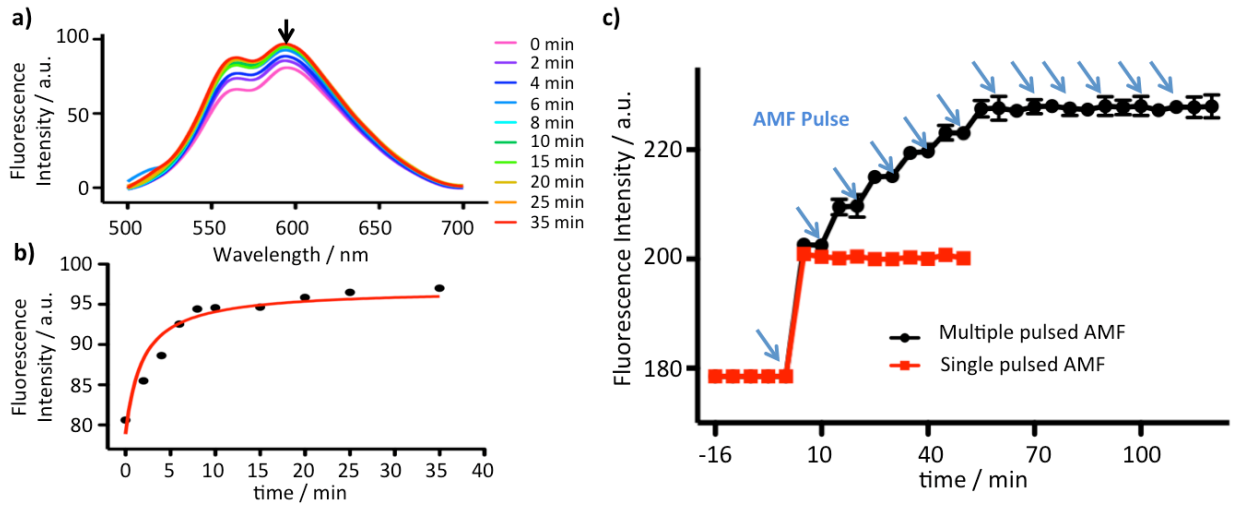

Figure 6.12. Dox releases using magnetic actuation. a) Fluorescence spectra of DoxCSMNPs after applying AMF with various duration times. b) The drug release profile of DoxCSMNPs by setting the fluorescence intensity of each duration time at their maximum intensity, *i.e.*, 593 nm, in a). c) Dox release profile of DoxCSMNPs after exposure from a 2-min duration single pulsed AC magnetic field (AMF) (red line) and multiple pulsed AMF (2 min duration with 10 min intermittence) (black line). DoxCSMNPs exposed to a single AMF exhibited 50% cargo release after an initial 2 min pulse (red line) and the rest of Dox released stepwise in a pulsatile AMF applications and reached a plateau at the 7th pulse (black line).

6.3.6. Therapeutic performance of DoxCSMNPs

We demonstrated 70-nm DoxCSMNPs could be used for *in vitro* drug delivery by releasing anticancer drugs, *i.e.*, Dox, in the DLD-1 colorectal adenocarcinoma cell line via magnetic actuation (**Figure 6.13.a and b**). 70-nm DoxCSMNPs were taken up by the cells and minimal drug release and cell damage were observed (**Figure 6.13.a**). In the presence of AMF, the local heating caused by the DoxCSMNPs trigger the release of Dox from the SMNPs, which induced cell apoptosis. After a 10 min exposure to AMF, a significant fluorescent intensity increases from the Dox (red) and accumulates into nuclei were seen as a result of drug delivery and drug release in the cells (**Figure 6.13.b**). It's worth to note that the both nucleus fragmentations (**Figure 6.13.b, DAPI staining image**) and apoptotic cell bodies (**Figure 6.13.b, DIC image**) can be observed under microscope, which shows the effective drug delivery performance of DoxCSMNPs. The cell viability was quantified by using CCK-8 assay (**Figure 6.13.c**). There is

negligible cytotoxicity observed from cells treated with 70-nm DoxCSMNPs (**Figure 6.13.c, before AMF**). When applying AMF for 10 min, ~30% of cells treated with 70-nm DoxCSMNPs were killed (**Figure 6.13.c, after AMF**). On the other hand, non-treated cells did not affect by the exposure of AMF. Thus, the cell death was attributed to the release of Dox.

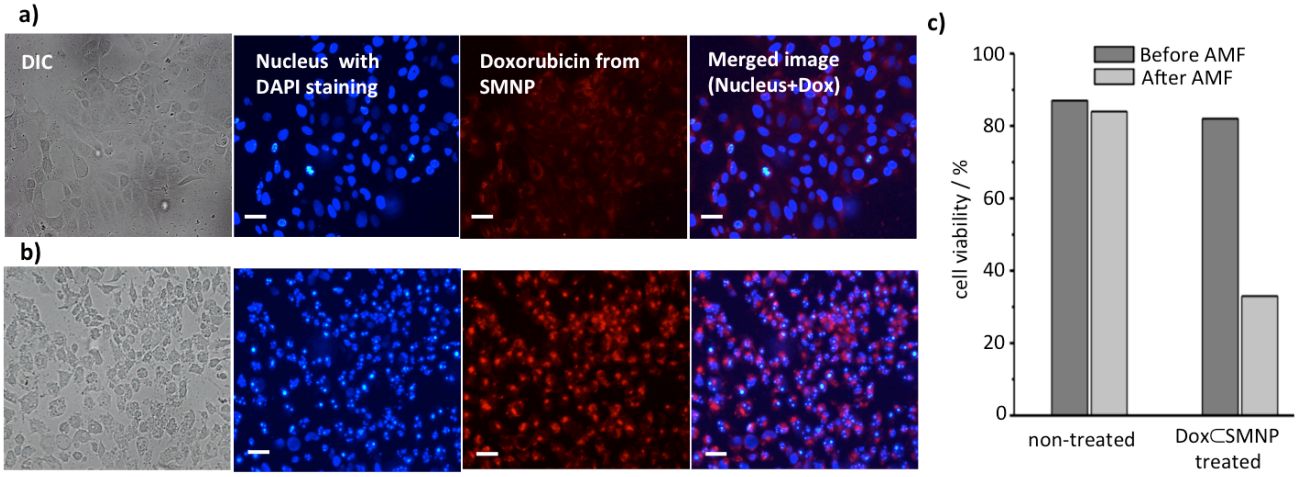

Figure 6.13. *In vitro* on-demand trigger release of DoxCSMNPs in DLD-1 cells without (a) and with (b) the application of a single pulsed AMF. DIC image, fluorescent image of DAPI, fluorescent image of Dox, and merged image of Dox and DAPI are shown for both cases. Scale bars: 5 uM. c) Quantification of cell death by CCK-8 assay. The viability of DLD-1 cells treated with DoxCSMNPs is lowered to ca. 30% after the application of AMF. The control group, non-treated cells are not affected by AMF.

We are now investigating *in vivo* therapeutic performance of 70-nm DoxCSMNPs in a DLD-1 xenografted mouse model. We first intravenously injected 150 μg/Kg of DoxCSMNPs to the mice with tumor size of 100 mm^3. After 36 h, the AMF (37.4 kA/m, 500 kHz) was applied to the mice for 10 min. The primary data in **Fig 6.14.** showed promising therapeutic efficacy compared to the control. We note that our system achieve similar therapeutic effect but with 2-3 orders of magnitude lower amount of drug compared to recent literatures,[31a, 176] which can be attributed to the burst release of drug at tumor sites that generate local high concentration of drugs at a short period of time. We are optimizing the treatment schedule in order to achieve the most therapeutic efficacy, *i.e.*, a secondary treatment will be carried out after a week. Also, more control groups,

such as, mice without any treatment and mice treated with AMF but without Dox⊂SMNPs injection, will be investigated.

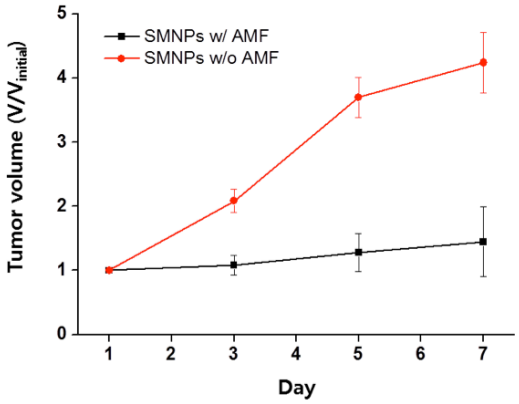

Figure 6.14. Passive tumor targeting of Dox⊂SMNPs and their *in vivo* therapeutic efficacy. DLD-1 xenografted mice (n=3) were subjected to Dox⊂SMNPs treatment when the tumor sizes reached to 100 mm^3. *In vivo* AMF application to the mice for the magnetically induced drug release 36 h post-injection. The result show delayed tumor growth for the group treated with both Dox⊂SMNPs and AMF compared to the control group without AMF application.

6.3.7. Conclusion

On the basis of these strategies, we develop doxorubicin-encapsulated supramolecular nanoparticles (Dox⊂SMNPs) with dual-modality for *in vivo* PET/MR imaging and controlled-release drug delivery. The successful results were obtained with them in animal models for imaging and we anticipate them to have promising *in vivo* controlled release therapy outcomes. We foresee that these rational strategies, as well as Dox⊂SMNPs, will be applied in both the diagnosis and therapy of many human diseases. These theranostic NPs are expected to have great contribution to optimize therapy efficacy for individual patients in clinical translation in the near future.

SUPPORTING INFORMATION

1. Material Synthesis

1.1. Synthesis of CD-PEI

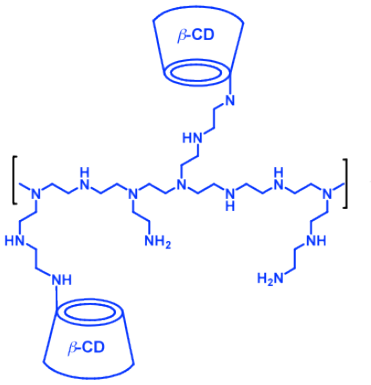

To a solution of branched PEI (100 mg, 10.0 μmol) in 100 mL DMSO, 6-OTs-β-CD (1.29 g, 1.0 mmol) was added. After reaction at 70 °C for 3 days, the mixture was transferred to a Slide-A-Lyzer® dialysis cassette (MWCO, 10 kD) and dialyzed against deionized (DI) water for 6 days. After dialysis, the reaction mixture was filtrated to remove the unreacted 6-OTs-β-CD as white precipitate, and the filtrate was lyophilized overnight to afford CD-PEI (150 mg, 8.3 μmol) as a white floppy solid in a 83% yield. ^{1}H NMR (400 MHz, D_2O) δ 4.92 (br, C_1H of CD), 3.27-3.66 S4 (m, $C_{2\text{-}6}H$ of CD), 2.3-3.0 (br, OCH_2 of PEI). The CD/PEI ratio in a CD-PEI molecule was calculated based on the proton integration of C_1H of CD versus CH_2 of PEI.

1.2. Synthesis of DOTA-CD-PEI

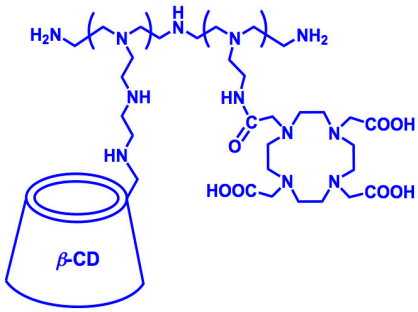

To a solution of CD-PEI (1.7 mg, 0.1 μmol, 1.0 equiv.) in PBS buffer solution (pH 7.2), DOTA-NHS (0.5 mg, 1.0 μmol, 10.0 equiv.) was added, and the reaction mixture was stirred at rt for 2 h. After the reaction completed, the mixture was purified by dialysis (Slide-A-Lyzer® dialysis cassette, MWCO 10 kD) against DI water overnight and lyophilized to yield DOTA-CD-PEI, which is ready for preparation of DOTA-grafted SNPs.

1.3. Synthesis of 8-Ad-PAMAM

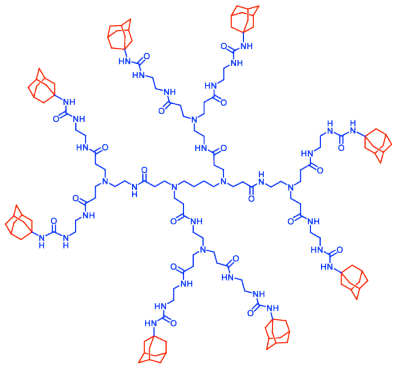

A methanol solution containing PAMAM (20% wt, 100 mg, 0.07 mmol) was added into a round-bottom flask. Methanol was evaporated in vacuo and the sticky solid was re-dissolved in 10 mL dry THF. 1-adamantane isocyanates (244.6 mg, 1.4 mmol) in 10 mL dry THF was directly added the PAMAM solution. After the reaction mixture was stirred at rt for 2 h, the solvent was removed in vacuo. Ether (100 mL) was added to the reaction residue to generate a white precipitate, which was collected through filtration. The white precipitate was washed with ether (100 mL x 3), and dried to give 8-Ad-PAMAM (169 mg, 0.06 mmol) as a white solid in 85% yield. ^{1}H NMR (400 MHz, $CDCl_3$): δ 7.82-7.98 (m, 12 H, CONH), 6.10 (s, 8 H, NHCONH), 5.37 (s, 8 H, NHCONH), 3.24 (br, 32 H, $COCH_2$), 2.34-2.76 (m, 64 H, NCH_2), 1.64-2.03 (m, 120 H, protons on Ad). ESI-MS: calcd. for $C_{152}H_{252}N_{34}O_{20}$ [M + H]+: m/z = 2875.98; found: 2875.78 (100%).

1.4. Synthesis of 4*-Ad-PAMAM

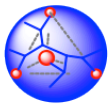

To a 10-mL THF solution containing PAMAM (100 mg, 0.07 mmol), a 10-mL dry THF solution containing 1-adamantane isocyanates (50.1 mg, 0.3 mmol) was slowly added through a syringe pump (with a injection rate of 10 mL h-1). After purification by precipitation from ether, 4*-Ad-PAMAM (89.7 mg, 0.04 mmol) was obtained as a white solid in 60% yield. ^{1}H NMR (400 MHz, $CDCl_3$): δ 7.83-7.95 (m, 12 H, CONH), 6.14 (s, 4 H, NHCONH), 5.42 (s, 4 H, NHCONH), 3.35 (br, 32 H, $COCH_2$), 2.35-2.81 (m, 64 H, NCH_2), 1.60-2.01 (m, 60 H, protons on Ad).

1.5. Synthesis of Ad-PEG

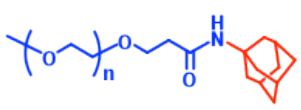

To a solution of 1-adamantanamine hydrochloride (187.7 mg, 1.0

mmol, 5.0 equiv.) in 10 mL CH_2Cl_2, triethylamine (105 mg, 1.0 mmol, 5.1 equiv.) and mPEG-NHS (1 g, 0.2 mmol, 1.0 equiv.) was added in sequence. The reaction mixture was stirred at rt for 2 h. After the reaction, the solvent was subsequently removed in vacuo, and water was added to the reaction residue. The solution was transferred into a centrifuge tube and centrifuged at 10,000 rpm for 10 min to remove the unreacted 1-adamantanamine. The solution was dialyzed with Slide-A-Lyzer® dialysis cassette (MWCO, 2 kD) against water overnight and lyophilized to yield Ad-PEG (0.92 g, 0.18 mmol) a white powder in 91% yield. ^{1}H NMR (400 MHz, DMSO-d6): δ 3.42-3.54 (br, 440H, OCH_2), 1.13-1.18 (br, 15H, protons on Ad).

1.6. Synthesis of Ad-PEG-RGD

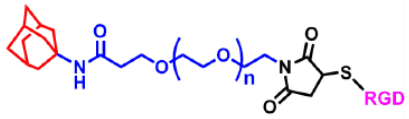

To a solution of 1-adamantanamine hydrochloride (0.94 mg, 5.0 μmol, 5.0 equiv.) in 1 mL CH_2Cl_2, triethylamine (0.6 mg, 5.0 μmol, 5.0 equiv.) and SCM-PEG-MAL (5 mg, 1.0 μmol, 1.0 equiv.) were added in sequence. The reaction mixture was stirred at room temperature for 2 h. After the reaction, the solvent was removed in vacuo, and the PBS buffer solution (1 mL) containing RGDC (2.25 mg, 5.0 μmol, 5.0 equiv.) was added to the reaction residue. The mixture was stirred for another 2 h at room temperature, followed by the removal of insoluble 1-adamantanamine by filtration. The solution was then dialyzed with Slide-A-Lyzer® dialysis cassette (MWCO, 2 kD) against water overnight and lyophilized to give Ad-PEG-RGD (3.4 mg, 0.6 μmol), a white powder in 68% yield. ^{1}H NMR (400 MHz, DMSO-d6): δ 7.83-9.12 (br, protons on RGD), 3.42-3.54 (br, protons on PEG), 1.13-1.18 (br, protons on Ad). MS (MALDI-TOF, positive mode, DHB): the observed Mn for SCM-PEG-MAL was 5373.49; the Mn value of RGD-PEG-Ad based on the SCM-PEG-MAL was calculated as 5859.78 ($M+H^+$); found: 5859.33.

1.7. Synthesis of Ad-PEG-TAT

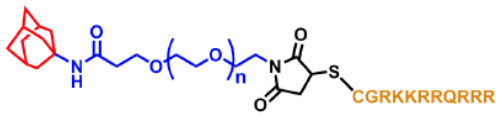

To a solution of 1-adamantanamine hydrochloride (0.94 mg, 5.0 μmol, 5.0 equiv.) in CH_2Cl_2(1 mL), triethylamine (0.60 mg, 5.0 μmol, 5.0 equiv.) and SCM-PEG-MAL (5 mg, 1.0 mmol, 1.0 equiv.) were added in sequence. The reaction mixture was stirred at rt for 2 h. After the reaction, the solvent was subsequently removed in vacuo, and the PBS buffer solution (1 mL) containing CGRKKRRQRRR (7.50 mg, 5.0 μmol, 5.0 equiv.) was added to the reaction residue. The mixture was stirred for another 2 h at rt, followed by remove of insoluble 1-adamantanamine by filtration. The solution was then dialyzed with Slide-A-Lyzer® dialysis cassette (MWCO, 3.5 kD) against water overnight and lyophilized to give Ad-PEG-TAT (4.2 mg, 0.65 μmol), a white powder in 65% yield. ^{1}H NMR (400 MHz, DMSO-d6): δ 7.76-9.32 (br, protons on TAT), 3.41-3.50 (br, protons on PEG), 1.12-1.23 (br, protons on Ad). MS (MALDI-TOF, positive mode, DHB): the observed Mn for SCM-PEG-MAL was 5373.49; the Mn value of TAT-PEG-Ad based on the SCM-PEG-MAL was calculated as 6911.08 ($M+H^+$); found: 6913.72.

1.8. Synthesis of poly(l-glutamic acid)-g-camptothecin (CPT-grafted PGA, CPT-PGA)

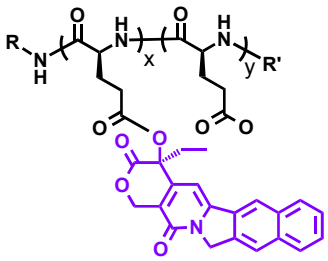

Bis(2-oxo-3-oxazolidinyl)phosphonic chloride (BOP-Cl, 175 mg, 0.68 mmol), DMAP (170 mg, 1.4 mmol), and diisopropyletheylamine (74 mg, 0.57 mmol) were added under nitrogen to a suspension of CPT (131 mg, 0.38 mmol) and dry PGA50 (310 mg, 2.4 mmol Glu) in anhydrous DMF (20 mL) cooled in an ice bath. The mixture was warmed to rt, stirred at 40 °C for 2 days, and cooled down in an ice bath. A 10% aqueous NaCl solution (40 mL) was added slowly to the reaction mixture under stirring. The resulting suspension was acidified to pH 2.5 by hydrochloric acid (0.5 M). The mixture was allowed to stir at rt for 1 h. The precipitate was filtered, washed with water (4 × 30 mL), dried under vacuum

(<1 mm, 12 h), and ground to a powder. The precipitate was suspended in 2% MeOH-CH2Cl2 (10 mL), stirred for 3 h, and filtered. This process was repeated 4 times to effect complete removal of free CPT. The product was then dried under vacuum to give 220 mg of CPT-PGA (yield 56%). Loading of CPT was 20–22 wt% determined by 1H NMR (TFA-*d*, 500 MHz).

2. Characterization

2.1. Dynamic light scattering (DLS)

DLS experiments were performed with a Zetasizer Nano instrument (Malvern Instruments, Malvern, Worcestershire, UK) equipped with a 10-mW helium-neon laser (λ = 632.8 nm) and thermoelectric temperature controller. Measurements were taken at a 90° scattering angle.

2.2. Zeta potential (ζ) measurements

Zeta Potential of samples was determined by photon correlation spectroscopy using a Zetasizer Nano instrument. The measurements were performed at 25 °C with a detection angle of 90°, and the raw data were subsequently correlated to zeta potential by the Zetasizer software program. The zeta potentials were averaged by three independent measurements.

2.3. Transmission electron microscopy (TEM)

The morphology and sizes of samples were examined on a Philips CM 120 transmission electron microscope, operating at an acceleration voltage of 120 kV. The TEM samples were prepared by drop-coating 2-μL of sample solutions onto carbon-coated copper grids. Excess amounts of droplets were removed with filter paper after 45 s. Subsequently, the surface-deposited sample solutions were negatively stained with 2% uranyl acetate for 45 s before TEM studies.

2.4. T_1 relaxation measurements

T_1 relaxation rate measurements were performed on a Bruker Avance 600 MHz spectrometer (Bruker BioSpin Corp., Billerica, MA, USA) equipped with a narrow-bore (54 mm) 14.1 T

magnet and a broadband probe at 295 K. Both inversion recovery (IR) and saturation recovery (SR) pulse sequences were acquired.

3. *In Vitro* Studies

3.1. General cell culture

NIH 3T3, HeLa, A549, U87 and IMR-90 cell lines were routinely maintained in DMEM containing 10% fetal bovine serum (FBS) and 1% penicillin/streptomycin (Invitrogen, Carlsbad, CA). MCF7 was cultured in EMEM containing 10% fetal bovine serum (FBS) and 1% penicillin/streptomycin. PC3 was cultured in RPMI-1640 containing 10% fetal bovine serum (FBS) and 1% penicillin/streptomycin.

3.2. Cell uptake of NPs

Cell cultures were maintained at 37 °C under a humidified condition with 5% CO_2. After 24 h of plating, the cells were washed once with PBS, and the solutions of particles were added respectively. After 20 min of incubation, the cells were washed three times with PBS to remove extra solution and their individual culture medium was added followed by 2 h incubation.

3.3. Gene transfection studies

Cells ($1x10^4$ cells / well) were plated in an 8-well chamber slides and allowed to adhere overnight. Each sample was diluted with 200 μL Opti-MEM medium and transferred to each well of an 8-well chamber slide (Lab-Tek®, Electron Microscopy Sciences, PA). Samples were incubated with the cells for 4 h, then removed by aspirating, and replaced with 400 μL/well of fresh regular culture medium. Cells were allowed to grow for 24 h at 37 °C and 5% CO_2 and then fixed (4% paraformaldehyde for 15 min at room temperature), washed with PBS three times, stained with DAPI and a final PBS rinse prior to EGFP expression analysis by fluorescence microscope.

3.4. *In vitro* viability study

Cell viability was measured by the MTT assay. After incubating cells with 100-μL samples along with controls with respective concentrations in 96 well-plates for 48 h, the solutions were removed and washed with PBS three times. Fresh medium containing 20-μL CellTiter-Blue reagent was added to each well, followed by 3 h incubation at 37 °C. The cell viability results were quantified using fluorescent plate-reader.

4. General *In Vivo* Study

The animal study protocol was reviewed and approved by the Animal Care and Use Committee of University of California, Los Angeles. Female C57Bl/6 mice, 4–5 week old, were anesthetized, shaved, and prepared for implantation of the tumor cells. Lewis lung carcinoma (LLC) cells were collected from culture, and 3×10^5 cells suspended in a 1:1 mixture of PBS buffer and matrigel were then injected subcutaneously into right flank of a mouse. After 6 days when tumors reached around 60–90 mm^3 in size, mice were divided into 4 groups of five mice, minimizing weight and tumor size difference. Tumor-bearing mice were treated by intravenous injection of PBS, PGA⊂SNPs, CPT-PGA⊂SNPs (13.6 mg/kg CPT) or intraperitoneal injection of CPT (13.6 mg/kg). Three doses were administrated with 5-day interval, ***i.e.***, at day 1, day 6 and day 11, respectively (except for CPT group, which only received a single dose at day 1 due to emerging toxicity[170]). After injections, the animals were monitored closely, and measurements of the tumor size and body weight for each animal were performed at regular intervals using calipers without knowledge of which injection each animal had received. The tumor volume for each time point was calculated according to the formula, (length) × $(width)^2/2$, where the long axis is the length, the short axis is the width. Tumor density is assumed as 1 mg/mm^3. If body weight loss is beyond 20% of pre-dosing weight, the animals were euthanized. When the tumor load reached 1500 mm^3 or the animal had become moribund, the

mouse was sacrificed. The statistical analysis was undertaken using a Student's *t*-test (two-tailed), and *p*-values < 0.05 were considered statistically significant, $p < 0.01$ were considered highly statistically significant.

5. General Imaging Preparation

5.1. Radio-labeling of SNPs

All liquids were pretreated with Chelex-100 (Bio-Rad, Herchules, CA) to remove trace metal contaminants. The ^{64}Cu chloride (MDS Nordion, Vancouver, Canada) was mixed with NH_4OAc buffer (pH 5.5, I = 0.1 M), and 800-fold excess of nanoparticles were added to above solution. The mixture was incubated for 1 h at 60 °C, and the ^{64}Cu-labeled SNPs product was purified by a molecular weight cut off filter (Centricon YM10, Billerica, MA) with a spin speed of 10000 g for 10 min. The labeling yield (> 90%) was determined by measuring the radioactivity in the filter, the filtrate and the retaintate, respectively. The ^{64}Cu-labeled SNPs are then re-suspended in PBS for *in vivo* injections.

5.2. Micro-PET/CT imaging

Micro-PET/CT imaging was performed with a micro-PET FOCUS 220 PET scanner (Siemens, Malvern, PA) and a MicroCAT II CT scanner (Siemens). Fifteen minutes before imaging, mice were anesthetized by using 1.5–2% isoflurane in a heated (30 °C) induction chamber, then transferred to a heated isolation/imaging chamber. 64Cu (100–300 μCi) was injected either via tail vein or in the footpad while the anesthetized animals were positioned on the scanner bed, and a dynamic PET scan was acquired for 1 h. The volume used for the tail vein injection were ~ 100 μL, and for the footpad injection < 20 μL. Mice were moved to the micro-CT in the same isolation/imaging chamber. PET images were reconstructed by filtered back projection, using a ramp filter to yield an image resolution of 1.7 mm. Immediately after the micro-PET scan, mice underwent a 7-min micro-CT scan, using routine image acquisition parameters. The micro-CT

scan was used for anatomical localization of the tissue concentrations of the ^{64}Cu over time by micro-PET. Static micro-PET scans were acquired on the following day (18–24 h after injection) with another micro-CT scan for anatomical co-registration. To determine temporal changes of tracer concentration in various tissues, ellipsoid regions of interest were placed in the region that exhibited the highest ^{64}Cu activity as determined by visual inspection. To ensure accurate anatomical positioning, regions of interest were placed on fused micro-PET/CT images generated by the AMIDE software. To minimize partial volume effects, care was taken not to include the anatomical borders of the organs. Considering the size of the studied organs and tumors and the spatial resolution of the PET scanner, partial volume effects are not expected to have a major impact on the results of quantitative analysis. Activity concentrations are expressed as percent of the decay-corrected injected activity per cm^3 of tissue (can be approximated as percentage ID/g), using the AMIDE software, and these values are normalized to an elliptic cylinder region of interest drawn over the entire mouse.

5.3. Phantom preparation and imaging

Imaging was performed on a Bruker Avance 600 MHz spectrometer (Bruker BioSpin Corp., Billerica, MA, USA) equipped with a Micro 5 gradient system (maximal gradient strength of 192 G/cm in three orthogonal directions). A saturation recovery pulse sequence was used for all phantom T1-weighted imaging. The imaging parameters were slice thickness = 2 mm, RG = 10, matrix size = 64x64, TE = 6.4 ms, TR = 25 s. Following an initial hard $\pi/2$ flip angle pulse (pulse length ~ 6 μs), a crusher gradient (GT = 76.8 G ms/cm) was applied to spoil the transverse magnetization.

The capillary dilution phantom images were acquired with an 8 mm saddle coil optimized to 1H (FOV = 0.8 cm). For the capillary dilution images shown in **Figure 3.7.a**, the magnetization

evolved 2.5 s before applying a spin echo pulse sequence to acquire the image. The 64x64 raw data was zero-filled to 512x512.

5.4. *In vivo* MR imaging

In vivo imaging studies used 4–6 week-old female NOD CB17-Prkdscid/IcrCr1B1tw (NOD/SCID), weighing 25–30 g, obtained from BioLASCO, Taiwan. All animal procedures were in accordance with the regulations approved by the Institution Animal Care and Utilization Committee at National Taiwan University. All the MR data were acquired on a Varian INOVA 7-T NMR spectrometer (Varian Inc., CA, USA) with microimaging capability. The images were obtained using a microimaging probehead and a 30 mm I.D. quadrature birdcage imaging RF coil (Varian Inc., CA, USA) with self-shielded gradient systems and a maximum strength of 100 G/cm in each of the x-, y- and z-directions (Resonance Research Inc., Billerica, MA, USA). T_1-weighted images were acquired along the coronal plane using a multiple-slice spin echo pulse sequence with the following parameters: TR/TE = 50/12 ms, matrix = 256 × 128, FOV (field of view) = 51.2 × 25.6 mm, slice thickness = 0.25 mm, NT = 4. We acquired 2 slices during each TR and total number of slices = 96. The total acquisition time was about 25 min. The three-dimensional T_1-weighted images were acquired before injection of Gd^{3+}•DOTA⊂SNPs and at the following times after injecting 20 μL of Gd^{3+}•DOTA⊂SNPs in the right foot pad of the NOD/SCID mouse: 40–65 min, 100–125 min, 160–185 min, 220–245 min, 280–305 min, and 340–365 min. Additionally, we acquired images 12 h and 24 h after injecting Gd^{3+}•DOTA⊂SNPs. No gross side effects were observed during or after injection of Gd^{3+}•DOTA⊂SNPs. For quantitative analysis of acquired images, we take the average signal in a 11 × 9 × 8 voxel volume containing the lymph nodes indicated by the circles, the region of interest (ROI).

APPENDIX

Publication List:

1. A Supramolecular Approach for Preparation of Size-Controlled Nanoparticles. (**2009**)
   Angew. Chem. Int. Ed. 48: 4344-4348.

2. Photothermal Effects of Supramolecular Assembled Gold Colloids for Targeted Treatment of Cancer Cells. (**2010**)
   Angew. Chem. Int. Ed. 49: 3777-3781.

3. A Small Library of DNA-Encapsulated Supramolecular Nanoparticles for Targeted Gene Delivery. (**2010**)
   Chem. Commun. 46: 1851-1853.

4. A Digital Microfluidic Droplet Generator Produces Self-assembled Supramolecular Nanoparticles for Targeted Cell Imaging. (**2010**)
   Nanotechnology 21: 445603-445610.

5. A Rapid Pathway Toward a Superb Gene Delivery System: Programming Structural and Functional Diversity into a Supramolecular Nanoparticle Library. (**2010**)
   ACS Nano 4: 6235-6243.

6. A Small MRI Contrast Agent Library of Gadolinium(III)-Encapsulated Supramolecular Nanoparticles for Improved Relaxivity and Sensitivity. (**2011**)
   Biomaterials 32: 2160-2165.

7. Delivery of Intact Transcription Factor Using Self-Assembled Supramolecular Nanoparticles. (**2011**)
   Angew. Chem. Int. Ed. 50: 3058-3062.

8. The Therapeutic Efficacy of Camptothecin-Encapsulated Supramolecular Nanoparticles. (**2011**)
   Biomaterials 33: 1162-1169.

Supramolecular Chemistry

DOI: 10.1002/anie.200900063

A Supramolecular Approach for Preparation of Size-Controlled Nanoparticles**

Hao Wang, Shutao Wang, Helen Su, Kuan-Ju Chen, Amanda Lee Armijo, Wei-Yu Lin, Yanju Wang, Jing Sun, Ken-ichiro Kamei, Johannes Czernin, Caius G. Radu,* and Hsian-Rong Tseng**

Over the past decades, significant efforts have been devoted to explore the use of nanoparticles in the fields of biology and medicine. Several different types of nanoparticles have successfully made their way into preclinical studies in animals, clinic trials in patients, or even successful commercial products used in routine clinical practice.[1] For example, gold nanoshells,[2] quantum dots,[3,4] and super-paramagnetic nanoparticles[5] that carry target-specific ligands have been employed for in vivo imaging of cancerous cells; drug molecules have been packaged into polymer-based nanoparticles and/or liposomes[6,7] to achieve controlled release at the disease sites;[8,9] and positively charged nanoparticles have served as nonviral delivery systems for both in vitro and in vivo genetic manipulation and programming.[1,10,11] However, there remains an imperious desire to develop novel synthetic approaches to produce a new generation of nanoparticles that have 1) controllable sizes and morphologies, 2) low toxicity, compatible immunogenicity and in vivo degradability, and 3) proper surface charges and chemistry for improved physiological stability and longer circulation time. Moreover, multiple functions,[12] such as reporter systems for real-time monitoring with imaging techniques (i.e., optical imaging, magnetic resonance imaging (MRI), and positron emission tomography (PET)), targeting ligands for disease-specific delivery, and a controllable mechanism for packaging and releasing drugs and genes, will be conferred to individual nanoparticles for conducting multiple applications in parallel.

Unlike conventional chemical synthesis, which is capable of forming/breaking covalent bonds, supramolecular chemistry combines two basic concepts: self assembly and molecular recognition. Supramolecular chemistry offers a powerful and convenient approach for the preparation of nanostructured materials from molecular building blocks.[13–18] The concept of self-assembly has been extensively used to prepare organic nanoparticles. For example, liposomes and nanoscaled vesicles[7] which were prepared using self-assembly of phospholipids can serve as powerful nanocarriers for drug and gene delivery; self-assembled amphiphilic copolymer building blocks spontaneously form nanoparticles, which can be utilized for drug delivery and molecular imaging.[19–22] However, it is apparent that the concept of "molecular recognition" seems to be an underappreciated factor, which could lead to much more sophisticated synthetic approaches,[23] allowing precise control over the properties of the resulting nanoparticles. β-Cyclodextrin (CD) is one of the most commonly used supramolecular building blocks for a diverse range of biomedical applications.[24,25] CD-containing cationic polymers have been employed as vectors for highly efficient delivery of siRNA. Through CD/adamantane (Ad) recognition, Ad-functionalized polyethylene glycol (PEG) chains were grafted onto the nanoparticles to enable long-term systemic circulation in vivo.[26]

Herein, we report a convenient, flexible, and modular synthetic approach (Figure 1) for the preparation of size-controllable supramolecular nanoparticles (SNPs). CD/Ad recognition was employed to achieve self-assembly of SNPs from three different molecular building blocks, namely 1) Ad-grafted first-generation polyamidoamine dendrimer, *n*-Ad-PAMAM, 2) β-CD-grafted branched polyethylenimine (MW = 10 kD), CD-PEI, and 3) Ad-functionalized PEG compound (MW = 5 kD), Ad-PEG. Although similar to a previously reported "bricks and mortar" strategy[23] to construct cross-linked network,[27] the uniqueness of our design is the use of a capping/solvation group. This solvation group Ad-PEG on the one hand competes with the dendrimer block *n*-Ad-PAMAM to constrain the continuous propagation of the cross-linked network, and on the other hand confers water-solubility to the SNPs. By tuning mixing ratios among the three molecular building blocks in phosphate-buffered saline (PBS) aqueous buffer solution (pH 7.2, containing 1.5 mM KH_2PO_4, 155 mM NaCl, and 2.7 mM Na_2HPO_4), the equilibrium between the propagation/aggregation and capping/solvation of the cross-linked network fragments can be altered, allowing arbitrary control over the sizes of the water-soluble SNPs. In contrast to the production of polymer-based nanoparticles,[19,20,22] where significant synthetic endeavors are required to prepare specific types of polymeric building blocks to achieve the desired level of control over the

[*] Dr. H. Wang,[+] Dr. S. T. Wang,[+] Dr. H. Su,[+] K.-J. Chen, A. L. Armijo, Dr. W.-Y. Lin, Dr. Y. Wang, Dr. J. Sun, Dr. K. Kamei, Prof. J. Czernin, Prof. C. G. Radu, Prof. H.-R. Tseng
Crump Institute for Molecular Imaging (CIMI)
Institute for Molecular Medicine (IMED)
Department of Molecular and Medical Pharmacology
California NanoSystems Institute (CNSI)
University of California, Los Angeles
570 Westwood Plaza, Los Angeles, CA 90095 (USA)
Fax: (+1) 310-206-8975
E-mail: hrtseng@mednet.ucla.edu

[+] These authors contributed equally to the work.

[**] H. R.T. and C.G.R. acknowledge support from the NIH-NCI NanoSystems Biology Cancer Center (U54A119347).

Supporting information for this article is available on the WWW under http://dx.doi.org/10.1002/anie.200900063.

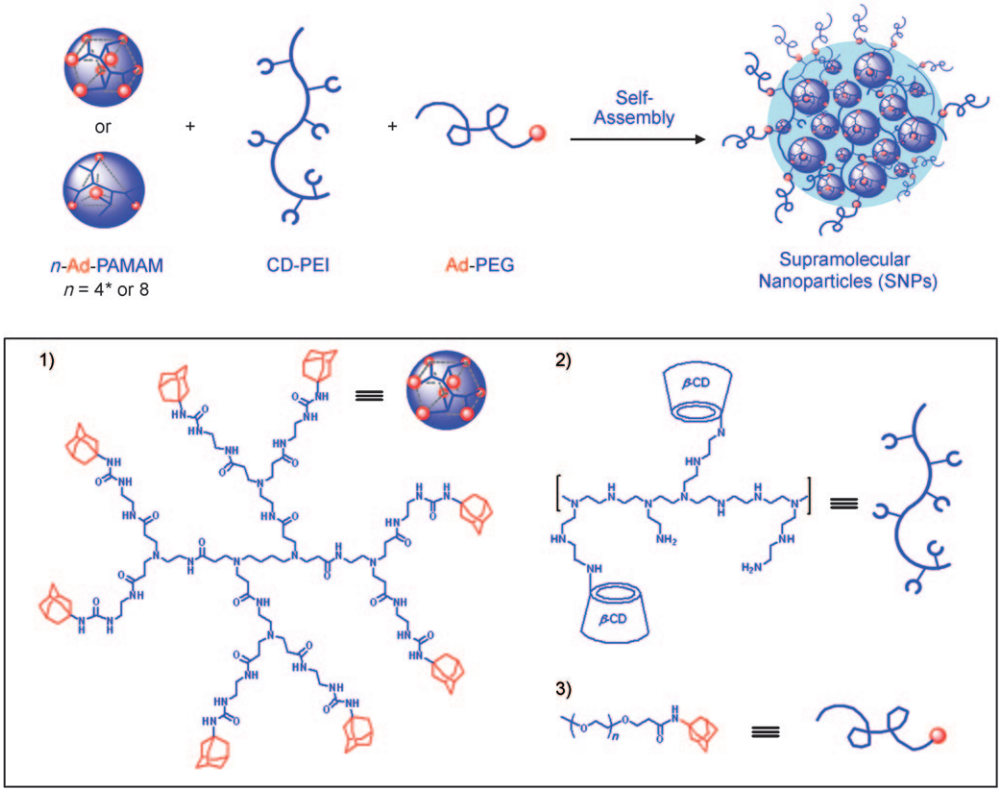

Figure 1. A convenient, flexible, and modular synthetic approach for preparation of size-controlled supramolecular nanoparticles (SNPs). A molecular recognition system based on adamantane (Ad) and β-cyclodextrin (CD) was employed to assemble three molecular building blocks 1) *n*-Ad-PAMAM (*n* = 4* or 8), 2) CD-PEI, and 3) Ad-PEG.

size, our three-component supramolecular approach offers synthetic convenience, flexibility, and modularity to alter the sizes and surface chemistry of the SNPs. By using such a supramolecular approach we were able to obtain a collection of SNPs with controllable sizes ranging from 30 to 450 nm. Further studies were carried out to unveil the unique properties of these SNPs, including 1) their stability at different temperatures and pH values, as well as in physiological ionic strength media, 2) their competitive disassembly in the presence of Ad molecules, and 3) reversible control over the size using in situ alteration of the mixing ratios of the molecular building blocks. Finally, whole-body biodistribution and lymph node drainage studies of both of the 30 and 100 nm ^{64}Cu-labeled SNPs in mice were carried out using microPET/CT imaging. The results showed that the sizes of SNPs are crucial factors which affect their in vivo properties.

The three molecular building blocks *n*-Ad-PAMAM, CD-PEI, and Ad-PEG were prepared and characterized (Supporting Information, Section 1.2). According to the ^{1}H NMR spectrum, in the polymer building block CD-PEI, there are about 7 to 8 CD recognition units grafted on a branched PEI backbone. It is well known that the CD modification increases the biocompatibility and reduces the toxicity of the PEI compounds.[28] In our experiments, two different dendrimer building blocks, 8-Ad-PAMAM with eight substituted Ad motifs and 4*-Ad-PAMAM[29] with four Ad motifs (on average, based on its ^{1}H NMR spectrum), were examined in parallel. To analyze how the mixing ratios between Ad-PAMAM and CD-PEI affect the sizes of the resulting SNPs, we utilized dynamic light scattering (DLS, N4 plus, USA) measurements to analyze the freshly prepared SNPs. To ensure sufficient supply of the capping/solvation group, an excess amount of Ad-PEG was added to each mixture. In the absence of Ad-PEG, direct mixing of *n*-Ad-PAMAM and CD-PEI resulted in aggregation and precipitation. The octa-substituted dendrimer 8-Ad-PAMAM was first tested. In this case, CD-PEI (168 μM) in PBS buffer was slowly added into the mixtures containing Ad-PEG (840 μM) and a variable amount (84 to 672 μM) of 8-Ad-PAMAM. A collection of water-soluble SNPs with variable sizes ranging between 30 and 450 nm were obtained (Figure 2a). The surface-charge densities of SNPs (with diameters ranging from 30 to 450 nm) were determined by zeta potential (ζ) measurements in PBS buffer solution (Zetasizer Nano, Malvern Instruments Ltd), which suggest that the SNPs carry zeta potentials in the range of (16.8 ± 1.2) to (28.5 ± 1.1) mV (Supporting Information, Figure S1). To ascertain the influence of the number of the Ad-substitution groups in a dendrimer core on the sizes of the respective SNPs, the tetra-substituted dendrimer 4*-Ad-PAMAM was also examined. SNPs with relative smaller sizes (30–120 nm) were obtained under similar self-assembly conditions. The morphology and size of the SNPs were also examined by using transmission electron microscopy (TEM, Philips CM-120). The TEM images suggest that the SNPs

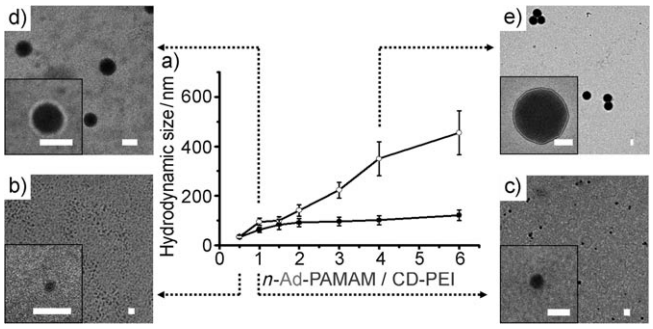

Figure 2. a) Titration plots summarize the relationship between SNP sizes and the mixing ratios of the two molecular building blocks (*n*-Ad-PAMAM/CD-PEI). Dynamic light scattering (DLS) was employed to measure SNP sizes. The titration plot for an octa-substituted dendrimer building block 8-Ad-PAMAM (○) and for a tetra-substituted dendrimer building block 4*-Ad-PAMAM (●). The standard deviation of each data point was contained from, at least, three repeats. TEM images of the resulting SNPs with different sizes of b) (32 ± 7) nm from 8-Ad-PAMAM, c) (61 ± 17) nm from 4*-Ad-PAMAM, d) (104 ± 16) nm from 8-Ad-PAMAM, and e) (340 ± 46) nm from 8-Ad-PAMAM. Scale bars: 100 nm.

exhibit spherical shapes and narrow size distributions (Figure 2b–e; Supporting Information, Figure S2), findings that are consistent with those observed using DLS.

The use of the supramolecular approach conferred dynamic characteristics to the self-assembled SNPs. To understand the dynamic stability of the SNPs, we employed real-time DLS measurements to monitor the size variation of the 30 and 100 nm SNPs (composed of the 8-Ad-PAMAM-based dendrimer) at different temperatures and pH values, and in physiological ionic strength media. First, the variable-temperature DLS measurements indicate that the SNPs are stable over a wide range of temperatures (7 to 50 °C; Supporting Information, Figure S4). Second, we observed negligible size variation of the SNPs at different pH values (pH 3.8–8.3) and physiological ionic strength (Supporting Information, see Figure S3 and S5). We note that the stability of these SNPs can be attributed to the multivalent CD/Ad recognition, which holds individual molecular building blocks in each SNP. Two sets of experiments were carried out to examine the dynamic characteristics (i.e. control of competitive disassembly and reversible alteration of the size) of these SNPs, which further validate the molecular mechanism of this supramolecular approach (Figure 3). First, we introduced 100 equivalents of a competitive reagent (i.e., 1-adamantamine hydrochloride) into a solution containing either 30 or 100 nm SNPs. After 10 minutes of sonication, disassembly of the SNPs was observed by DLS as a result of competitive inclusion of the free 1-adamantamine hydrochloride into CD-PEI. As a control, without the addition of 1-adamantamine hydrochloride, sonication alone could not disassemble the SNPs (Supporting Information, Figure S6). Second, starting from 100 nm SNPs (8-Ad-PAMAM/CD-PEI = 1:1, mol/mol), we were able to reduce the size of the SNPs to 30 nm by adding the polymer component CD-PEI in situ (8-Ad-PAMAM/CD-PEI = 1:2, mol/mol), or increase the size of the SNPs to 140 nm by adding the dendrimer component 8-Ad-PAMAM in situ (8-Ad-PAMAM/CD-PEI = 2:1, mol/mol). In these studies, 10 minutes of sonication was employed to facilitate the conversion among the three sizes of the SNPs (Figure 3).

We characterized the in vivo biodistribution (Figure 4a; Supporting Information, Figure S7) of the 30 and 100 nm ^{64}Cu-labeled SNPs (composed of the 8-Ad-PAMAM-based dendrimer, see Supporting Information for the SNP-labeling protocols) by systemically injecting the SNPs into mice through the tail veins (Supporting Information, Figure S8d). MicroPET/CT studies suggested that the biodistribution patterns of the 30 and 100 nm SNPs were quite similar (Supporting Information, Figure S8a and b). In both cases, rapid blood clearance through liver accumulation (30–50 % ID/g of the SNPs accumulated in the liver within 5 min after injection) was observed, and there was less accumulation in the kidneys (16–20 % ID/g) and lungs (8–12 % ID/g). A nonlinear two-phase decay fit of the SNPs plasma concentrations yielded initial elimination half-lives of 0.87 and 1.1 minutes for the 30 and 100 nm SNPs, respectively. The terminal elimination half-lives were also quite different (68 minutes for 30 nm SNPs was, and 108 minutes for 100 nm SNPs). Together, the results indicated that the in vivo clearance of the 30 nm SNPs is faster than that of the 100 nm SNPs.

To explore the use of the SNPs for immune modulation, we investigated the lymph node trafficking of both 30 and 100 nm ^{64}Cu-labeled SNPs by using front footpad injection (Supporting Information, Figure S8d). The path of lymph drainage from footpad injections is well known, and hence this is a common method for the delivery of immunological agents.[30] We injected the 30 and the 100 nm SNPs into different sides of the footpads of a mouse, and microPET/CT imaging was carried out for 40 minutes immediately after injection (Figure 4b, left) and 20 hours after injection (Figure 4b, right). We observed that the 30 nm SNPs drained

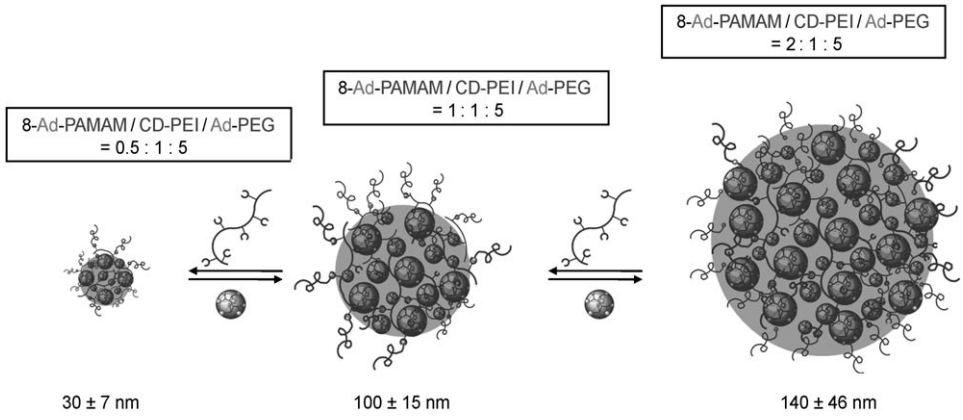

Figure 3. Reversible control of the size of SNPs.

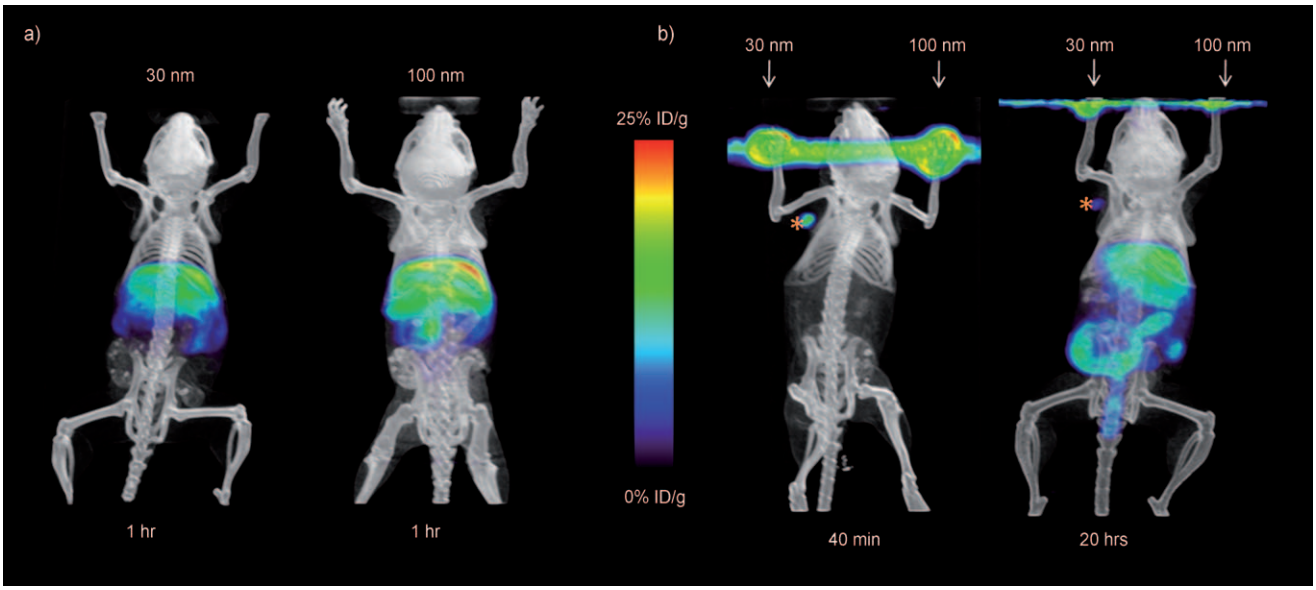

Figure 4. MicroPET/CT studies at various times after injecting the mice with 30 and 100 nm ^{64}Cu-labeled SNPs. a) In vivo biodistribution studies of the SNPs by systemically injecting the SNPs into mice through the tail veins. Left panel: 30 nm SNPs; right panel: 100 nm SNPs. b) Lymph node trafficking studies of SNPs using front footpad injections. The 30 and 100 nm SNPs were injected on different sides of footpads of a mouse. MicroPET/CT was carried out for 40 min immediately after injection (left) and 20 h after injection (right).

into the local auxiliary lymph node and peaked at 5 minutes post injection with (58.6 ± 15.6) % ID/g of signal accumulation (Supporting Information, Figure S8c). This signal decreased to (26.6 ± 5.8) % ID/g at 40 minutes post injection, and further reduced to (7.0 ± 2.2) % ID/g by 20 hours post injection. No significant accumulation was detected in the lymph nodes on the same side where the 100 nm SNPs were injected. Other than the footpad injection site and the lymph node into which the 30 nm SNPs drained, the SNPs did not distribute in vivo to other regions 1 hour after injection. The results revealed that the sizes of the SNPs are critical factors for their lymph node trafficking.

In conclusion, we have successfully developed a convenient, flexible, and modular synthetic approach for the preparation of size-controllable SNPs. PET imaging studies were carried out by injecting ^{64}Cu-labeled SNPs of different sizes into mice. Both whole-body biodistribution and lymph node drainage studies showed that the sizes of the SNPs affect their in vivo characteristics. Besides the imaging studies shown herein, we are currently exploring the use of the size-controllable SNPs for other biomedical applications. Extensive and in-depth study will show the potentials of these SNPs.

Received: January 6, 2009
Published online: May 7, 2009

Keywords: adamantanes · biodistribution · cyclodextrins · nanoparticles · positron emission tomography

[1] M. E. Davis, Z. G. Chen, D. M. Shin, *Nat. Rev. Drug Discovery* **2008**, *7*, 771.
[2] C. Loo, A. Lin, L. Hirsch, M. H. Lee, J. Barton, N. Halas, J. West, R. Drezek, *Technol. Cancer Res. Treat.* **2004**, *3*, 33.
[3] X. Gao, Y. Cui, R. M. Levenson, L. W. Chung, S. Nie, *Nat. Biotechnol.* **2004**, *22*, 969.
[4] S. M. Nie, Y. Xing, G. J. Kim, J. W. Simons, *Annu. Rev. Biomed. Eng.* **2007**, *9*, 257.
[5] Y. W. Jun, J. H. Lee, J. Cheon, *Angew. Chem.* **2008**, *120*, 5200; *Angew. Chem. Int. Ed.* **2008**, *47*, 5122.
[6] J. R. Heath, M. E. Davis, *Annu. Rev. Med.* **2008**, *59*, 251.
[7] V. P. Torchilin, *Nat. Rev. Drug Discovery* **2005**, *4*, 145.
[8] M. E. Napier, J. M. Desimone, *Polym. Rev.* **2007**, *47*, 321.
[9] S. E. Gratton, S. S. Williams, M. E. Napier, P. D. Pohlhaus, Z. Zhou, K. B. Wiles, B. W. Maynor, C. Shen, T. Olafsen, E. T. Samulski, J. M. Desimone, *Acc. Chem. Res.* **2008**, *41*, 1685.
[10] J. J. Green, R. Langer, D. G. Anderson, *Acc. Chem. Res.* **2008**, *41*, 749.
[11] D. W. Pack, A. S. Hoffman, S. Pun, P. S. Stayton, *Nat. Rev. Drug Discovery* **2005**, *4*, 581.
[12] W. B. Cai, X. Y. Chen, *Small* **2007**, *3*, 1840.
[13] C. D. Meyer, C. S. Joiner, J. F. Stoddart, *Chem. Soc. Rev.* **2007**, *36*, 1705.
[14] I. Hwang, W. S. Jeon, H. J. Kim, D. Kim, H. Kim, N. Selvapalam, N. Fujita, S. Shinkai, K. Kim, *Angew. Chem.* **2007**, *119*, 214; *Angew. Chem. Int. Ed.* **2007**, *46*, 210.
[15] M. J. W. Ludden, D. N. Reinhoudt, J. Huskens, *Chem. Soc. Rev.* **2006**, *35*, 1122.
[16] S. Y. Park, A. K. R. Lytton-Jean, B. Lee, S. Weigand, G. C. Schatz, C. A. Mirkin, *Nature* **2008**, *451*, 553.
[17] J. F. Stoddart, H. R. Tseng, *Proc. Natl. Acad. Sci. USA* **2002**, *99*, 4797.
[18] Y. Liu, H. Wang, P. Liang, H. Y. Zhang, *Angew. Chem.* **2004**, *116*, 2744; *Angew. Chem. Int. Ed.* **2004**, *43*, 2690.
[19] G. Sun, J. Xu, A. Hagooly, R. Rossin, Z. Li, D. A. Moore, C. J. Hawker, M. J. Welch, K. L. Wooley, *Adv. Mater.* **2007**, *19*, 3157.
[20] L. Ferreira, J. M. Karp, L. Nobre, R. Langer, *Cell Stem Cell* **2008**, *3*, 136.
[21] S. R. Bull, M. O. Guler, R. E. Bras, T. J. Meade, S. I. Stupp, *Nano Lett.* **2005**, *5*, 1.
[22] P. A. Bertin, J. M. Gibbs, C. K. F. Shen, C. S. Thaxton, W. A. Russin, C. A. Mirkin, S. T. Nguyen, *J. Am. Chem. Soc.* **2006**, *128*, 4168.

[23] A. K. Boal, F. Ilhan, J. E. DeRouchey, T. Thurn-Albrecht, T. P. Russell, V. M. Rotello, *Nature* **2000**, *404*, 746.
[24] G. Wenz, B. H. Han, A. Muller, *Chem. Rev.* **2006**, *106*, 782.
[25] J. Li, X. J. Loh, *Adv. Drug Delivery Rev.* **2008**, *60*, 1000.
[26] D. W. Bartlett, H. Su, I. J. Hildebrandt, W. A. Weber, M. E. Davis, *Proc. Natl. Acad. Sci. USA* **2007**, *104*, 15549.
[27] N. C. Bellocq, D. W. Kang, X. H. Wang, G. S. Jensen, S. H. Pun, T. Schluep, M. L. Zepeda, M. E. Davis, *Bioconjugate Chem.* **2004**, *15*, 1201.
[28] M. E. Davis, M. E. Brewster, *Nat. Rev. Drug Discovery* **2004**, *3*, 1023.
[29] According to mass spectrometry analysis, 4*-Ad-PAMAM is composed of six different Ad-substituted PAMAMs, including 2-Ad-PAMAM, 3-Ad-PAMAM, 4-Ad-PAMAM, 5-Ad-PAMAM, 6-Ad-PAMAM and 7-Ad-PAMAM. See detailled MS data in the Supporting Information.
[30] L. J. Peek, C. R. Middaugh, C. Berkland, *Adv. Drug Delivery Rev.* **2008**, *60*, 915.

DOI: 10.1002/anie.201000062

Nanotechnology

Photothermal Effects of Supramolecularly Assembled Gold Nanoparticles for the Targeted Treatment of Cancer Cells**

Shutao Wang, Kuan-Ju Chen, Ting-Hsiang Wu, Hao Wang, Wei-Yu Lin, Minori Ohashi, Pei-Yu Chiou,* and Hsian-Rong Tseng**

Noble-metal nanostructures with unique photophysical properties have been considered as prime candidate agents for the photothermal treatment of cancer.[1–4] Typically, the photothermal properties of these nanostructures can be controlled by manipulating their sizes and shapes.[4,5] Over the past decade, significant endeavors have been devoted to the production of a variety of gold nanostructures, such as nanoparticles,[6,7] nanoshells,[8–10] nanorods,[11,12] and nanocages,[5,13,14] which are able to overcome limitations of organic-dye-based photothermal agents,[7] such as low light absorption and undesired photobleaching. For sufficient energy to be harvested/generated to damage tumor cells, the size of these nanostructure-based agents are required in the range of tens to hundreds nm.[15] However, the relatively "large" size of the agents often leads to poor bioclearance (i.e., accumulation in the liver, spleen, and kidneys), which is a major obstacle to their in vivo application.[16–18] Alternatively, the photophysical properties of noble-metal nanostructures can be altered systematically by the formation of aggregates through self-assembly.[19–30] The antibody-assisted aggregation of Au nanoparticles on cell membranes or in intracellular environments led to the enhancement of photothermal performance[31] as a result of the collective effects[32,33] associated with the assembled structures. Therefore, the self-assembly of small noble-metal building blocks, that is, noble-metal colloids with diameters of less than 8 nm[16–18] (compatible with renal clearance) would be a promising approach toward a new class of noble-metal photothermal agents.

Recently, we demonstrated a convenient, flexible, and modular self-assembly approach for the preparation of supramolecular nanoparticles (SNPs) of controlled size through multivalent molecular recognition based on β-cyclodextrin (CD) and adamantane (Ad) motifs.[34] Size-controlled SNPs were prepared by mixing three molecular building blocks: 1) an Ad-grafted polyamidoamine dendrimer with a diameter of approximately 1.9 nm, 2) CD-grafted branched polyethylenimine (CD-PEI), and 3) Ad-grafted polyethylene glycol (Ad-PEG). We hypothesized that such a supramolecular synthetic approach could be further explored to assemble inorganic building blocks (i.e., 2 nm Au colloids) into a collection of Au supramolecular nanoparticles (Au-SNPs) with defined sizes. We anticipated that the resulting Au-SNPs might exhibit enhanced photothermal effects[19] and could thus be promising candidate agents for photothermal cancer treatment. The use of a supramolecular approach enables[34,35] the convenient incorporation of targeting ligands to provide target-specific Au-SNPs.

In this study, we adopted a supramolecular approach to prepare size-controlled Au-SNPs for use as a new type of photothermal agent from three building blocks: Ad-grafted 2 nm Au colloids, CD-PEI, and Ad-PEG (Figure 1). We used transmission electron microscopy (TEM) and zeta-potential measurements to characterize the size/morphology and surface charge densities, respectively, of the resulting Au-SNPs. We carried out further studies to unveil the unique physical properties of the Au-SNPs, including 1) their stability at different temperatures and pH values, 2) their size-dependent photophysical properties, and 3) their thermally induced disassembly. Moreover, laser-induced microbubble-generation experiments were performed with the 118 nm Au-SNPs to demonstrate their significantly enhanced photothermal effects relative to those of the 2 nm Au colloids. We used arginine–glycine–aspartic acid (RGD) peptide as a targeting ligand and $\alpha_v\beta_3$-positive/negative cells as the corresponding biological system to test the specificity and selectivity of RGD-Au-SNPs, which were generated from Au-SNPs by dynamic in situ ligand exchange,[35] and observed selective damage of the $\alpha_v\beta_3$-positive cells (no damage of neighboring $\alpha_v\beta_3$-negative cells).

The three molecular building blocks, Ad-grafted 2 nm Au colloids (Figure 2a), CD-PEI, and Ad-PEG, were prepared and characterized as shown in the Supporting Information.

[*] Dr. S. T. Wang, K.-J. Chen, Dr. H. Wang, Dr. W.-Y. Lin, M. Ohashi, Prof. H.-R. Tseng
Department of Molecular and Medical Pharmacology
Crump Institute for Molecular Imaging (CIMI)
California NanoSystems Institute (CNSI)
Institute for Molecular Medicine (IMED)
University of California, Los Angeles
570 Westwood Plaza, Building 114, Los Angeles, CA 90095-1770 (USA)
Fax: (+1) 310-206-8975
E-mail: shutaowang@mednet.ucla.edu
hrtseng@mednet.ucla.edu
Homepage: http://labs.pharmacology.ucla.edu/tsenglab/
Prof. P.-Y. Chiou
Department of Mechanical and Aerospace Engineering
University of California, Los Angeles
420 Westwood Plaza, EIV 37-138, Los Angeles, CA 90095 (USA)
E-mail: pychiou@seas.ucla.edu
T.-H. Wu
Department of Electrical Engineering
University of California, Los Angeles
420 Westwood Plaza, EIV 37-138, Los Angeles, CA 90095 (USA)

[**] This research was supported by NIH-NCI NanoSystems Biology Cancer Center (U54CA119347).

Supporting information for this article is available on the WWW under http://dx.doi.org/10.1002/anie.201000062.

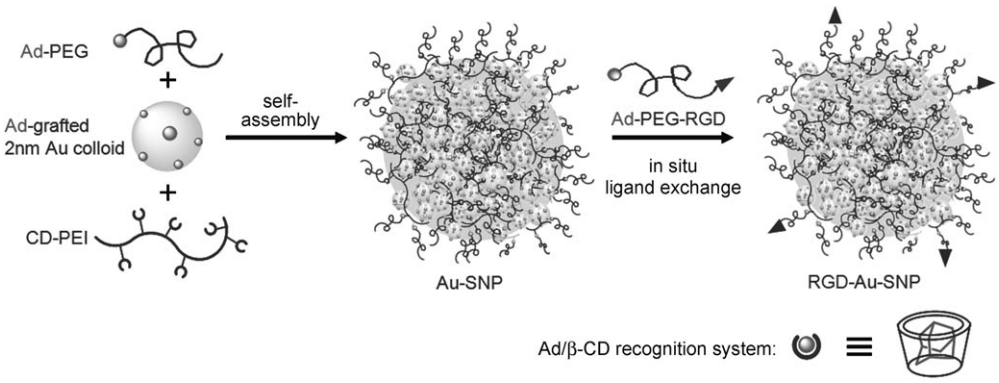

Figure 1. Supramolecular synthetic approach for the preparation of size-controlled gold supramolecular nanoparticles (Au-SNPs). A molecular-recognition system based on adamantane (Ad) and β-cyclodextrin (CD) was employed to assemble three building blocks: Ad-grafted 2 nm Au colloids, CD-PEI, and Ad-PEG. Ad-PEG-RGD was introduced onto Au-SNPs by in situ ligand exchange to give RGD-Au-SNPs that could recognize a certain type of tumor cell with membrane $\alpha_v\beta_3$ integrin receptors.

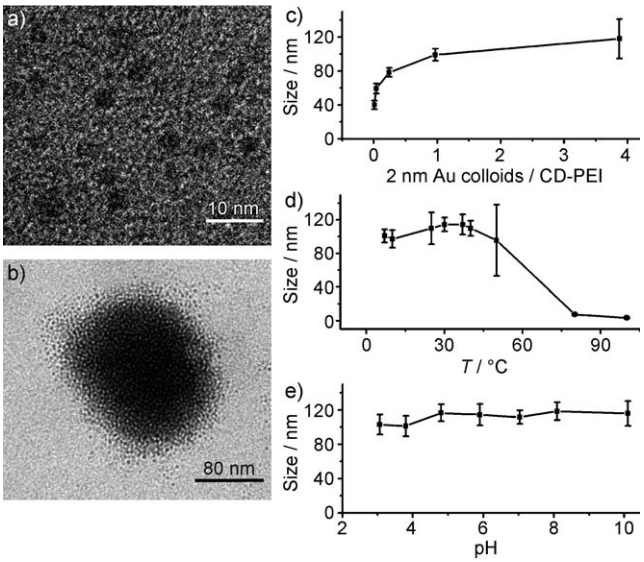

Figure 2. Analysis by transmission electron microscopy (TEM). a) Ad-grafted 2 nm Au colloids: the inorganic building blocks of Au-SNPs. b) A single 118 nm Au-SNP obtained by the supramolecular synthetic approach. c) Titration plot showing the relationship between the size of Au-SNPs and the mixing ratio of the Au colloids and CD-PEI. d,e) Effect of temperature (d) and the pH value (e) on the stability of 118 nm Au-SNPs.

We then prepared size-controlled Au-SNPs (Figure 2b) by slowly adding phosphate-buffered saline (PBS, pH 7.2) with Ad-grafted 2 nm Au colloids (0.0213 mg mL^{-1}) to PBS solutions with variable amounts of CD-PEI (0.0725–5.73 mg mL^{-1}) and Ad-PEG (4.2 mg mL^{-1}), followed by incubation at room temperature overnight. By simply tuning the ratio between the Ad-grafted 2 nm Au colloids and CD-PEI, we were able to obtain a collection of Au-SNPs with variable sizes ranging between 40 and 118 nm (Figure 2c). The formation mechanism originally proposed for SNPs[34] can be used to explain the size controllability observed for Au-SNPs. In short, the mixing ratios of the three building blocks altered the equilibrium between the propagation/aggregation of the Au colloid/CD-PEI hydrogel network and the Ad-PEG-induced capping/solvation of the hydrogel network, and changes in this equilibrium led to changes in the size of the Au-SNPs.

TEM images indicated that the Au-SNPs had spherical shapes with a narrow size distribution (Figure 2b; see also the Supporting Information). Figure 2b shows a highly magnified typical TEM image of a single Au-SNP; individual 2 nm Au colloids are clearly visible. Zeta-potential measurements (Zetasizer Nano, Malvern Instruments) revealed that the Au-SNPs carried surface charge densities covering the range of 11–20 mV (see Figure S1 in the Supporting Information) as a result of the incorporation of positively charged CD-PEI. Since the Au-SNPs were prepared by supramolecular assembly, we characterized their dynamic stability under different environmental conditions. We monitored the size variation of 118 nm Au-SNPs in PBS by TEM[36] at temperatures ranging from 7 to 100 °C (Figure 2d) and at pH values from 3 to 10 (Figure 2e). The results indicated that 118 nm Au-SNPs are stable in PBS at 7–40 °C and pH 5–10. Also, Au-SNPs can maintain their size and morphology in PBS either with or without 10% serum, most likely because the "stealth" effect imparted by PEG grafted on the outside of the Au-SNPs could lower the further agglomeration of particles.[37] These results suggest that Au-SNPs can be used under physiological conditions. At higher temperatures (> 50 °C, Figure 2d), they dissociated into small fragments, and a broader size distribution of the Au-SNPs was observed by TEM. Complete disassembly of the 118 nm Au-SNPs into 2 nm Au colloids was observed when the temperature was increased to 100 °C. The thermal disassembly of 118 nm Au-SNPs can be attributed to the weakened Ad/CD supramolecular interactions at elevated temperatures.[38]

To test the feasibility of the application of Au-SNPs as photothermal agents, we chose 118 nm Au-SNPs as the model system.[39] For comparison, 2 nm Au colloids were employed as a control. First, we investigated the photophysical properties of 118 nm Au-SNPs and 2 nm Au colloids by UV/Vis spectroscopy (Figure 3a). Given the characteristic surface-plasmon-resonance absorption of Au-SNPs and Au colloids (between 500 and 530 nm),[19] we chose a 532 nm green pulsed laser to test their photothermal effects and performed laser-induced microbubble-generation studies to monitor the locally accumulated heat of individual Au-SNPs. We tested a broad range of energy densities (3–265 mJ cm^{-2}) of a 532 nm pulsed laser with a 6 ns pulse duration. Au-SNPs and Au-colloid suspensions in PBS (with a normalized Au concentration of 4.67 mg mL^{-1}) were irradiated with the laser at

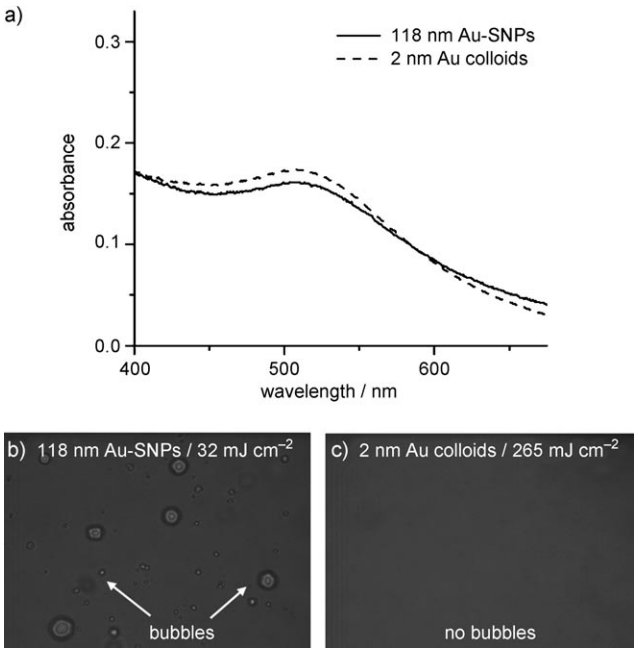

Figure 3. a) UV/Vis absorption spectra of 2 nm Au colloids and 118 nm Au-SNPs. b,c) Time-resolved bright-field micrographs of suspensions of 118 nm Au-SNPs (b) and Ad-grafted 2 nm Au colloids (c) during the scanning of a pulsed laser (6 ns, 532 nm; 32 mJ cm^{-2} for 118 nm Au-SNPs and 265 mJ cm^{-2} for Ad-grafted 2 nm Au colloids).

different energies. For the 118 nm Au-SNPs, a laser threshold of 32 mJ cm^{-2} was sufficient for the generation of microbubbles upon laser irradiation (Figure 3b). In contrast, no microbubbles were observed for 2 nm Au colloids even at the maximum laser energy tested (265 mJ cm^{-2}; Figure 3c). The significant enhancement of the photothermal effects in 118 nm Au-SNPs can be attributed to the collective heating effect[33] in Au-SNPs. Interestingly, we also found that the efficiency of the collective heating effect was size-dependent: 40 nm Au-SNPs exhibited a threshold of 61 mJ cm^{-2}.

The formation of explosive vapor bubbles on individual Au-SNPs requires an elevated local temperature higher than the critical temperature of the liquid medium (374 °C for water).[40] We hypothesize that upon the formation of microbubbles, the localized accumulated heat could facilitate the thermal disassembly of Au-SNPs into smaller fragments, in a process similar to that observed for 118 nm Au-SNPs when the temperature was above 100 °C (Figure 2d). To monitor laser-induced Au-SNP disassembly, we used a pulsed laser (with a 6 ns pulse duration) to irradiate Au-SNPs at a repetition rate of 1 Hz. Microbubble formation was captured by the time-resolved imaging setup 70 ns after the arrival of the laser pulse. We observed a dramatic decrease in the number of laser-induced microbubbles after irradiation with several laser pulses. Thus, most of the Au-SNPs in the solution appeared to have thermally disassembled into smaller fragments, which attenuates their photothermal characteristics.[7,19] In the following studies on photothermal treatment, a fixed laser power of 120 mJ cm^{-2} was used to ensure microbubble formation on the 118 nm Au-SNPs.

Through the incorporation of targeting ligands, photothermal agents based on Au nanostructures can be utilized for the targeted photothermal treatment of certain types of cancer cells.[6,12,41,42] In our study, RGD-Au-SNPs that could recognize tumor cells with membrane $\alpha_v\beta_3$ integrin receptors were produced by dynamic ligand exchange (Ad-PEG-RGD (0.21 mg) was added to a solution (1.0 mL) of 118 nm Au-SNPs (4.67 mg mL^{-1}); see the Supporting Information).[43] The 118 nm RGD-Au-SNPs were used along with the controls (RGD-grafted 2 nm Au colloids and nontargeting 118 nm Au-SNPs) for targeted photothermal treatment in four-well chamber slides containing both $\alpha_v\beta_3$-positive U87 glioblastoma cells and $\alpha_v\beta_3$-negative MCF7 breast cancer cells. To make it easier to visually distinguish the two different types of cells, we labeled the U87 and MCF7 cells with green and red fluorescent dyes (DiO and DiD cell-labeling solution, Invitrogen), respectively. After incubation for 20 min with the three agents and subsequent replacement of the culture media (to remove the free agents), the cells in the culture chambers were exposed to pulsed laser irradiation (6 ns, 120 mJ cm^{-2}) with a beam diameter of 1 mm (a photomask was used; see the Supporting Information). The irradiated cells were kept in an incubator (5% CO_2, 37 °C) for 2 h, during which time the cells damaged by microbubble formation could detach from the substrates. An inverted fluorescence microscope (Nikon TE2000) was employed to examine the cells within the irradiated regions. Cell detachment was observed for the U87 cells treated with RGD-Au-SNPs (Figure 4a). In contrast, negligible cell detachment was observed for MCF7 cells treated with RGD-Au-SNPs (Figure 4b) as well as for both types of cells treated with nontargeted Au-SNPs. These results suggest that 1) RGD peptide confers target specificity to the Au-SNPs to enable the photothermal treatment of $\alpha_v\beta_3$-positive U87 cells, and 2) nontargeting Au-SNPs have no significant effect on cancer cells, as their surface-grafted PEG chains[44] are capable of reducing nonspecific binding to cells. Furthermore, no cell detachment was detected for the U87 cells treated with Au colloids (Figure 4c); this result validated our previous observation that 2 nm Au colloids exhibit minute photothermal effects at the given pulsed laser irradiation.

To demonstrate the selectivity of RGD-Au-SNPs for target-specific photothermal treatment, we investigated the targeted depletion of $\alpha_v\beta_3$-positive cells in a cell mixture containing both $\alpha_v\beta_3$-positive U87 and $\alpha_v\beta_3$-negative MCF7 cells. We treated a 1:1 cell mixture (Figure 4d, middle) containing U87 cells (green) and MCF7 cells (red) with RGD-Au-SNPs (4.67 mg mL^{-1}). After the removal of free RGD-Au-SNPs, the cell mixture was irradiated with a pulsed laser. In the irradiated region, U87 cells (green) were depleted, and the remaining MCF7 cells (red) were able to be continuously cultured on the substrates (Figure 4d, right). In the region outside the laser footprint, both the positive and the negative cells remained. These results suggest that the photothermal treatment of RGD-Au-SNPs is highly selective for targeted cells. Besides the specific targeting effects of RGD-Au-SNPs, the use of a pulsed laser led to effective photothermal effects in a defined location within a nanosecond time frame and thus enabled localized cell damage in a spatially confined fashion.

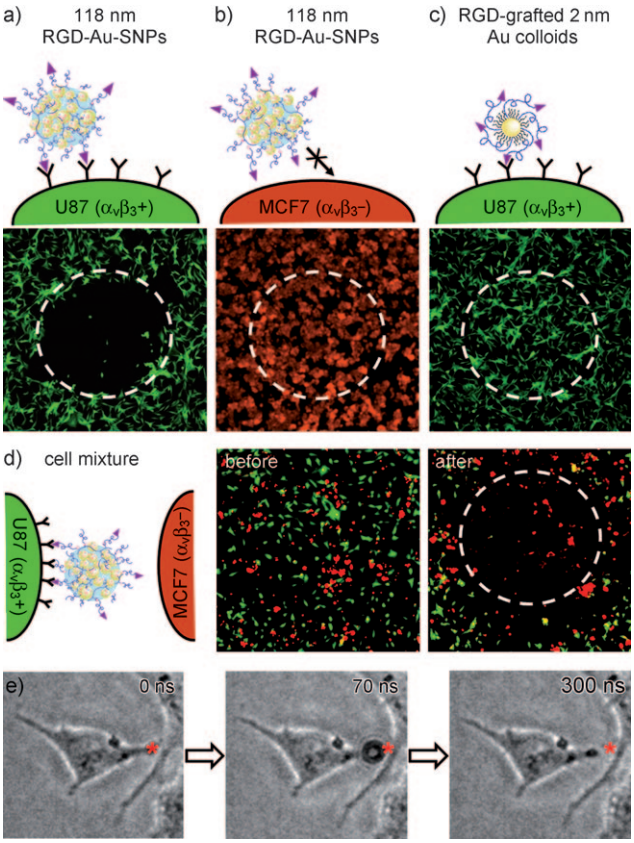

Figure 4. a–c) Fluorescence micrographs of U87 cells ($\alpha_v\beta_3$+, labeled green) treated with 118 nm RGD-Au-SNPs (a), MCF7 cells ($\alpha_v\beta_3$-, labeled red) treated with 118 nm RGD-Au-SNPs (b), and U87 cells treated with RGD-grafted 2 nm Au colloids (c) after irradiation with a pulsed laser (6 ns, 120 mJ cm^{-2}). A mask was employed to confine the laser beam to a circular region with a diameter of 1 mm (as indicated by the white dashed circles). d) Fluorescence micrographs of a 1:1 mixture of U87 and MCF7 cells. After treatment with RGD-Au-SNPs and subsequent medium exchange, the cell mixture was irradiated with a pulsed laser. In the irradiated region after culture for 2 h, U87 cells (green) were depleted, whereas MCF7 cells (red) were left alive on the substrate. e) Time-resolved images of an $\alpha_v\beta_3$-positive U87 cell with a 118 nm RGD-Au-SNP attached to it. Upon irradiation with the 6 ns pulsed laser (120 mJ cm^{-2}), fast contraction of the cellular protrusion was observed as the result of the localized mechanical destruction caused by the formation of microbubbles.

In contrast, the previous use of continuous-wave radiation often led to a large area of cell damage as a result of heat diffusion from the targeted cells to the surrounding medium over the relatively long period of light irradiation.[45]

The cell-damage mechanism is based on the mechanical destruction associated with the formation of explosive microbubbles. It is similar to those proposed for photothermal agents based on Au nanoparticles[6,46,47] or carbon nanotubes,[48] but is dramatically different from the heating-damage mechanism observed for other photothermal agents.[7,8,41,49] To visualize the microbubble-induced mechanical destruction[46] of the targeted cell, we used time-resolved imaging to monitor how an RGD-Au-SNP-grafted cell responded to microbubble formation right after laser irradiation. To ensure that a small number of RGD-Au-SNPs were grafted on the cells, we treated the $\alpha_v\beta_3$-positive U87 cells with 118 nm RGD-Au-SNPs at low concentration (0.93 mg mL^{-1}). Figure 4e shows the time-dependant response of a U87 cell treated with RGD-Au-SNPs to irradiation with the 6 ns pulsed laser (120 mJ cm^{-2}). After irradiation, a fast contraction of the cellular protrusion was observed as a result of the localized mechanical destruction caused by a microbubble.

In conclusion, we have successfully demonstrated the synthesis of size-controlled Au-SNPs from 2 nm Au colloids by a supramolecular self-assembly approach. The resulting Au-SNPs exhibited significantly enhanced photothermal effects and were used to demonstrate the targeted photothermal treatment of a subpopulation of cancer cells after the incorporation of target-specific ligands. We envision that 1) such a supramolecular assembly approach could be used to assemble other "small" inorganic nanoparticles (e.g., superparamagnetic oxide nanoparticles[50]) for broader application in materials science and biomedicine; 2) diverse functional building blocks and therapeutic loads (e.g., DNA, proteins, drugs) could be packaged into Au-SNPs, the laser-induced disassembly of which could be used as a controlled release mechanism; and 3) a two-photon laser[51] could be employed to overcome the tissue-penetration limitation.

Received: January 6, 2010
Published online: April 9, 2010

Keywords: gold · nanoparticles · photothermal effects · self-assembly · tumor therapy

[1] R. R. Anderson, J. A. Parrish, *Science* **1983**, *220*, 524.
[2] P. K. Jain, X. H. Huang, I. H. El-Sayed, M. A. El-Sayed, *Acc. Chem. Res.* **2008**, *41*, 1578.
[3] K. An, T. Hyeon, *Nano Today* **2009**, *4*, 359.
[4] S. Lal, S. E. Clare, N. J. Halas, *Acc. Chem. Res.* **2008**, *41*, 1842.
[5] S. E. Skrabalak, J. Chen, Y. Sun, X. Lu, L. Au, C. M. Cobley, Y. Xia, *Acc. Chem. Res.* **2008**, *41*, 1587.
[6] D. O. Lapotko, E. Lukianova, A. A. Oraevsky, *Laser Surg. Med.* **2006**, *38*, 631.
[7] X. H. Huang, P. K. Jain, I. H. El-Sayed, M. A. El-Sayed, *Lasers Med. Sci.* **2008**, *23*, 217.
[8] A. M. Gobin, M. H. Lee, N. J. Halas, W. D. James, R. A. Drezek, J. L. West, *Nano Lett.* **2007**, *7*, 1929.
[9] K. W. Hu, T. M. Liu, K. Y. Chung, K. S. Huang, C. T. Hsieh, C. K. Sun, C. S. Yeh, *J. Am. Chem. Soc.* **2009**, *131*, 14186.
[10] J. Kim, S. Park, J. E. Lee, S. M. Jin, J. H. Lee, I. S. Lee, I. Yang, J. S. Kim, S. K. Kim, M. H. Cho, T. Hyeon, *Angew. Chem.* **2006**, *118*, 7918; *Angew. Chem. Int. Ed.* **2006**, *45*, 7754.
[11] E. B. Dickerson, E. C. Dreaden, X. H. Huang, I. H. El-Sayed, H. H. Chu, S. Pushpanketh, J. F. McDonald, M. A. El-Sayed, *Cancer Lett.* **2008**, *269*, 57.
[12] Y. F. Huang, K. Sefah, S. Bamrungsap, H. T. Chang, W. Tan, *Langmuir* **2008**, *24*, 11860.
[13] J. Chen, D. Wang, J. Xi, L. Au, A. Siekkinen, A. Warsen, Z. Y. Li, H. Zhang, Y. Xia, X. Li, *Nano Lett.* **2007**, *7*, 1318.
[14] L. Au, D. Zheng, F. Zhou, Z. Y. Li, X. Li, Y. Xia, *ACS Nano* **2008**, *2*, 1645.
[15] A. R. Lowery, A. M. Gobin, E. S. Day, K. Y. Shah, N. J. Halas, J. L. West, *Clin. Cancer Res.* **2005**, *11*, 9097s.
[16] S. Mitragotri, J. Lahann, *Nat. Mater.* **2009**, *8*, 15.

[17] H. S. Choi, W. Liu, P. Misra, E. Tanaka, J. P. Zimmer, B. Itty Ipe, M. G. Bawendi, J. V. Frangioni, *Nat. Biotechnol.* **2007**, *25*, 1165.
[18] A. E. Nel, L. Madler, D. Velegol, T. Xia, E. M. V. Hoek, P. Somasundaran, F. Klaessig, V. Castranova, M. Thompson, *Nat. Mater.* **2009**, *8*, 543.
[19] B. Khlebtsov, V. Zharov, A. Melnikov, V. Tuchin, N. Khlebtsov, *Nanotechnology* **2006**, *17*, 5167.
[20] Z. D. Lu, J. Goebl, J. P. Ge, Y. D. Yin, *J. Mater. Chem.* **2009**, *19*, 4597.
[21] J. Zhuang, H. Wu, Y. Yang, Y. C. Cao, *Angew. Chem.* **2008**, *120*, 2240; *Angew. Chem. Int. Ed.* **2008**, *47*, 2208.
[22] T. S. Troutman, J. K. Barton, M. Romanowski, *Adv. Mater.* **2008**, *20*, 2604.
[23] Y. Ofir, B. Samanta, V. M. Rotello, *Chem. Soc. Rev.* **2008**, *37*, 1814.
[24] R. Elghanian, J. J. Storhoff, R. C. Mucic, R. L. Letsinger, C. A. Mirkin, *Science* **1997**, *277*, 1078.
[25] S. Lin, M. Li, E. Dujardin, C. Girard, S. Mann, *Adv. Mater.* **2005**, *17*, 2553.
[26] E. Katz, I. Willner, *Angew. Chem.* **2004**, *116*, 6166; *Angew. Chem. Int. Ed.* **2004**, *43*, 6042.
[27] W. L. Cheng, N. Y. Park, M. T. Walter, M. R. Hartman, D. Luo, *Nat. Nanotechnol.* **2008**, *3*, 682.
[28] M. M. Maye, I. I. S. Lim, J. Luo, Z. Rab, D. Rabinovich, T. B. Liu, C. J. Zhong, *J. Am. Chem. Soc.* **2005**, *127*, 1519.
[29] C. M. Niemeyer, *Angew. Chem.* **2001**, *113*, 4254; *Angew. Chem. Int. Ed.* **2001**, *40*, 4128.
[30] R. Klajn, M. A. Olson, P. J. Wesson, L. Fang, A. Coskun, A. Trabolsi, S. Soh, J. F. Stoddart, B. A. Grzybowski, *Nat. Chem.* **2009**, *1*, 733.
[31] D. Lapotko, E. Lukianova, M. Potapnev, O. Aleinikova, A. Oraevsky, *Cancer Lett.* **2006**, *239*, 36.
[32] A. O. Govorov, H. H. Richardson, *Nano Today* **2007**, *2*, 30.
[33] H. H. Richardson, M. T. Carlson, P. J. Tandler, P. Hernandez, A. O. Govorov, *Nano Lett.* **2009**, *9*, 1139.
[34] H. Wang, S. Wang, H. Su, K. J. Chen, A. L. Armijo, W. Y. Lin, Y. Wang, J. Sun, K. Kamei, J. Czernin, C. G. Radu, H. R. Tseng, *Angew. Chem.* **2009**, *121*, 4408; *Angew. Chem. Int. Ed.* **2009**, *48*, 4344.
[35] H. Wang, K.-J. Chen, S. T. Wang, M. Ohashi, K.-I. Kamei, J. Sun, J. H. Ha, K. Liu, H.-R. Tseng, *Chem. Commun.* **2010**, *46*, 1851.
[36] It is well-known that the overall aggregate size as measured by dynamic light scattering (DLS) is much larger than the average size determined by TEM, especially for inorganic nanoparticles (see: R. Shenhar, T. B. Norsten, V. M. Rotello, *Adv. Mater.* **2005**, *17*, 657). We obtained the size distribution of Au-SNPs from TEM measurements.
[37] J. M. Harris, R. B. Chess, *Nat. Rev. Drug Discovery* **2003**, *2*, 214.
[38] M. V. Rekharsky, Y. Inoue, *Chem. Rev.* **1998**, *98*, 1875.
[39] It is widely recognized that the diameter of nanoparticle therapeutics for cancer should be roughly in the range of 10–120 nm (see: M. E. Davis, Z. Chen, D. M. Shin, *Nat. Rev. Drug Discovery* **2008**, *7*, 771 – 782).
[40] V. Kotaidis, A. Plech, *Appl. Phys. Lett.* **2005**, *87*.
[41] C. M. Pitsillides, E. K. Joe, X. Wei, R. R. Anderson, C. P. Lin, *Biophys. J.* **2003**, *84*, 4023.
[42] C. G. Wang, J. Chen, T. Talavage, J. Irudayaraj, *Angew. Chem.* **2009**, *121*, 2797; *Angew. Chem. Int. Ed.* **2009**, *48*, 2759.
[43] Z. Liu, W. B. Cai, L. N. He, N. Nakayama, K. Chen, X. M. Sun, X. Y. Chen, H. J. Dai, *Nat. Nanotechnol.* **2007**, *2*, 47.
[44] *Poly(ethylene glycol) Chemistry: Biotechnical and Biomedical Applications* (Ed.: J. M. Harris), Plenum, New York, **1992**.
[45] D. P. O'Neal, L. R. Hirsch, N. J. Halas, J. D. Payne, J. L. West, *Cancer Lett.* **2004**, *209*, 171.
[46] E. Y. Hleb, J. H. Hafner, J. N. Myers, E. Y. Hanna, B. C. Rostro, S. A. Zhdanok, D. O. Lapotko, *Nanomedicine* **2008**, *3*, 647.
[47] T.-H. Wu, S. Kalim, C. Callahan, M. A. Teitell, P.-Y. Chiou, *Opt. Express* **2010**, *18*, 938.
[48] B. Kang, D. Yu, Y. Dai, S. Chang, D. Chen, Y. Ding, *Small* **2009**, *5*, 1292.
[49] X. Huang, I. H. El-Sayed, W. Qian, M. A. El-Sayed, *J. Am. Chem. Soc.* **2006**, *128*, 2115.
[50] J. H. Lee, Y. W. Jun, S. I. Yeon, J. S. Shin, J. Cheon, *Angew. Chem.* **2006**, *118*, 8340; *Angew. Chem. Int. Ed.* **2006**, *45*, 8160.
[51] J. R. Starkey, A. K. Rebane, M. A. Drobizhev, F. Q. Meng, A. J. Gong, A. Elliott, K. McInnerney, C. W. Spangler, *Clin. Cancer Res.* **2008**, *14*, 6564.

A small library of DNA-encapsulated supramolecular nanoparticles for targeted gene delivery†

Hao Wang,* Kuan-Ju Chen, Shutao Wang, Minori Ohashi, Ken-ichiro Kamei, Jing Sun, Ji Hoon Ha, Kan Liu and Hsian-Rong Tseng*

Received (in Austin, TX, USA) 11th November 2009, Accepted 20th January 2010
First published as an Advance Article on the web 11th February 2010
DOI: 10.1039/b923711a

We demonstrated a convenient, flexible and modular synthetic approach for preparation of a small library of DNA-encapsulated supramolecular nanoparticles SNPs⊃DNA and RGD-SNPs⊃DNA with different sizes and RGD target ligand coverage for targeted gene delivery.

Gene therapy generally requires delivery vehicles that are capable of (i) carrying/protecting genetic materials, *e.g.*, DNA and siRNA, and (ii) target-specific delivery to desired tissues or subsets of cells.[1] Over the past decades, significant endeavors have been devoted to develop non-viral gene delivery vehicles[2,3] as alternatives to their viral counterparts, whose applications are restricted due to the potential safety issues and complex processes of preparing. Among the existing non-viral gene delivery systems,[4–8] nanoparticle-based gene delivery vehicles[9–12] have received extensive attention.

Recently, we developed a novel assembly approach[13] for the preparation of size-controllable supramolecular nanoparticles (**SNPs**) *via* multivalent molecular recognition based on β-cyclodextrin (CD) and adamantane (Ad) motifs. A collection of **SNPs** with sizes ranging from 30 to 450 nm were prepared by mixing three molecular building blocks, including (i) cationic Ad-grafted polyamidoamine dendrimer (**Ad-PAMAM**), (ii) cationic CD-grafted branched polyethylenimine (**CD-PEI**) and (iii) Ad-grafted polyethylene glycol (**Ad-PEG**), all at different concentrations. Given the fact that the interior of **SNPs** is composed of a cationic **Ad-PAMAM/CD-PEI** hydrogel network, it is conceivable that **SNPs** can encapsulate anionic plasmid DNA *via* electrostatic interactions. This new type of gene delivery system can provide significant protection of the encapsulated DNA from degradation in an extracellular context.

Here, we adopted this supramolecular assembly approach to prepare a small library of DNA-encapsulated **SNPs** (**SNPs⊃DNA** and **RGD-SNPs⊃DNA**, Scheme 1) with controllable sizes and tunable surface coverage of a targeting ligand, *i.e.*, arginine-glycine-aspartic (RGD) peptide. A two-step preparation process has been developed to first generate both 100 and 300 nm **SNPs⊃DNA** from **Ad-PAMAM**, **CD-PEI**, **Ad-PEG** and DNA, followed by *in situ* RGD ligand exchange of **SNPs⊃DNA** to give six different **RGD-SNPs⊃DNA** with ligand coverage of 1, 5 and 10 mol% (based on **Ad-PEG**). In this proof-of-concept study, a plasmid DNA encoded with an enhanced green fluorescent protein (EGFP) driven by a CMV promoter was used as a reporter system, and the RGD ligand[14] was employed to recognize the $\alpha_v\beta_3$ integrin receptor on the membranes of certain types of tumor cells. To characterize the sizes, morphologies and surface charges of the resulting **SNPs⊃DNA** and **RGD-SNPs⊃DNA**, we carried out dynamic light scattering (DLS), transmission electron microscope (TEM) and zeta potential measurements, respectively. Finally, the gene transfection efficiency and specificity of each **SNPs⊃DNA** and **RGD-SNPs⊃DNA** in the small library were examined using $\alpha_v\beta_3$ high-expressed and low-expressed cells, along with the control delivery systems.

We first determined the DNA loading capacity to be used for preparation of **SNPs⊃DNA** and **RGD-SNPs⊃DNA**. Similar to cationic polymer based gene delivery systems,[15,16] the DNA loading capacity of **SNPs** depends on the net cationic charges embedded in the interior **Ad-PAMAM/CD-PEI** hydrogel network. We utilized both electrophoresis analysis[17] and ethidium bromide exclusion assay[18] to measure the DNA

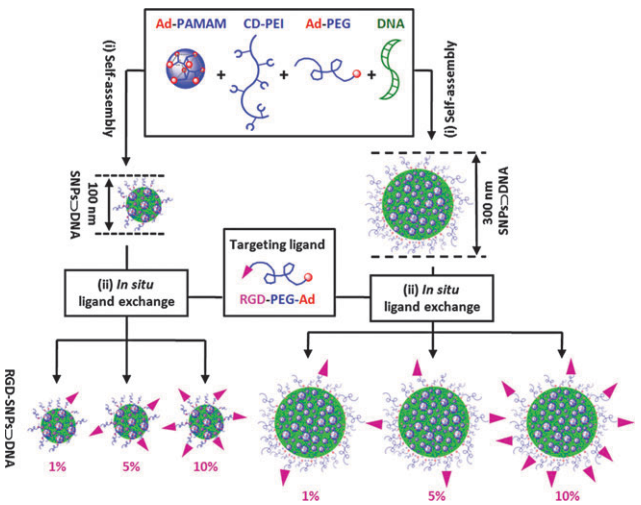

Scheme 1 A two-step modular assembly approach for preparation of a small library of DNA-encapsulated supramolecular nanoparticles (**SNPs⊃DNA** and **RGD-SNPs⊃DNA**) with controllable sizes and tunable RGD ligand coverage.

Department of Molecular and Medical Pharmacology, Crump Institute for Molecular Imaging (CIMI), Institute for Molecular Medicine (IMED), California NanoSystems Institute (CNSI), University of California, Los Angeles, 570 Westwood Plazas, CNSI Building, Los Angeles, CA 90095-1770, USA. E-mail: haowang@mednet.ucla.edu, hrtseng@medent.ucla.edu; Fax: 310-206-8975; Tel: 310-794-1977

† Electronic supplementary information (ESI) available: Preparation and characterization of **SNPs⊃DNA** and **RGD-SNPs⊃DNA**, electrophoresis analysis, ethidium bromide exclusion assay, dynamic light scattering experiments, and gene transfection protocol. See DOI: 10.1039/b923711a

loading capacity of the **Ad-PAMAM/CD-PEI** hydrogel (Fig. S1 and S2, ESI†), resulting in the respective nitrogen/phosphate (N/P) ratios of 2.6 and 5.0. The N/P ratio of 5.0 was chosen to ensure complete DNA encapsulation in our studies. Next, **SNPs⊃DNA** with 100 and 300 nm diameters were prepared separately by slowly adding a PBS solution (pH = 7.2) of **CD-PEI** (600 nM) into PBS solution containing **Ad-PAMAM** (300 nM for 100 nm **SNPs⊃DNA** and 600 nM for 300 nm **SNPs⊃DNA**), **Ad-PEG** (3 μM) and DNA (2.2 nM), followed by incubation at room temperature for 20 min. The DLS measurements indicated that the hydrodynamic sizes of the 100 and 300 nm **SNPs⊃DNA** were 106 ± 14 and 312 ± 47 nm, respectively. Subsequently, the samples of each size of **SNPs⊃DNA** were split into four aliquots, and three of them were subjected to the *in situ* ligand exchange by adding 30, 150 or 300 nM of **RGD-PEG-Ad** (Scheme S1, ESI†). A collection of **RGD-SNPs⊃DNA** with different RGD coverage,[19] namely **100-1%**, **100-5%**, **100-10%**, **300-1%**, **300-5%** and **300-10%**, were obtained accordingly. After *in situ* ligand exchange, the hydrodynamic sizes of **RGD-SNPs⊃DNA** exhibited negligible changes (<5%, Fig. S4, ESI†). The morphologies of **SNPs⊃DNA** and **RGD-SNPs⊃DNA** were then examined by using TEM. The TEM images (Fig. 1) showed smaller sizes (62 ± 8 for 100 nm **SNPs⊃DNA** and 210 ± 24 nm for 300 nm **SNPs⊃DNA**), spherical shapes and narrow size distributions of **SNPs⊃DNA** and **RGD-SNPs⊃DNA**. Zeta potential measurements indicated that the surface-charge densities of 100 and 300 nm **SNPs⊃DNA** were 3.7 ± 0.4 and 6.8 ± 0.5 mV, respectively. After ligand exchange, small increases (3–11%) in zeta potentials of **RGD-SNPs⊃DNA** were observed (Fig. S5, ESI†).

We carried out an *in vitro* EGFP transfection study of a collection of **SNPs⊃DNA** and **RGD-SNPs⊃DNA** along with the controls, *i.e.*, DNA, DNA complexes of **CD-PEI**, **CD-PEI**/**Ad-PEG** and RGD-jet-PEI, in 8-well chamber slides containing two $\alpha_v\beta_3$ high-expressed cells (*i.e.*, U87 and scraping-collected 3T3 cells)[20] and two $\alpha_v\beta_3$ low-expressed cells (*i.e.*, MCF7 and 0.25% trypsin-treated 3T3 cells).[21]

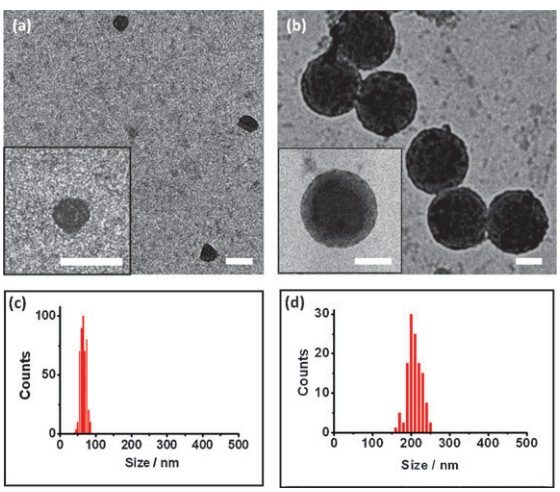

Fig. 1 TEM micrographs of (a) 100 nm **SNPs⊃DNA** and (b) 300 nm **SNPs⊃DNA**. Insets: the respective higher magnification TEM images. Scale bars: 100 nm. (c) and (d) Histograms summarize the size distributions of 100 nm **SNPs⊃DNA** and 300 nm **SNPs⊃DNA** in dry states.

For the purpose of comparison, an equal amount of EGFP-encoded plasmid DNA (100 ng) was added to individual cell culture chambers in this transfection study. The resulting 48 individual EGFP transfection experiments were incubated at 37 °C (5% CO_2) for 24 h. After paraformaldehyde fixation and DAPI nuclear staining, a fluorescence microscope was used to quantify the EGFP expression levels in individual cells. These levels were then used to determine the transfection efficiency for each vehicle. The transfection study was repeated three times, and the results of average transfection efficiency of gene delivery vehicles for different cell lines were summarized in Fig. 2. First, DNA complexes based on each of the molecular building blocks (**CD-PEI** and **CD-PEI**/**Ad-PEG**) gave very poor transfection performance similar to free plasmid DNA, indicating that the formation of supramolecular nanoparticles is crucial for achieving enhanced transfection efficiency. Second, it is apparent that 100-nm **RGD-SNPs⊃DNA** exhibited higher transfection efficiency than those of 300-nm analogues. This observation is consistent with the results from the reported polymer-based gene delivery systems,[22–24] in which vehicles with 10–100 nm size range display better gene transfection efficiency.[13] Third, **100-5% RGD-SNPs⊃DNA** gave the highest transfection efficiency compared to those observed for **SNPs⊃DNA** and other targeted **RGD-SNPs⊃DNA**. The reduced transfection efficiency observed for **100-10% RGD-SNPs⊃DNA** can be attributed to an excess amount of free RGD ligand in the culture medium, which compromised the targeted binding of **RGD-SNPs⊃DNA** as a result of a competition effect.[11] Overall, **100-5% RGD-SNPs⊃DNA** demonstrated the best transfection efficiencies (57 ± 11% and 31 ± 8% for $\alpha_v\beta_3$ high-expressed 3T3 and U87, respectively). These results are comparable to those observed for the commercially available RGD-jet-PEI (64 ± 15% and 38 ± 9% for $\alpha_v\beta_3$ high expressed 3T3 and U87, respectively), which is a well-known selective and efficient transfection reagent for integrin-expressing cell lines.[25] Fourth, in addition to high transfection efficiency, **100-5% RGD-SNPs⊃DNA** also exhibited outstanding delivery specificity to the $\alpha_v\beta_3$ high expressed cells, U87 (31 ± 8%) and 3T3 (57 ± 11%), over the $\alpha_v\beta_3$ low expressed cells, MCF7 (21 ± 6%) and trypsin-treated 3T3 (15 ± 4%). Four-fold difference in transfection efficiencies were observed for **100-5% RGD-SNPs⊃DNA** between $\alpha_v\beta_3$ high-expressed and $\alpha_v\beta_3$ low expressed 3T3 cells, while only 1.2-fold difference was observed for RGD-jet-PEI. In contrast to non-target-specific transfection performance of RGD-jet-PEI, **100-5% RGD-SNPs⊃DNA** had higher transfection efficiency for the U87 cell line with respect to the MCF7 cell line, which indicated good transfection specificity of **RGD-SNPs⊃DNA** for the $\alpha_v\beta_3$ high expressed cell lines. Moreover, we tested the toxicity of **SNPs⊃DNA** and **RGD-SNPs⊃DNA** by using the cell viability assay. The cells transfected by **SNPs⊃DNA** and **RGD-SNPs⊃DNA** were compared with the cells cultured in the normal medium. There were no significant differences in viability (97 ± 2%), which suggested that the toxicity of **SNPs⊃DNA** and **RGD-SNPs⊃DNA** is negligible for *in vitro* transfection studies (Fig. S6, ESI†).

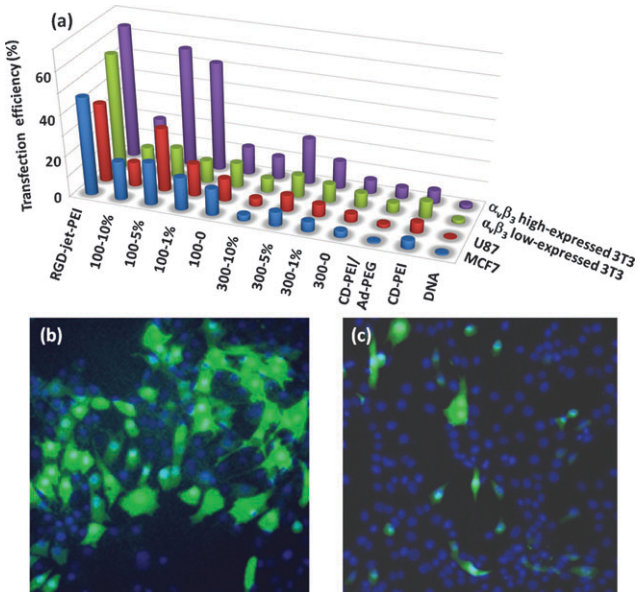

Fig. 2 (a) EGFP transfection efficiency of a collection of **SNPs⊃DNA** and **RGD-SNPs⊃DNA** along with control delivery systems for two $\alpha_v\beta_3$ high-expressed cells (U87 and scraping-collected 3T3 cells) and two $\alpha_v\beta_3$ low-expressed cells (MCF7 and 0.25% trypsin-treated 3T3 cells). The representative fluorescence micrographs of 57 ± 11% and 9 ± 4% transfection efficiencies observed for (b) 5 mol% RGD-grafted 100 nm **RGD-SNPs⊃DNA** (**100-5%**)-treated $\alpha_v\beta_3$ high-expressed 3T3 cells and (c) 1 mol% RGD-grafted 300 nm **RGD-SNPs⊃DNA** (**300-1%**)-treated $\alpha_v\beta_3$ low-expressed 3T3 cells.

In conclusion, we demonstrated a convenient, flexible and modular synthetic approach for preparation of a small library of **SNPs⊃DNA** and **RGD-SNPs⊃DNA** with different sizes and RGD ligand coverage. Gene transfection studies of **SNPs⊃DNA** and **RGD-SNPs⊃DNA** library for $\alpha_v\beta_3$ high-expressed cells and $\alpha_v\beta_3$ low-expressed cells were performed. The results revealed that the size and target ligand coverage of **RGD-SNPs⊃DNA** played a critical role in the target-specific gene delivery. In conjunction with the use of a miniaturized high throughput screening platform[26] and molecular imaging technology,[13] we will dramatically accelerate the discovery processes of **SNPs**-based gene delivery vehicles toward *in vivo* application.

This research was supported by NIH-NCI NanoSystems Biology Cancer Center (U54CA119347) and NIH R21 grant (EB008419–01). We appreciate the reviewers suggestive comments to help us improve our manuscript.

Notes and references

1 D. H. Kim and J. J. Rossi, *Nat. Rev. Genet.*, 2007, **8**, 173–84.
2 D. J. Glover, H. J. Lipps and D. A. Jans, *Nat. Rev. Genet.*, 2005, **6**, 299–310.
3 N. L. Rosi and C. A. Mirkin, *Chem. Rev.*, 2005, **105**, 1547–1562.
4 T. Niidome and L. Huang, *Gene Ther.*, 2002, **9**, 1647–1652.
5 C. A. H. Prata, Y. Li, D. Luo, T. J. McIntosh, P. Barthelemy and M. W. Grinstaff, *Chem. Commun.*, 2008, 1566–1568.
6 K. A. Woodrow, Y. Cu, C. J. Booth, J. K. Saucier-Sawyer, M. J. Wood and W. M. Saltzman, *Nat. Mater.*, 2009, **8**, 526–533.
7 Y. Chen, L. Yu, Z. Feng, S. Hou and Y. Liu, *Chem. Commun.*, 2009, 4106–4108.
8 V. P. Torchilin, T. S. Levchenko, R. Rammohan, N. Volodina, B. Papahadjopoulos-Sternberg and G. G. D'Souza, *Proc. Natl. Acad. Sci. U. S. A.*, 2003, **100**, 1972–1977.
9 H. Liang, D. Harries and G. C. Wong, *Proc. Natl. Acad. Sci. U. S. A.*, 2005, **102**, 11173–11178.
10 A. Kumar and V. Kumar, *Chem. Commun.*, 2009, 5433–5435.
11 L. Bazin, M. Gressier, P. L. Taberna, M. J. Menu and P. Simon, *Chem. Commun.*, 2008, 5004–5006.
12 J. Cheon and J. H. Lee, *Acc. Chem. Res.*, 2008, **41**, 1630–1640.
13 H. Wang, S. T. Wang, H. Su, K. J. Chen, A. L. Armijo, W. Y. Lin, Y. J. Wang, J. Sun, K. Kamei, J. Czernin, C. G. Radu and H. R. Tseng, *Angew. Chem., Int. Ed.*, 2009, **48**, 4344–4348.
14 Z. Liu, W. B. Cai, L. N. He, N. Nakayama, K. Chen, X. M. Sun, X. Y. Chen and H. J. Dai, *Nat. Nanotechnol.*, 2007, **2**, 47–52.
15 S. Srinivasachari and T. M. Reineke, *Biomaterials*, 2009, **30**, 928–938.
16 J. Li, C. Yang, H. Z. Li, X. Wang, S. H. Goh, J. L. Ding, D. Y. Wang and K. W. Leong, *Adv. Mater.*, 2006, **18**, 2969–2970.
17 G. T. Zugates, D. G. Anderson, S. R. Little, I. E. B. Lawhorn and R. Langer, *J. Am. Chem. Soc.*, 2006, **128**, 12726–12734.
18 M. Meyer, A. Philipp, R. Oskuee, C. Schmidt and E. Wagner, *J. Am. Chem. Soc.*, 2008, **130**, 3272–3273.
19 When mixing ratios of RGD to target ligand were 1, 5 and 10%, the actual RGD ligand coverages on the 100 nm **RGD-SNPs⊃DNA** were 0.8 ± 0.2%, 2.9 ± 0.5% and 6.7 ± 0.8%, respectively. For 300 nm **RGD-SNPs⊃DNA**, the RGD ligand coverages were 0.9 ± 0.2%, 2.2 ± 0.4% and 6.7 ± 0.6%, respectively. For details see ESI†.
20 Q. K. T. Ng, M. K. Sutton, P. Soonsawad, L. Xing, H. Cheng and T. Segura, *Mol. Ther.*, 2009, **17**, 828–836.
21 J. Xie, K. Chen, H. Y. Lee, C. J. Xu, A. R. Hsu, S. Peng, X. Y. Chen and S. H. Sun, *J. Am.Chem. Soc.*, 2008, **130**, 7542–7543.
22 M. E. Davis, Z. Chen and D. M. Shin, *Nat. Rev. Drug Discovery*, 2008, **7**, 771–782.
23 H. J. Yu and E. Wagner, *Curr. Opin. Mol. Ther.*, 2009, **11**, 165–178.
24 S. Fukushima, K. Miyata, N. Nishiyama, N. Kanayama, Y. Yamasaki and K. Kataoka, *J. Am. Chem. Soc.*, 2005, **127**, 2810–2811.
25 P. Erbacher, J. S. Remy and J. P. Behr, *Gene Ther.*, 1999, **6**, 138–45.
26 (*a*) W.-Y. Lin, Y. Wang, S. Wang and H.-R. Tseng, *Nano Today*, 2009, **4**, 470–481; (*b*) Y. J. Wang, W. Y. Lin, K. Liu, R. J. Lin, M. Selke, H. C. Kolb, N. G. Zhang, X. Z. Zhao, M. E. Phelps, C. K. F. Shen, K. F. Faull and H. R. Tseng, *Lab Chip*, 2009, **9**, 2281–2285; (*c*) J. Wang, G. Sui, V. P. Mocharla, R. J. Lin, M. E. Phelps, H. C. Kolb and H.-R. Tseng, *Angew. Chem., Int. Ed.*, 2006, **45**, 5276–5281.

A digital microfluidic droplet generator produces self-assembled supramolecular nanoparticles for targeted cell imaging

2010 Nanotechnology 21 445603

(http://iopscience.iop.org/0957-4484/21/44/445603)

Nanotechnology **21** (2010) 445603 (8pp) doi:10.1088/0957-4484/21/44/445603

A digital microfluidic droplet generator produces self-assembled supramolecular nanoparticles for targeted cell imaging

Kan Liu[1,2,3,4,5,6,7], **Hao Wang**[2,3,4,5,6,7], **Kuan-Ju Chen**[2,3,4,5], **Feng Guo**[2,3,4,5], **Wei-Yu Lin**[2,3,4,5], **Yi-Chun Chen**[2,3,4,5], **Duy Linh Phung**[2,3,4,5], **Hsian-Rong Tseng**[2,3,4,5,7] **and Clifton K-F Shen**[2,3,4,7]

[1] College of Electronics and Information Engineering, Wuhan Textile University, Wuhan 430073, People's Republic of China
[2] Department of Molecular and Medical Pharmacology, David Geffen School of Medicine at University of California, Los Angeles, 23-120 Center for Health Science, Los Angeles, CA 90095, USA
[3] Crump Institute for Molecular Imaging, 570 Westwood Plaza, Los Angeles, CA 90095, USA
[4] California Nanosystems Institute, 570 Westwood Plaza, Los Angeles, CA 90095, USA
[5] Institute for Molecular Medicine, University of California, Los Angeles, CA 90095, USA

E-mail: liukan2002@gmail.com, haowangkevin@gmail.com, HRTseng@mednet.ucla.edu and kshen@mednet.ucla.edu

Received 14 May 2010, in final form 16 September 2010
Published 8 October 2010
Online at stacks.iop.org/Nano/21/445603

Abstract
Controlling the size distribution of polymer-based nanoparticles is a challenging task due to their flexible core and surface structures. To accomplish such as task requires very precise control at the molecular level. Here we demonstrate a new approach whereby uniform-sized supramolecular nanoparticles (SNPs) can be reliably generated using a digital microfluidic droplet generator (DMDG) chip. A microfluidic environment enabled precise control over the processing parameters, and therefore high batch-to-batch reproducibility and robust production of SNPs with a very narrow size distribution could be realized. Digitally adjustment of the mixing ratios of the building blocks on the DMDG chip allowed us to rapidly scan a variety of synthesis conditions without consuming significant amounts of reagents. Nearly uniform SNPs with sizes ranging from 35 to 350 nm were obtained and characterized by transmission electron microscopy and dynamic light scattering. In addition, we could fine-tune the surface chemistry of the SNPs by incorporating an additional building block functionalized with specific ligands for targeting cells. The sizes and surface properties of these SNPs correlated strongly with their cell uptake efficiencies. This study showed a feasible method for microfluidic-assisted SNP production and provided a great means for preparing size-controlled SNPs with desired surface ligand coverage.

S Online supplementary data available from stacks.iop.org/Nano/21/445603/mmedia

1. Introduction

The study of nanoparticles exhibiting unique properties that differ from those observed in corresponding bulk materials has emerged as a growing field of intensive research [1–5]. Over the past two decades, there have been significant efforts devoted to exploring the use of nanoparticles for biomedical applications, especially in molecular imaging of disease and drug/gene delivery [6–10]. Recently, our research group has developed a multi-component self-assembly approach toward the preparation of supramolecular nanoparticles (SNPs); this

[6] These authors contributed equally to this study.
[7] Authors to whom any correspondence should be addressed.

0957-4484/10/445603+08$30.00

protocol exhibits the advantageous characteristics of synthetic convenience, flexibility, and modularity [11, 12]. The uniqueness of this self-assembly approach is that it allows the surfaces of the SNPs to be decorated with various targeting ligands, while offering flexibility in the selection of many different loadings. The SNPs can also be tailored to meet desired mechanical and functional properties. For example, SNPs can be programmed by simply switching the nature of the building blocks or by mixing them at different ratios, offering the possibility of combining structural diversity with unique functions [11, 12]. In a previous work, we observed size-dependent lymph node uptake of SNPs, with biodistributions also influenced by size [11]. In addition, we have found that the surface chemistry of such nanoparticles dictates their stability, solubility, cell binding specificity, and internalization capability [12]. To control SNP self-assembly, several essential parameters (structures of the building blocks, reaction temperature, pH, concentration) must be varied to determine the optimal conditions for the production of SNPs having the desired sizes and surface chemistries. With conventional production methods, however, several major issues often arise: poor reproducibility, tedious synthetic procedures, and non-uniform particles having a wide size distribution [13]. Consequently, the current practice of nanoparticle production is usually time-consuming, labor-intensive, and sample-consuming. Further advances in this field will require practical strategies for optimizing and producing SNPs in a highly reproducible matter.

Several examples of nanoparticle syntheses using microfluidic platforms have been reported [14–21]. There are many advantages to using microfluidic platforms, including minimal consumption of building blocks, reduced reaction times, the capability for parallel processing, and the ability to perform multi-step syntheses [22–25]. Most importantly, the quality of the resulting nanoparticles is greatly improved when they are produced within a microfluidic environment [26, 27]. Due to the expected benefits from microfluidics, such as enhanced reaction kinetics, superior reaction control, high production reliability, safety and facile automation and integration with downstream processing, several microfluidic platforms have been developed recently for nanoparticle synthesis [28–34], especially in the format of microdroplet-based microreactors that allow one to compartmentalize and isolate samples and reactants within individual droplets [35–37]. The application of microdroplets enables an unprecedented degree of control over reaction conditions on short time scales [33, 38, 39]. Each droplet becomes an individual, miniature batch reactor, characterized by uniform volume, temperature, and concentration. The various reagents are typically either (i) combined into the multi-component droplets at the instant of droplet formation or (ii) first formed as single-component droplets that are later merged together through on-chip droplet manipulation [32, 33, 40]. Rapid mixing is achieved simply by moving droplets along microchannels or surfaces [41]. The high droplet throughput and well-defined droplet size and reagent composition make microdroplet technology ideal for nanoparticle syntheses.

Several requirements must be met if we are to perform SNP syntheses using self-assembly processes in microfluidic devices: (1) the ratio of all the building blocks must be precisely controlled; (2) the building blocks and final SNPs must be free from contaminants; and (3) the sizes and surface chemistries of the SNPs must readily accommodate different building blocks as well as various mixing ratios [10–12]. To date, no suitable microfluidic devices have been developed that are capable of synthesizing SNPs because they have all been incapable of precisely adjusting the ratio of building blocks or removing the second immiscible phase in the final droplets [28, 32, 33, 42].

In this paper we report a new approach to the optimization and synthesis of SNPs using a digital microfluidic droplet generator (DMDG) [42, 43], which permits precise control over the composition and size of multi-component droplets on demand. In addition, the droplets are separated using nitrogen slugs to avoid contamination, thereby greatly simplifying the subsequent purification/dispensing of the resulting SNPs. This DMDG chip provides a very practical platform for optimizing the synthetic parameters and producing uniform SNPs, with narrow size distributions, in a highly reproducible manner. We used this DMDG chip to generate SNPs of various sizes and surface chemistries. Subsequent *in vitro* studies indicated a close relationship between the size/surface chemistry and the cell uptake efficiency.

2. Experimental details

2.1. Materials

Reagents and solvents were purchased from Sigma-Aldrich (St Louis, MO, USA) and used as-received without further purification, unless otherwise noted. Branched polyethyleneimine (PEI; MW = 10 kDa) was purchased from Polysciences (Washington, PA, USA); the polymer contained primary, secondary, and tertiary amino groups in a ratio of about 25:50:25. A first-generation polyamidoamine (PAMAM) dendrimer featuring a 1,4-diaminobutane core and amino terminal groups was purchased as a 20 wt% MeOH solution from Dendritic Nanotechnologies (Mount Pleasant, MI, USA). 1-Adamantanamine (Ad) hydrochloride and β-cyclodextrin (β-CD) were purchased from TCI America (San Francisco, CA, USA). *N*-hydroxysuccinimide (SCM) and maleimido (MAL) hetero-functionalized polyethylene glycol (SCM-PEG-MAL; MW = 5 kDa) were obtained from NANOCS (New York, NY, USA). 6-Monotosyl-β-cyclodextrin (6-OTs-β-CD) was prepared following the literature method [44]. The octa-Ad-grafted PAMAM dendrimer (Ad-PAMAM, **1 or 1′**), CD-grafted branched PEI (CD-PEI, **3**), and Ad-grafted polyethylene glycol (Ad-PEG, **2**) were prepared using previously reported methods [11]. CH_2Cl_2 was dried under reflux over CaH_2 and freshly distilled prior to use. MCF7 breast cancer and U87 brain cancer cell lines were purchased from the American Type Culture Collection. Dulbecco's modified Eagle's medium (DMEM), Earl's modified Eagle's medium (EMEM), and penicillin/streptomycin were obtained from Invitrogen (Carlsbad, CA, USA). Fetal bovine serum (FBS) was obtained from Lonza Walkersville (Walkersville, MD, USA). 4′,6-Diamidino-2-phenylindole (DAPI)

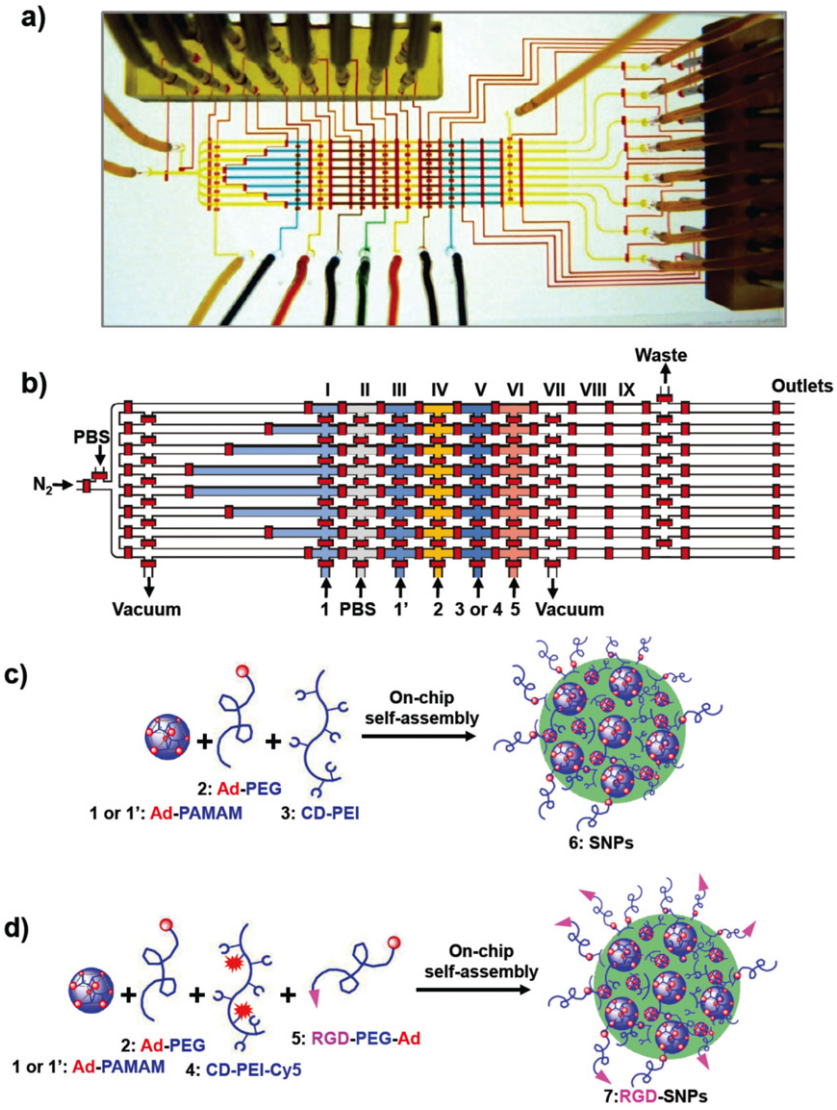

Figure 1. (a) Photograph of the PDMS microfluidic device. (b) Schematic representation of the main features of the microfluidic device. Each filling region (chambers II–IX) has a length of 1500 μm, a width of 300 μm, a height of 45 μm, and a volume of about 15 nl. The volumes of step-filling chambers I are about 15, 30, 45, and 60 nl. Two different concentrations of Ad-PAMAM (84 and 168 μM), Ad-PEG (840 μM), CD-PEI (168 μM), and RGD-PEG-Ad (21 μM) were loaded individually into the chip through inlets Ad-PAMAM **1** (84 μM), Ad-PAMAM **1**′ (186 μM), Ad-PEG **2**, CD-PEI **3** or CD-PEI-Cy5 **4**, and RGD-PEG-Ad **5**, respectively. (c), (d) Graphical representations of the on-chip approach to the preparation of size- and surface chemistry-controllable SNPs **6** and RGD-SNPs **7**.

was purchased from Invitrogen. Argininylglycyl aspartyl cysteine (RGDC) was purchased from GenScript (Piscataway, NJ, USA).

CD-PEI-Cy5 **4** was synthesized as follows. Cy5-*N*-hydroxysuccinimidyl ester (0.9 mg, 1.0 μmol, 10.0 equiv.) was added to a solution of CD-PEI **3** (1.7 mg, 0.1 μmol, 1.0 equiv.) in PBS buffer solution (pH 7.2). After stirring at room temperature for 2 h, the mixture was purified through dialysis (Slide-A-Lyzer® dialysis cassette, ThermoFisher, Canoga Park, CA, USA; MWCO: 3 kD) against deionized (DI) water overnight and lyophilized to yield CD-PEI-Cy5 **4** (supporting information available at stacks.iop.org/Nano/21/445603/mmedia). The degree of Cy5 dye substitution on the CD-PEI **3** backbone was calculated based on the molar extinction coefficient of Cy5 (ε = 250 000 M^{-1} cm^{-1}), suggesting that there were five to six Cy5 molecules grafted per CD-PEI polymer.

2.2. Microfluidic device design and fabrication

A two-layer polydimethylsiloxane (PDMS) microfluidic device was fabricated using common multilayer soft lithography technology (figure 1(a)) [45, 46]. The upper and lower layers of the microchannel network functioned as fluidic and control channels, respectively. By applying positive pressure (approximately 450 kPa) via electronic solenoid valves (series S070, SMC, Japan), the control channels could be deformed, thereby functioning as on-chip microvalves to close the fluidic channels at locations where the control channels directly overlapped the fluidic channels [46]. Figure 1(b) provides a schematic

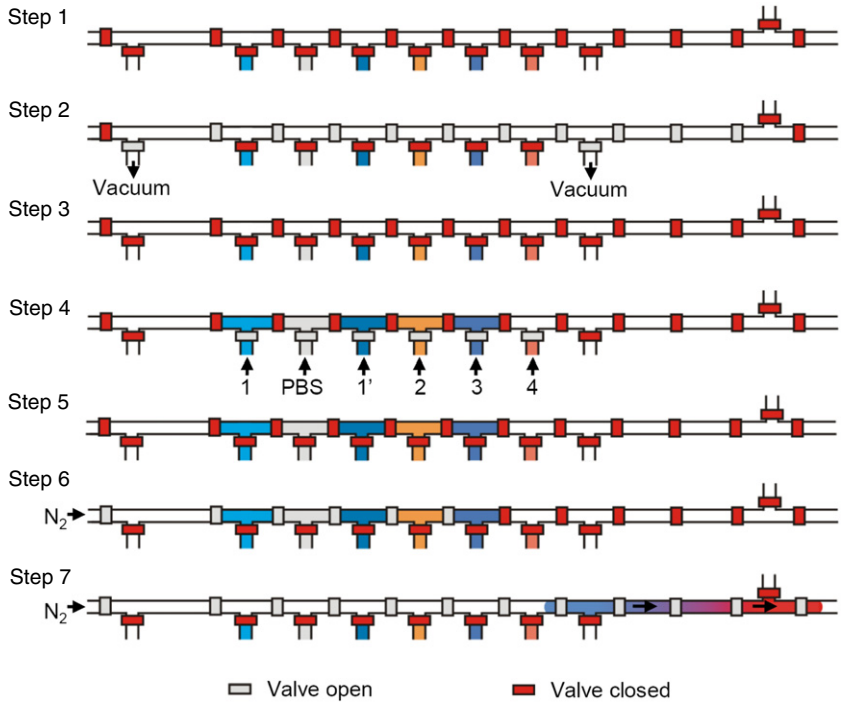

Figure 2. Time sequence of the droplet generation process in a single droplet generation unit of the parallel microfluidic device.

representation of the main features of the DMDG chip. The core consisted of eight parallel droplet generation units. Each droplet generation unit could be isolated from the surrounding channels by microvalves; the volume of the filling chambers in each droplet generation unit could also be dynamically controlled by using dividing microvalves.

*2.3. Production of SNPs **5** in a DMDG chip*

Three molecular building blocks, Ad-PAMAM **1**′ (84 μM) or **1**′ (168 μM), Ad-PEG **2** (840 μM), and CD-PEI **3** (168 μM), were used to assemble SNPs **6** (figure 1(c)). Eight parallel droplets having the desired volumes/ratios of building blocks could be digitally generated by performing one cycle of operation of the mechanically acting microvalves in the DMDG chip. The detailed sequence of valve states used to generate the composition-controlled droplets in each droplet generation unit of the parallel DMDG chip is presented in figure 2. The process involved seven steps. Step 1: close all microvalves to initialize the microfluidic device (ca. 50 ms). Step 2: release the backpressure of the droplet generation unit (ca. 150 ms) by applying a vacuum (ca. −75 kPa). Step 3: form the desired volume of the reagent filling chambers (ca. 50 ms) by closing the dividing microvalves. Step 4: fill the individual chambers with the building blocks and PBS by applying a positive pressure (ca. 200 kPa, ca. 150 ms); in this step, the RGD-PEG-Ad **5** building block was not placed into the reagent filling chamber VI. Step 5: seal the reagent filling chambers (ca. 50 ms). Step 6: merge reagents to form one droplet (ca. 50 ms). Step 7: open the trap valve at the end of the droplet generation unit to expel the droplet from the device using nitrogen (ca. 60 kPa). In the parallel droplet generation process, eight droplets could be generated in parallel by sequentially opening the trap valves at the end of each unit (step 7) and expelling them from the microfluidic device using nitrogen (ca. 100 ms for each droplet generation unit). The total time required to generate the eight droplets when using the parallel DMDG chip was ca. 1.3 s. The droplets having the desired volumes/ratios of building blocks were expelled and passed through individual tubes into PCR/Eppendorf tubes. Finally, the eight batches of SNPs **6** were produced in parallel simultaneously using the DMDG chip. Each experiment was performed in triplicate.

Eight different batches of SNPs **6** prepared from different ratios of Ad-PAMAM and CD-PEI were produced by adjusting the volume or concentration of Ad-PAMAM. The first four batches of SNPs **6** were produced by filling Ad-PAMAM **1** (84 μM) alone into the reagent step-filling chamber I and using PBS to fill both filling chambers II and III. Each building block was placed into the destined chamber at a fixed volume to ensure an equal amount of each building block in each droplet. Because chamber I could be sectioned into four different volumes, four different ratios of Ad-PAMAM and CD-PEI (0.5, 1.0, 1.5, and 2.0) were generated to prepare SNPs**6** in four different batches. Next, another four batches of SNPs were produced by filling Ad-PAMAM **1** (84 μM) into the step-filling chamber I and then placing a different concentration of Ad-PAMAM **1**′ (168 μM) into both filling chambers II and III. Using this approach, another four different batches of SNPs **6** were generated with four different ratios of Ad-PAMAM and CD-PEI (2.5, 3.0, 3.5, and 4.0). By scaling the cycle number of the droplet generation steps, 200 μl samples of SNPs **6** were produced under each set of conditions. In addition to the cases using CD-PEI, the same procedures were also performed using CD-PEI-Cy5 **4** (168 μM) to aid visualization.

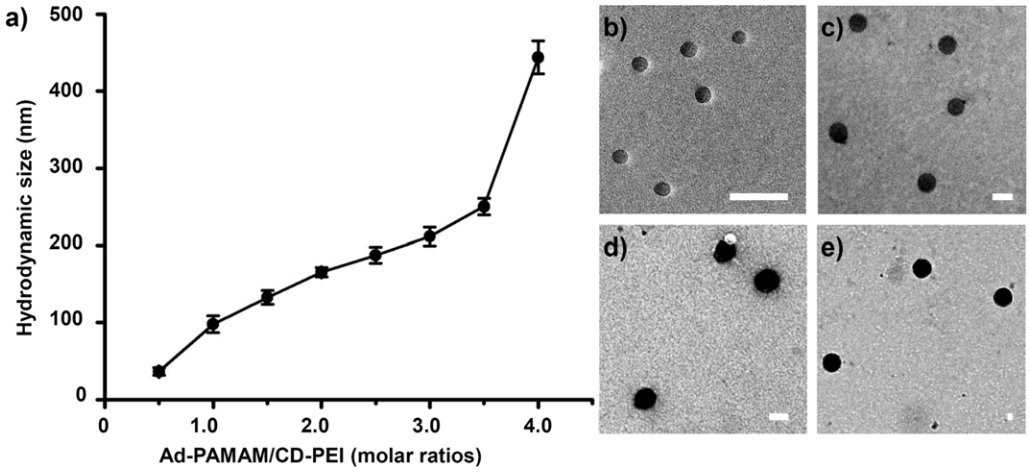

Figure 3. (a) Relationship between the sizes of the SNPs **6** and the ratio of Ad-PAMAM/CD-PEI, obtained through DLS analysis. (b)–(e) TEM images of SNPs **6** having sizes of 36.7 ± 5.7, 110 ± 9.2, 148 ± 9.5, and 344 ± 15.3 nm, obtained at Ad-PAMAM/CD-PEI ratios of 0.5, 1.5, 2.5, and 4.0, respectively. Scale bar: 100 nm.

2.4. Production of RGD-SNPs 7 in a DMDG chip

To explore the biological applications of SNPs, the RGD (argininylglycyl aspartic acid) ligand, which recognizes the $\alpha_v\beta_3$ integrin receptor on the membranes of certain types of tumor cells [47], was incorporated onto the surfaces of the SNPs. Four molecular building blocks—Ad-PAMAM **1** (84 μM), Ad-PEG **2** (840 μM), CD-PEI-Cy5 **4** (168 μM), and RGD-PEG-Ad **5** (21 μM)—were used to assemble RGD-targeted SNPs (RGD-SNPs **7**, figure 1(d)). By using a similar operating principle, eight parallel droplets having the desired volumes/ratios of building blocks were generated by the DMDG chip. In this case, all the parallel droplets were generated having the same number of building blocks by filling Ad-PAMAM **1** into chamber III (leaving chambers I and II empty), and Ad-PEG **2** and CD-PEI-Cy5 **4** into chambers IV and V, respectively. Four different SNPs having RGD ligand coverage of 0, 2.5, 5, and 10% (based on the total amount of Ad-PEG **2**) were created by filling different amounts of RGD-PEG-Ad **5** (21 μM) into chambers VI–IX with volume units of 0, 1, 2, and 4, respectively.

2.5. Characterization of SNPs 5 and RGD-SNPs 6

Dynamic light scattering (DLS) experiments were performed using a Zetasizer Nano instrument (Malvern Instruments, UK) equipped with a 10 mW helium–neon laser ($\lambda = 632.8$ nm) and a thermoelectric temperature controller. Measurements were taken at a 90° scattering angle. The morphology and sizes of the SNPs **6** and RGD-SNPs **7** were examined directly using a Philips CM 120 electron microscope operated at an acceleration voltage of 120 kV. Samples for transmission electron microscopy (TEM) were prepared by drop-coating solutions of the SNPs **6** and RGD-SNPs **7** (2 μl) onto carbon-coated copper grids. Excess amounts of the droplets were removed after 45 s using filter paper. The surface-deposited SNPs **6** and RGD-SNPs **7** were then negatively stained with 2% uranyl acetate for 45 s prior to TEM analysis.

2.6. In vitro cell uptake study

U87 cell lines were routinely maintained in DMEM containing 10% FBS and 1% penicillin/streptomycin (Invitrogen). MCF7 was cultured in DMEM containing 10% FBS and 1% penicillin/streptomycin.

Cells (1×10^4 cells/well) were plated in eight-well chamber slides and left to adhere overnight. The SNPs **6** or RGD-SNPs **7** (4 μM) were added into individual wells containing DMEM (200 μl). SNPs or RGD-SNPs were incubated with the cells for 12 h and then removed by aspirating and washed with PBS (three times). Cells were fixed with 4% paraformaldehyde for 15 min at room temperature, washed with PBS (three times), stained with DAPI, and then rinsed with PBS prior to imaging using a fluorescence microscope.

The eight-well chamber slide was mounted onto a Nikon TE2000S inverted fluorescence microscope equipped with a CCD camera (Photomatrix, Cascade II), X-Cite 120 Mercury lamp, automatic stage, and filters for three fluorescent channels (W1 (DAPI) and W2 (Cy5)). Following image acquisition, MetaMorph software (Molecular Devices, v. 7.5.6.0) was used to quantify the Cy5 expressing cells. The multi-wavelength cell scoring module of the MetaMorph software allowed image analysis. A nuclei counting application in the module allowed the total cell number to be calculated. To determine the cell uptake ability, the Cy5 intensities of the individual cells were quantified using the MetaMorph program. The highest fluorescence intensity was observed from the U87 cells treated with 35 nm SNPs with 5% RGD target ligand coverage. This fluorescence intensity was used to normalize other readings as depicted in figure 4(b).

3. Results and discussion

The DMDG chip allowed us to successfully prepare SNPs. Unlike other SNP synthesis processes performed in continuous flow microfluidic devices, we used the digitally controllable

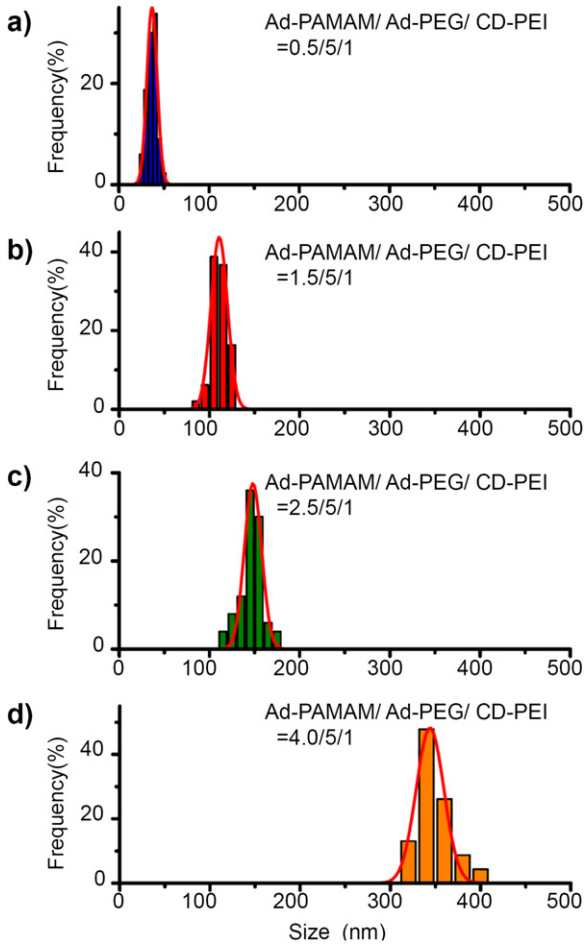

Figure 4. TEM analyses of size distributions of SNPs **6**. SNPs of various sizes (36.7 ± 5.7, 110 ± 9.2, 148 ± 9.5, and 344 ± 15.3 nm) were obtained by varying the mixing ratio of Ad-PAMAM to CD-PEI.

(This figure is in colour only in the electronic version)

microvalves of our DMDG chip to adjust the reagents and building blocks to the desired ratios/volumes and to merge them together into end-to-end droplets that could then be mixed after flowing along the mixing channel [41]. In addition, this present approach allowed larger amounts of sample(s) to be produced rapidly by scaling the cycle number of droplet generation steps. Our parallel microfluidic device could not only precisely adjust the ratio of building blocks but could also produce four different conditions for the SNPs in parallel (0.5–1 ml h^{-1} for each condition) or produce just one condition (2–4 ml h^{-1}, without using the reagent step-filling chamber I). Furthermore, because we used nitrogen to separate each droplet, the final SNPs could be applied directly to the next step or to *in vitro* applications without requiring an oil removal step. Combining all the advantages mentioned above allowed us to readily evaluate small 'batches' of samples (e.g. several droplets) through TEM analyses.

In a previous study, we found that the sizes of the SNPs depended on the mixing ratio of Ad-PAMAM and CD-PEI [11]. Using the DMDG chip, we produced eight SNPs **6** from different mixing ratios of Ad-PAMAM and CD-PEI by adjusting the volume of the Ad-PAMAM building block. Figure 3(a) reveals that the average size of the SNPs increased upon increasing the molar ratio of Ad-PAMAM to CD-PEI. When we increased the ratio of Ad-PAMAM to CD-PEI from 0.5 to 4, the mean size (DLS) of the SNPs increased continuously from 36 ± 4.9 to 443 ± 21.3 nm, primarily because of the increased degree of cross-linking between the Ad-PAMAM and CD-PEI units. We observed similar trends in previous studies [11, 12]. In addition to the DMDG chip producing precisely size-controlled SNPs **6**, it also provided a high reproducibility for each SNP synthesis. Under the same conditions, the 'mean' size differences of the SNPs obtained from different batches were quite small (from 3.8 to 13.5%; see the error bars in figure 3(a)). This reproducible microfluidic-assisted SNP production presumably arose from the precise control exerted over the volume/ratio of each building block and over the reaction parameters within the microfluidic device [32, 33]. The resulting SNPs **6** possessed spherical morphologies, with sizes consistent with those determined using DLS (figures 3(b)–(e)).

Using our DMDG chip, microdroplets were generated in an end-to-end manner very precisely; they could be mixed rapidly upon moving along a straight channel. Unlike other precisely tuned continuous flow droplet generators that can perform mixing in only a single ratio (or alternate between two or more different ratios), our system provided complete control over a wide range of droplet ratios, even changing the mixing ratio on demand. Its multi-chamber design enabled us to perform simultaneous mixing of multiple reagents over a wide range of ratios; its parallel channel design improved the rate of product output. We fitted the size and size distribution data of the SNPs **6** ($n = 200$), obtained from TEM analysis, to individual Gaussian curves using the Origin Software Package (Origin 6.0); the correlation coefficients were all greater than 0.95 (figure 4). For Ad-PAMAM/CD-PEI ratios of 0.5, 1.5, 2.5, and 4.0, the peak positions (mean sizes of the SNPs **6** synthesized using the DMDG chip) determined using the Origin Software Package were 36.7, 110, 148, and 344 nm, respectively, and full widths at half maximum (FWHM; 11.4, 18.4, 19.1 and 30.7 nm, respectively) that are narrower than those obtained using conventional methods (15.8, 26.6, 27.2, and 45.8 nm, respectively) [11, 12]. We attribute this narrower size distribution for the SNPs **6** to the rapid and homogeneous mixing microenvironment afforded by the DMDG chip (see table S1 in supporting information available at stacks.iop.org/Nano/21/445603/mmedia). It is well documented [33, 41] that multiple reagents combined in an end-to-end format in droplets are rapidly mixed as they flow through microfluidic channels. Taking advantage of an internal recirculation flow pattern, the three building blocks (Ad-PAMAM, Ad-PEG, and CD-PEI) were mixed thoroughly after moving along the microfluidic channel and tubes (>10 cm distance) with high flow rates (>10 cm s^{-1})—on timescales as fast as milliseconds [33, 41]. Using this droplet-based approach prevented the aggregation of SNPs and provided highly homogeneous mixed solutions within a short period of time for the rapid self-assembly of SNPs having uniform sizes. Indeed, SNPs of different sizes were simply and reproducibly synthesizable through

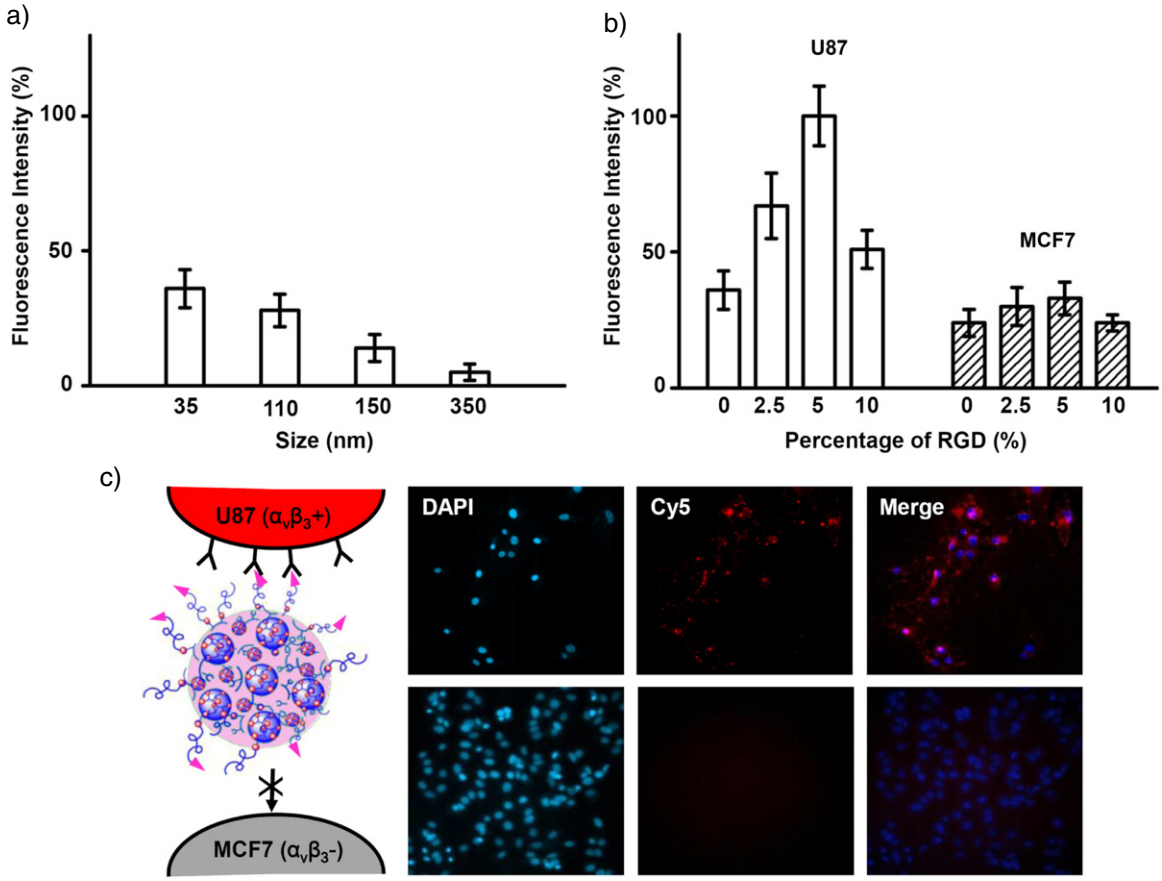

Figure 5. (a) Uptake efficiency of SNPs of various sizes (from 35 to 350 nm) by the U87 cell line. (b) Uptake of 35 nm RGD-SNPs of various RGD ligand coverages (from 0 to 10%) by U87 and MCF7 cell lines. (c) Fluorescence microscopy images of 35 nm RGD-SNPs **7** (5% RGD ligand coverage) taken up by U87 and MCF7 cell lines. The cell nuclei were stained by DAPI; the RGD-SNPs **7** were labeled with Cy5 units.

programmed adjustment of the filling chamber volumes of Ad-PAMAM in the microfluidic device. The entire operation could be performed very smoothly, reliably, and predictably—even on the very first attempt; it did not require any special tuning procedure to arrive at a stable flow of the correct reagent ratio, as in the case of continuous flow systems. Therefore, our DMDG chip platform is capable of digitally generating mircodroplets in a highly efficient matter (in seconds) and, at the same time, conserving the reagents.

Next, we produced SNPs **6** of various sizes to perform a cell uptake study. It is currently believed that the optimal diameter of nanoparticle-based therapeutics for cancer therapy should be between 10 and 100 nm. This lower boundary was established based on the measurement of sieving coefficients for the glomerular capillary wall; it is estimated that the threshold for first-pass elimination by the kidneys is about 10 nm [48]. The upper boundary, however, is not as well defined at present. To visualize the SNP traffic in the cells, we used CD-PEI-Cy5, rather than CD-PEI, to assemble the SNPs in the latter experiments. According to the experimental data on cell uptake in figure 5(a), it appears that smaller-sized SNPs (i.e. 35 nm SNPs) were taken up more readily by the U87 cells after incubation for 12 h at 37 °C (5% CO_2). Furthermore, because the surface chemistry of nanoparticles affects their cell-specific uptake efficiency [1], we introduced the RGD target ligand, which recognizes $\alpha_v\beta_3$ integrin receptors on the membranes of certain types of tumor cells [47], to functionalize the SNPs **6**; we then tested their cell-specific uptake efficiency. By varying the mixing ratio of RGD-PEG-Ad with respect to the other building blocks, we obtained 35 nm RGD-SNPs **7** having RGD ligand coverages of 0, 2.5, 5, and 10% (based on the Ad-PEG) in the DMDG chip (figure 1(d)). We fed the resulting RGD-SNPs **7** into both $\alpha_v\beta_3$-positive U87 and $\alpha_v\beta_3$-negative MCF7 cells [12]. After incubation for 12 h, the 35 nm RGD-SNPs **7** having 5% RGD coverage exhibited the highest cell uptake efficiency (figure 5(b)). The fluorescence intensity was stronger in the $\alpha_v\beta_3$ integrin-positive U87 cells than that in the $\alpha_v\beta_3$ integrin-negative MCF7 cells (cf figures 5(b) and (c)). Thus, the 35 nm RGD-SNPs **7** having 5% RGD ligand coverage exhibited significantly improved $\alpha_v\beta_3$ integrin-dependent cell uptake behavior.

4. Conclusion

We have developed a microfluidic approach toward producing size- and surface chemistry-controlled SNPs merely by adjusting the ratios of the building blocks with high flexibility and reducibility. Using our method, SNPs with different compositions can be generated and screened at high speed

(>2 s per condition) using only a very small sample volume (<1 μl per condition). Compared with conventional methods, the size distributions of our SNPs were narrow because of the homogeneous assembly within the microfluidic environment and the precise control exerted over the mixing ratios of the building blocks. Our methodology produced a collection of uniform SNPs having different sizes and surface chemistries; *in vitro* experiments indicated that these features were correlated strongly with the cell uptake efficiency. We predict that this method could be widely applicable to high speed screening of optimal conditions to make desired nanoparticulate composites for gene/drug delivery systems and molecular imaging [49].

Acknowledgments

We thank the US Department of Energy (DE-PS02-09ER09-08, DE-PS02-09ER09-18) and the UC Discovery Grant (bio07-10665, bio08-129095) for financial support.

References

[1] Cheon J and Lee J H 2008 *Acc. Chem. Res.* **41** 1630–40
[2] Murphy C J, Gole A M, Stone J W, Sisco P N, Alkilany A M, Goldsmith E C and Baxter S C 2008 *Acc. Chem. Res.* **41** 1721–30
[3] Stewart M E, Anderton C R, Thompson L B, Maria J, Gray S K, Rogers J A and Nuzzo R G 2008 *Chem. Rev.* **108** 494–521
[4] Nie S M, Xing Y, Kim G J and Simons J W 2007 *Annu. Rev. Biomed. Eng.* **9** 257–88
[5] Shenhar R, Norsten T B and Rotello V M 2005 *Adv. Mater.* **17** 657–69
[6] Davis M E, Chen Z and Shin D M 2008 *Nat. Rev. Drug Discov.* **7** 771–82
[7] Liu T Y, Hu S H, Liu D M, Chen S Y and Chen I W 2009 *Nano Today* **4** 52–65
[8] Ofir Y, Samanta B and Rotello V M 2008 *Chem. Soc. Rev.* **37** 1814–23
[9] Byrne J D, Betancourt T and Brannon-Peppas L 2008 *Adv. Drug Deliv. Rev.* **60** 1615–26
[10] Green J J, Langer R and Anderson D G 2008 *Acc. Chem. Res.* **41** 749–59
[11] Wang H *et al* 2009 *Angew. Chem. Int. Edn* **48** 4344–8
[12] Wang H, Chen K J, Wang S T, Ohashi M, Kamei K I, Sun J, Ha J H, Liu K and Tseng H R 2010 *Chem. Commun.* **46** 1851–3
[13] Hawker C J and Wooley K L 2005 *Science* **309** 1200–05
[14] He P, Greenway G and Haswell S J 2008 *Nanotechnology* **19** 315603
[15] Singh A, Limaye M, Singh S, Lalla N P, Malek C K and Kulkarni S 2008 *Nanotechnology* **19** 245613
[16] Duraiswamy S and Khan S A 2009 *Small* **5** 2828–34
[17] Abou-Hassan A, Bazzi R and Cabuil V 2009 *Angew. Chem. Int. Edn* **48** 7180–3
[18] Wang H Z, Li X Y, Uehara M, Yamaguchi Y, Nakamura H, Miyazaki M P, Shimizu H and Maeda H 2004 *Chem. Commun.* 48–9
[19] Weng C H, Huang C C, Yeh C S, Lei H Y and Lee G B 2009 *Microfluid. Nanofluid.* **7** 841–8
[20] Day D and Gu M 2009 *Nanotechnology* **20** 169801
[21] Luan W L, Yang H W, Tu S T and Wang Z M 2007 *Nanotechnology* **18** 175603
[22] Hong J W and Quake S R 2003 *Nat. Biotechnol.* **21** 1179–83
[23] Park J I, Nie Z, Kumachev A, Abdelrahman A I, Binks B R, Stone H A and Kumacheva E 2009 *Angew. Chem. Int. Edn* **48** 5300–4
[24] deMello A J 2006 *Nature* **442** 394–402
[25] Adamson D N, Mustafi D, Zhang J X J, Zheng B and Ismagilov R F 2006 *Lab Chip* **6** 1178–86
[26] Hwang D K, Dendukuri D and Doyle P S 2008 *Lab Chip* **8** 1640–7
[27] Hung L H, Choi K M, Tseng W Y, Tan Y C, Shea K J and Lee A P 2006 *Lab Chip* **6** 174–8
[28] Nguyen N T and Wu Z G 2005 *J. Micromech. Microeng.* **15** R1–16
[29] Wan Z, Yang H W, Luan W L, Tu S T and Zhou X G 2010 *Nanoscale Res. Lett.* **5** 130–7
[30] Nakamura H, Tashiro A, Yamaguchi Y, Miyazaki M, Watari T, Shimizu H and Maeda H 2004 *Lab Chip* **4** 237–40
[31] Murphy E R, Martinelli J R, Zaborenko N, Buchwald S L and Jensen K F 2007 *Angew. Chem. Int. Edn* **46** 1734–7
[32] Teh S Y, Lin R, Hung L H and Lee A P 2008 *Lab Chip* **8** 198–220
[33] Song H, Chen D L and Ismagilov R F 2006 *Angew. Chem. Int. Edn* **45** 7336–56
[34] Chan E M, Mathies R A and Alivisatos A P 2003 *Nano Lett.* **3** 199–201
[35] Liu K, Ding H J, Chen Y and Zhao X Z 2007 *Microfluid. Nanofluid.* **3** 239–43
[36] Liu K, Ding H J, Liu J, Chen Y and Zhao X Z 2006 *Langmuir* **22** 9453–7
[37] Hettiarachchi K, Talu E, Longo M L, Dayton P A and Lee A P 2007 *Lab Chip* **7** 463–8
[38] Abou-Hassan A, Sandre O, Neveu S and Cabuil V 2009 *Angew. Chem. Int. Edn* **48** 2342–5
[39] Shestopalov I, Tice J D and Ismagilov R F 2004 *Lab Chip* **4** 316–21
[40] Zeng S J, Li B W, Su X O, Qin J H and Lin B C 2009 *Lab Chip* **9** 1340–3
[41] Rhee M and Burns M A 2008 *Langmuir* **24** 590–601
[42] Liu K, Chen Y C, Tseng H R, Shen K F and van Dam R M 2010 *Microfluid. Nanofluid.* **9** 933–43
[43] Liu K, Lepin E J, Wang M W, Guo F, Lin W Y, Chen Y C, Sirk S J, van Dam R M, Wu A M and Shen K F 2010 *Mol. Imaging* doi:10.2310/7290.2010.00043
[44] Petter R C, Salek J S, Sikorski C T, Kumaravel G and Lin F T 1990 *J. Am. Chem. Soc.* **112** 3860–8
[45] Melin J and Quake S R 2007 *Annu. Rev. Biophys. Biomol. Struct.* **36** 213–31
[46] Unger M A, Chou H P, Thorsen T, Scherer A and Quake S R 2000 *Science* **288** 113–6
[47] Liu Z, Cai W B, He L N, Nakayama N, Chen K, Sun X M, Chen X Y and Dai H J 2007 *Nat. Nanotechnol.* **2** 47–52
[48] Venturoli D and Rippe B 2005 *Am. J. Physiol. Renal. Physiol* **288** F605–13
[49] Wang H *et al* 2010 *ACS Nano* at press

A Rapid Pathway Toward a Superb Gene Delivery System: Programming Structural and Functional Diversity into a Supramolecular Nanoparticle Library

Hao Wang,[○,‡,§,⊥,¶] Kan Liu,[○,†] Kuan-Ju Chen,[‡,§,⊥,¶] Yujie Lu,[#] Shutao Wang,[‡,§,⊥,¶] Wei-Yu Lin,[‡,§,⊥,¶] Feng Guo,[‡,§,⊥,¶,▽] Ken-ichiro Kamei,[‡,§,⊥,¶] Yi-Chun Chen,[‡,§,⊥,¶] Minori Ohashi,[‡,§,⊥,¶] Mingwei Wang,[‡,§,⊥,¶] Mitch André Garcia,[‡,§,⊥,¶] Xing-Zhong Zhao,[▽] Clifton K.-F. Shen,[‡,§,⊥,*] and Hsian-Rong Tseng[‡,§,⊥,¶,*]

[†]College of Electronics and Information Engineering, Wuhan Textile University, Wuhan, 430073, China, [‡]Crump Institute for Molecular Imaging, [§]California NanoSystems Institute, [⊥]Department of Molecular and Medical Pharmacology, [¶]Institute for Molecular Medicine, University of California, Los Angeles, California 90095, United States, [#]Center for Molecular Imaging, Institute of Molecular Medicine, University of Texas Health Science Center at Houston, 1825 Pressler Street SRB 330A, Houston, Texas 77030, United States, and [▽]Department of Physics, School of Physics, Center of Nanoscience and Nanotechnology, Wuhan University, Wuhan, 430072, China. [○]These authors contributed equally to the work.

ABSTRACT Nanoparticles are regarded as promising transfection reagents for effective and safe delivery of nucleic acids into a specific type of cells or tissues providing an alternative manipulation/therapy strategy to viral gene delivery. However, the current process of searching novel delivery materials is limited due to conventional low-throughput and time-consuming multistep synthetic approaches. Additionally, conventional approaches are frequently accompanied with unpredictability and continual optimization refinements, impeding flexible generation of material diversity creating a major obstacle to achieving high transfection performance. Here we have demonstrated a rapid developmental pathway toward highly efficient gene delivery systems by leveraging the powers of a supramolecular synthetic approach and a custom-designed digital microreactor. Using the digital microreactor, broad structural/functional diversity can be programmed into a library of DNA-encapsulated supramolecular nanoparticles (DNA⊂SNPs) by systematically altering the mixing ratios of molecular building blocks and a DNA plasmid. *In vitro* transfection studies with DNA⊂SNPs library identified the DNA⊂SNPs with the highest gene transfection efficiency, which can be attributed to cooperative effects of structures and surface chemistry of DNA⊂SNPs. We envision such a rapid developmental pathway can be adopted for generating nanoparticle-based vectors for delivery of a variety of loads.

KEYWORDS: supramolecular nanoparticle · gene delivery · digital microreactor · combinatorial library · cyclodextrin · molecular recognition

Gene delivery constitutes one of the most critical steps in gene manipulation and therapy.[1,2] By mimicking the size and function of viral vectors, numerous nonviral gene delivery systems based on biocompatible nanostructured materials,[3−5] for example, inorganic nanoparticles,[6−9] carbon nanotubes,[10] liposomes,[11] cationic polymers[12,13] and dendrimers,[14] have been developed to provide an alternative approach to the problems in viral gene delivery. However, an emerging challenge of nanoparticle-based delivery reagents is their low transfection performance.[3] To overcome this problem researchers have attempted to modulate[15] the structural (sizes[16] and shapes) and functional (surfaces chemistry and charges) properties of nanoparticles,[15] often requiring multiple optimization cycles to gradually improve the performance of nanoparticle-based delivery reagents. Such procedures have proven to be time-intensive and have demonstrated limited diversity over the past decades. Alternatively, it is believed that exploration of a new developmental pathway capable of rapid and parallel programming of a combinatorial library of nanoparticle-based delivery systems could lead to revolutionary breakthroughs in nanoparticle-based delivery systems.

Herein, we describe a rapid developmental pathway (Figure 1) that leverages the powers of (i) a combinatorial synthetic approach (Figure 1a) based on supramolecular assembly[17−19] and (ii) a digital microreactor[20,21] (Figure 1b-d), toward the generation of a highly efficient nanoparticle-based gene delivery system. Unlike the slow, multistep syntheses employed for producing existing gene-delivery materials,[3] our supramolecular method (Figure 1a) enables a convenient, flexible, and modular method[22] for generating a combinatorial library of DNA⊂SNPs, in which a broad structural/functional diversity covering the size variation, surface chemistry, and DNA loading capacity was programmed

*Address correspondence to kshen@mednet.ucla.edu, hrtseng@mednet.ucla.edu.

Received for review August 4, 2010 and accepted September 24, 2010.

Published online October 6, 2010. 10.1021/nn101908e

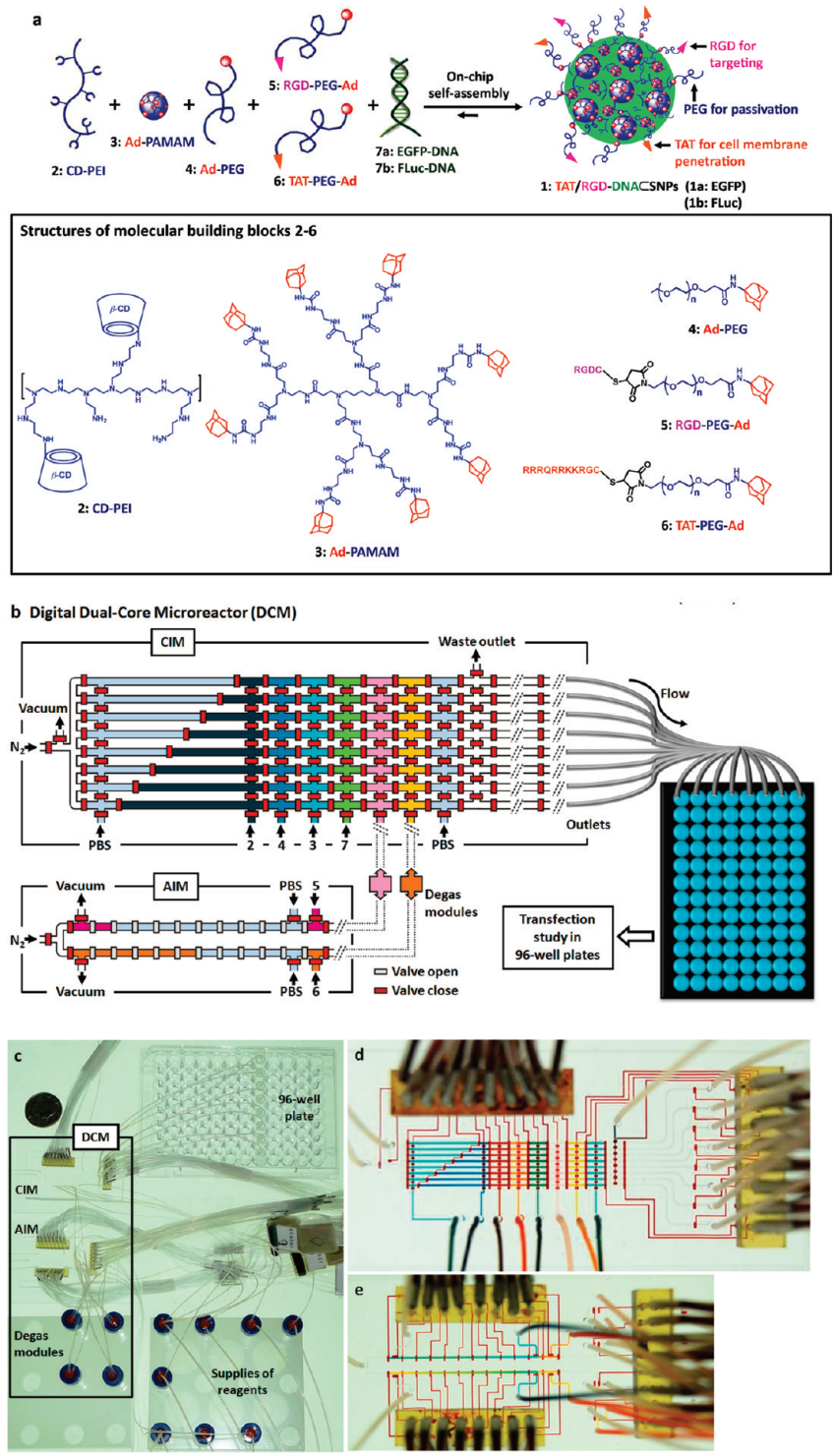

Figure 1. A rapid developmental pathway that leverages the powers of (i) a combinatorial synthetic approach based on supramolecular assembly and (ii) an automated microreactor has been demonstrated for screening and production of a highly efficient nanoparticle-based gene delivery system. (a) Graphical schematic representations of the self-assembly approach for producing a combinatorial library of DNA encapsulated supramolecular nanoparticles (DNA⊂SNPs), in which a broad structural/functional diversity can be programmed into individual DNA⊂SNPs (1) by systematically altering the mixing ratios of the five functional molecular building blocks, *i.e.*, CD-PEI (2), Ad-PAMAM(3), Ad-PEG (4), RGD-PEG-Ad (5), and TAT-PEG-Ad (6), as well as DNA plasmid ((7a) enhanced green fluorescent protein (EGFP) and (7b) firefly luciferase (FLuc)). (b) Graphical illustration of a digital Dual-Core Microreactor (DCM). The device settings are composed of a central integrated mixer (CIM), an auxiliary integrated mixer (AIM), and degas modules bridges. The operation of the circuit was computer controlled using color-coded pressure-driven valves: red, positive pressure, off/on; yellow, peristaltic pumping; green, vacuum. Eight slugs containing eight different formulated DNA-encapsulated DNA⊂SNPs were generated in parallel and transferred to a 96-well plate through PTFE tubes. The gene transfection performance for each combination was evaluated by a plate reader. (c) The picture of the whole set of actual instrument. Panels (d) and (e) show optical images of the CIM and AIM, respectively. The various channels were loaded with dyes to visualize the different components.

into individual DNA⊂SNPs by systematically altering the mixing ratios of five functional molecular building blocks (**2**−**6**), DNA plasmid (**7a**, enhanced green fluorescent protein (EGFP), and **7b**, firefly luciferase (FLuc)). To reduce human operational errors, accelerate handling procedures, enhance experimental fidelity, and achieve economical use of reagents, a digital Dual-Core Microreactor (DCM, Figure 1b−d) was designed and implemented to allow automated sampling, dilution, metering, and mixing of **2**−**7**, resulting in a combinatorial library composed of 648 different DNA⊂SNPs within 2.5 h. The structural/functional diversity of the DNA⊂SNPs library can be translated into diversity in performance by conducting transfection studies of individual DNA⊂SNPs in 96 well plates containing mouse fibroblast cells. A small group of DNA⊂SNPs that facilitates high levels of delivery performance was identified. We then carried out comprehensive characterizations on these DNA⊂SNPs revealing that improved transfection performance can be attributed to the defined size, surface chemistry, zeta potential, uniformity, and dynamic stability. Compared to the leading gene transfection reagents, such as lipofectamine 2000 and RGD-jet-PEI, the identified 40-nm TAT/RGD-DNA⊂SNPs (**1**) with defined surface chemistry (RGD,[23−26] a $\alpha_v\beta_3$ binding peptide and TAT[27−29] a cell-penetrating peptide) exhibited significantly improved gene transfection efficiency and low toxicity in a number of cancer cell lines and fibroblast cells.

RESULTS AND DISCUSSION

The five molecular building blocks (Figure 1a), CD-PEI (**2**), Ad-PAMAM (**3**), Ad-PEG (**4**), RGD-PEG-Ad (**5**), and TAT-PEG-Ad (**6**), were prepared according to literature,[17,22] otherwise, see Supporting Information. The functions of the five molecular building blocks are summarized below. First, the complementary CD-PEI (**2**) and Ad-PAMAM (**3**) are responsible for constructing cationic hydrogel networks that can encapsulate anionic DNA (**7**) forming the cores of DNA⊂SNPs. Therefore, the DNA loading capacity of DNA⊂SNPs is dependent on the net positive charges embedded in the hydrogel networks. By using electrophoresis analysis and ethidium bromide exclusion assay,[22] the nitrogen/phosphate (N/P) ratio above five was determined. Second, Ad-PEG (**4**) serves as a capping/solvation reagent that not only constrains continuous growth of the DNA-encapsulated hydrogel networks but also confers desired water solubility, structural stability, and passivation performance to the resulting DNA⊂SNPs. Third, the two functional ligands (**5** and **6**) can be incorporated onto the surfaces of DNA⊂SNPs *via* dynamic exchange in order to enable delivery specificity (to recognize a certain population of cells with $\alpha_v\beta_3$-integrin receptors) and cell transfusion capability (to foster internalization through membrane) of the resulting DNA⊂SNPs, respectively. By systematically altering the mixing ratios among the five molecular building blocks (**2**−**6**) and DNA (**7**), distinct structural/functional properties (*i.e.*, sizes and surface chemistry) can be programmed into individual DNA⊂SNPs in the combinatorial library. It is important to point out that, in contrast to the lipid-like gene delivery system where the diversity was built upon the binary combination of a plethora of molecular precursors,[30,31] the diversity of our DNA⊂SNPs library was generated by ratiometric combination of only the five molecular building blocks and DNA loading.

It is feasible to manually prepare the DNA⊂SNPs library by pipetting and mixing individual molecular building blocks and DNA plasmid at different ratios, while potential operation errors, slow handling speed, and a significant amount of sample consumption might compromise the throughput, fidelity, and efficiency of the study. Digital microfluidic reactors[32−35] are promising platforms to overcome these challenges. In our case, an oil-free, digital DCM (Figure 1b−d) composed of (i) a central integrated mixer (CIM) and (ii) an auxiliary integrated mixer (AIM), was designed and implemented to systematically program the structural/functional diversity into the DNA⊂SNPs libraries.

As illustrated in Figure 1b, there are eight parallel microchannels in CIM, capable of parallel generation of eight slugs with different mixing ratios of **2**−**7**. Each microchannel was partitioned by hydraulic-actuated microvalves into nine confined plug regions, which were assigned for precise metering of five molecular building blocks (**2**−**6**), a DNA plasmid, (**7a**, EGFP or **7b**, FLuc) and phosphate buffered saline (PBS). AIM incorporates a pair of fractionally partitioned microchannels, capable of synchronized supply of functional ligands (**5** and **6**) at different concentrations. CIM and AIM were coupled together by a pair of degas modules (Supporting Information) that remove gas through liquid transferring processes.

By using the digital DCM, the automated preparation of DNA⊂SNPs library was achieved by systematically modulating the mixing ratios of CD-PEI (**2**), RGD-PEG-Ad (**5**), and TAT-PEG-Ad (**6**), against fixed amounts of Ad-PAMAM (**3**), Ad-PEG (**4**), and plasmid DNA (**7**). In CIM, constant concentrations of **3** (3.0 μM), **4** (60.0 μM), and **7** (100 ng/μL) were assigned to fill into plug regions (*ca.* 20 nL per region). To adjust the quantities of CD-PEI (**2**), the eight uneven partitioned plug regions on the west side of CIM were utilized to accommodate different volumes of **2** (4.0 μM, 10−80 nL). The concentration modulation of the two functional ligands (**5** and **6**) was accomplished in AIM, where each fractionally partitioned microchannel is responsible for ratiometric mixing of the respective ligand (**5**, 0−9.6 μM; **6**, 0−12.0 μM) with PBS. In each operation cycle, CIM generate eight 200-nL slugs containing different precursor mixtures, which were introduced into 96-well plates by nitrogen through eight poly(tetrafluoroethylene) (PTFE) tubes attached at the east side of CIM. To produce suf-

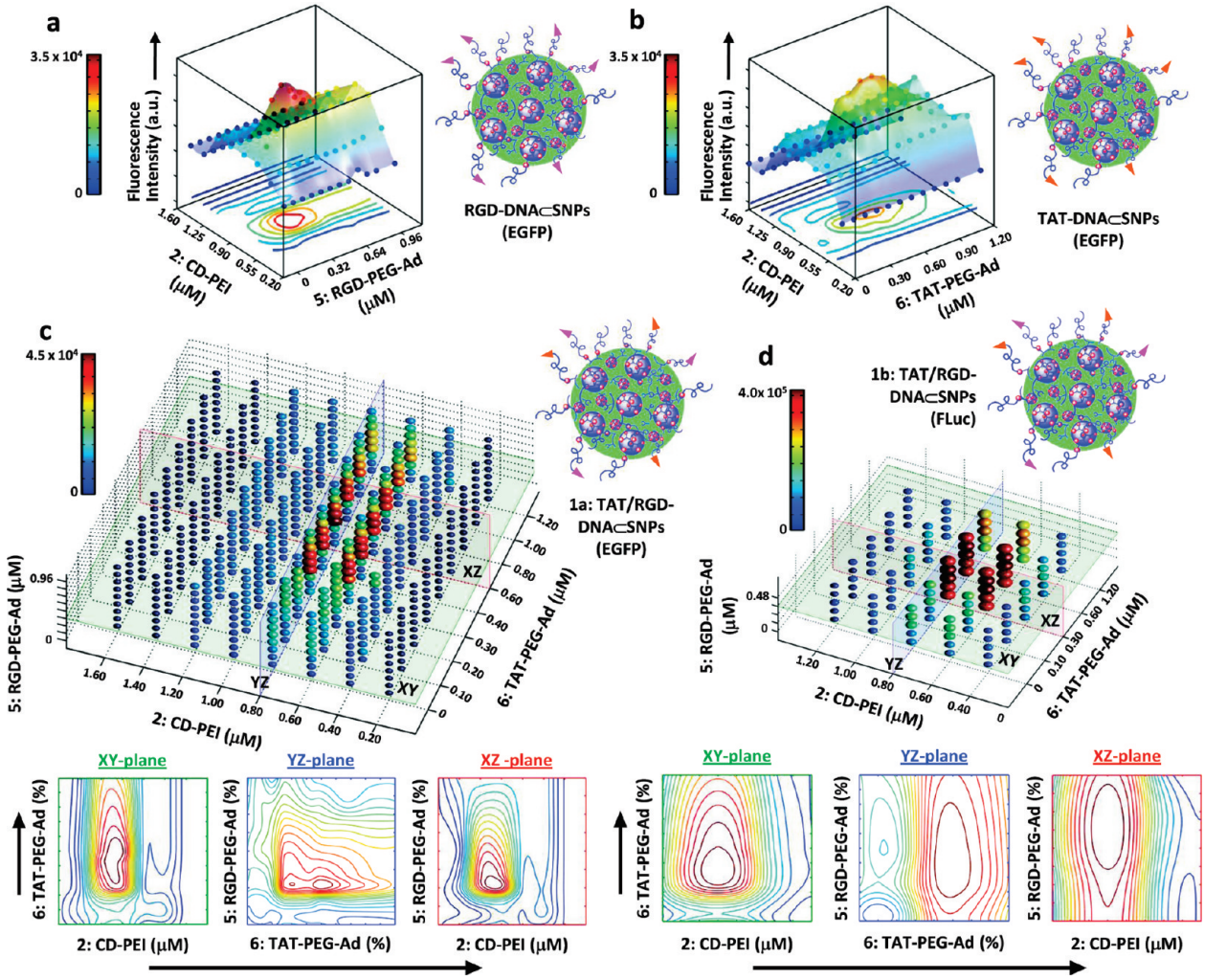

Figure 2. (a) A 3D profile of gene transfection performance of RGD-DNA⊂SNPs (EGFP) with variation of CD-PEI (2) and RGD coverage (96 data points). (b) A 3D profile of gene transfection performance of TAT-DNA⊂SNPs (EGFP) with variation of CD-PEI (2) and TAT coverage (96 data points). (c) A 4D profile of gene transfection performance of TAT/RGD-DNA⊂SNPs (EGFP) with variation of CD-PEI (2), TAT and RGD coverages (648 data points). The XY, YZ, and XZ plates across the best performance were simplified and denoted 2D contour images. (d) A 4D profile of gene transfection performance of TAT/RGD-DNA⊂SNPs (FLuc) with variation of CD-PEI (2), TAT, and RGD coverages (125 data points). The XY, YZ, and XZ plates across the best performance were simplified and denoted 2D contour images.

ficient quantity of DNA⊂SNPs for subsequent transfection studies, 50 cycles were performed continuously in CIM within 90 s, affording eight different DNA⊂SNP solutions (*ca.* 10 μL each, 100 ng DNA). (See the movie clip and Supporting Information). The resulting DNA⊂SNPs libraries were incubated in the 96-well plates for 20 min at room temperature prior to transferring to the 96-well plates containing NIH 3T3 cells (*ca.* 8000 cells/well) for transfection studies in parallel. The gene transfection efficiency was evaluated by a plate reader after culturing the cells at 37 °C (5% CO_2) for 24 h.

In proof-of-concept trials a CMV promoter-driven EGFP-encoded plasmid DNA was encapsulated into the DNA⊂SNPs. Before a full-scale screening with three variables (*i.e.*, CD-PEI (**2**), RGD-PEG-Ad (**5**), and TAT-PEG-Ad (**6**)), simplified studies on two pairs of variables (*i.e.*, CD-PEI (**2**) *vs* RGD-PEG-Ad (**5**) and CD-PEI (**2**) *vs* TAT-PEG-Ad (**6**)) were conducted in search of the optimal transfection performance of RGD-DNA⊂SNPs and TAT-DNA⊂SNPs, respectively. The transfection outcomes (96 data points in each case) were fitted into two 3-dimensional (3D) profiles (Figure 2a and b). The full-scale screening was accomplished by systematically programming the three variables, that is, eight different concentrations for CD-PEI (**2**), nine for RGD-PEG-Ad (**5**), and nine for TAT-PEG-Ad (**6**). Using the digital DCM, a combinatory library composed of 648 different DNA⊂SNPs was generated within 2.5 h to fill up seven 96-well plates. To ensure the operation fidelity, all the experiments were conducted in triplicate. A 4D gene expression plot was employed to summarize the results from the full-scale screening of the combinatorial library revealing that the optimal transfection performance of DNA⊂SNPs was achieved at CD-PEI (**2**) concentration of 0.6−0.8 μM, a RGD-PEG-Ad (**5**) of 0.24−0.48 μM, and TAT-PEG-Ad (**6**) of 0.4−0.8 μM. We also note the transfection performance of the TAT/RGD-DNA⊂SNPs (**1a**) is significantly improved compared

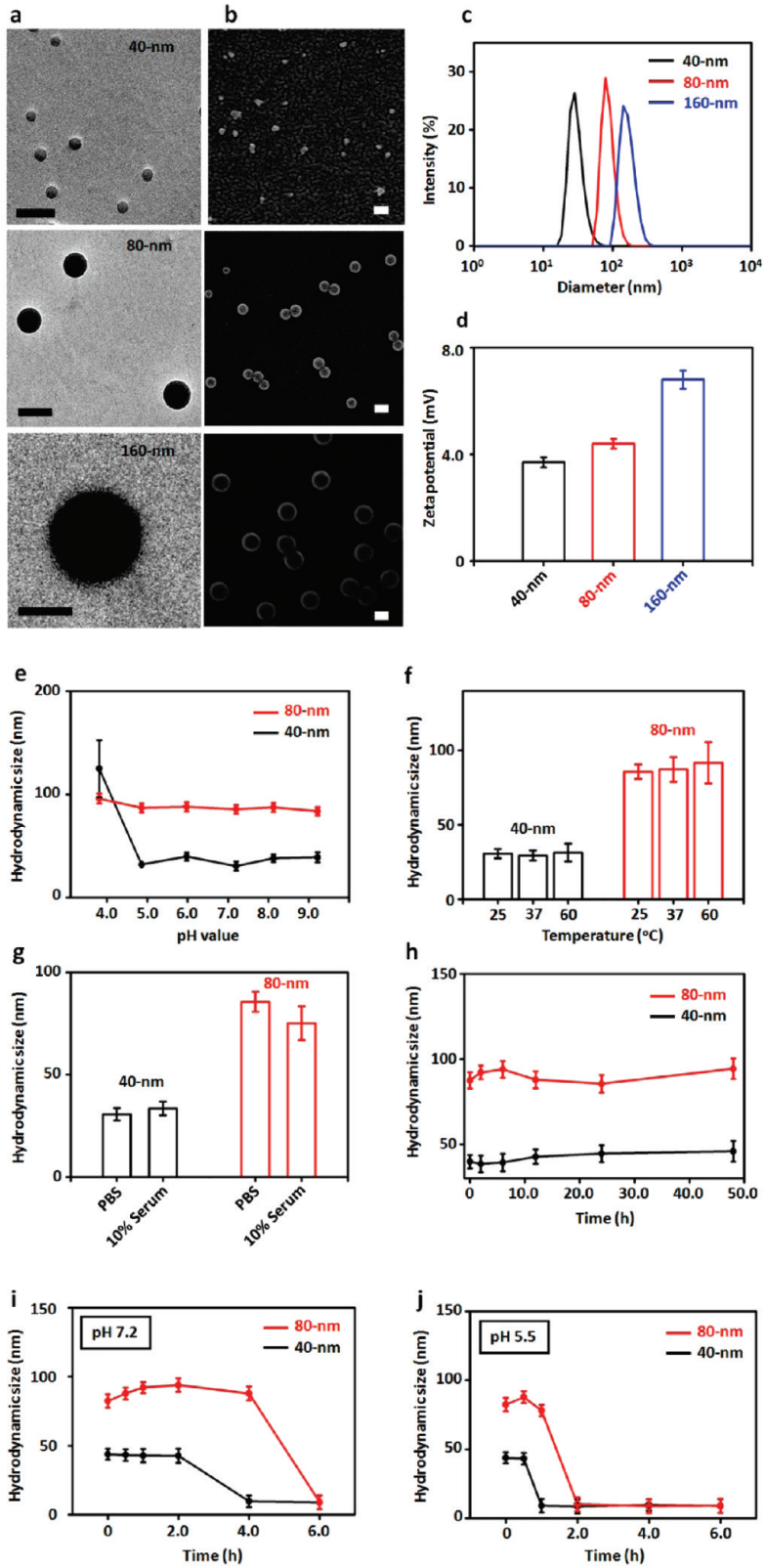

Figure 3. (a and b) TEM and SEM images of the resulting TAT/RGD-DNACSNPs with different sizes of 42 ± 4, 86 ± 9, and 160 ± 13 nm. Scale bars: 100 nm. (c) Dynamic light scattering (DLS) was employed to measure DNACSNPs hydrodynamic sizes in PBS buffer. (d) Zeta potentials variations of DNACSNPs in PBS buffer. Stability studies of 40- and 80-nm DNACSNPs under different conditions: (e) pH-dependent size variations of DNACSNPs in the respective buffer solutions with pH values ranging from 3.8 to 9.2. Error bars are obtained from three measurements. (f) Temperature-dependent size variation of DNACSNPs in PBS buffer (pH = 7.2) with different temperatures at 25, 37, and 60 °C. (g) Size variations of DNACSNPs in presence and absence of 10% serum containing PBS buffer after 4 h incubation. Error bars are obtained from three measurements. (h) Time-dependent size variation of DNACSNPs from 0−48 h in PBS (pH 7.2). (i and j) Time-dependent dynamic stability of DNACSNPs under dialysis at pH 5.5 and 7.2, respectively.

TABLE 1. Comparison of TAT/RGD-DNA⊂SNPs Synthesized by DCM and Conventional Pipetting

	DCM	pipetting[22]
throughput	250 conditions/h	<20 conditions/h
size distribution	excellent (PDI[a]: <0.05)	good (PDI[a]: 0.10−0.20)
operation error	no	possible
reproducibility	high	modest

[a]PDI: The polydispersity index obtained from DLS measurements.

with those observed for RGD-DNA⊂SNPs and TAT-DNA⊂SNPs. To validate the general applicability of this developmental pathway, we performed a relatively smaller screening to identify DNA⊂SNPs capable of highly efficient delivery of FLuc-encoded plasmid DNA. We manipulated three variables (5 × 5 × 5 concentrations) resulting in a combinatorial library of 125 different TAT/RGD-DNA⊂SNPs (**1b**). The consistent results (Figure 2d) were observed for the transfection performance of TAT/RGD-DNA⊂SNPs (**1b**) for delivering FLuc-DNA plasmid. All four sets of screening studies suggested that the TAT/RGD-DNA⊂SNPs (**1**) composed of CD-PEI (**2**, 0.7 ± 0.1 μM), RGD-PEG-Ad (**5**, 0.28 ± 0.04 μM), and TAT-PEG-Ad (**6**, 0.60 ± 0.20 μM) show the best transfection performance.

To understand how the identified synthetic variables contribute to the optimal transfection performance we scaled up the production of TAT/RGD-DNA⊂SNPs (**1a**) under three sets of synthetic variables for characterization at three CD-PEI (**2**) concentrations (0.6, 0.8, and 1.2 μM) while keeping concentrations of the RGD-PEG-Ad (0.28 μM) and TAT-PEG-Ad (0.60 μM) constant. We realize that CD-PEI (**2**) concentration affects the cross-linking degrees of the CD-PEI/Ad-PAMAM hydrogel cores in TAT/RGD-DNA⊂SNPs (**1**), leading to the size variation. Both transmission electron microscopy (TEM, Figure 3a) and scanning electron microscopy (SEM, Figure 3b) were employed to examine the morphology and sizes of the resulting TAT/RGD-DNA⊂SNPs (**1**). Three distinct sizes of 42 ± 4, 86 ± 9, and 160 ± 13 nm were observed for those produced at CD-PEI (**2**) concentrations of 0.6, 0.8, and 1.2 μM, respectively. Interestingly, we also noticed that the size distributions of the DCM-produced DNA⊂SNPs are much narrower than those prepared manually (Table 1), and these results were confirmed by dynamic light scattering (Zetasizer Nano, Malvern Instruments Ltd.) measurements (Figure 3c). We attribute the greater control upon DNA⊂SNP size distribution to the precision and reproducibility of the sampling, metering, and mixing processes in the digital DCM. In addition, no significant size variations were observed by introducing different concentrations ranging from 0 to 1.2 μM of ligands (**5** and/or **6**). We also characterized the surface potentials of these TAT/RGD-DNA⊂SNPs (Figure 3d), which spanned a range of 3.7 ± 0.2 − 6.8 ± 0.3 mV. In addition, the actual surface coverages of RGD-PEG-Ad (**5**) and TAT-PEG-Ad (**6**) were estimated by measuring absorption intensity of a FITC-labeled analogue (*i.e.*, FITC-PEG-Ad)[22] on the DNA⊂SNPs prepared by the respective synthetic parameters (see Supporting Information). The results indicated that 0.28 and 0.60 μM of RGD-PEG-Ad (**5**) and TAT-PEG-Ad (**6**) reflect 5 and 9% of surface coverage on the resulting DNA⊂SNPs, respectively. In short, TAT/RGD-DNA⊂SNPs (**1**) with sizes of 40 and 80 nm, as well as 5% RGD-PEG-Ad (**5**) and 9% TAT-PEG-Ad (**6**) coverages[22] exhibited optimal cell transfection performance. Finally, to understand the dynamic stability of 40- and 80-nm TAT/RGD-DNA⊂SNPs (**1**) we employed real-time DLS measurements to monitor their size variation (i) at different pH values (pH 3.8−9.2) and temperatures (25, 37, and 60 °C), (ii) in the presence of 10% serum, and (iii) at different storage times in the presence of physiological salt concentrations (Figure 3e−h). The stability of the TAT/RGD-DNA⊂SNPs (**1**) can be attributed to the multivalent CD/Ad recognition and electrostatic interactions between Ad-PAMAM/CD-PEI hydrogel and DNA. To study the role of Ad-PEG (**4**) for dynamic stability of DNA⊂SNPs we monitored the size variation of DNA⊂SNPs (Figure 3i,j) by removing the excess amount of Ad-PEG (**4**) in the mixture through membrane dialysis (MWCO 10kD) under pH 5.5 and 7.2. It was found that the 40- and 80-nm TAT/RGD-DNA⊂SNPs (**1**) were disassembled gradually within 6 h at both pH conditions. In addition, the TAT/RGD-DNA⊂SNPs (**1**) exhibited faster disassembly behavior at pH 5.5 (<2 h) than at pH 7.2, which allows the TAT/RGD-DNA⊂SNPs (**1**) efficiently degraded inside the endosomes and released the DNA intracelluarly.[36]

To compare the transfection performance of the optimal 40-nm TAT/RGD-DNA⊂SNPs (**1**) with the leading transfection reagents (*i.e.*, RGD-jet-PEI and lipofectamine 2000) we carried out the dose-dependent gene transfection studies in 24-well plates with encapsulated-DNA (50 and 1000 ng per well) by using a collection of cells, including NIH 3T3 (mouse fibroblast cell line), HeLa (human cervix epithelial carcinoma cell line), A549 (human lung cancer cell line), U87 (human glioblastoma cell line), MCF7 (human breast adenocarcinoma cell line), PC3 (human prostate cancer cell line), and IMR-90 (human fibroblast cell line). The gene transfection studies results (Figure 4a and b) indicated that the 40-nm TAT/RGD-DNA⊂SNPs (**1**) exhibited significantly improved transfection performance compared to those observed for RGD-jet-PEI and lipofectamine 2000 across the different cancer and fibroblast cell lines at high dosage of DNA (1000 ng DNA per well). Higher than 70% transfection efficiencies were observed across various cancer cell lines we tested, even for the PC3 cell line that is difficult to be transfected by those two commercial reagents. IMR-90, one of the hard-to-transfect human fibroblast cell lines, was tested and

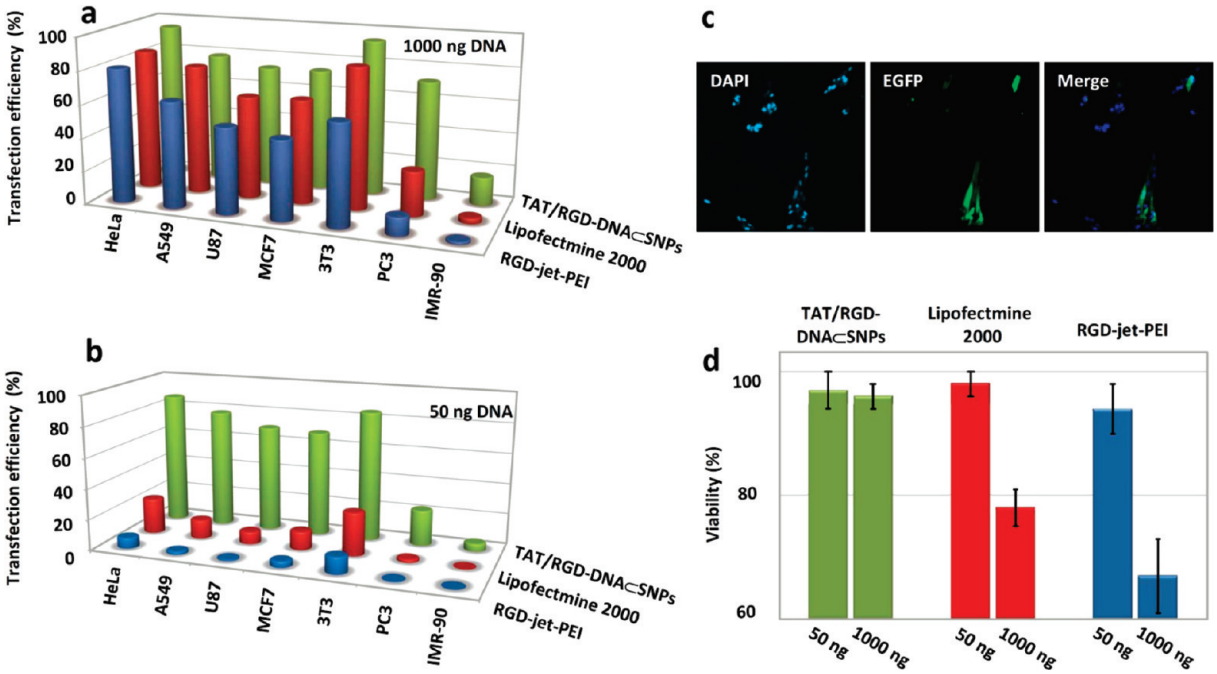

Figure 4. (a and b) Transfection efficiencies of the optimal 40-nm TAT/RGD-DNA⊂SNPs at high (1000 ng DNA per well) and low (50 ng DNA per well) DNA dosage along with control delivery reagents (lipofectamine 2000 and RGD-jet-PEI) for a collection of cell lines, including NIH 3T3 (mouse fibroblast cell line), HeLa (human cervix epithelial carcinoma cell line), A549 (human lung cancer cell line), U87 (human glioblastoma cell line), MCF7 (human breast adenocarcinoma cell line), PC3 (human prostate cancer cell line), and IMR-90 (human fibroblast cell line) in 24-well plates. (c) The representative fluorescence micrographs of IMR-90 cells transfected by 40-nm TAT/RGD-DNA⊂SNPs at high dosage of DNA (1000 ng DNA/well). (d) Cytotoxicity of RGD-jet-PEI, lipofectamine 2000 and 40-nm TAT/RGD-DNA⊂SNPs at high and low dosage of DNA transfected NIH 3T3 cells determined by cell viability assay after 48 h of transfection.

the transfection efficiency of DNA⊂SNPs toward IMR-90 cells reached to 17 ± 7%, which can be visualized by the fluorescence micrographs (Figure 4c). The transfection efficiency of 40-nm TAT/RGD-DNA⊂SNPs (**1**) for IMR-90 cells is 11-fold and 5-fold higher than that of RGD-jet-PEI and lipofectamine 2000, respectively. It is important to note that 40-nm TAT/RGD-DNA⊂SNPs (**1**) still achieved high transfection efficiency at low dosage of DNA (50 ng per well), indicating the outstanding gene delivery ability of DNA⊂SNPs. Moreover, the cell viability assay results indicated that the 40-nm TAT/RGD-DNA⊂SNPs (**1**) exhibited negligible cytotoxicity. More than 96 ± 3% of DNA⊂SNPs-transfected cells showed normal viability even in the presence of high dosage of reagent (1000 ng DNA per well). In contrast, at high DNA dose more than 34% and 22% NIH 3T3 cells died after treatment by RGD-jet-PEI and lipofectamine 2000 for 48 h (Figure 4d).

CONCLUSION

In conclusion, we have demonstrated a rapid developmental pathway toward generation of a highly efficient gene delivery system by leveraging the powers of a supramolecular synthetic approach and a custom-designed digital microreactor. This pathway can be adopted for the development of nanoparticle-based vectors capable of delivering a variety of loads, such as gene, drugs, proteins, and their mixtures. We are currently exploring the use of the DNA⊂SNP-based transfection reagents for reprogramming of human primary fibroblast cells in order to generate induced pluripotent stem cells that are crucial in the field of regulative medicine.[38]

EXPERIMENTAL SECTION

General. Reagents and solvents were purchased from Sigma-Aldrich (St. Louis, MO) and used as received without further purification or otherwise noted. Branched polyethylenimine (PEI, MW = 10 kD) was purchased from Polysciences, Inc. (Washington, PA). The polymers contain primary, secondary, and tertiary amine groups in approximately 25/50/25 ratio. First-generation polyamidoamine dendrimer (PAMAM) with 1,4-diaminobutane core and amine terminals in 20 wt % methanol solution was purchased from Dendritic Nanotechnologies, Inc. (Mount pleasant, MI). 1-Adamantanamine (Ad) hydrochloride and β-cyclodextrin (β-CD) were purchased from TCI America (San Francisco, CA). *N*-Hydroxysuccinimide (SCM) and maleimido (MAL) heterofunctionalized polyethylene glycol (SCM-PEG-MAL, MW = 5 kD) was obtained from NANOCS, Inc. (New York, NY). Phosphate-buffered saline (PBS, 1X, pH = 7.2 ± 0.05) for sample preparation. 6-Monotosyl-β-cyclodextrin (6-OTs-β-CD) was prepared following the literature reported method.[37] Octa-Ad-grafted polyamidoamine dendrimer (Ad-PAMAM), CD-grafted branched polyethylenimine (CD-PEI), and Ad-grafted polyethylene glycol (Ad-PEG) were prepared as described in a previous method.[17] Dry CH_2Cl_2 was obtained by refluxing over CaH_2 and was freshly dis-

tilled before use. NIH 3T3 (mouse embryonic fibroblast cell line), HeLa (human cervix epithelial carcinoma cell line), A549 (human lung cancer cell line), U87 (human glioblastoma cell line), MCF7 (human breast adenocarcinoma cell line), PC3 (human prostate cancer cell line), and IMR-90 (human primary fibroblasts cell line) were purchased from American Type Culture Collection (ATCC). The Dulbecco's Modified Eagle Medium (DMEM), Earl's Modified Eagle's Medium (EMEM) growth medium, RPMI-1640, Opti-MEM reduced serum medium, and penicillin/streptomycin were obtained from Invitrogen (Carlsbad, CA). Fetal bovine serum (FBS) and EGFP-encoded plasmid DNA (pMAX EGFP, 4.3 kb) and luciferase-encoded plasmid DNA (FLuc-DNA, 6.6 kb) were obtained from Lonza Walkerrsville, Inc. (Walkerrsville, MD). 4′,6-Diamidino-2-phenylindole (DAPI) was purchased from Invitrogen (Carlsbad, CA). RGD (RGDC) and TAT peptides (CGRKKRRQRRR) were purchased from GenScript Corp. (Piscataway, NJ).

^{1}H NMR spectra were recorded on a Bruker Avance 400 spectrometer in deuterated solvents. Mass spectra were acquired using an Applied Biosystems Voyager DE-STR MALDI-TOF mass spectrometer (Framingham, MA). Dynamic light scattering and zeta potentials of DNA⊂SNPs (**1**) were measured on Zetasizer Nano instrument (Malvern Instruments Ltd., United Kingdom). Transmission electron microscope (TEM) images were measured on Philips CM 120 electron microscope operating with an acceleration voltage of 120 kV. SEM images of DNA⊂SNPs (**1**) were obtained with a JEOL JSM-6700F SEM. Freeze-dried samples on a silicon surface were sputter-coated with gold before measurement. Cell imaging and gene transfection studies were performed on a Nikon TE2000S inverted fluorescent microscope with a CCD camera (Photomatrix, Cascade II), X-Cite 120 Mercury lamp, automatic stage, and filters for three fluorescent channels (W1 (DAPI), W2 (EGFP and AO) and W3 (PI)).

The Fabrication and Operations of Digital Dural Core Microreactor (DCM). The fabrication and operations of Digital Dural Core Microreactor (DCM) are described in the Supporting Information.

Programming Supramolecular Nanoparticles in a Digital Dual-Core Microreactor. By using the digital DCM, two 3D and two 4D screenings were performed sequentially. In Figure 2a, 96 different RGD-DNA⊂SNPs were generated by altering concentrations of CD-PEI (0.2, 0.4, 0.6, 0.8, 1.0, 1.2, 1.4, and 1.6 μM) and RGD-Ad-PEG (0, 0.08, 0.16, 0.24, 0.32, 0.40, 0.48, 0.56, 0.64, 0.72, 0.80, 0.88, and 0.96 μM). In Figure 2b, 96 different TAT-DNA⊂SNPs were generated by altering concentrations of CD-PEI (0.2, 0.4, 0.6, 0.8, 1.0, 1.2, 1.4, and 1.6 μM) and TAT-Ad-PEG (0, 0.10, 0.20, 0.30, 0.40, 0.50, 0.60, 0.70, 0.80, 0.90, 1.00, 1.10, and 1.20 μM). In Figure 2c, 648 different TAT/RGD-DNA⊂SNPs (**1a**) were generated by altering concentrations of CD-PEI (0.2, 0.4, 0.6, 0.8, 1.0, 1.2, 1.4, and 1.6 μM), TAT-Ad-PEG (0, 0.10, 0.20, 0.30, 0.40, 0.60, 0.80, 1.00, and 1.20 μM) and RGD-Ad-PEG (0, 0.08, 0.16, 0.24, 0.32, 0.48, 0.64, 0.80, and 0.96 μM). In Figure 2d, 125 different TAT/RGD-DNA⊂SNPs (**1b**) were generated by altering concentrations of CD-PEI (0.4, 0.6, 0.8, 1.0, and 1.2 μM), TAT-Ad-PEG (0, 0.10, 0.30, 0.60, and 1.20 μM), and RGD-Ad-PEG (0, 0.16, 0.24, 0.32, and 0.48 μM).

Dynamic Light Scattering (DLS). DLS experiments were performed with a Zetasizer Nano instrument (Malvern Instruments Ltd., United Kingdom) equipped with a 10-mW helium−neon laser (λ = 632.8 nm) and thermoelectric temperature controller. Measurements were taken at a 90° scattering angle. The sizes and the standard derivations of assembled TAT/RGD-DNA⊂SNPs (**1**) were calculated by averaging the values of at least three measurements.

Transmission Electron Microscope (TEM). The morphology and sizes of TAT/RGD-DNA⊂SNPs were directly examined using transmission electron microscope. The studies were carried out on a Philips CM 120 electron microscope, operating at an acceleration voltage of 120 kV. The TEM samples were prepared by drop-coating 2 μL of TAT/RGD-DNA⊂SNPs solutions onto carbon-coated copper grids. Excess amounts of slugs were removed by filter papers after 45 s. Subsequently, the surface-deposited TAT/RGD-DNA⊂SNPs were negatively stained with 2% uranyl acetate for 45 s before the TEM studies.

Scanning Electron Microscope (SEM). We prepared the TAT/RGD-DNA⊂SNPs samples for SEM observation by a standard procedure: Briefly, 2 μL of TAT/RGD-DNA⊂SNPs solution was drop-coated onto silica substrate and freeze-dried by dry ice. Then, the samples were sputter coated with gold before examination with a Hitachi S800 field emission SEM at an accelerating voltage of 10 keV.

Zeta Potential Measurements. Zeta potentials of TAT/RGD-DNA⊂SNPs (**1**) were determined by photon correlation spectroscopy using a Zetasizer Nano instrument, (Malvern Instruments, Malvern, Worcestershire, UK). The measurements were performed at 25 °C with a detection angle of 90°, and the raw data were subsequently correlated to *Z* average mean size using a cumulative analysis by the Zetasizer software package.

Stability Studies of 40 and 80-nm TAT/RGD-DNA⊂SNPs. ***Stability of 40 and 80-nm TAT/RGD-DNA⊂SNPs in Different pH Values.*** Information on the stability of TAT/RGD-DNA⊂SNPs in variable pH environments is needed to understand its characteristics under physiological conditions and to provide a reasonable pH range for chemical modification of TAT/RGD-DNA⊂SNPs for further experiments. The pH-dependent stability of TAT/RGD-DNA⊂SNPs as a function of pH was tested at a range from 3.8 to 9.2 by DLS analysis. The stock solutions of 40- and 80-nm TAT/RGD-DNA⊂SNPs were prepared in PBS buffer containing monobasic potassium phosphate (I = 1.5 mM), sodium chloride (I = 155 mM), and dibasic sodium phosphate (I = 2.7 mM). The following buffers were used to adjust the pH values of the TAT/RGD-DNA⊂SNPs samples in the stock solution: 100 mM HCl-KCl buffer (pH 0−2.0), 100 mM Glycine-HCl buffer (pH 2.2−3.6), 100 mM $CH_3COOH-CH_3COONa$ buffer (pH 3.7−5.6), 100 mM $Na_2HPO_4-NaH_2PO_4$ buffer (pH 5.8−8.0), 100 mM Tris-HCl buffer (pH 7.0−9.0), and 100 mM $Na_2CO_3-NaHCO_3$ buffer (pH 9.2−10.8). Typically, a 100-μL portion of TAT/RGD-DNA⊂SNPs stock solution was mixed with a 900-μL portion of different pH value buffer solutions (I = 100 mM). The resulting solutions were shaken and equilibrated until the pH stabilized. The final pH values were determined by pH meter.

Stability of 40- and 80-nm TAT/RGD-DNA⊂SNPs under Different Temperatures. To understand the thermal stability of the TAT/RGD-DNA⊂SNPs we employed real-time DLS measurements to monitor the size variation of both of the 40- and 80-nm TAT/RGD-DNA⊂SNPs in PBS at 25, 37, and 60 °C. In each case the samples were equilibrated under a specific temperature for 20 min prior to data acquisitions.

Stability of 40 and 80-nm TAT/RGD-DNA⊂SNPs in 10% Serum. To understand the stability of the TAT/RGD-DNA⊂SNPs in the presence of serum we employed DLS measurements to observe the size variation of both of the 40- and 80-nm TAT/RGD-DNA⊂SNPs in the mixture of serum and PBS (1:9, V/V). The samples were kept at room temperature for 4 h prior to data acquisitions.

Stability of 40 and 80-nm TAT/RGD-DNA⊂SNPs under a Physiological Ionic Strength. To ensure the *in vivo* stability of the TAT/RGD-DNA⊂SNPs, it is critical to examine the size variation of them under a physiological ionic strength. The 40- and 80-nm TAT/RGD-DNA⊂SNPs were prepared in PBS solutions (pH = 7.2). We employed real-time DLS measurements to monitor the size variation of both of the 40- and 80-nm TAT/RGD-DNA⊂SNPs at different times. The TAT/RGD-DNA⊂SNPs sizes were recorded for 48 h.

Cell Culture. NIH 3T3, HeLa, A549, U87 and IMR-90 cell lines were routinely maintained in DMEM containing 10% fetal bovine serum (FBS) and 1% penicillin/streptomycin (Invitrogen, Carlsbad, CA). MCF7 was cultured in EMEM containing 10% fetal bovine serum (FBS) and 1% penicillin/streptomycin. PC3 was cultured in RPMI-1640 containing 10% fetal bovine serum (FBS) and 1% penicillin/streptomycin.

Gene Transfection Studies. Cells (5×10^4 cells/well) were plated in 24-well plates and allowed to adhere overnight. EGFP-encoded DNA was diluted in 1x TE buffer. The 40-nm TAT/RGD-DNA⊂SNPs were prepared on DCM and incubated for 20 min at room temperature before transfection experiments. The 40-nm TAT/RGD-DNA⊂SNPs in PBS (10 μL) was diluted with 100 μL Opti-MEM medium and subsequently transferred to each well. For the control groups, RGD-jet-PEI and lipofectamine 2000 were used as a standard transfection reagent and operated according to the protocol provided by the manufacturers. TAT/RGD-DNA⊂SNPs along with controls were incubated with the cells for 4 h then removed by aspirating, and replaced with 500 μL/well

of fresh culture media. Cells were allowed to grow for 24 h at 37 °C and 5% CO_2 and then fixed (4% paraformaldehyde for 15 min at room temperature), then washed with PBS three times, stained with DAPI, and finally rinsed with PBS prior to EGFP expression analysis by fluorescence microscope.

Acknowledgment. This research was supported by NIH-NCI NanoSystems Biology Cancer Center (U54CA119347), R21 Grant (EB008419-01), and California Institute of Regenerative Medicine (RT1-01022-1).

Supporting Information Available: Synthesis of TAT-PEG-Ad, DCM setup, and operation, microscope settings, imaging processing, and data analysis and cell viability assay. This material is available free of charge *via* the Internet at http://pubs.acs.org.

REFERENCES AND NOTES

1. Glover, D. J.; Lipps, H. J.; Jans, D. A. Towards Safe, Nonviral Therapeutic Gene Expression in Humans. *Nat. Rev. Genet.* **2005**, *6*, 299–310.
2. Kim, D. H.; Rossi, J. J. Strategies for Silencing Human Disease Using RNA Interference. *Nat. Rev. Genet.* **2007**, *8*, 173–84.
3. Davis, M. E.; Chen, Z.; Shin, D. M. Nanoparticle Therapeutics: An Emerging Treatment Modality for Cancer. *Nat. Rev. Drug Discovery* **2008**, *7*, 771–82.
4. Niemeyer, C. M. Nanoparticles, Proteins, And Nucleic Acids: Biotechnology Meets Materials Science. *Angew. Chem., Int. Ed.* **2001**, *40*, 4128–58.
5. Ferrari, M. Cancer Nanotechnology: Opportunities and Challenges. *Nat. Rev. Cancer* **2005**, *5*, 161–71.
6. De, M.; Ghosh, P. S.; Rotello, V. M. Applications of Nanoparticles in Biology. *Adv. Mater.* **2008**, *20*, 4225–41.
7. Nie, S. M.; Xing, Y.; Kim, G. J.; Simons, J. W. Nanotechnology Applications in Cancer. *Annu. Rev. Biomed. Eng.* **2007**, *9*, 257–88.
8. Torney, F.; Trewyn, B. G.; Lin, V. S. Y.; Wang, K. Mesoporous Silica Nanoparticles Deliver DNA and Chemicals into Plants. *Nat. Nanotechnol.* **2007**, *2*, 295–300.
9. Rosi, N. L.; Giljohann, D. A.; Thaxton, C. S.; Lytton-Jean, A. K. R.; Han, M. S.; Mirkin, C. A. Oligonucleotide-Modified Gold Nanoparticles for Intracellular Gene Regulation. *Science* **2006**, *312*, 1027–30.
10. Liu, Z.; Cai, W. B.; He, L. N.; Nakayama, N.; Chen, K.; Sun, X. M.; Chen, X. Y.; Dai, H. J. *In Vivo* Biodistribution and Highly Efficient Tumour Targeting of Carbon Nanotubes in Mice. *Nat. Nanotechnol.* **2007**, *2*, 47–52.
11. Tseng, Y. C.; Mozumdar, S.; Huang, L. Lipid-Based Systemic Delivery of siRNA. *Adv. Drug Delivery Rev.* **2009**, *61*, 721–31.
12. Yu, H. J.; Wagner, E. Bioresponsive Polymers for Nonviral Gene Delivery. *Curr. Opin. Mol. Ther.* **2009**, *11*, 165–78.
13. Woodrow, K. A.; Cu, Y.; Booth, C. J.; Saucier-Sawyer, J. K.; Wood, M. J.; Saltzman, W. M. Intravaginal Gene Silencing Using Biodegradable Polymer Nanoparticles Densely Loaded with Small-Interfering RNA. *Nat. Mater.* **2009**, *8*, 526–33.
14. Jang, W. D.; Selim, K. M. K.; Lee, C. H.; Kang, I. K. Bioinspired Application of Dendrimers: From Biomimicry to Biomedical Applications. *Prog. Polym. Sci.* **2009**, *34*, 1–23.
15. Mitragotri, S.; Lahann, J. Physical Approaches to Biomaterial Design. *Nat. Mater.* **2009**, *8*, 15–23.
16. Jiang, W.; Kim, B. Y. S.; Rutka, J. T.; Chan, W. C. W. Nanoparticle-Mediated Cellular Response Is Size-Dependent. *Nat. Nanotechnol.* **2008**, *3*, 145–50.
17. Wang, H.; Wang, S. T.; Su, H.; Chen, K. J.; Armijo, A. L.; Lin, W. Y.; Wang, Y. J.; Sun, J.; Kamei, K.; Czernin, J. A Supramolecular Approach for Preparation of Size-Controlled Nanoparticles. *Angew. Chem., Int. Ed.* **2009**, *48*, 4344–48.
18. Silva, G. A.; Czeisler, C.; Niece, K. L.; Beniash, E.; Harrington, D. A.; Kessler, J. A.; Stupp, S. I. Selective Differentiation of Neural Progenitor Cells by High-Epitope Density Nanofibers. *Science* **2004**, *303*, 1352–55.
19. Klajn, R.; Olson, M. A.; Wesson, P. J.; Fang, L.; Coskun, A.; Trabolsi, A.; Soh, S.; Stoddart, J. F.; Grzybowski, B. A. Dynamic Hook-and-Eye Nanoparticle Sponges. *Nat. Chem.* **2009**, *1*, 733–38.
20. Lee, C. C.; Sui, G. D.; Elizarov, A.; Shu, C. Y. J.; Shin, Y. S.; Dooley, A. N.; Huang, J.; Daridon, A.; Wyatt, P.; Stout, D. Multistep Synthesis of a Radiolabeled Imaging Probe Using Integrated Microfluidics. *Science* **2005**, *310*, 1793–96.
21. Lin, W.-Y.; Wang, Y.; Wang, S.; Tseng, H.-R. Integrated Microfluidic Reactors. *Nanotoday* **2009**, *4*, 470–81.
22. Wang, H.; Chen, K.-J.; Wang, S.; Ohashi, M.; Kamei, K.-i.; Sun, J.; Ha, J. H.; Liu, K.; Tseng, H.-R. A Small Library of DNA-Encapsulated Supramolecular Nanoparticles for Targeted Gene Delivery. *Chem. Commun.* **2010**, *46*, 1851–53.
23. Cai, W. B.; Chen, X. Y. Nanoplatforms for Targeted Molecular Imaging in Living Subjects. *Small* **2007**, *3*, 1840–54.
24. Ishikawa, A.; Zhou, Y.-M.; Kambe, N.; Nakayama, Y. Enhancement of Star Vector-Based Gene Delivery to Endothelial Cells by Addition of RGD-Peptide. *Bioconjugate Chem.* **2008**, *19*, 558–61.
25. Merkel, O. M.; Germershaus, O.; Wada, C. K.; Tarcha, P. J.; Merdan, T.; Kissel, T. Integrin αvβ3 Targeted Gene Delivery Using RGD Peptidomimetic Conjugates with Copolymers of PEGylated Poly(ethylene imine). *Bioconjugate Chem.* **2009**, *20*, 1270–80.
26. Zuber, G.; Dontenwill, M.; Behr, J.-P. Synthetic Viruslike Particles for Targeted Gene Delivery to αvβ3 Integrin-Presenting Endothelial Cells. *Mol. Pharm.* **2009**, *6*, 1544–52.
27. Jung, J.; Solanki, A.; Memoli, K. A.; Kamei, K.-i.; Kim, H.; Drahl, M. A.; Williams, L. J.; Tseng, H.-R.; Lee, K. Selective Inhibition of Human Brain Tumor Cells through Multifunctional Quantum-Dot-Based siRNA Delivery. *Angew. Chem., Int. Ed.* **2010**, *49*, 103–07.
28. Torchilin, V. P. Cell Penetrating Peptide-Modified Pharmaceutical Nanocarriers for Intracellular Drug and Gene Delivery. *Peptide Sci.* **2008**, *90*, 604–10.
29. Roy, R.; Jerry, D. J.; Thayumanavan, S. Virus-Inspired Approach to Nonviral Gene Delivery Vehicles. *Biomacromolecules* **2009**, *10*, 2189–93.
30. Green, J. J.; Langer, R.; Anderson, D. G. A Combinatorial Polymer Library Approach Yields Insight into Nonviral Gene Delivery. *Acc. Chem. Res.* **2008**, *41*, 749–59.
31. Akinc, A.; Zumbuehl, A.; Goldberg, M.; Leshchiner, E. S.; Busini, V.; Hossain, N.; Bacallado, S. A.; Nguyen, D. N.; Fuller, J.; Alvarez, R. A Combinatorial Library of Lipid-Like Materials for Delivery of RNAi Therapeutics. *Nat. Biotechnol.* **2008**, *26*, 561–69.
32. Whitesides, G. M. The Origins and the Future of Microfluidics. *Nature* **2006**, *442*, 368–73.
33. Thorsen, T.; Maerkl, S. J.; Quake, S. R. Microfluidic Large-Scale Integration. *Science* **2002**, *298*, 580–84.
34. Vincent, M. E.; Liu, W.; Haney, E. B.; Ismagilov, R. F. Microfluidic Stochastic Confinement Enhances Analysis of Rare Cells by Isolating Cells and Creating High Density Environments for Control of Diffusible Signals. *Chem. Soc. Rev.* **2010**, *39*, 974–84.
35. Marre, S.; Jensen, K. F. Synthesis of Micro- And Nanostructures in Microfluidic Systems. *Chem. Soc. Rev.* **2010**, *39*, 1183–202.
36. Overly, C. C.; Lee, K. D.; Berthiaume, E.; Hollenbeck, P. J. Quantitative Measurement of Intraorganelle Ph in the Endosomal Lysosomal Pathway in Neurons by Using Ratiometric Imaging with Pyranine. *Proc. Natl. Acad. Sci. U.S.A.* **1995**, *92*, 3156–60.
37. Petter, R. C.; Salek, J. S.; Sikorski, C. T.; Kumaravel, G.; Lin, F. T. Cooperative Binding by Aggregated Mono-6-(alkylamino)-beta-cyclodextrins. *J. Am. Chem. Soc.* **1990**, *112*, 3860–68.
38. Maherali, N.; Hochedlinger, K. Guidelines and Techniques for the Generation of Induced Pluripotent Stem Cells. *Cell Stem Cell* **2008**, *3*, 595–605.

Biomaterials 32 (2011)

Contents lists available at ScienceDirect

Biomaterials

journal homepage: www.elsevier.com/locate/biomaterials

A small MRI contrast agent library of gadolinium(III)-encapsulated supramolecular nanoparticles for improved relaxivity and sensitivity

Kuan-Ju Chen [a,1,3], Stephanie M. Wolahan [b,2,3], Hao Wang [a,1], Chao-Hsiung Hsu [c,d], Hsing-Wei Chang [e,f], Armando Durazo [b,2], Lian-Pin Hwang [e,f], Mitch A. Garcia [a,1], Ziyue K. Jiang [g], Lily Wu [g], Yung-Ya Lin [b,2,**], Hsian-Rong Tseng [a,*]

[a] Department of Molecular and Medical Pharmacology, California NanoSystems Institute (CNSI), Crump Institute for Molecular Imaging (CIMI), University of California, Los Angeles, 570 Westwood Plaza, Building 114, Los Angeles, CA 90095-1770, USA
[b] Department of Chemistry & Biochemistry, University of California, Los Angeles, 607 Charles E. Young Drive East (courier), Los Angeles, CA 90095-1569, USA
[c] Department of Chemistry, National Tsing-Hua University, Hsinchu, Taiwan
[d] Molecular Science and Technology Program, Taiwan International Graduate Program, Institute of Atomic and Molecular Sciences, Academia Sinica, Taipei, Taiwan
[e] Department of Chemistry, National Taiwan University, Taipei, Taiwan
[f] Institute of Atomic and Molecular Sciences, Academia Sinica, Taipei 10617, Taiwan
[g] Department of Medical and Molecular Pharmacology, University of California, Los Angeles, 10833 Le Conte Ave. Los Angeles, CA 90095, USA

ARTICLE INFO

Article history:
Received 26 October 2010
Accepted 15 November 2010
Available online 16 December 2010

Keywords:
Supramolecular Chemistry
Cyclodextrin
T1-weighted Contrast Agent
MRI
Gadolinium
Dynamic imaging

ABSTRACT

We introduce a new category of nanoparticle-based T_1 MRI contrast agents (CAs) by encapsulating paramagnetic chelated gadolinium(III), i.e., Gd^{3+}·DOTA, through supramolecular assembly of molecular building blocks that carry complementary molecular recognition motifs, including adamantane (Ad) and β-cyclodextrin (CD). A small library of Gd^{3+}·DOTA-encapsulated supramolecular nanoparticles (Gd^{3+}·DOTA⊂SNPs) was produced by systematically altering the molecular building block mixing ratios. A broad spectrum of relaxation rates was correlated to the resulting Gd^{3+}·DOTA⊂SNP library. Consequently, an optimal synthetic formulation of Gd^{3+}·DOTA⊂SNPs with an r_1 of 17.3 s^{-1} mM^{-1} (ca. 4-fold higher than clinical Gd^{3+} chelated complexes at high field strengths) was identified. T_1-weighted imaging of Gd^{3+}·DOTA⊂SNPs exhibits an enhanced sensitivity with a contrast-to-noise ratio (C/N ratio) ca. 3.6 times greater than that observed for free Gd^{3+}·DTPA. A Gd^{3+}·DOTA⊂SNPs solution was injected into foot pads of mice, and MRI was employed to monitor dynamic lymphatic drainage of the Gd^{3+}·DOTA⊂SNPs-based CA. We observe an increase in signal intensity of the brachial lymph node in T_1-weighted imaging after injecting Gd^{3+}·DOTA⊂SNPs but not after injecting Gd^{3+}·DTPA. The MRI results are supported by ICP-MS analysis *ex vivo*. These results show that Gd^{3+}·DOTA⊂SNPs not only exhibits enhanced relaxivity and high sensitivity but also can serve as a potential tool for diagnosis of cancer metastasis.

1. Introduction

Magnetic resonance imaging (MRI) is a medical imaging technique capable of three-dimensional (3D), high-resolution visualization of specific tissues or organs in the body and has been extensively used in neurological, cardiovascular, and oncological diagnosis [1–3]. Paramagnetic MRI contrast agents (CAs), usually composed of gadolinium(III) ion (Gd^{3+}), are capable of reducing the longitudinal relaxation time (T_1) of surrounding water protons, thus increasing signal intensity in T_1-weighted MRI. In general, the performance of T_1-weighted MRI CAs is determined by the relaxivity (r_1), which can be correlated to several parameters, including the loading capacity (Gd^{3+} quantity in the intraparticular space) and the water accessibility (the distance of closest approach between water and Gd^{3+}, the number of water molecules associated with Gd^{3+}, and/or the diffusion of water) as described by relaxation theory [4]. Based on this fundamental understanding, researchers have incorporated Gd^{3+} onto or into nanoscale carriers to enhance r_1 of paramagnetic CAs. Compared to small Gd^{3+} chelated complexes alone, nanocarriers (e.g., dendrimers [5–8,12], polymers

* Corresponding author. Tel.: +1 310 794 1977; fax: +1 310 206 8975.
** Corresponding author. Tel.: +1 310 206 2856.
E-mail addresses: yylin@chem.ucla.edu (Y.-Y. Lin), hrtseng@mednet.ucla.edu (H.-R. Tseng).
URL: http://labs.pharmacology.ucla.edu/tsenglab/.
[1] Tel.: +1 310 206 7320; fax: +1 310 206 8975.
[2] Tel.: +1 310 206 2856.
[3] These two authors contributed equally to the work.

0142-9612/$ – see front matter © 2010 Elsevier Ltd. All rights reserved.
doi:10.1016/j.biomaterials.2010.11.043

[9,10,14], liposomes [11,13,15,16], and inorganic nanoparticles (NPs) [17–20]) allow dramatically increased Gd^{3+} loading. In some cases, poor water accessibility to the intraparticular Gd^{3+} buried inside the carriers can compromise the performance in T_1-weighted MRI [21] and this challenge can be tackled by, for example, using porous nanocarriers [8,22] where a water molecule can travel from the bulk water into the interior space. Nevertheless, fine-tuning the balance of the relevant parameters in a synergistic fashion is challenging due to the lack of direct correlations among the parameters, not to mention the unsatisfactory synthetic approach employed for the development of Gd^{3+}-incorporated nanocarriers that are considered to be time-consuming and cumbersome [23]. Therefore, there is a need to establish a method capable of effective optimization of all parameters to achieve high relaxivity enhancement of T_1-weighted MRI CAs.

Previously, we introduced a convenient, flexible, and modular self-assembly approach [24] for the preparation of supramolecular NPs (SNPs) by mixing three molecular building blocks, including an adamantane-grafted (Ad-grafted) polyamidoamine dendrimer (Ad-PAMAM), a β-cyclodextrin-grafted (CD-grafted) branched polyethylenimine (CD-PEI), and an Ad-grafted polyethylene glycol (Ad-PEG). A variety of SNPs with controllable sizes, surface chemistry, and cross-linking degree of the Ad-PAMAM/CD-PEI hydrogel network in the SNP cores were prepared. We were able to demonstrate that the uniqueness of this supramolecular synthetic approach facilitates the preparations of different SNPs for applications in PET imaging [24], gene delivery [25,26], and photothermal treatment [27]. We set out to further explore such a self-assembled approach to develop Gd^{3+}·DOTA-encapsulated SNPs (Gd^{3+}·DOTA⊂SNPs, Fig. 1) that can be utilized as highly efficient T_1-weighted MRI CAs. In our design, Gd^{3+} chelated complex (Gd^{3+}·DOTA) is covalently conjugated onto CD-PEI building block to give Gd^{3+}·DOTA-CD-PEI, which enhances r_1 due to a distinct chemical environment with a high Gd^{3+} loading capacity inside the pseudo porous polymer-dendrimer hydrogel network and good water accessibility to the intraparticular space. By altering the mixing ratios among Gd^{3+}·DOTA-CD-PEI and the other two molecular building blocks (Ad-PAMAM and Ad-PEG), a small library of Gd^{3+}·DOTA⊂SNPs can be produced with different sizes and cross-linking degrees of the corresponding hydrogel networks. A systematic variation of SNP sizes and cross-linking degrees results in a broad performance diversity of r_1 in the Gd^{3+}·DOTA⊂SNP library due to the respective changes in relaxation parameters. By finding the balance between the material's properties and r_1 performance of the resulting library, Gd^{3+}·DOTA⊂SNPs could serve as a powerful and efficient SNP-based T_1-weighted MRI CA for dynamic imaging of biological processes *in vivo*.

Herein, we demonstrate the self-assembly of a small library of Gd^{3+}·DOTA⊂SNPs from three molecular building blocks – namely, Gd^{3+}·DOTA-CD-PEI, Ad-PAMAM, and Ad-PEG as depicted in Fig. 1. By systematically mixing the molecular building blocks, a broad spectrum of r_1 is correlated to the resulting Gd^{3+}·DOTA⊂SNP library by evaluating the relaxation rate. In addition, we use T_1-weighted imaging to detect Gd^{3+}·DOTA⊂SNP *in vitro*. We monitored lymphatic system uptake of Gd^{3+}·DOTA⊂SNPs *in vivo* with MRI over time and compared results with ICP-MS analysis of brachial lymph node tissue *ex vivo*. The results show that Gd^{3+}·DOTA⊂SNPs not only exhibits enhanced relaxivity and high sensitivity but can also serve as a potential tool for diagnosis of cancer metastasis.

2. Materials and methods

2.1. Materials

Reagents and solvents were purchased from Sigma–Aldrich (St. Louis, MO) and used as received without further purification otherwise noted. 1-Adamantanamine (Ad) hydrochloride and β-cyclodextrin (β-CD) were purchased from TCI America (San Francisco, CA). DOTA/CD-grafted branched polyethylenimine (DOTA-CD-PEI) and Ad-grafted polyethylene glycol (Ad-PEG) were prepared via the method previously reported by our group [24].

2.2. Synthesis of Gd^{3+}·DOTA-CD-PEI

Various quantities of $GdCl_3 \cdot 6H_2O$ (0.1, 0.2, 0.5, 1.0, 1.2 and 2.0 mg, verified with ICP-MS) were added to a 750-μL solution of DOTA-CD-PEI and the reaction mixture was stirred at rt for 20 min to obtain Gd^{3+}·DOTA-CD-PEI with different Gd^{3+} loading concentration.

2.3. Synthesis of Gd^{3+}·DOTA⊂SNPs

To a 750-μL solution of Ad-PEG (9 mg/mL), various concentrations of Ad-PAMAM (22.5, 15, 11.3, 7.5 mg/mL) in 15-μL DMSO were slowly injected under vigorous stirring. A 750-μL Gd^{3+}·DOTA-CD-PEI solution containing different Gd^{3+} loading concentration (0.32, 0.63, 1.61, 3.22, 3.9 and 6.44 mM, verified with ICP-MS) was sequentially added into the mixture to obtain a collection of Gd^{3+}·DOTA⊂SNPs.

2.4. Dynamic light scattering (DLS)

DLS experiments were performed with a Zetasizer Nano instrument (Malvern Instruments Ltd., United Kingdom) equipped with a 10-mW helium-neon laser (λ = 632.8 nm) and thermoelectric temperature controller. Measurements were taken at a 90° scattering angle.

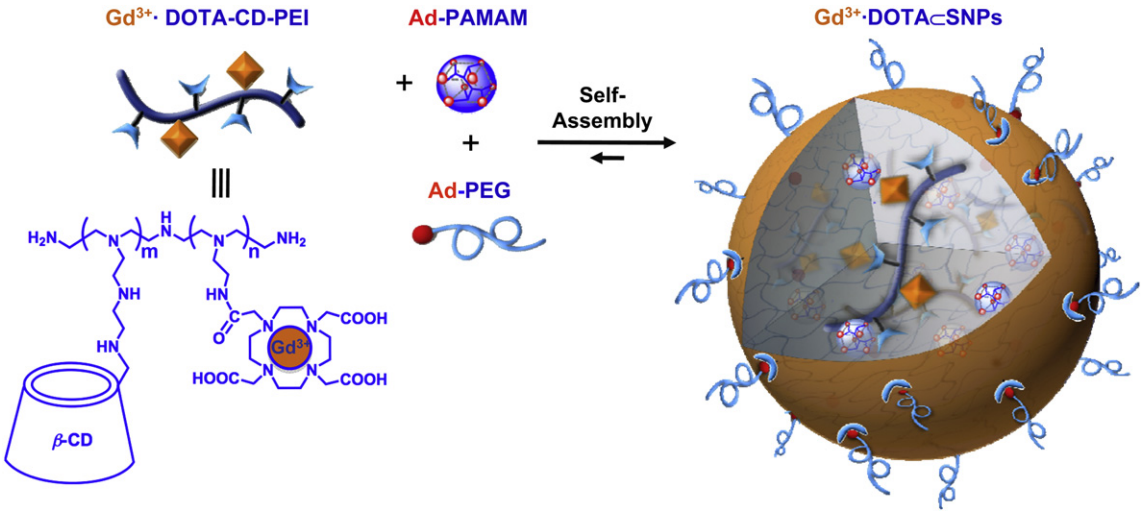

Fig. 1. Schematic representation of self-assembly approach for preparation of Gd^{3+}·DOTA-encapsulated supramolecular nanoparticles (Gd^{3+}·DOTA⊂SNPs).

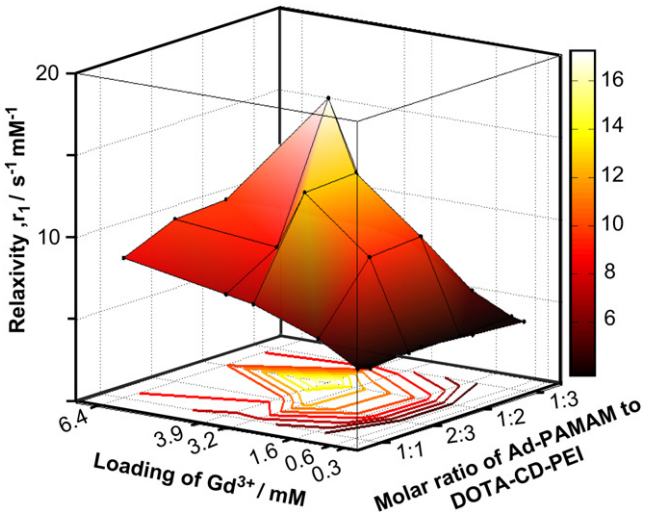

Fig. 2. A mesh plot of r_1 relaxivity performance of Gd^{3+}·DOTA⊂SNPs with variation of (i) ratio of two molecular building blocks, i.e., Ad-PAMAM and DOTA-CD-PEI, and (ii) loading of Gd^{3+} (24 data points). The peak value indicates the highest r_1 relaxivity (Gd^{3+}·DOTA⊂SNPs with a ratio of 1:2 and at a Gd^{3+} concentration of 3.9 mM).

2.5. Transmission electron microscope (TEM)

The morphology and sizes of Gd^{3+}·DOTA⊂SNPs were examined on a Philips CM 120 transmission electron microscope (TEM), operating at an acceleration voltage of 120 kV. The TEM samples were prepared by drop-coating 2 μL of Gd^{3+}·DOTA⊂SNPs solutions onto carbon-coated copper grids. Excess amounts of droplets were removed by filter papers after 45 s. Subsequently, the surface-deposited Gd^{3+}·DOTA⊂SNPs were negatively stained with 2% uranyl acetate for 45 s before the TEM studies.

2.6. Zeta potential measurements

Zeta potentials of Gd^{3+}·DOTA⊂SNPs were determined by photon correlation spectroscopy using a Zetasizer Nano instrument, (Malvern Instruments, Malvern, Worcestershire, UK). The measurements were performed at 25 °C with a detection angle of 90°, and the raw data were subsequently correlated to Z average mean size using a cumulative analysis by the Zetasizer software package.

2.7. ICP-MS analysis

Samples (20 μL) were diluted to a total volume of 2.00 mL using aqueous 2% nitric acid. 20 μL of a 5-ppm aqueous indium ion solution (ICP-MS grade) was then added to each tube as an internal standard and the contents vortexted vigorously. ICP measurements were then conducted on an Agilent 7500 Series ICP-MS in helium collision gas mode. Reported measurements of gadolinium in each sample represent the average of 3 measurements, and are back-calculated to offset the initial dilution. The individual measurements are typically obtained with a relative standard deviation of approximately 3% or less per sample.

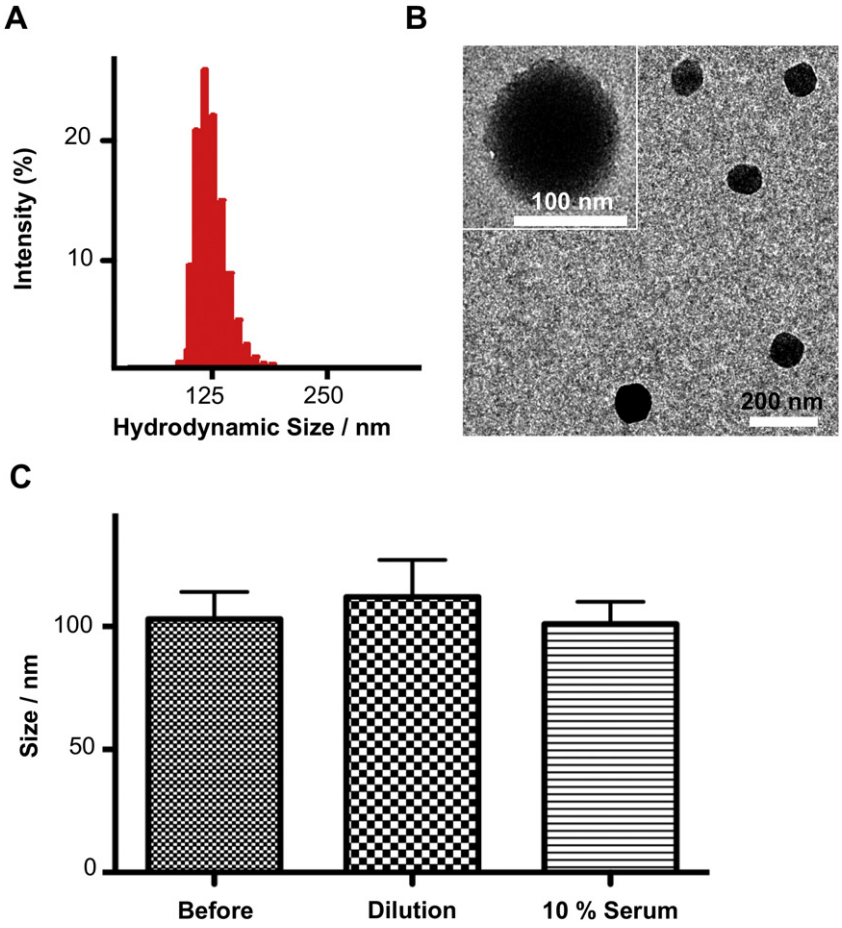

Fig. 3. (A) Dynamic light scattering (DLS) results and (B) TEM image show the narrow size distribution and spherical morphology of the resulting Gd^{3+}·DOTA⊂SNPs (formulate with a ratio of 1:2 and at a Gd^{3+} concentration of 3.9 mM). (C) Stability studies of Gd^{3+}·DOTA⊂SNPs before (left) and after 24 h incubation under different conditions: 400 times dilution in water (center) and 10% serum (right). All the sizes of Gd^{3+}·DOTA⊂SNPs were characterized by TEM after 24 h incubation. (Each sample has at least 20 counts.)

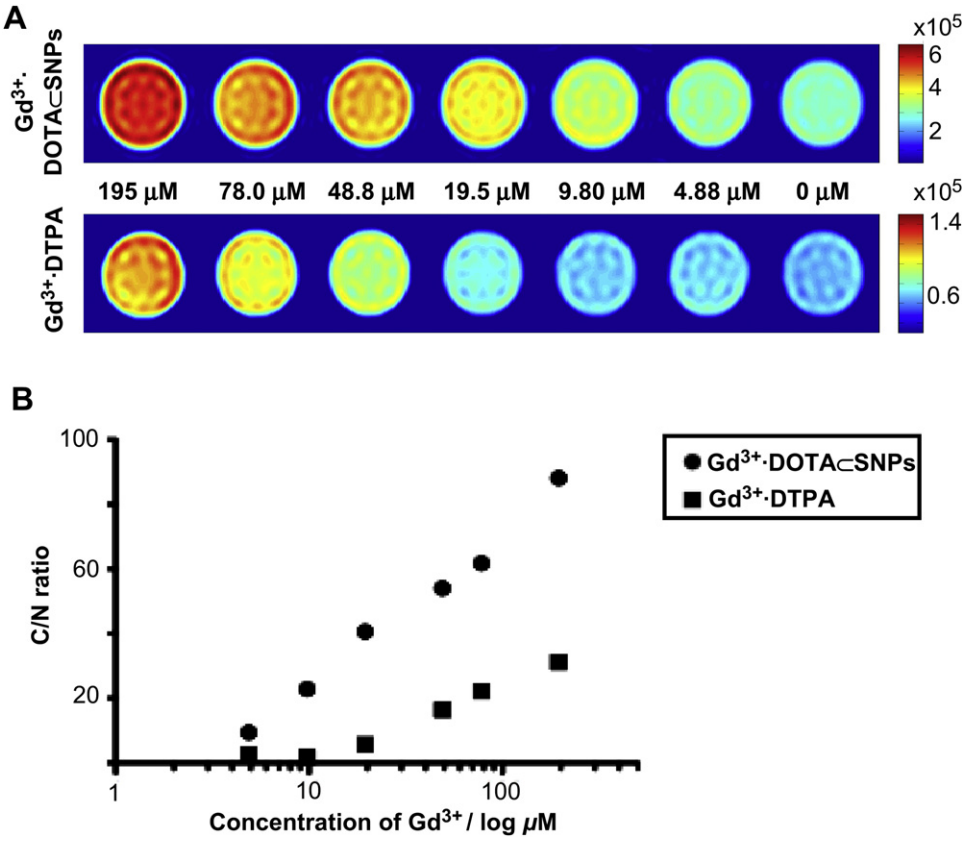

Fig. 4. (A) Phantom images for capillaries containing Gd^{3+}·DOTA⊂SNPs (formulate with a ratio of 1:2 and at a Gd^{3+} concentration of 3.9 mM, top) and Gd^{3+}·DTPA diluted with deionized water (bottom). The capillary on the right contains deionized water (labeled 0 μM) and the concentration of Gd^{3+} in the capillaries increases from 4.88 μM to 195 μM from right to left. (B) Plot of contrast-to-noise (C/N) ratios as a function of Gd^{3+} concentration for Gd^{3+}·DOTA⊂SNPs (circles) and Gd^{3+}·DTPA (squares) of the phantom images. The C/N ratio between Gd^{3+}·DOTA⊂SNPs and DI water is higher than the C/N ratio between Gd^{3+}·DTPA and DI water at all concentrations.

2.8. Encapsulation efficiency of Gd^{3+}·DOTA⊂SNPs

The encapsulation efficiency is defined as the amount of Gd^{3+} within the SNPs divided by the total amount of Gd^{3+}. 400 μL of Gd^{3+}·DOTA⊂SNPs prepared at various concentrations of Gd^{3+} (0.7, 1.4, 2.1, 3.5, 6.0, 6.7, 9.2, 11, 12, 14 and 17 mM) was added into a centrifugal filter at 10 K rpm for 30 min. After recovering filtrate containing free Gd^{3+} and supernatant containing encapsulated Gd^{3+}, the quantity of Gd^{3+} in both solutions was quantified by ICP-MS. The encapsulation efficiencies of each resulting Gd^{3+}·DOTA⊂SNPs are summarized in Fig. S1.

2.9. Relaxation measurements

T_1 relaxation rate measurements were performed on a Bruker Avance 600 MHz spectrometer (Bruker BioSpin Corp., Billerica, MA, USA) equipped with a narrow-bore (54 mm) 14.1 T magnet and a broadband probe at 295 K. Both inversion recovery (IR) and saturation recovery (SR) pulse sequences were acquired.

2.10. Phantom preparation and imaging

For the dilution phantom imaging study, 90 mm capillaries were filled with the diluted solution at concentrations ranging from 4.88 μM to 195 μM and placed together in an 8 mm NMR tube containing D_2O. Imaging was performed on a Bruker Avance 600 MHz spectrometer (Bruker BioSpin Corp., Billerica, MA, USA) equipped with a Micro 5 gradient system (maximal gradient strength of 192 G/cm in three orthogonal directions). A saturation recovery pulse sequence was used for phantom T_1-weighted imaging and the magnetization evolved 2.5 s before applying a spin echo pulse sequence to acquire the image.

2.11. In vivo imaging

In vivo imaging studies used 4–6 week-old female NOD CB17-Prkd^{scid}/IcrCr1B1tw (NOD/SCID), weighing 25–30 g, obtained from BioLASCO, Taiwan. All animal procedures were in accordance with the regulations approved by the Institution Animal Care and Utilization Committee at National Taiwan University. All the MR data were acquired on a Varian INOVA 7-T NMR spectrometer (Varian Inc., CA, USA) with microimaging capability. The images were obtained using a microimaging probehead and a 30 mm I.D. quadrature birdcage imaging RF coil (Varian Inc., CA, USA) with self-shielded gradient systems and a maximum strength of 100 G/cm in each of the x-, y- and z-directions (Resonance Research Inc., Billerica, MA, USA). T_1-weighted images were acquired along the coronal plane using a multiple-slice spin echo pulse sequence with the following parameters: TR/TE = 50/12 ms, matrix = 256 × 128, FOV (field of view) = 51.2 × 25.6 mm, slice thickness = 0.25 mm, NT = 4. We acquired 2 slices during each TR and total number of slices = 96. The total acquisition time was about 25 min. The three-dimensional T_1-weighted images were acquired before injection of Gd^{3+}·DOTA⊂SNPs and at the following times after injecting 20 μL of Gd^{3+}·DOTA⊂SNPs in the right foot pad of the NOD/SCID mouse: 40–65 min, 100–125 min, 160–185 min, 220–245 min, 280–305 min, and 340–365 min. Additionally, we acquired images 12 h and 24 h after injecting Gd^{3+}·DOTA⊂SNPs. No gross side effects were observed during or after injection of Gd^{3+}·DOTA⊂SNPs. For quantitative analysis of acquired images, we take the average signal in a 11 × 9 × 8 voxel volume containing the lymph nodes indicated by the circles, the region of interest (ROI).

3. Results and discussion

The three molecular building blocks, Gd^{3+}·DOTA-CD-PEI, Ad-PAMAM, and Ad-PEG (Fig. 1), were prepared and characterized according to literature [24]. By systematically changing (i) the concentration of encapsulated Gd^{3+} (0.32, 0.63, 1.61, 3.22, 3.90 and 6.44 mM) and (ii) the Ad-PAMAM/DOTA-CD-PEI ratios (1:1, 2:3, 1:2 and 1:3), a small library composed of 24 different formulations of Gd^{3+}·DOTA⊂SNPs (Fig. 2) was prepared. The size and cross-linking degree of the hydrogel core are dependent on the Ad-PAMAM/DOTA-CD-PEI ratio. The 24 different formulations of Gd^{3+}·DOTA⊂SNPs result from mixing Gd^{3+}·DOTA-CD-PEI, prepared at one of six Gd^{3+} concentrations, with solutions of Ad-PAMAM/Ad-PEG prepared at one of four Ad-PAMAM concentrations. The dynamic nature of the supramolecular synthetic approach leads to 80–95% of Gd^{3+} encapsulated into Gd^{3+}·DOTA⊂SNPs, which was quantified by ICP-MS (see

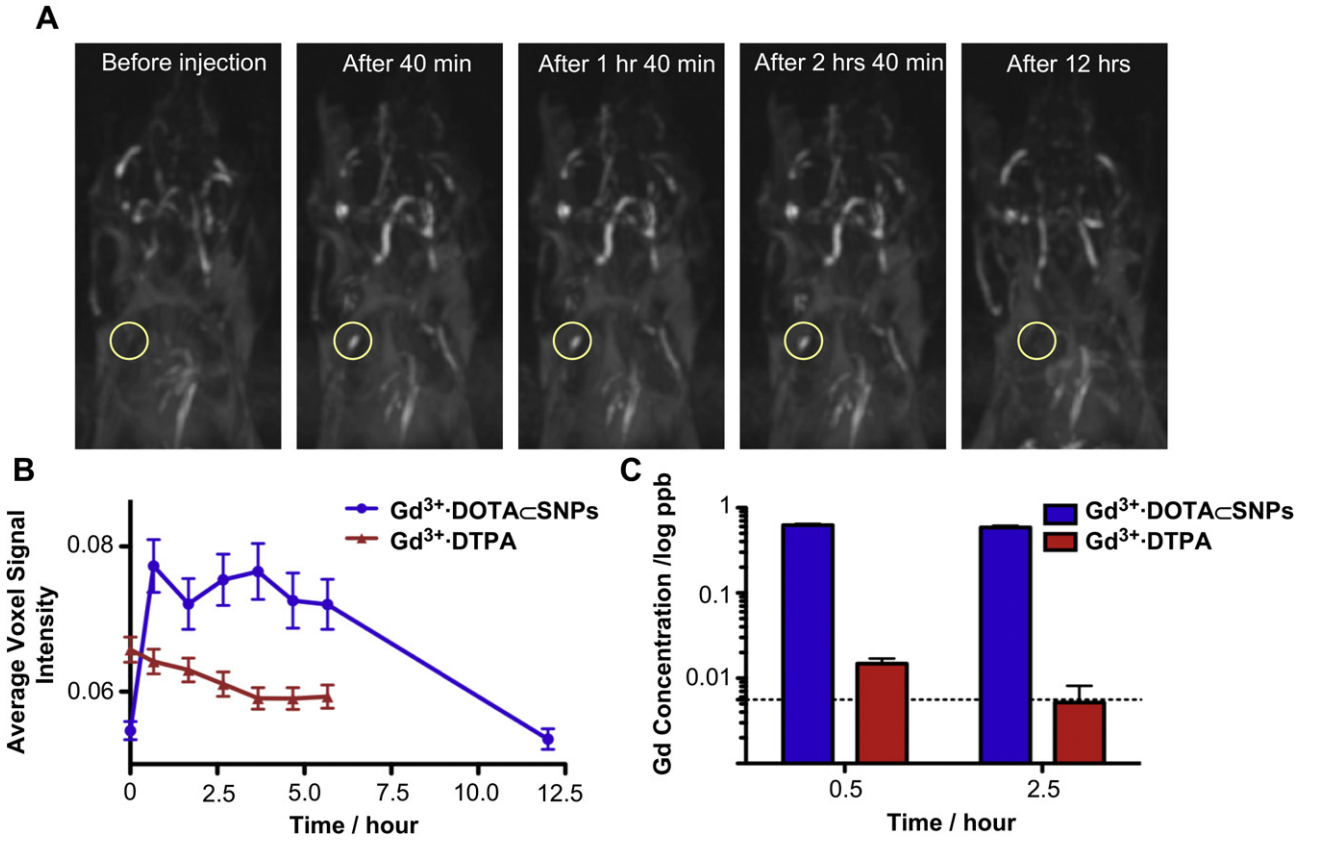

Fig. 5. (A) Three-dimensional (3D) T_1-weighted MR images show dynamic lymphatic drainage of Gd^{3+}·DOTA⊂SNPs. The yellow circle contains the right brachial lymph node. The five images were acquired before injecting and at four times after injecting 20 μL of Gd^{3+}·DOTA⊂SNPs (formulate with a ratio of 1:2 and at a Gd^{3+} concentration of 3.9 mM) as labeled. (B) Average voxel signal intensity plotted as a function of image acquisition time (0 h represents data acquired before injecting the MRI CA). (C) Gd^{3+} concentration from ICP-MS measurements on lymph node tissue removed 30 min and 2.5 h after injecting the MRI CA. Dashed line represents the baseline measurement on untreated brachial lymph node tissue. Note the log scale for the Gd^{3+} concentration axis.

Supporting information, Fig. S1). A broad spectrum of r_1 emerges from the resulting Gd^{3+}·DOTA⊂SNPs library with r_1 ranging from 4.19 s^{-1} mM^{-1} to 17.3 s^{-1} mM^{-1}. Measurements were performed in water on a 600 MHz NMR spectrometer and are presented in a mesh plot in Fig. 2. The results highlight an optimal synthetic formulation of Gd^{3+}·DOTA⊂SNPs (1:2 M ratio and 3.9 mM of Gd^{3+}) with a relaxivity of 17.3 s^{-1} mM^{-1} (proposed attribution of relaxation enhancement described in Supporting information, Fig. S4). We do not measure a difference in Gd^{3+}·DOTA⊂SNPs relaxation between 300 and 600 MHz (results not shown). This is significantly higher than clinical Gd^{3+} chelated complexes, i.e., Gd^{3+}·DTPA, which has r_1 ~4.0 s^{-1} mM^{-1} at 300 MHz and 600 MHz. We characterize the resulting Gd^{3+}·DOTA⊂SNPs by measuring the hydrodynamic size of Gd^{3+}·DOTA⊂SNPs with DLS (Fig. 3A) and the results are consistent with TEM images. As shown in Fig. 3B, the TEM images indicate that Gd^{3+}·DOTA⊂SNPs have an average diameter of 103 ± 10 nm with a spherical morphology and narrow size distribution. The hydrodynamic size of Gd^{3+}·DOTA⊂SNPs (124 nm) measured by DLS analysis was larger than the value obtained from TEM, probably due to the swelling of the PEG shell layer on the Gd^{3+}·DOTA⊂SNPs in water. The zeta potential of the resulting optimal Gd^{3+}·DOTA⊂SNPs is 22.5 ± 1.4 mV. The stability tests of Gd^{3+}·DOTA⊂SNPs were carried out under two conditions: (i) 400 times dilution in water and (ii) 10% serum. The solutions were prepared from Gd^{3+}·DOTA⊂SNPs with 3.9 mM of Gd^{3+} and then incubated under the conditions for 24 h. The sizes of both solutions were characterized by TEM and summarized in Fig. 3C. The original size of Gd^{3+}·DOTA⊂SNPs is 103 ± 10 nm (Fig. 3C, left). The size after 400 times dilution is 112 ± 15 nm (Fig. 3C, center) and in 10% serum is 101 ± 9 nm (Fig. 3C, right). There are no distinct changes in the average sizes of Gd^{3+}·DOTA⊂SNPs after dilution and in 10% serum; therefore, we conclude that the Gd^{3+}·DOTA⊂SNPs remain stable under these conditions.

To test feasibility of Gd^{3+}·DOTA⊂SNPs as a sensitive MRI CA, we performed a series dilution study of Gd^{3+}·DOTA⊂SNPs with deionized (DI) water to establish the minimum Gd^{3+} concentration detectable by MRI. Fig. 4 shows T_1-weighted imaging results of the series dilution for Gd^{3+}·DOTA⊂SNPs solution and Gd^{3+}·DTPA (Fig. 4A) at seven concentrations (from 195 to 4.88 μM) and Fig. 4B plots the C/N ratios as a function of Gd^{3+} concentration for Gd^{3+}·DOTA⊂SNPs (circles) and Gd^{3+}·DTPA (squares). The Gd^{3+}·DOTA(SNPs and $Gd3^{3+}$·DTPA phantoms were imaged separately (note different scale bars) and the C/N ratio between Gd^{3+}·DOTA⊂SNPs and DI water are higher than the C/N ratio between Gd^{3+}·DTPA and DI water at all concentrations. The results indicate that the significant sensitivity improvement and relaxivity enhancement of Gd^{3+}·DOTA⊂SNPs compared to Gd^{3+}·DTPA is maintained after diluting the CA solutions down to μM concentrations of Gd^{3+}.

The lymphatic system is a common route for metastatic spread of cancer [28–30]. Dynamic imaging of lymphatic drainage has been regarded as a powerful diagnostic protocol for monitoring cancer metastasis. We attempted to explore the use of Gd^{3+}·DOTA⊂SNPs as a new type of NPs for dynamic imaging of lymphatic drainage compared with conventional Gd^{3+} chelated complexes. Fig. 5A shows 3D maximum intensity projection (MIP) [31] T_1-weighted *in vivo* imaging results before and after injecting Gd^{3+}·DOTA⊂SNPs into NOD/SCID mice (experimental details in Supporting information). The yellow circles contain the right brachial lymph node of the mouse.

We injected 20 μL of a 3.9 mM MRI CA solution into the front right foot pad of a NOD/SCID mouse and monitored the changes with MRI. The draining of the lymph nodes was clearly visualized with the Gd^{3+}·DOTA⊂SNPs. The average voxel signal intensity increases in the right brachial lymph node after injecting Gd^{3+}·DOTA⊂SNPs but not after injecting Gd^{3+}·DTPA (Fig. 5B and also see Supporting information Fig. S2). Meanwhile, the average signal intensity in the left brachial lymph node remains around 20% less than the right lymph node (see Supporting information, Fig. S3). After 12 h, the average signal intensity in both lymph nodes decreases close to the values before injecting the Gd^{3+}·DOTA⊂SNPs. To support detection with MRI of Gd^{3+}·DOTA⊂SNPs drainage in the brachial lymph node, we used ICP-MS analysis on *ex vivo* tissue removed at two time points after injecting MRI CA, i.e., Gd^{3+}·DOTA⊂SNPs and Gd^{3+}·DTPA, into the front foot pads of the mice following the same procedure used for *in vivo* imaging. We removed the brachial lymph nodes of mice after 30 min and 2.5 h. The brachial lymph nodes were dissected and underwent ICP-MS measurement. The ICP-MS analysis revealed that Gd^{3+} concentration decreased by approximately 6% after 2.5 h. As a comparison, the Gd^{3+} concentration from mice treated with Gd^{3+}·DTPA was negligible and close to the baseline measurement on untreated brachial lymph node tissue. The results show that the ICP-MS measurements are in good agreement and validate the T_1-weighted MRI results (experimental details of ICP-MS analysis are in Supporting Information).

4. Conclusion

We have successfully demonstrated the systematic synthesis of a small library of Gd^{3+}·DOTA⊂SNPs by a supramolecular self-assembly approach. The results highlight an optimal synthetic formulation of Gd^{3+}·DOTA⊂SNPs with an r_1 of 17.3 s^{-1} mM^{-1}, which is ca. 4-fold higher than clinical Gd^{3+} chelated complexes at high field strengths. In addition, the resulting Gd^{3+}·DOTA⊂SNPs were detected by T_1-weighted imaging at a concentration of 4.88 μM Gd^{3+} with a contrast-to-noise ratio (C/N ratio) of 9.46, ca. 3.6 times greater than the C/N ratio for Gd^{3+}·DTPA at the same concentration, signaling a higher sensitivity than conventional MRI CAs. Moreover, the dynamic lymph node drainage MRI demonstrated the applicability of Gd^{3+}·DOTA⊂SNPs *in vivo*.

Acknowledgment

This research was supported by NIH grant (R21 EB008419).

Appendix

Figures with essential colour discrimination. Figs. 1–3 and 5 in this article, are difficult to interpret in black and white. The full colour images can be found in the on-line version, at doi:10.1016/j.biomaterials.2010.11.043.

Appendix. Supporting information

Supplementary data related to this article can be found online at doi:10.1016/j.biomaterials.2010.11.043.

References

[1] Benaron DA. The future of cancer imaging. Cancer Metastasis Rev 2002;21(1):45–78.
[2] Marcu CB, Beek AM, van Rossum AC. Clinical applications of cardiovascular magnetic resonance imaging. Can Med Assoc J 2006;175(8):911–7.
[3] Frisoni GB, Fox NC, Jack CR, Scheltens P, Thompson PM. The clinical use of structural MRI in Alzheimer disease. Nat Rev Neurol 2010;6(2):67–77.
[4] Caravan P, Ellison JJ, McMurry TJ, Lauffer RB. Gadolinium(III) chelates as MRI contrast agents: structure, dynamics, and applications. Chem Rev 1999;99(9):2293–352.
[5] Boswell CA, Eck PK, Regino CA, Bernardo M, Wong KJ, Milenic DE, et al. Synthesis, characterization, and biological evaluation of integrin alphavbeta3-targeted PAMAM dendrimers. Mol Pharm 2008;5(4):527–39.
[6] Kobayashi H, Brechbiel MW. Nano-sized MRI contrast agents with dendrimer cores. Adv Drug Deliv Rev 2005;57(15):2271–86.
[7] Rudovsky J, Botta M, Hermann P, Hardcastle KI, Lukes I, Aime S. PAMAM dendrimeric conjugates with a Gd-DOTA phosphinate derivative and their adducts with polyaminoacids: the interplay of global motion, internal rotation, and fast water exchange. Bioconjug Chem 2006;17(4):975–87.
[8] Cheng Z, Thorek DLJ, Tsourkas A. Gadolinium-conjugated dendrimer nanoclusters as a tumor-targeted T_1 magnetic resonance imaging contrast agent. Angew Chem Int Ed 2010;49:346–50.
[9] Duarte MG, Gil MH, Peters JA, Colet JM, Elst LV, Muller RN, et al. Synthesis, characterization, and relaxivity of two linear Gd(DTPA)-polymer conjugates. Bioconjug Chem 2001;12(2):170–7.
[10] Plush SE, Woods M, Zhou YF, Kadali SB, Wong MS, Sherry AD. Nanoassembled capsules as delivery vehicles for large payloads of high relaxivity Gd3+ agents. J Am Chem Soc 2009;131(43):15918–23.
[11] Glogard C, Stensrud G, Aime S. Novel radical-responsive MRI contrast agent based on paramagnetic liposomes. Magn Reson Chem 2003;41(8):585–8.
[12] Rudovsky J, Hermann P, Botta M, Aime S, Lukes I. Dendrimeric Gd(III) complex of a monophosphinated DOTA analogue: optimizing relaxivity by reducing internal motion. Chem Commun 2005;(18):2390–2.
[13] Vaccaro M, Accardo A, Tesauro D, Mangiapia G, Lof D, Schillen K, et al. Supramolecular aggregates of amphiphilic gadolinium complexes as blood pool MRI/MRA contrast agents: physicochemical characterization. Langmuir 2006;22(15):6635–43.
[14] Aime S, Botta M, Garino E, Crich SG, Giovenzana G, Pagliarin R, et al. Non-covalent conjugates between cationic polyamino acids and Gd-III chelates: a route for seeking accumulation of MRI-contrast agents at tumor targeting sites. Chem Eur J 2000;6(14):2609–17.
[15] Erdogan S, Medarova ZO, Roby A, Moore A, Torchilin VP. Enhanced tumor MR imaging with gadolinium-loaded polychelating polymer-containing tumor-targeted liposomes. J Magn Reson Imaging 2008;27(3):574–80.
[16] Glogard C, Stensrud G, Hovland R, Fossheim SL, Klaveness J. Liposomes as carriers of amphiphilic gadolinium chelates: the effect of membrane composition on incorporation efficacy and in vitro relaxivity. Int J Pharm 2002;233(1–2):131–40.
[17] Fortin MA, Petoral RM, Soderlind F, Klasson A, Engstrom M, Veres T, et al. Polyethylene glycol-covered ultra-small Gd2O3 nanoparticles for positive contrast at 1.5 T magnetic resonance clinical scanning. Nanotechnology 2007;18(39):395501–10.
[18] Rieter WJ, Taylor KML, Lin WB. Surface modification and functionalization of nanoscale metal-organic frameworks for controlled release and luminescence sensing. J Am Chem Soc 2007;129(32):9852–3.
[19] Santra S, Bagwe RP, Dutta D, Stanley JT, Walter GA, Tan W, et al. Synthesis and characterization of fluorescent, radio-opaque, and paramagnetic silica nanoparticles for multimodal bioimaging applications. Adv Mater 2005;17(18):2165–9.
[20] Rieter WJ, Kim JS, Taylor KML, An HY, Lin WL, Tarrant T, et al. Hybrid silica nanoparticles for multimodal Imaging. Angew Chem Int Ed 2007;46(20):3680–2.
[21] Tilcock C, Unger E, Cullis P, Macdougall P. Liposomal Gd-Dtpa - Preparation and characterization of relaxivity. Radiology 1989;171(1):77–80.
[22] Cheng Z, Thorek DLJ, Tsourkas A. Porous polymersomes with encapsulated Gd-labeled dendrimers as highly efficient MRI contrast agents. Adv Funct Mater 2009;19:3753–9.
[23] Nakamura E, Makino K, Okano T, Yamamoto T, Yokoyama M. A polymeric micelle MRI contrast agent with changeable relaxivity. J Control Release 2006;114(3):325–33.
[24] Wang H, Wang S, Su H, Chen KJ, Armijo AL, Lin WY, et al. A supramolecular approach for preparation of size-controlled nanoparticles. Angew Chem Int Ed 2009;48(24):4344–8.
[25] Wang H, Chen K-J, Wang S, Ohashi M, Kamei K-I, Sun J, et al. A small library of DNA-encapsulated supramolecular nanoparticles for targeted gene delivery. Chem Commun 2010;46:1851–3.
[26] Wang H, Liu K, Chen K-J, Lu Y, Wang S, Lin W-Y, et al. A Rapid Pathway Toward a Superb Gene Delivery System: Programming Structural and Functional Diversity into a Supramolecular Nanoparticle Library. ACS Nano 2010;4(10):6235–43.
[27] Wang S, Chen K-J, Wu T-H, Wang H, Lin W-Y, Ohashi M, et al. Photothermal effects of supramolecularly assembled gold nanoparticles for the targeted treatment of cancer cells. Angew Chem Int Ed 2010;49(22):3777–81.
[28] Barrett T, Choyke PL, Kobayashi H. Imaging of the lymphatic system: new horizons. Contrast Media Mol Imaging 2006;1:230–45.
[29] Ravizzini G, Turkbey B, Barrett T, Kobayashi H, Choyke PL. Nanoparticles in sentinel lymph node mapping. Wiley Interdiscip Rev Nanomed Nanobiotechnol 2009;1:610–23.
[30] Alitalo K, Tammela T, Petrova TV. Lymphangiogenesis in development and human disease. Nature 2005;438(7070):946–53.
[31] MATLAB Central. Viewer 3D by Dirk-Jan Kroon. University of Twente. Available from: http://www.mathworks.com/matlabcentral/fileexchange/21993-viewer3d; 2010.

Protein Delivery

DOI: 10.1002/anie.201005740

Delivery of Intact Transcription Factor by Using Self-Assembled Supramolecular Nanoparticles**

Yang Liu, Hao Wang, Ken-ichiro Kamei, Ming Yan, Kuan-Ju Chen, Qinghua Yuan, Linqi Shi,* Yunfeng Lu,* and Hsian-Rong Tseng**

Protein delivery[1] has been considered as the most straightforward strategy for modulating cellular behavior without the safety concerns and expression performance issues associated with gene deliver approaches. Two major challenges remain to be overcome in order to enable practical applications in biology and medicine 1) how to foster cellular uptake of protein molecules and 2) how to retain their stabilities and functions[2] over the delivery process. Recently, attempts have been made to develop a variety of delivery vectors, including liposomes,[3] polymer micelles,[4] and nanoparticle,[5] to enhance the uptake of protein molecules in target cells, and at the same time, to stabilize the encapsulated proteins. Owing to the time-consuming procedures employed in optimization of delivery materials, significant endeavors have been made in search of better delivery systems, although there has been limited progress in the field to date. Alternatively, recombinant technology[6] can be utilized to conjugate cell-penetrating peptides[7] (CPPs) onto protein molecules, this is the most commonly used protein delivery system with improved delivery efficiency. In this case, the major bottlenecks associated with the complicated procedure of generating recombinant proteins and the lack of protection mechanism against protein denature need to be solved.

Transcription factor (TF) is a protein responsible for regulating gene transcription in cellular circuitry.[8] In general, TFs contain one or more DNA-binding domains (DBDs), which recognize matching DNA sequences adjacent to the genes they regulate. Apparently, highly efficient delivery of TFs can provide a powerful technology for modulating cellular behavior. One of the most important in-vitro applications that required highly efficient TF delivery is the generation of human induced pluripotent stem cells (hiPSCs) which has recently been demonstrated by introducing CPPs-fused reprogramming TFs (i.e., OCT4, SOX2, KLF4, and c-MYC)[9] into human somatic cells. The resulting hiPSCs have the potential to revolutionize regenerative medicine.[10] However, the high costs of the four reprogramming TFs in their recombinant forms, means it is unlikely that this approach can be used for large-scale hiPSCs generation without further improvement in the delivery performance of the reprogramming proteins. Therefore, it is crucial to develop a new type of vector capable of delivering intact (unmodified) TFs in a highly efficient manner.

Previously, we demonstrated a convenient, flexible, and modular self-assembly approach for the preparation of supramolecular nanoparticles (SNPs) from a small collection of molecular building blocks through a multivalent molecular recognition based on adamantane (Ad) and β-cyclodextrin (CD) motifs. Such a self-assembly synthetic strategy enables control upon the sizes, surfaces chemistry, zeta potentials, and payloads of the resulting SNPs, which open up many interesting opportunities for biomedical applications, for example, positron emission tomography (PET) imaging,[11] magnetic resonance imaging (MRI),[12] photothermal treatment of cancer cells,[13] and highly efficient gene delivery.[14]

Considering the unique role of TF, we attempted to explore the use of SNPs as a new type of nanoscale vector for delivering intact (unmodified) TFs with an efficiency superior to that of existing approaches. Our idea is to achieve the encapsulation of a TF into cationic SNP vectors by introducing anionic characteristics to the TF. A DNA plasmid with a matching recognition sequence specific to a TF can be employed to form an anionic TF·DNA complex, which can be subsequently encapsulated into SNPs, resulting in TF-encapsulated SNPs (TF·DNA⊂SNPs).

Herein, we introduce a new type of protein delivery system capable of highly efficient transduction of intact TFs. In this proof-of-concept study, a mammalian orthogonal fusion TF, GAL4-VP16 was chosen to serve as a model TF.

[*] Y. Liu, Dr. H. Wang, Dr. K. Kamei, K.-J. Chen, Prof. H.-R. Tseng
Department of Molecular and Medical Pharmacology, Crump Institute for Molecular Imaging (CIMI), California NanoSystems Institute (CNSI), Institute for Molecular Medicine (IMED)
University of California, Los Angeles
570 Westwood Plaza, Building 114, Los Angeles, CA 90095-1770 (USA)
E-mail: haowang@mednet.ucla.edu
hrtseng@mednet.ucla.edu
Homepage: http://labs.pharmacology.ucla.edu/tsenglab/

Y. Liu, Dr. M. Yan, Prof. Y. Lu
Department of Chemical & Biomolecular Engineering
University of California, Los Angeles
420 Westwood Plaza, BH5573G, Los Angeles, CA 90095 (USA)
E-mail: luucla@ucla.edu
Homepage: http://www.seas.ucla.edu/~lu/

Y. Liu, Prof. L. Shi
Key Laboratory of Functional Polymer Materials, Ministry of Education (China)
and
Institute of Polymer Chemistry and Physics, Nankai University
Tianjin (China)
E-mail: shilinqi@nankai.edu.cn

Dr. K. Kamei, Q. Yuan
Institute for Integrated Cell-Material Sciences, Kyoto University (Japan)

[**] This research was supported by National Institutes of Health (NIH), Defense Threat Reducing Agency (DTRA), and National Science Foundation of China, NSFC (50625310 and 50830103).

Supporting information for this article is available on the WWW under http://dx.doi.org/10.1002/anie.201005740.

Since GAL4-VP16 is an artificial transcription factor, there should be no background concentration in the mammalian cells employed in the delivery studies. To facilitate the encapsulation of the model TF into the SNP vectors, a DNA plasmid (i.e., pG5E4T-Fluc) that contains five tandem copies of GAL4-VP16 matching recognition sequences and a conjugated luciferase reporter was designed. The incorporation of multivalent recognition sequences enhances dynamic binding between GAL4-VP16 and pG5E4T-Fluc, allowing improved encapsulation and dynamic releasing of the intact TF. In addition, the conjugated luciferase reporter can be specifically activated by GAL4-VP16, providing a real-time readout reflecting the activities of the TF after its intracellular delivery. As shown in Figure 1, three types of molecular

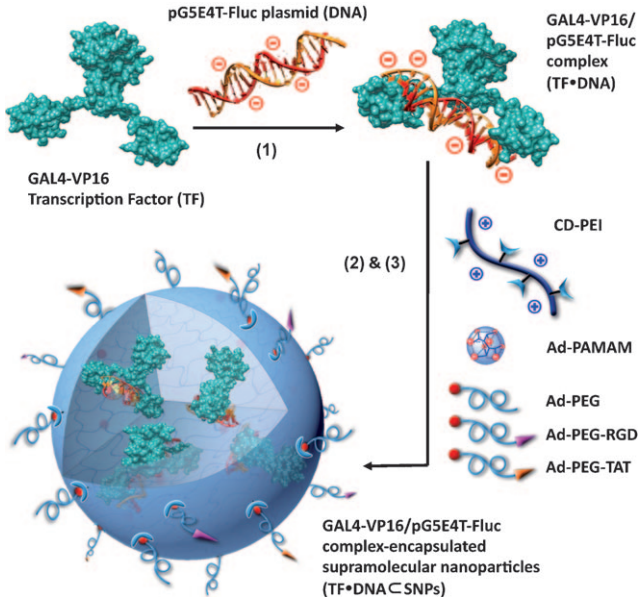

Figure 1. Schematic representation of the self-assembly approach for the preparation of transcription factor-incorporated supramolecular nanoparticles (TF·DNA⊂SNPs). Three types of molecular recognition mechanisms, including 1) specific binding between GAL4-VP16 (a mammalian-orthogonal fusion TF) and pG5E4T-Fluc vector (with five tandem copies of GAL4-VP16 matching recognition sequences and a conjugated luciferase reporter) for formation of an anionic TF·DNA complex, 2) the Ad/CD-based molecular recognition for generation of SNP vectors with cationic PEI/PAMAM hydrogel cores, and 3) electrostatic interactions that facilitate incorporation of anionic TF·DNA into SNPs, were harnessed for the self-assembly of TF·DNA⊂SNPs by simply mixing TF·DNA with five functional molecular building blocks: CD-PEI, Ad-PAMAM, Ad-PEG, Ad-PEG-RGD, and Ad-PEG-TAT. See text for details. TAT provides the nanoparticle with the capacity to penetrate cell membranes, RGD with cell targeting, and PEG passivation.

recognition mechanisms were employed to facilitate the preparation of TF-encapsulated SNP (TF·DNA⊂SNPs). First, the specific binding (the dissociate constant $K_d \approx 10$ nM)[15] between GAL4-VP16 (TF) and pG5E4T-Fluc (DNA) led to the formation of an anionic TF·DNA complex. Second, the Ad/CD-based molecular recognition ($K = 1.1 \times 10^5\ M^{-1}$)[16] was utilized to form the SNP vectors with cationic hydrogel cores. Third, electrostatic interactions assist the incorporation of TF·DNA into SNPs to give TF·DNA⊂SNPs. The preparation of TF·DNA⊂SNPs can be accomplished by simply mixing TF·DNA complex with other five functional building blocks (i.e., CD-PEI: CD-grafted branched polyethylenimine, Ad-PAMAM: Ad-grafted polyamidoamine dendrimer, Ad-PEG: Ad-grafted polyethylene glycol, Ad-PEG-RGD: Ad-grafted polyethylene glycol with RGD targeting ligand, and Ad-PEG-TAT: Ad-grafted polyethylene glycol with TAT-based CPP). Among the three ligand compounds, Ad-PEG plays a role of a capping/solvation reagent that can not only confine continuous propagation of the TF·DNA-encapsulated PEI/PAMAM hydrogel networks, but also impart desired water solubility, structural stability, and passivation performance to the resulting TF·DNA⊂SNPs. In addition, Ad-PEG-RGD and Ad-PEG-TAT, which were incorporated onto the surfaces of TF·DNA⊂SNPs during the one-pot mixing process,[14b] enable delivery specificity (to recognize a certain population of cells with αvβ3-integrin receptors) and cell transfusion capability (to foster internalization through membrane and releasing from endosome trapping), respectively, of TF·DNA⊂SNPs. The previous study revealed a set of optimal synthetic parameters[14a] that produce DNA-encapsulated SNPs which have good gene transfection performance. Additionally, the results suggested that the presence of both 5% RGD and 9% TAT ligands[17] is a crucial factor in the enhanced efficiency. In this study, we took the advantage of these optimal synthetic parameters for the preparation of TF·DNA⊂SNPs. We were able to demonstrated unprecedented performance for delivery intact TF when TF·DNA⊂SNPs is compared with the conventional CPPs-based protein delivery strategy. Moreover, the intracellular TF delivered by TF·DNA⊂SNPs retained its bioactivity, which was confirmed by monitoring the bioluminescence intensity of TF·DNA⊂SNPs-treated cells.

The model plasmid pG5E4T-Fluc and all other molecular building blocks (i.e. CD-PEI, Ad-PAMAM, Ad-PEG, Ad-PEG-RGD, and Ad-PEG-TAT), were synthesized and characterized as described in the Supporting Information. The model transcription factor, GAL4-VP16 was obtained from commercial sources. pG5E4T-Fluc is orthogonal to mammalian genome, thus cannot be activated to express luciferase in the absence of GAL4-VP16.[18] Prior to the preparation of TF·DNA⊂SNP, GAL4-VP16 was incubated with a slight excess amount of pG5E4T-Fluc (GAL4-VP16/pG5E4T-Fluc = 1: 0.35 n/n, each pG5E4T-Fluc contains five tandem copies of GAL4-VP16 recognition sequences thus might accommodate more than one TF) for 30 min at 4 °C to generate TF·DNA. Subsequently, TF·DNA⊂SNPs were prepared by slowly adding CD-PEI (4.32 μg) in 1 μL phosphate-buffered saline (PBS, pH 7.2) into a 19 μL of PBS solution containing TF·DNA complex (200 ng GAL4-VP16 and 2 μg pG5E4T-Fluc), Ad-PEG (5.94 μg), Ad-PEG-RGD (0.297 μg), Ad-PEG-TAT (0.535 μg), and Ad-PAMAM (0.528 μg). After a brief stirring, the mixture was incubated at 4 °C for another 30 min.

To determine hydrodynamic size of the resulting TF·DNA⊂SNPs, we performed dynamic light scattering (DLS) measurements (Figure 2b), indicating a uniform size of (50 ± 3) nm. In parallel, the morphology of

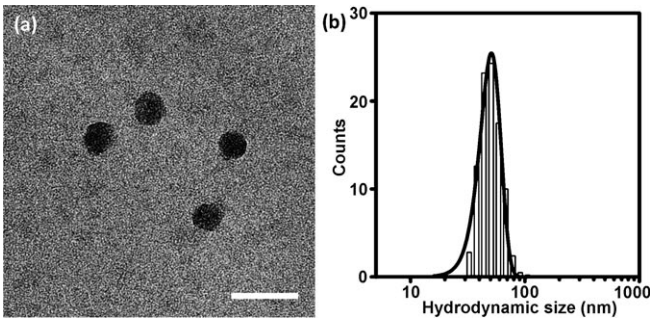

Figure 2. a) Transmission electron microscopy (TEM) micrographs of TF·DNA⊂SNPs. Scale bar: 80 nm. b) Histograms summarize the hydrodynamic size distribution obtained from DLS measurement of (50 ± 3) nm TF·DNA⊂SNPs.

TF·DNA⊂SNPs was characterized by transmission electron microscopy (TEM), suggesting homogeneous, narrow size-distributed spherical nanoparticles with size of (40 ± 3) nm (Figure 2a). Finally, the encapsulation rate of TF in TF·DNA⊂SNPs was characterized by quantifying the SNP-encapsulated TF. For the convenience of using a florescence spectroscopy, Cy5-labeled GAL4-VP16 was prepared and employed (see detail procedure in Supporting Information). The result indicated that more than (81 ± 12) % of the TFs was successfully encapsulated into SNPs to give a TF·DNA⊂SNP under the synthetic parameters described above.

To examine the delivery performance of TF·DNA⊂SNPs, we perform their cell uptake studies using by incubating TF·DNA⊂SNPs (10 ng TF per well) with HeLa cells in a 96-well plate (10^4 cells per well). Again, GAL4-VP16 was labeled by Cy5 dye to allow quantitative monitoring of the delivery performance of TF·DNA⊂SNPs. Control experiments based on Cy5-labeled-TF alone (TF), Cy5-labeled-TF·DNA complex and Cy5-labeled-TF with TAT-conjugation (TAT-TF) were carried out in parallel under the same experimental conditions. After incubation for various periods (i.e., 0.5, 1, 2, 6, 12, and 24 h) and removal of non-uptaken reagents in the media, the delivery performances of individual studies were quantified by measuring their fluorescence intensities in a plate reader (Fujifilm BAS-5000). As shown in Figure 3b, Cy5-labeled TF·DNA⊂SNPs exhibited dramatically enhanced delivery performance in contrast to those observed in the control studies. It is noteworthy that the delivery efficiency of TF·DNA⊂SNPs was approximately five-times greater than that of TAT-TF, which was commonly used as a standard method for TF delivery. The time-dependent uptake studies (Figure 3c) of TF·DNA⊂SNPs revealed that accumulation of the fluorescence signals increased with the incubation time and reached saturation at 12 h. Fluorescence micrographs (Figure 3d) indicated that localization of Cy5-labeled TF in the cell nuclei, suggesting that the TF molecules were delivered to cell nuclei, where TF functioned as a regulator by controlling the translation of specific gene(s). This result was also confirmed by the co-localization of Cy5-labeled TF and 4',6-diamidino-2-phenylindole (DAPI) stained cell nuclei using fluorescence microscopy (Supporting Information).

To confirm that the GAL4-VP16 (TF) retained its activity after delivery, we quantified the luciferase expression by measuring the bioluminescence intensity of TF·DNA⊂SNPs-treated cells (Figure 4). Again, the pG5E4T-Fluc (DNA) used in our study contains a luciferase reporter that can be specifically activated by GAL4-VP16. Therefore, the activity of GAL4-VP16 is reflected in the bioluminescence intensity of TF·DNA⊂SNPs-treated cells as a result of luciferase expression. After the incubation of HeLa cells with TF·DNA⊂SNPs and the control reagents (including SNP vector, TF·DNA, and DNA⊂SNPs), the cells were lysed for quantification of bioluminescence. After incubation with luciferin for 2 min, the bioluminescence intensities were recorded by both a plate reader (Figure 4b) and a cooled charge-coupled device (CCD) camera (IVIS, Xenogen; Figure 4c). Compared to the background-level bioluminescence intensities observed from the control experiments, that observed for TF·DNA⊂SNPs-treated cells is significantly higher, suggesting that the GAL4-VP16 retains its activity to trigger the luciferase expression after intracellular delivery. The dose-dependent studies (Figure 4b) indicated that bio-

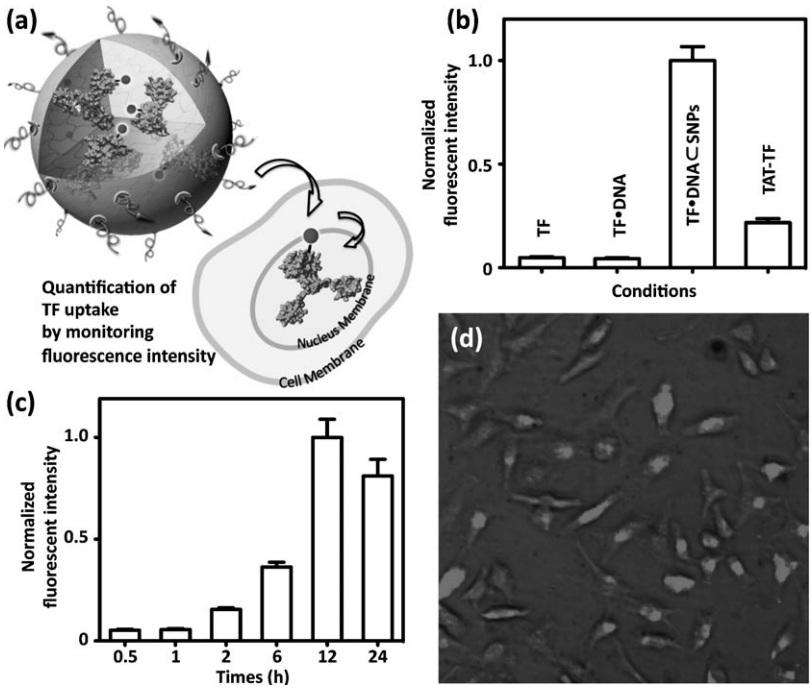

Figure 3. a) Quantification studies on the delivery performance of TF·DNA⊂SNPs. b) Delivery efficiency of Cy5-labeled TF·DNA⊂SNPs, Cy5-labeled-TF alone (TF), Cy5-labeled-TF·DNA complex, and Cy5-labeled-TF with TAT-conjugation (TAT-TF). c) Time-dependent uptake studies of TF·DNA⊂SNPs. d) Fluorescence micrographs of HeLa cells after incubating with TF·DNA⊂SNPs for 12 h. Cy5-labeled TF was localized in the cell nuclei, where TF functioned as a regulator to control the translation of a specific gene.

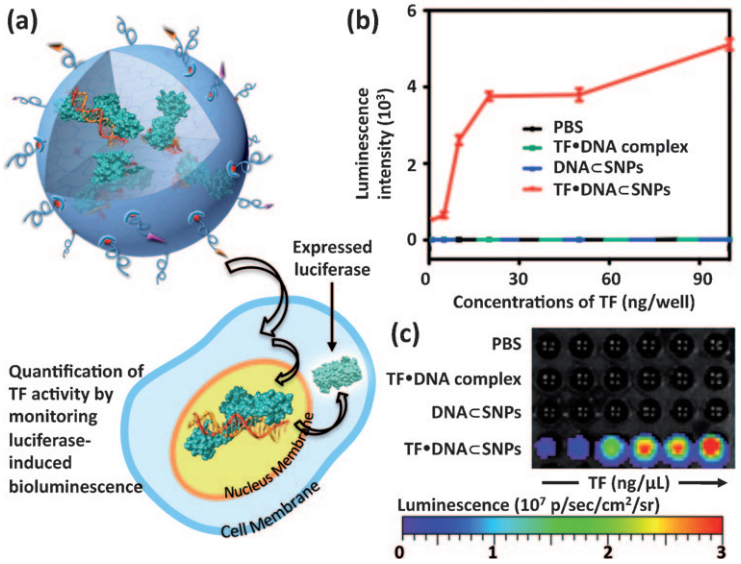

Figure 4. a) Bioluminescence study on TF·DNA⊂SNPs-treated cells. The activity of GAL4-VP16 can be reflected in the bioluminescence intensity as a result of luciferase expression. b) Dose-dependent profile and c) bioluminescence imaging of TF·DNA⊂SNPs-treated cells along with the controlled experiments based on TF·DNA complex and DNA⊂SNPs. Error bars in (b) were obtained from three independent experiments.

luminescence intensities of the TF·DNA⊂SNPs-treated cells increased with the TF dosages. In addition, we also conducted a set of control studies, where the functional gene (pG5E4T-Fluc) and TF are delivered separately using the respective SNP-based delivery systems at different ratios. We were able to observe very similar bioluminescent outcomes as shown in Figure 4, validating the release of TF from the SNP vector, as well as the dominance of TF amount to the expression level of luciferase (Supporting Information). Moreover, the cell viability assays carried out at different doses of TF·DNA⊂SNPs indicated that the TF·DNA⊂SNPs exhibit negligible toxicity. (Supporting Information)

In conclusion, we have successfully demonstrated the feasibility of applying TF·DNA⊂SNPs for delivery of intact (unmodified) transcription factor (TF) in a highly efficient manner. The uniqueness of our self-assembly synthetic strategy for the preparation of TF·DNA⊂SNPs has to do with the combined use of three types of molecular recognition mechanisms, including 1) specific binding between TF and matching DNA plasmid for formation of an anionic TF·DNA complex, 2) the Ad/CD-based molecular recognition for generation of SNP vectors with cationic hydrogel cores, and 3) electrostatic interactions that facilitate encapsulation of anionic TF·DNA into SNPs. We believe such a TF delivery approach provides a powerful method for manipulating cellular behaviors. A potential application is for generating human induced pluripotent stem cells (hiPSCs), which required the delivery of four reprogramming TFs. We note that, in conjunction with the use of a miniaturized high-throughput screening platform[19] and biological assays,[20] to achieve hiPSCs generation in a highly efficient manner, it is feasible to optimize the ratios of the four reprogramming TFs, something that could be possible through the use of TF·DNA⊂SNPs.

Received: September 14, 2010
Revised: December 20, 2010
Published online: March 2, 2011

Keywords: nanoparticles · protein delivery · self-assembly · supramolecular chemistry · transcription factors

[1] a) B. C. S. Cross, I. Sinning, J. Luirink, S. High, *Nat. Rev. Mol. Cell Biol.* **2009**, *10*, 255–264; b) I. Brasnjevic, H. W. M. Steinbusch, C. Schmitz, P. Martinez-Martinez, *Prog. Neurobiol.* **2009**, *87*, 212–251; c) B. Leader, Q. J. Baca, D. E. Golan, *Nat. Rev. Drug Discovery* **2008**, *7*, 21–39; d) J. K. Tessmar, A. M. Goepferich, *Adv. Drug Delivery Rev.* **2007**, *59*, 274–291; e) K. Y. Lee, S. H. Yuk, *Prog. Polym. Sci.* **2007**, *32*, 669–697; f) J. E. Galan, H. Wolf-Watz, *Nature* **2006**, *444*, 567–573; g) T. Kost, J. Condreay, D. Jarvis, *Nat. Biotechnol.* **2005**, *23*, 567–575; h) T. Muth, M. Caplan, *Annu. Rev. Cell Dev. Biol.* **2003**, *19*, 333–366; i) K. G. Ford, B. E. Souberbielle, D. Darling, F. Farzaneh, *Gene Ther.* **2001**, *8*, 1–4; j) Z. Cao, R. Tong, A. Mishra, W. Xu, G. Wong, J. Cheng, Y. Lu, *Angew. Chem.* **2009**, *121*, 6616–6620; *Angew. Chem. Int. Ed.* **2009**, *48*, 6494–6498.

[2] a) N. Tokuriki, D. S. Tawfik, *Science* **2009**, *324*, 203–207; b) Z. S. Haidar, R. C. Hamdy, M. Tabrizian, *Biomaterials* **2008**, *29*, 1207–1215; c) S. Frokjaer, D. E. Otzen, *Nat. Rev. Drug Discovery* **2005**, *4*, 298–306.

[3] a) E. M. Rezler, D. R. Khan, J. Lauer-Fields, M. Cudic, D. Baronas-Lowell, G. B. Fields, *J. Am. Chem. Soc.* **2007**, *129*, 4961–4972; b) I. Cheong, X. Huang, C. Bettegowda, L. A. Diaz, K. W. Kinzler, S. Zhou, B. Vogelstein, *Science* **2006**, *314*, 1308–1311; c) V. P. Torchilin, *Nat. Rev. Drug Discovery* **2005**, *4*, 145–160.

[4] a) Y. Lee, T. Ishii, H. Kim, N. Nishiyama, Y. Hayakawa, K. Itaka, K. Kataoka, *Angew. Chem.* **2010**, *122*, 2606–2609; *Angew. Chem. Int. Ed.* **2010**, *49*, 2552–2555; b) L. J. De Cock, S. De Koker, B. G. De Geest, J. Grooten, C. Vervaet, J. P. Remon, G. B. Sukhorukov, M. N. Antipina, *Angew. Chem.* **2010**, *122*, 7108–7127; *Angew. Chem. Int. Ed.* **2010**, *49*, 6954–6973; c) S. F. M. van Dongen, W. P. R. Verdurmen, R. J. R. W. Peters, R. J. M. Nolte, R. Brock, J. C. M. van Hest, *Angew. Chem.* **2010**, *122*, 7371–7374; *Angew. Chem. Int. Ed.* **2010**, *49*, 7213–7216; d) M. Amidi, E. Mastrobattista, W. Jiskoot, W. E. Hennink, *Adv. Drug Delivery Rev.* **2010**, *62*, 59–82; e) Y. Lee, T. Ishii, H. Cabral, H. Kim, J. H. Seo, N. Nishiyama, H. Oshima, K. Osada, K. Kataoka, *Angew. Chem.* **2009**, *121*, 5413–5416; *Angew. Chem. Int. Ed.* **2009**, *48*, 5309–5312; f) M. George, T. E. Abraham, *J. Controlled Release* **2006**, *114*, 1–14.

[5] a) M. Yan, J. Du, Z. Gu, M. Liang, Y. Hu, W. Zhang, S. Priceman, L. Wu, Z. H. Zhou, Z. Liu, T. Segura, Y. Tang, Y. Lu, *Nat. Nanotechnol.* **2010**, *5*, 48–53; b) P. Ghosh, X. Yang, R. Arvizo, Z.-J. Zhu, S. S. Agasti, Z. Mo, V. M. Rotello, *J. Am. Chem. Soc.* **2010**, *132*, 2642–2645; c) P. Ghosh, X. C. Yang, R. Arvizo, Z. J. Zhu, S. S. Agasti, Z. H. Mo, V. M. Rotello, *J. Am. Chem. Soc.* **2010**, *132*, 2642–2645; d) H. Li, Y. Ma, Y. Chen, Y. Sang, T. Zhou, M. Qiu, X. Huang, C. Zhou, Z. Su, *Angew. Chem.* **2010**, *122*, 5050–5053; *Angew. Chem. Int. Ed.* **2010**, *49*, 4930–4933; e) M. Skwarczynski, M. Zaman, C. Urbani, I. C. Lin, Z. Jia, M. Batzloff, M. Good, M. Monteiro, I. Toth, *Angew. Chem.* **2010**, *122*, 5878–5881; *Angew. Chem. Int. Ed.* **2010**, *49*, 5742–5745;

f) Y. Huang, Y. Park, C. Moon, A. David, H. Chung, V. Yang, *Angew. Chem.* **2010**, *122*, 2784 – 2787; *Angew. Chem. Int. Ed.* **2010**, *49*, 2724 – 2727; g) D. Giljohann, D. Seferos, W. Daniel, M. Massich, P. Patel, C. Mirkin, *Angew. Chem.* **2010**, *122*, 3352 – 3366; *Angew. Chem. Int. Ed.* **2010**, *49*, 3280 – 3294; h) J. Liu, A. Stace-Naughton, X. Jiang, C. J. Brinker, *J. Am. Chem. Soc.* **2009**, *131*, 1354 – 1355; i) P. Ghosh, G. Han, M. De, C. K. Kim, V. M. Rotello, *Adv. Drug Delivery Rev.* **2008**, *60*, 1307 – 1315.

[6] L. A. Fothergill-Gilmore, *Protein Biotechnology* (Ed.: F. Franks), Humana, New York, **1993**, pp. 467 – 487.

[7] a) S. Asoh, S. Ohta, *Adv. Drug Delivery Rev.* **2008**, *60*, 499 – 516; b) A. Fittipaldi, M. Giacca, *Adv. Drug Delivery Rev.* **2005**, *57*, 597 – 608; c) J. Wadia, S. Dowdy, *Adv. Drug Delivery Rev.* **2005**, *57*, 579 – 596; d) A. Abbing, U. K. Blaschke, S. Grein, M. Kretschmar, C. M. B. Stark, M. J. W. Thies, J. Walter, M. Weigand, D. C. Woith, J. Hess, C. O. A. Reiser, *J. Biol. Chem.* **2004**, *279*, 27410 – 27421; e) S. Console, C. Marty, C. García-Echeverría, R. Schwendener, K. Ballmer-Hofer, *J. Biol. Chem.* **2003**, *278*, 35109 – 35114.

[8] Y. Kumagai, D. Sumi, *Annu. Rev. Pharmacol. Toxicol.* **2007**, *47*, 243 – 262.

[9] D. Kim, C.-H. Kim, J.-I. Moon, Y.-G. Chung, M.-Y. Chang, B.-S. Han, S. Ko, E. Yang, K. Y. Cha, R. Lanza, K.-S. Kim, *Cell Stem Cell* **2009**, *4*, 472 – 476.

[10] a) N. Maherali, K. Hochedlinger, *Cell Stem Cell* **2008**, *3*, 595 – 605; b) K. Takahashi, S. Yamanaka, *Cell* **2006**, *126*, 663 – 676.

[11] H. Wang, S. Wang, H. Su, K.-J. Chen, A. L. Armijo, W.-Y. Lin, Y. Wang, J. Sun, K.-I. Kamei, J. Czernin, C. G. Radu, H.-R. Tseng, *Angew. Chem.* **2009**, *121*, 4408 – 4412; *Angew. Chem. Int. Ed.* **2009**, *48*, 4344 – 4348.

[12] K.-J. Chen, S. M. Wolahan, H. Wang, C.-H. Hsu, H.-W. Chang, A. Durazo, L.-P. Hwang, M. A. Garcia, Z. K. Jiang, L. Wu, Y.-Y. Lin, H.-R. Tseng, *Biomaterials* **2010**, *32*, 2160 – 2165.

[13] S. Wang, K.-J. Chen, T.-H. Wu, H. Wang, W.-Y. Lin, M. Ohashi, P.-Y. Chiou, H.-R. Tseng, *Angew. Chem.* **2010**, *122*, 3865 – 3869; *Angew. Chem. Int. Ed.* **2010**, *49*, 3777 – 3781.

[14] a) H. Wang, K. Liu, K.-J. Chen, Y. Lu, S. Wang, W.-Y. Lin, F. Guo, K. Kamei, Y.-C. Chen, M. Ohashi, M. Wang, X.-Z. Zhao, C. K.-F. Shen, H.-R. Tseng, *ACS Nano* **2010**, *4*, 6235 – 6243; b) H. Wang, K.-J. Chen, S. Wang, M. Ohashi, K.-I. Kamei, J. Sun, J. H. Ha, K. Liu, H.-R. Tseng, *Chem. Commun.* **2010**, *46*, 1851 – 1853.

[15] K. K. Rodgers, J. E. Coleman, *Protein Sci.* **1994**, *3*, 608 – 619.

[16] a) M. J. W. Ludden, J. K. Sinha, G. Wittstock, D. N. Reinhoudt, J. Huskens, *Org. Biomol. Chem.* **2008**, *6*, 1553 – 1557; b) M. V. Rekharsky, Y. Inoue, *Chem. Rev.* **1998**, *98*, 1875 – 1918.

[17] According to the previous study, the optimal delivery efficiency was achieved when the DNA⊂SNP surface was covered with 5% RGD targeting ligand and 9% TAT CPPs. For details see Ref. [14a].

[18] I. Sadowski, J. Ma, S. Triezenberg, M. Ptashne, *Nature* **1988**, *335*, 563 – 564.

[19] a) C.-C. Lee, G. Sui, A. Elizarov, C. J. Shu, Y.-S. Shin, A. N. Dooley, J. Huang, A. Daridon, P. Wyatt, D. Stout, H. C. Kolb, O. N. Witte, N. Satyamurthy, J. R. Heath, M. E. Phelps, S. R. Quake, H.-R. Tseng, *Science* **2005**, *310*, 1793 – 1796; b) J. Wang, G. Sui, V. P. Mocharla, R. J. Lin, M. E. Phelps, H. C. Kolb, H.-R. Tseng, *Angew. Chem.* **2006**, *118*, 5402 – 5407; *Angew. Chem. Int. Ed.* **2006**, *45*, 5276 – 5281; c) W.-Y. Lin, Y. Wang, S. Wang, H.-R. Tseng, *Nano Today* **2009**, *4*, 470 – 481; d) Y. Wang, W.-Y. Lin, K. Liu, R. J. Lin, M. Selke, H. C. Kolb, N. Zhang, X.-Z. Zhao, M. E. Phelps, C. K. F. Shen, K. F. Faull, H.-R. Tseng, *Lab Chip* **2009**, *9*, 2281 – 2285; e) K. Liu, H. Wang, K. J. Chen, F. Guo, W. Y. Lin, Y.-C. Chen, D. L. Phung, H. R. Tseng, C. K. Shen, *Nanotechnology* **2010**, *21*, 445603 – 445608.

[20] a) K.-i. Kamei, S. Guo, Z. T. F. Yu, H. Takahashi, E. Gschweng, C. Suh, X. Wang, J. Tang, J. McLaughlin, O. N. Witte, K.-B. Lee, H.-R. Tseng, *Lab Chip* **2009**, *9*, 555 – 563; b) K.-i. Kamei, M. Ohashi, E. Gschweng, Q. Ho, J. Suh, J. Tang, Z. T. For Yu, A. T. Clark, A. D. Pyle, M. A. Teitell, K.-B. Lee, O. N. Witte, H.-R. Tseng, *Lab Chip* **2010**, *10*, 1113 – 1119; c) J. Sun, M. D. Masterman-Smith, N. A. Graham, J. Jiao, J. Mottahedeh, D. R. Laks, M. Ohashi, J. DeJesus, K.-i. Kamei, K.-B. Lee, H. Wang, Z. T. F. Yu, Y.-T. Lu, S. Hou, K. Li, M. Liu, N. Zhang, S. Wang, B. Angenieux, E. Panosyan, E. R. Samuels, J. Park, D. Williams, V. Konkankit, D. Nathanson, R. M. van Dam, M. E. Phelps, H. Wu, L. M. Liau, P. S. Mischel, J. A. Lazareff, H. I. Kornblum, W. H. Yong, T. G. Graeber, H.-R. Tseng, *Cancer Res.* **2010**, *70*, 6128 – 6138.

Biomaterials 33 (2012)

Contents lists available at SciVerse ScienceDirect

Biomaterials

journal homepage: www.elsevier.com/locate/biomaterials

The therapeutic efficacy of camptothecin-encapsulated supramolecular nanoparticles

Kuan-Ju Chen [a,1], Li Tang [b,1], Mitch André Garcia [a], Hao Wang [a], Hua Lu [b], Wei-Yu Lin [a], Shuang Hou [a], Qian Yin [b], Clifton K.-F. Shen [a], Jianjun Cheng [b,*], Hsian-Rong Tseng [a,**]

[a] Department of Molecular and Medical Pharmacology, California NanoSystems Institute (CNSI), Crump Institute for Molecular Imaging (CIMI), University of California, Los Angeles, 570 Westwood Plaza, Building 114, Los Angeles, CA 90095-1770, USA
[b] Department of Materials Science and Engineering, University of Illinois at Urbana-Champaign-Urbana, 1304 West Green Street, Urbana, IL 61801, USA

ARTICLE INFO

Article history:
Received 3 September 2011
Accepted 16 October 2011
Available online 8 November 2011

Keywords:
Supramolecular assembly
Nanoparticles
Drug delivery
Positron emission tomography
Cancer therapeutics

ABSTRACT

Nanomaterials have been increasingly employed as drug(s)-incorporated vectors for drug delivery due to their potential of maximizing therapeutic efficacy while minimizing systemic side effects. However, there have been two main challenges for these vectors: (i) the existing synthetic approaches are cumbersome and incapable of achieving precise control of their structural properties, which will affect their biodistribution and therapeutic efficacies, and (ii) lack of an early checkpoint to quickly predict which drug(s)-incorporated vectors exhibit optimal therapeutic outcomes. In this work, we utilized a new rational developmental approach to rapidly screen nanoparticle (NP)-based cancer therapeutic agents containing a built-in companion diagnostic utility for optimal therapeutic efficacy. The approach leverages the advantages of a self-assembly synthetic method for preparation of two different sizes of drug-incorporated supramolecular nanoparticles (SNPs), and a positron emission tomography (PET) imaging-based biodistribution study to quickly evaluate the accumulation of SNPs at a tumor site *in vivo* and select the favorable SNPs for *in vivo* therapeutic study. Finally, the enhanced *in vivo* anti-tumor efficacy of the selected SNPs was validated by tumor reduction/inhibition studies. We foresee our rational developmental approach providing a general strategy in the search of optimal therapeutic agents among the diversity of NP-based therapeutic agents.

1. Introduction

Nanoparticles (NPs) have been regarded as promising vectors for controlled delivery of anti-cancer drug(s), providing an emerging therapeutic strategy with enhanced anti-tumor efficacy and reduced systemic side effects [1–10]. However, even after decades of development, there are few successful examples that have reached clinical usage [2,11]. One of the major bottlenecks can be attributed to the expensive, time-consuming and labor-intensive pipeline adopted for the development of drug(s)-incorporated NPs, by which numerous optimization/evaluation cycles, including molecular design, multistep syntheses and *in vitro*/*in vivo* assays are repeated. Such a developmental pipeline does not guarantee generating drug(s)-incorporated NPs that exhibit improved therapeutic efficacy in clinic.

Herein, we utilize a new rational developmental approach to rapidly screen NP-based cancer therapeutic agents containing a built-in companion diagnostic utility for optimal therapeutic efficacy. The approach leverages the advantages of a self-assembly synthetic method for preparation of supramolecular nanoparticles (SNPs), and a positron emission tomography (PET) imaging-based biodistribution study to quickly evaluate the accumulation of SNPs at a tumor site *in vivo*. The self-assembly synthetic method enables a convenient, flexible and modular production of a small collection of drug-incorporated NPs with precisely controlled sizes ranging from 37 to 104 nm, below the threshold of NP size (200 nm) that allows the efficient extravasation of NPs into the leaky tumor vasculatures and accumulation of the NPs in the tumor tissues via enhanced permeability and retention (EPR) effect [12–17].

* Corresponding author. Tel.: +1 217 244 3924; fax: +1 217 333 2736.
** Corresponding author. Department of Medical and Molecular Pharmacology, University of California, Los Angeles, 570 Westwood Plaza, Building 114, Los Angeles, CA 90095-1770, USA. Tel.: +1 310 794 1977; fax: +1 310 206 8975.
E-mail addresses: jianjunc@illinois.edu (J. Cheng), hrtseng@mednet.ucla.edu (H.-R. Tseng).
URLs: http://cheng.mse.uiuc.edu/index.htm, http://labs.pharmacology.ucla.edu/tsenglab/
[1] These authors contributed equally to the work.

0142-9612/$ – see front matter © 2011 Elsevier Ltd. All rights reserved.
doi:10.1016/j.biomaterials.2011.10.044

Subsequently, PET imaging-based biodistribution studies are employed to correlate the sizes of drug-incorporated NPs with their delivery performances. Thus, a specific size of drug-incorporated NPs that exhibit optimal accumulation and prolonged retention in tumor tissue can be readily identified, resulting in potentially the lead modality with improved therapeutic efficacy and reduced side effect that is subject to comprehensive pre-clinical studies.

Previously, we demonstrated a convenient, flexible, and modular self-assembly synthetic method for crafting SNPs as outstanding delivery vectors for highly efficient delivery of genes, [18,19] proteins [20] and inorganic nanoparticles [21]. Given the versatile utility of such a self-assembly synthetic method, we attempted to explore the use of SNP-based vectors for delivering an anti-cancer drug. In this case, camptothecin (CPT), a cytotoxic quinoline alkaloid that inhibits the topoisomerase I, was selected for the proof-of-concept demonstration. On the other hand, we have already demonstrated the incorporation of radioisotopes and a contrast agent into SNPs for PET [22] and magnetic resonance (MR) imaging, [23] respectively. PET imaging [24–26] is a sensitive, non-invasive technology that can be utilized to determine the biodistribution profiles of small molecules, polymers or NPs at a whole body level. The resulting biodistribution information [27] can be utilized to facilitate the implementation of pre-clinical studies. Moreover, once the drug-incorporated NPs with optimal therapeutic efficacy are identified, they will contain a built-in companion diagnostic utility that can be readily utilized if desired.

2. Materials and methods

2.1. General

Camptothecin (CPT) and other chemicals were purchased from Sigma–Aldrich (St. Louis, MO) and used as received without further purification unless otherwise noted. 1-Adamantanamine (Ad) hydrochloride and β-cyclodextrin (β-CD) were purchased from TCI America (San Francisco, CA). N-hydroxysuccinimide (SCM) and maleimido (MAL) hetero-functionalized poly(ethylene glycol) (SCM-PEG-MAL, MW = 5 kD) were obtained from NANOCS Inc (New York, NY). CD-grafted branched poly(ethylenimine) (CD-PEI), Ad-grafted poly(ethylene glycol) (Ad-PEG) and DOTA-grafted CD-PEI (CD-PEI-DOTA) were prepared via the method previously reported by our group [22,23]. Phosphate-Buffered Saline (PBS), Dulbecco's Modified Eagle Medium (DMEM), Eagle's Minimum Essential Medium (EMEM), and penicillin/streptomycin were obtained from Invitrogen (Carlsbad, CA). MCF7 breast cancer cell line and Lewis Lung Carcinoma (LLC) cell line were purchased from American Type Culture Collection (Manassas, VA). Fetal Bovine Serum (FBS) was obtained from Lonza Walkerrsville Inc (Walkerrsville, MD). 96 well BD Falcon culture plates were purchased from Fisher Scientific. CellTiter-Blue® Cell Viability Assay was purchased from Promega Corporation (Madison, WI). Human serum was purchased from Sigma–Aldrich.

The molecular weight of the PBLG were determined on a gel permeation chromatograph (GPC, also called size-exclusion chromatography (SEC)) equipped with an isocratic pump (Model 1100, Agilent Technology, Santa Clara, CA), a DAWN HELEOS 18-angle laser light scattering detector (Wyatt Technology, Santa Barbara, CA), and an Optilab rEX refractive index detector (Wyatt Technology, Santa Barbara, CA). The wavelength of the HELEOS detector was set at 658 nm. The size-exclusion columns used were serially connected on the GPC (Phenogel columns 100 Å, 500 Å, 103 Å and 104 Å, 5 μm, 300 × 7.8 mm, Phenomenex, Torrance, CA). DMF (HPLC grade) was used as the mobile phase for GPC. HPLC analysis was performed on a Beckman Gold system (Beckman Coulter, Fullerton, CA) equipped with a 126P solvent module, a System Gold 128 UV detector and an analytical C18 column (Luna C18, 250 × 4.6 mm, 5 μ, Phenomenex, Torrance, CA). NMR analyses were conducted on a Varian U500, VXR500 or UI500NB (500 MHz).

2.2. Synthesis of Poly(L-glutamic acid) (PGA)

Poly(γ-benzyl-L-glutamate) ($PBLG_{50}$) was synthesized according to the procedure previously published. [28,29] The N-terminus of PBLG was capped by a carbobenzyloxy (Cbz) group. The M_n was 12,600 g/mol and the MW distributions (MWD = M_w/M_n) was 1.05 as determined by GPC (Fig. S1 in Supporting Information). The deprotection of $PBLG_{50}$ was performed using standard HBr condition as described below: $PBLG_{50}$ (500 mg, 2.28 mmol glutamate residues) was dissolved in TFA (15 mL) in an ice bath. HBr (33 wt% in HOAc, 4 mL) was added dropwise into stirred solution. The reaction mixture was stirred in the ice bath for an additional 2 h and then poured into cold ether (60 mL) in two 50-mL centrifuge tubes. The polymer precipitate was collected by centrifuge and washed with ether (30 mL × 3). The polymer was dried under vacuum to give the crude product. The polymer was dissolved in NaOH (2 M × 10 mL) and was stirred at room temperature (rt)

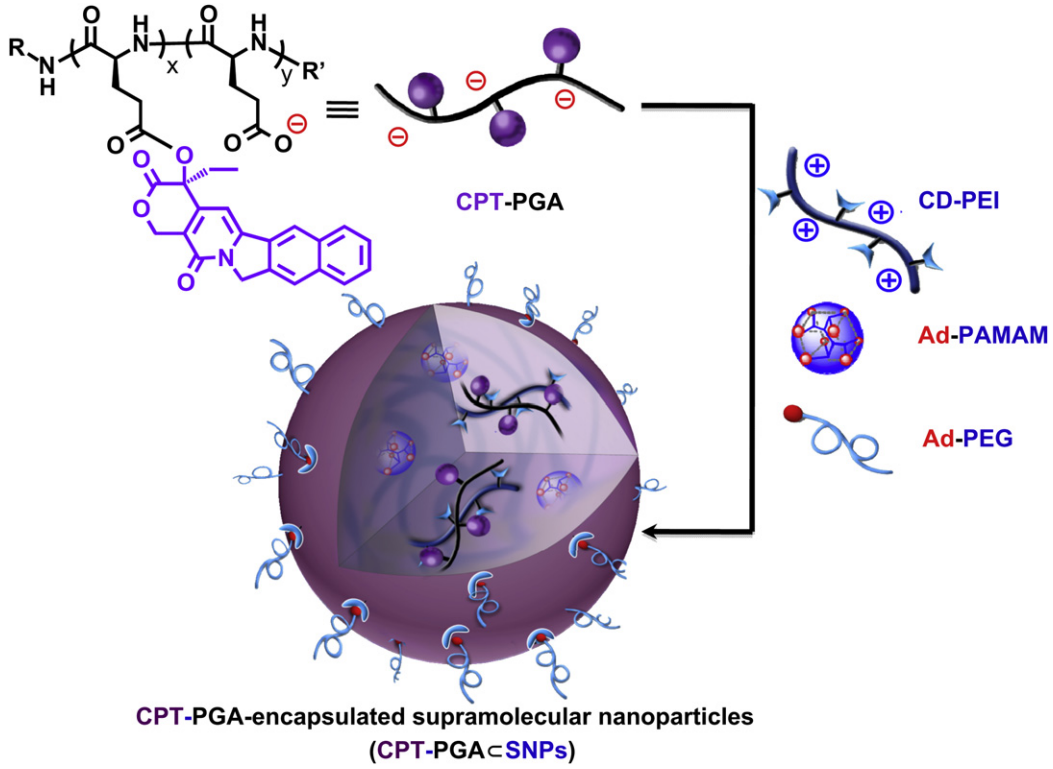

Scheme 1. Schematic representations of the self-assembly synthetic method for the production of CPT-grafted PGA encapsulated Supramolecular NanoParticles (CPT-PGA⊂SNPs) from the respective molecular building blocks and CPT-PGA (camptothecin-grafted poly(L-glutamic acid)).

overnight. The clear solution was acidified by 2 M HCl to pH 2. The product was purified by dialysis against DI water and dried by lyophilization to give a white powder. ^{1}H NMR (D_2O, 500 MHz): δ 4.86 (1H), 2.68 (2H), 2.34 (1H), 2.19 (1H).

2.3. Synthesis of Poly(L-glutamic acid)-g-camptothecin (CPT-grafted PGA, CPT-PGA)

The synthesis of CPT-PGA (Scheme 2) was performed with a slightly modified protocol as reported before. [30] Bis(2-oxo-3-oxazolidinyl)phosphonic chloride (BOP-Cl, 175 mg, 0.68 mmol), DMAP (170 mg, 1.4 mmol), and diisopropyletheylamine (74 mg, 0.57 mmol) were added under nitrogen to a suspension of CPT (131 mg, 0.38 mmol) and dry PGA_{50} (310 mg, 2.4 mmol Glu) in anhydrous DMF (20 mL) cooled in an ice bath. The mixture was warmed to rt, stirred at 40 °C for 2 days, and cooled down in an ice bath. A 10% aqueous NaCl solution (40 mL) was added slowly to the reaction mixture under stirring. The resulting suspension was acidified to pH 2.5 by hydrochloric acid (0.5 M). The mixture was allowed to stir at rt for 1 h. The precipitate was filtered, washed with water (4 × 30 mL), dried under vacuum (<1 mm, 12 h), and ground to a powder. The precipitate was suspended in 2% MeOH-CH_2Cl_2 (10 mL), stirred for 3 h, and filtered. This process was repeated 4 times to effect complete removal of free CPT. The product was then dried under vacuum to give 220 mg of CPT-PGA (yield 56%). Loading of CPT was 20–22 wt% determined by ^{1}H NMR (TFA-*d*, 500 MHz). The ^{1}H NMR data of the obtained CPT-PGA was similar as reported by the literature. (Fig. S2 in Supporting Information).

2.4. Synthesis of PGA⊂SNPs (drug-free vectors)

To a 200-μL solution of Ad-PEG (10 mg, 50 mg/mL), 10-μL DMSO solution of Ad-PAMAM (24 mg/mL) was slowly injected under vigorous stirring. Followed by addition of 120-μL CD-PEI (10.44 mg, 87 mg/mL) into the mixture and incubating at rt for 20 min. After the incubation, the mixture was slowly added into 700-μL CPT-PGA (10 mg/mL) solution and heated to 50 °C for an additional 20 min. PGA⊂SNPs with the size of 35 ± 5 nm were obtained after the solution cooled down.

2.5. Synthesis of CPT-PGA encapsulated SNPs (CPT-PGA⊂SNPs)

To a 200-μL solution of Ad-PEG (10 mg, 50 mg/mL), 10-μL DMSO solution of Ad-PAMAM with various concentrations (22 and 44 mg/mL) was slowly injected under vigorous stirring. Followed by addition of 120-μL CD-PEI (10.44 mg, 87 mg/mL) into the mixture and incubating at rt for 20 min. After the incubation, the mixture was slowly added into 700-μL CPT-PGA (10 mg/mL) solution and heated to 50 °C for an additional 20 min. Two different sizes of CPT-PGA⊂SNPs (37-nm and 104-nm CPT-PGA⊂SNPs) were obtained after the solution cooled down.

2.6. Synthesis of DOTA-grafted CPT-PGA⊂SNPs

To a 200-μL solution of Ad-PEG (10 mg, 50 mg/mL), 10-μL DMSO solution of Ad-PAMAM with two different concentrations (22, 44 mg/mL) was slowly injected under vigorous stirring followed by addition of 120-μL CD-PEI-DOTA (10 mg, 87 mg/mL) into the mixture. The mixture was incubated at rt for 20 min. After the incubation, the mixture was slowly added into 700-μL CPT-PGA (10 mg/mL) solution and heated to 50 °C for another 20 min. The resulting DOTA-grafted CPT-PGA⊂SNPs (37-nm and 104-nm, respectively) were obtained when the solution was cooled to rt.

2.7. ^{64}Cu labeling of DOTA-grafted CPT-PGA⊂SNPs

All liquids were pretreated with Chelex-100 (Bio-Rad, Herchules, CA) to remove trace amount of metal contaminants. The ^{64}Cu chloride (Washington university at St. Louis) was mixed with NH_4OAc buffer (pH 5.5, I = 0.1 M); DOTA-grafted CPT-PGA⊂SNPs in 800-fold excess were added to the solution. The mixture was incubated for 1 h at 60 °C. The ^{64}Cu-labeled DOTA-grafted CPT-PGA⊂SNPs product was purified by a molecular weight cut off filter (Centricon YM10, Billerica, MA) at 10,000 × *g* for 10 min. The labeling yield (>95%) was determined by measuring the radioactivity in the filter, the filtrate and the retaintate, respectively. The ^{64}Cu-labeled DOTA-grafted CPT-PGA⊂SNPs were re-suspended in saline for *in vivo* injections.

2.8. Dynamic light scattering (DLS)

DLS experiments were performed with a Zetasizer Nano instrument (Malvern Instruments Ltd., United Kingdom) equipped with a 10-mW helium-neon laser (λ = 632.8 nm) and thermoelectric temperature controller. Measurements were taken at a 90° scattering angle.

2.9. Transmission electron microscope (TEM)

The morphology and sizes of CPT-PGA⊂SNPs were examined on a Philips CM 120 transmission electron microscope (TEM), operating at an acceleration voltage of 120 kV. The TEM samples were prepared by drop-coating 2-μL of CPT-PGA⊂SNPs solutions onto carbon-coated copper grids. Excess amounts of droplets were removed with filter paper after 45 s. Subsequently, the surface-deposited CPT-PGA⊂SNPs were negatively stained with 2% uranyl acetate for 45 s before TEM studies.

2.10. Zeta potential (ζ) measurements

Zeta potentials of CPT-PGA⊂SNPs were determined by photon correlation spectroscopy using a Zetasizer Nano instrument (Malvern Instruments, Malvern, Worcestershire, UK). The measurements were performed at 25 °C with a detection

A

Formulation	TEM	DLS	Zeta potential
37-nm CPT-PGA⊂SNPs	37 ± 8 nm	56 ± 4 nm	-11 ± 0.7 mV
104-nm CPT-PGA⊂SNPs	104 ± 12 nm	180 ± 11 nm	-4 ± 0.2 mV

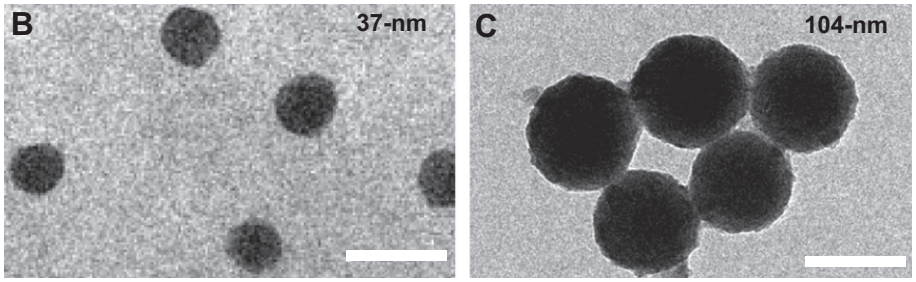

Fig. 1. Two different sizes of CPT-PGA⊂SNPs were obtained by altering the mixing ratio between two building blocks (Ad-PAMAM and CD-PEI). (A) The characterizations of the resulting CPT-PGA⊂SNPs. (B and C) TEM images of 37-nm and 104-nm CPT-PGA⊂SNPs, respectively. Scale bar = 100 nm.

angle of 90°, and the raw data were subsequently correlated to Z average mean size using a cumulative analysis by the Zetasizer software package.

2.11. Drug encapsulation efficiency

Free CPT was removed from CPT-PGA⊂SNPs by centrifugation of CPT-PGA⊂SNPs solution at 1300 rpm for 30 min using centrifugal filter devices (3000 NMWL). After recovering the filtrate containing free CPT, CPT concentration was analyzed by ultraviolet absorption at a wavelength of 370 nm. The measurements were performed in triplicate. The amount of the CPT encapsulated in the SNPs was then calculated by the total loading amount of CPT subtracts the free CPT in the filtrate.

2.12. Time-dependent stability study

To ensure the *in vivo* stability of the resulting CPT-PGA⊂SNPs, it is critical to examine their size variation under a physiological ionic strength. Following the procedure described above, the 37-nm and 104-nm CPT-PGA⊂SNPs were prepared in PBS solutions (pH = 7.2, containing 1.5 mM KH_2PO_4, 155 mM NaCl and 2.7 mM Na_2HPO_4). After mixing the three molecular building blocks in their respective ratios, we employed real-time DLS measurements to monitor the hydrodynamic size variation of the 37-nm and 104-nm CPT-PGA⊂SNPs at different times. The sizes of CPT-PGA⊂SNPs were recorded up to 6 days.

2.13. Drug release profile

CPT-PGA (0.249 mg/mL) or 37-nm CPT-PGA⊂SNPs (0.977 mg/mL) was dispersed in 50% human serum (human serum:1 × PBS = 1:1, v/v) and equally distributed to 20 vials with 1 mL solution per vial, and then incubated at 37 °C. At selected time intervals, one selected vial of each group was taken out of the incubator. The solution was mixed with an equal volume of methanol (1 mL) and centrifuged at 15,000 rpm for 10 min. The supernatant (1 mL) was transferred to an eppendorf tube without disturbing the precipitates and brought to pH 2 with phosphoric acid (85%, 100 μL). The resulting solution was directly injected into an HPLC equipped with an analytical C18 column. A mixture of acetonitrile and water (containing 0.1% TFA) at a volume ratio of 1:3 was used as the mobile phase. The flow rate was set at 1 mL/min. The area of the HPLC peak of the released CPT (λ_{abs} = 370 nm) was intergraded for the quantification of CPT as compared to a standard curve of free CPT prepared separately. The accumulative release of CPT is shown in Fig. 2B.

2.14. In vitro cell viability

Cell viability was measured by the MTT assay. After incubating MCF-7 breast cancer cell line with 100-μL 37-nm CPT-PGA⊂SNPs, 104-nm CPT-PGA⊂SNPs, free CPT, CPT-PGA and PGA⊂SNPs with respective concentrations in 96 well-plates for 48 h, the solutions were removed and washed with PBS three times. Fresh medium containing 20-μL CellTiter-Blue reagent was added to each well, followed by 3 h incubation at 37 °C. The cell viability results were quantified using fluorescent plate-reader.

2.15. Micro-PET imaging

C57BL/6 mice were purchased from DLAM Breeding Colony Services (Los Angeles, CA). All animal manipulations were performed with sterile technique and were approved by the University of California at Los Angeles Animal Research Committee (ARC protocol# 2006-135-12). C57BL/6 mice were injected subcutaneously in the right flank with LLC cells suspended in a 1:1 mixture of PBS buffer and matrigel (BD Biosciences, Franklin Lakes, NJ, USA). Prior to use in tumor induction, LLC cells were cultured in DMEM medium. Tumors were grown for 9 days and then 100-μL ^{64}Cu (150 μCi) labeled DOTA-grafted CPT-PGA⊂SNPs solution was injected via tail vein while the animal was anesthetized. Micro-PET imaging of the mice occurred 24 h post injection and was performed with a micro-PET FOCUS 220 PET scanner (Siemens, Malvern, PA). The mice were anesthetized by using 1.5–2% isoflurane in a heated (30 °C) induction chamber 15 min prior to imaging. The mice were then transferred to a heated isolation/imaging chamber for imaging. Static micro-PET scans (10 min) were then acquired. To determine the supramolecular nanoparticle concentration in various tissues, ellipsoid regions of interest were placed in the region that exhibited the highest ^{64}Cu activity as determined by visual inspection using the Amide software. Relative intensity is expressed as the percentage of activity in the organ of interest to that of the sum of all activity in the organs listed.

2.16. In vivo study

C57BL/6 mice (female) were purchased from Charles River, USA. Feed and water was available *ad libitum*. The animal study protocol was reviewed and approved by the Animal Care and Use Committee of University of Illinois at Urbana-Champaign. Female C57Bl/6 mice, 4–5 week old, were anesthetized, shaved, and prepared for implantation of the tumor cells. LLC cells were collected from culture, and 3×10^5 cells suspended in a 1:1 mixture of PBS buffer and matrigel were then injected subcutaneously into right flank of a mouse. After 6 days when tumors reached around

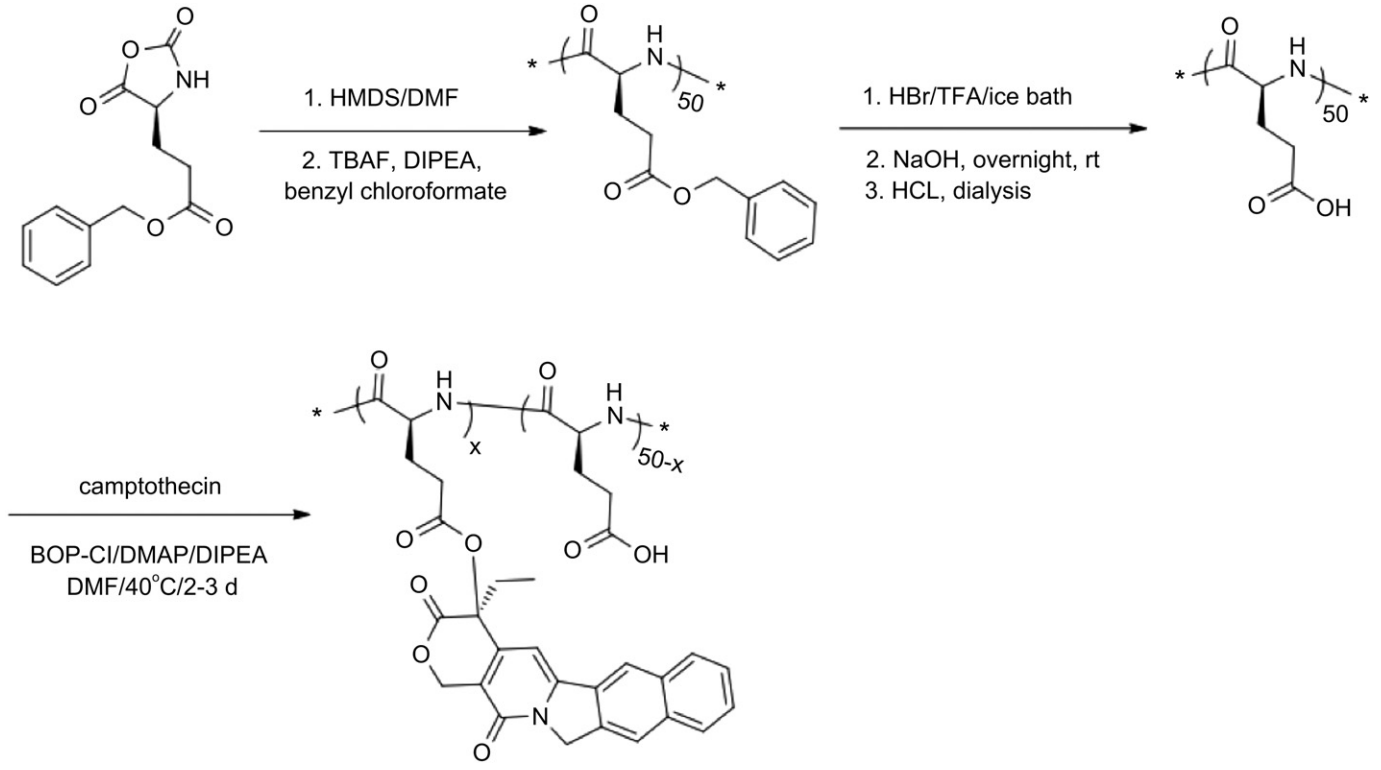

Scheme 2. Schematic representation of the synthesis of poly(L-glutamic acid)-g-camptothecin (CPT-PGA).

60–90 mm^3 in size, mice were divided into 4 groups of five mice, minimizing weight and tumor size difference. Tumor-bearing mice were treated by intravenous injection of PBS, PGA⊂SNPs, CPT-PGA⊂SNPs (13.6 mg/kg CPT) or intraperitoneal injection of CPT (13.6 mg/kg). Three doses were administrated with 5-day interval, i.e. at day 1, day 6 and day 11, respectively (except for CPT group, which only received a single dose at day 1 due to emerging toxicity [31]). After injections, the animals were monitored closely, and measurements of the tumor size and body weight for each animal were performed at regular intervals using calipers without knowledge of which injection each animal had received. The tumor volume for each time point was calculated according to the formula, (length) × $(width)^2/2$, where the long axis is the length, the short axis is the width. Tumor density is assumed as 1 mg/mm^3. If body weight loss is beyond 20% of pre-dosing weight, the animals were euthanized. When the tumor load reached 1500 mm^3 or the animal had become moribund, the mouse was sacrificed. The statistical analysis was undertaken using a Student's *t*-test (two-tailed), and *p*-values < 0.05 were considered statistically significant, $p < 0.01$ were considered highly statistically significant. Median tumor growth curves prepared for each group depicted the median tumor size as a function of time (Fig. 4A).

3. Results and discussion

Similar to the self-assembly preparation of DNA encapsulated SNPs, [18,19] which used the coulombic interactions between the negatively charged DNA plasmid with the positively charged SNP vector, 5 KD anionic poly(L-glutamic acid) (PGA) [28,29] was employed as a carrier to covalently link with CPT molecules, enabling encapsulation into SNP vectors. Approximately five CPT molecules were conjugated to each PGA polymer chain (via ester bond formation) to give CPT-grafted PGA, denoted as CPT-PGA. [30] It is noteworthy that the connecting ester bonds can be degraded via esterase-mediated hydrolysis, which allows controlled release of CPT under physiological conditions. The encapsulation of CPT-PGA into SNP vectors to generate CPT-PGA encapsulated SNPs (CPT-PGA⊂SNPs) can be accomplished (Scheme 1) by simply mixing the drug conjugated polymer, CPT-PGA (Scheme 2), with the other two SNP building blocks (CD-PEI: CD-grafted branched polyethylenimine and Ad-PAMAM: Ad-grafted polyamidoamine dendrimer), as well as a solvation ligand (Ad-PEG: Ad-grafted poly(ethylene glycol)). By altering the mixing ratios between the two SNP building blocks (Ad-PAMAM/CD-PEI = 0.125 and 0.25), two different sizes (37 and 104 nm) of CPT-PGA⊂SNPs can be obtained with narrow size distributions after annealing at 50 °C for 20 min. Both transmission electron microscopy (TEM) and dynamic light scattering (DLS) measurements were performed to characterize the sizes and morphologies of the resulting CPT-PGA⊂SNPs and the results are summarized in Fig. 1A. The hydrodynamic sizes obtained from DLS for the two different formulations were slightly larger than what was observed by TEM. These size characterizations show that the resulting CPT-PGA⊂SNPs possessed homogeneous size distributions (Fig. 1B and C). Moreover, other studies, including zeta potential (The zeta potentials of the resulting 37-nm CPT-PGA⊂SNPs and 104-nm CPT-PGA⊂SNPs are −11 ± 0.7 and −4 ± 0.2 mV, respectively.), drug encapsulation efficiency (The drug encapsulation efficiency for 37-nm and 104-nm CPT-PGA⊂SNPs are 90 ± 3% and 95 ± 2%, respectively.), stability (The results in Fig. 2A indicate that the resulting CPT-PGA⊂SNPs exhibit good stability in PBS solution under a physiological ionic strength up to 6 days.), drug release kinetics (The accumulative release of free CPT from CPT-PGA⊂SNPs was quantified by HPLC. The data in Fig. 2B point out that CPT-PGA⊂SNPs release 20% of CPT after 6

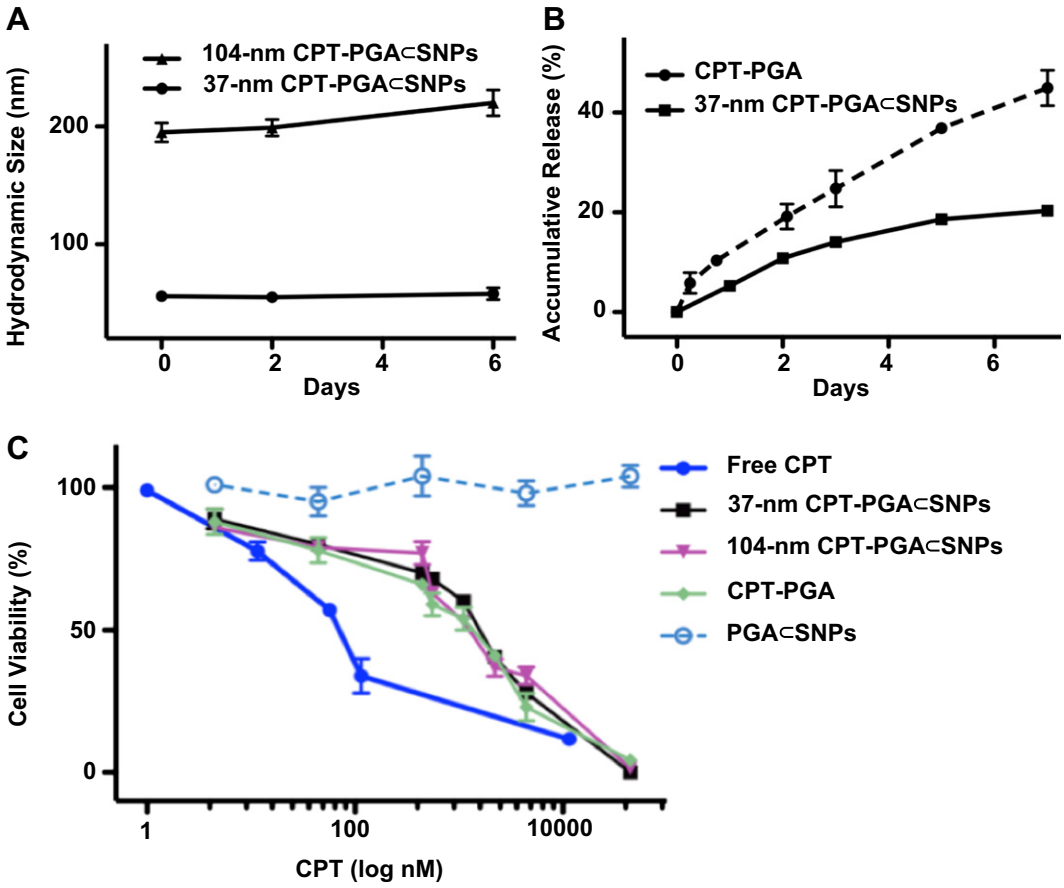

Fig. 2. (A) Time-dependent studies on the stability of 37-nm and 104-nm CPT-PGA⊂SNPs in 1 × PBS. (B) Release kinetics of CPT-PGA and 37-nm CPT-PGA⊂SNPs in 50% human serum (human serum:1 × PBS = 1:1, v/v). Released CPT was quantified by HPLC. (C) Dose-dependent cell viability studies of two different sizes of CPT-PGA⊂SNPs along with controls.

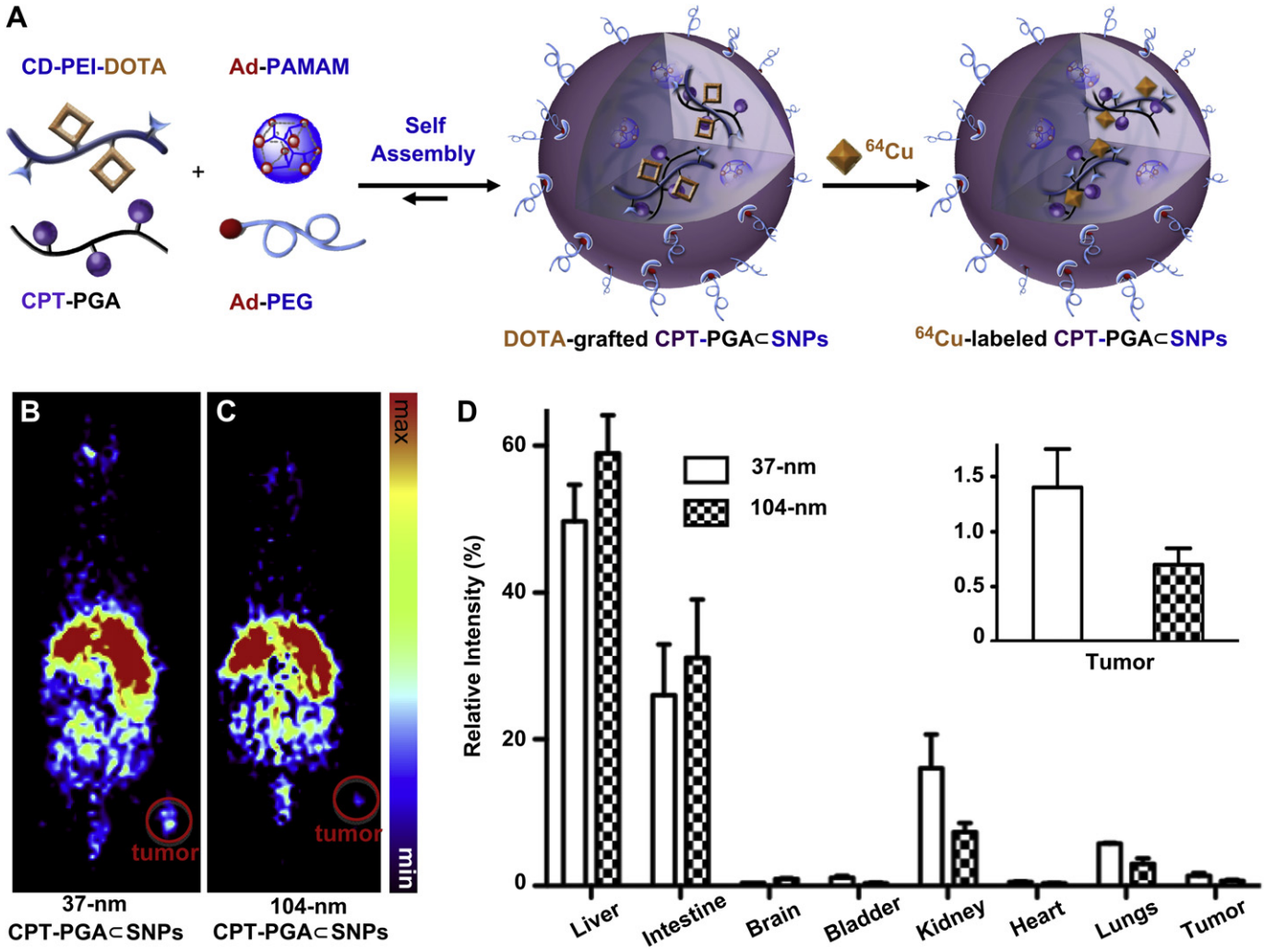

Fig. 3. (A) Schematic illustration of the incorporation of a radioisotope, *i.e.*, ^{64}Cu, into SNPs, resulting in ^{64}Cu-labeled CPT-PGA⊂SNPs. Static micro-PET images of C57Bl/6 mice bearing Lewis lung carcinoma (LLC) tumor at 24 h post injection of (B) 37-nm and (C) 104-nm ^{64}Cu-labeled CPT-PGA⊂SNPs. Tumor volumes are approximately 245 mm^3. (D) *In vivo* biodistribution of 37-nm and 104-nm ^{64}Cu-labeled CPT-PGA⊂SNPs after 24 h intravenous injection. 37-nm ^{64}Cu-labeled CPT-PGA⊂SNPs had higher tumor-specific uptake than 104-nm ^{64}Cu-labeled CPT-PGA⊂SNPs. The error bar corresponds to the standard deviation calculated by the Amide software.

days without any associated burst release.) and *in vitro* viability treatments (The IC_{50} values, the concentration at which 50% inhibition of cellular growth occurs, were around 100 nM for free CPT and approximately 400 nM for CPT-PGA⊂SNPs and CPT-PGA (Fig. 2C). There were negligible difference among CPT-PGA and the two other sizes of CPT-PGA⊂SNPs, which is probably due to the slow release of the drug from polymer (Fig. 2B). Note that the cells treated with PGA⊂SNPs present high viability, indicating low cytotoxicity attributed to our SNPs.), of the resulting CPT-PGA⊂SNPs were also carried out and the details can be found in EXPERIMENTAL SECTION.

Different sizes of CPT-PGA⊂SNPs will have distinctive biodistribution patterns and varying therapeutic performances due to their differential EPR effects [12–14]. Instead of directly performing the *in vivo* efficacy studies of all of the two sizes of CPT-PGA⊂SNPs, which would require a significant quantity of CPT-PGA⊂SNPs and a large cohort of animals, we utilized micro-PET imaging technology to understand the biodistribution properties of the 37-nm and 104-nm CPT-PGA⊂SNPs. We anticipated that the resulting biodistribution data would correlate the sizes of CPT-PGA⊂SNPs with their delivery performances. Thus, the specific size of drug-incorporated NPs that exhibit preferential accumulation in the tumor can be identified for subsequent pre-clinical studies. The radio-labeling of SNP vectors and subsequent pre-clinical micro-PET imaging in mice have been previously demonstrated by our group [22]. Similarly, ^{64}Cu-labeled CPT-PGA⊂SNPs (with the sizes of 37 and 104 nm) can be prepared (Fig. 3A) by incorporating CD-PEI-DOTA as one of the precursors (along with CD-PEI, Ad-PAMAM, Ad-PEG and CPT-PGA), followed by ratiometric mixing and labeling by ^{64}Cu (see the Experimental Section). The 37-nm and 104-nm ^{64}Cu-labeled CPT-PGA⊂SNPs were instantaneously injected into LLC tumor-bearing C57Bl/6 mice via tail vein intravenous (*i.v.*) administration. The respective biodistribution data (Fig. 3B–D) were acquired by micro-PET imaging technology 24 h post injection. Static micro-PET images of the two sizes of ^{64}Cu-labeled CPT-PGA⊂SNPs (Fig. 3B and C, respectively) revealed that 37-nm ^{64}Cu-labeled CPT-PGA⊂SNPs exhibited significantly enhanced tumor accumulation. Semi-quantitative biodistribution data (Fig. 3D and insert therein) of ^{64}Cu-labeled CPT-PGA⊂SNPs in major organs were obtained by taking the average signal per voxel in the organ of interest and multiplying that value by the total volume of the organ via Amide software (see Experimental Section). The PET imaging-based biodistribution studies revealed that the 37-nm ^{64}Cu-labeled CPT-PGA⊂SNPs exhibited 100% more accumulation in the

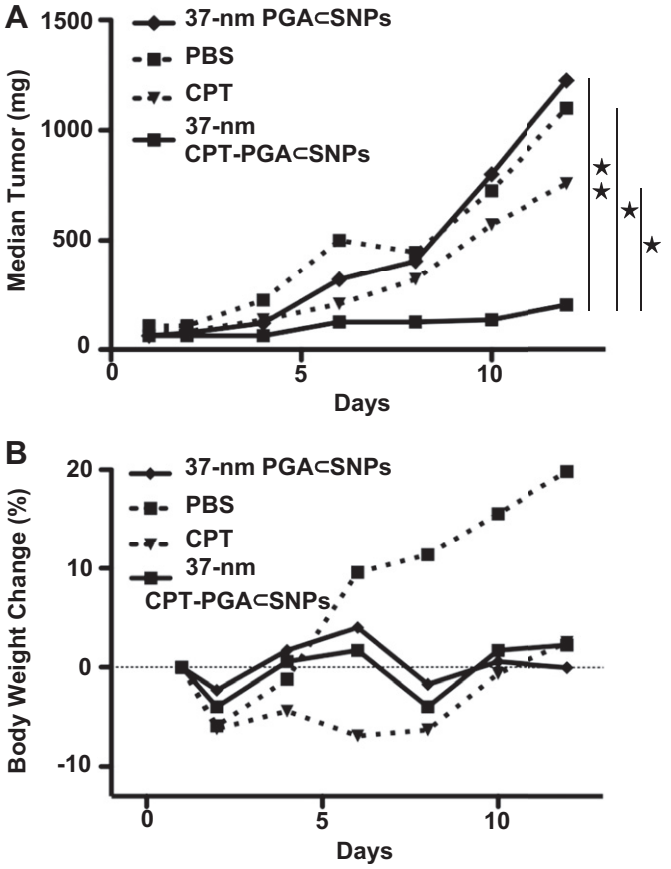

Fig. 4. (A) *In vivo* anti-tumor efficacy studies of 37-nm CPT-PGA⊂SNPs (13.6 mg CPT equivalent/kg) along with controls, *i.e.*, free CPT (13.6 mg/kg), PBS and PGA⊂SNPs (equivalent to the amount of SNPs in the CPT-PGA⊂SNPs group). LLC tumor-bearing C57Bl/6 mice were treated with different groups via intravenous injection at day 1, 6 and 11 (except for CPT group, which was only treated once at day 1 via intraperitoneal injection). 37-nm CPT-PGA⊂SNPs showed delayed tumor growth from day 6 compared to PGA⊂SNPs group and also significantly outperformed CPT group from day 4 ($^{*}p < 0.05$; $^{**}p < 0.01$; Student's *t*-test). (B) Body weight changes of the four groups over the course of treatments.

tumor than that observed for the 104-nm ^{64}Cu-labeled CPT-PGA⊂SNPs. We suggest that the preferential accumulation of 37-nm ^{64}Cu-labeled CPT-PGA⊂SNPs in xenografted LLC tumors CPT-PGA⊂SNPs is due to their higher blood retention concentrations (see Supporting Information Fig. S3) that facilitated the EPR effect [12]-mediated accumulation of the SNPs in tumors.

Given the preferential tumor accumulation of the 37-nm ^{64}Cu-labeled CPT-PGA⊂SNPs as compared to the larger SNPs, we next performed tumor reduction/inhibition studies using the 37-nm CPT-PGA⊂SNPs in C57/BL6 mice bearing subcutaneously implanted LLC tumors on the right flank. After the tumors developed to approximately 60–90 mm^3, we performed comparative efficacy studies by dividing animals into four groups ($N = 5$) in a way to minimize weight and tumor size differences. The following regimens were administrated three times via *i.v.* injection on day 1, 6 and 11 including PBS, PGA⊂SNPs (equivalent to the amount of SNPs in the CPT-PGA⊂SNP group), 37-nm CPT-PGA⊂SNPs at 13.6 mg CPT equivalent/kg, while another group received a single dose of emulsified CPT at 13.6 mg CPT/kg through intraperitoneal injection (*i.p.*). CPT is very insoluble in aqueous solution and is acutely lethal when given to mice at such a high dose via *i.v.* due to embolization induced by the particulate matter in the drug suspension [31]. Fig. 4A depicts the median tumor size for each group as a function of time, and clearly shows that the 37-nm CPT-PGA⊂SNPs had the best anti-tumor efficacy among all groups tested. As compared with PGA⊂SNPs (drug-free vectors), 37-nm CPT-PGA⊂SNPs started to show statistically significant efficacy in delaying tumor growth from day 6 ($^{*}p < 0.05$ at day 6 and 8, Student's *t*-test) and even higher significant inhibition effect at day 10 and 12 ($^{**}p < 0.01$ at day 10 and 12). However, there was no statistical significance between the data points of PGA⊂SNPs group and PBS group indicating that the efficacy of the 37-nm CPT-PGA⊂SNPs was ascribed to the released CPT. The 37-nm CPT-PGA⊂SNPs also significantly outperformed CPT in this study with statistical significance from day 6 to day 12 ($^{*}p < 0.05$). It is noteworthy that one of the five mice treated with 37-nm CPT-PGA⊂SNPs experienced complete tumor reduction on day 10. The final mean tumor burden of the 37-nm CPT-PGA⊂SNPs group was 265.5 ± 101.3 mm^3 (mean ± SEM), which was smaller than any other group ($^{*}p < 0.05$). On the other hand, no obvious body weight loss was observed for the group treated with the 37-nm CPT-PGA⊂SNPs at the tested dosage throughout the study (Fig. 4B), indicating there is no acute toxicity of the 37-nm CPT-PGA⊂SNPs. As a comparison, the CPT group showed emerging toxicity after a single dose with around 9% body weight loss at day 5 (data not shown). The results demonstrate that 37-nm CPT-PGA⊂SNPs group is the most efficacious group among all the groups with reduced toxicity compared to free drug. Presumably, the reason for the enhanced efficacy of 37-nm CPT-PGA⊂SNPs may be the preferential tumor accumulation due to EPR effect as demonstrated. After the SNPs reached the tumor tissues, the sustained release of CPT from CPT-PGA⊂SNPs (Fig. 2B) was ascribed to the extended inhibition on tumor growth.

4. Conclusion

We have successfully demonstrated a rational developmental approach that leverages the advantages of (i) a self-assembly synthetic method for preparation of SNP vectors and (ii) PET imaging technology to generate 37-nm CPT-PGA⊂SNPs with optimal therapeutic performance in tumor xenografted mouse model. The integration of the two technologies can lead to a breakthrough in the development of a new generation of cancer therapeutic agents. We foresee our work providing a general strategy in the search of optimal therapeutic agents among the diversity of NP-based therapeutic agents by utilizing imaging technology as a fast and early checkpoint prior to performing large-scale pre-clinical studies. In principle, this work can also be adopted for discovery of other NP-based vectors for delivery of various payloads (e.g., DNAs, RNAs, proteins or their combinations).

Acknowledgments

This research was supported by NIH R21 1R21EB008419 (HRT) and NIH 1R21CA152627 (JC).

Appendix. Supplementary material

Supplementary material associated with this article can be found, in the online version, at doi:10.1016/j.biomaterials.2011.10.044.

References

[1] Davis ME, Chen Z, Shin DM. Nanoparticle therapeutics: an emerging treatment modality for cancer. Nat Rev Drug Discov 2008;7(9):771–82.
[2] Petros RA, DeSimone JM. Strategies in the design of nanoparticles for therapeutic applications. Nat Rev Drug Discov 2010;9(8):615–27.
[3] De M, Ghosh PS, Rotello VM. Applications of nanoparticles in biology. Adv Mater 2008;20(22):4225–41.

[4] Bae Y, Kataoka K. Intelligent polymeric micelles from functional poly(ethylene glycol)-poly(amino acid) block copolymers. Adv Drug Deliv Rev 2009;61(10): 768–84.
[5] Wiradharma N, Zhang Y, Venkataraman S, Hedrick JL, Yang YY. Self-assembled polymer nanostructures for delivery of anticancer therapeutics. Nano Today;4(4):302–317.
[6] Duncan B, Kim C, Rotello VM. Gold nanoparticle platforms as drug and biomacromolecule delivery systems. J Control Release 2010;148(1):122–7.
[7] Meng HA, Liong M, Xia TA, Li ZX, Ji ZX, Zink JI, et al. Engineered design of mesoporous silica nanoparticles to deliver doxorubicin and p-glycoprotein siRNA to overcome drug resistance in a cancer cell line. ACS Nano 2010;4(8): 4539–50.
[8] Nguyen HN, Wey SP, Juang JH, Sonaje K, Ho YC, Chuang EY, et al. The glucose-lowering potential of exendin-4 orally delivered via a pH-sensitive nanoparticle vehicle and effects on subsequent insulin secretion in vivo. Biomaterials 2011;32(10):2673–82.
[9] Sherlock SP, Tabakman SM, Xie LM, Dai HJ. Photothermally enhanced drug delivery by ultrasmall multifunctional FeCo/graphitic shell nanocrystals. ACS Nano 2011;5(2):1505–12.
[10] Chow EK, Zhang X-Q, Chen M, Lam R, Robinson E, Huang H, et al. Nanodiamond therapeutic delivery agents mediate enhanced chemoresistant tumor treatment. Sci Transl Med 2011;3:73.
[11] Peer D, Karp JM, Hong S, FaroKHzad OC, Margalit R, Langer R. Nanocarriers as an emerging platform for cancer therapy. Nat Nanotechnol 2007;2(12): 751–60.
[12] Maeda H, Wu J, Sawa T, Matsumura Y, Hori K. Tumor vascular permeability and the EPR effect in macromolecular therapeutics: a review. J Control Release 2000;65(1–2):271–84.
[13] Weissig V, Whiteman KR, Torchilin VP. Accumulation of protein-loaded long-circulating micelles and liposomes in subcutaneous Lewis lung carcinoma in mice. Pharm Res-Dordr 1998;15(10):1552–6.
[14] Decuzzi P, Godin B, Tanaka T, Lee SY, Chiappini C, Liu X, et al. Size and shape effects in the biodistribution of intravascularly injected particles. J Control Release 2010;141(3):320–7.
[15] Perrault SD, Walkey C, Jennings T, Fischer HC, Chan WCW. Mediating tumor targeting efficiency of nanoparticles through design. Nano Lett 2009;9(5): 1909–15.
[16] Matsumura Y, Maeda H. A new concept for macromolecular therapeutics in cancer-chemotherapy – mechanism of tumoritropic accumulation of proteins and the antitumor agent smancs. Cancer Res 1986;46(12):6387–92.
[17] Goodman TT, Olive PL, Pun SH. Increased nanoparticle penetration in collagenase-treated multicellular spheroids. Int J Nanomedicine 2007;2:265.
[18] Wang H, Liu K, Chen K-J, Lu Y, Wang S, Lin WY, et al. A rapid pathway toward a superb gene delivery system: programming structural and functional diversity into a supramolecular nanoparticle library. ACS Nano 2010;4(10): 6235–43.
[19] Wang H, Chen K-J, Wang S, Ohashi M, Kamei K-I, Sun J, et al. A small library of DNA-encapsulated supramolecular nanoparticles for targeted gene delivery. Chem Commun 2010;45:1851.
[20] Liu Y, Wang H, Kamei K, Yan M, Chen K-J, Yuan Q, et al. Delivery of intact transcription factor using self-assembled supramolecular nanoparticles. Angew Chem Int Ed 2011;50:3058.
[21] Wang S, Chen K-J, Wu T-H, Wang H, Lin W-Y, Ohashi M, et al. Photothermal effects of supramolecularly assembled gold nanoparticles for the targeted treatment of cancer cells. Angew Chem Int Ed 2010;49(22):3777–81.
[22] Wang H, Wang ST, Su H, Chen K-J, Armijo AL, Lin WY, et al. A supramolecular approach for preparation of size-controlled nanoparticles. Angew Chem Int Ed 2009;48(24):4344–8.
[23] Chen K-J, Wolahan MS, Wang H, Hsu C-H, Chang H-W, Durazo A, et al. A small MRI contrast agent library of gadolinium(III)-encapsulated supramolecular nanoparticles for improved relaxivity and sensitivity. Biomaterials 2011; 32(8):2160–5.
[24] Phelps ME. Positron emission tomography provides molecular imaging of biological processes. Proc Nat Acad Sci 2000;97(16):9226–33.
[25] Czernin J, Phelps ME. Positron emission tomography scanning: current and future applications. Annu Rev Med 2002;53:89–112.
[26] Phelps ME. PET: molecular imaging and its biological applications. New York: Springer; 2004.
[27] Li SD, Huang L. Pharmacokinetics and biodistribution of nanoparticles. Mol Pharmaceut 2008;5(4):496–504.
[28] Lu H, Cheng JJ. Hexamethyldisilazane-mediated controlled polymerization of alpha-amino acid N-carboxyanhydrides. J Am Chem Soc 2007;129(46): 14114–5.
[29] Lu H, Wang J, Bai Y, Lang J, Liu S, Lin Y, et al. Ionic polypeptides with unusual helical stability. Nat Commun 2011;2:206.
[30] Bhatt RL, de Vries P, Tulinsky J, Bellamy G, Baker B, Singer JW, et al. Synthesis and in vivo antitumor activity of poly(L-glutamic acid) conjugates of 20(S)-camptothecin. J Med Chem 2003;46(1):190–3.
[31] Cheng J, Khin KT, Davis ME. Antitumor activity of beta-cyclodextrin polymer - camptothecin conjugates. Mol Pharmaceut 2004;1(3):183–93.

REFERENCES

[1] Z. G. C. Mark E. Davis, Dong M. Shin, *Nature Reviews Drug Discovery* **2008**, *7*, 771-782.

[2] A. R. V. Jinjun Shi, Omid C. Farokhzad, Robert Langer, *Nano Letters* **2010**, *10*, 3223.

[3] W. C. W. C. Steven D. Perrault, *Proceedings of the National Academy of Sciences* **2010**, *107*, 11194.

[4] Á. G.-F. Banu S. Zolnik, Nakissa Sadrieh and Marina A. Dobrovolskaia, *Endocrinology* **2010**, *151*, 458-465.

[5] P. Aggarwal, J. B. Hall, C. B. McLeland, M. A. Dobrovolskaia, S. E. McNeil, *Adv Drug Deliver Rev* **2009**, *61*, 428-437.

[6] J. Kolosnjaj-Tabi, K. B. Hartman, S. Boudjemaa, J. S. Ananta, G. Morgant, H. Szwarc, L. J. Wilson, F. Moussa, *Acs Nano* **2010**, *4*, 1481-1492.

[7] M. M. Schmidt, K. D. Wittrup, *Mol Cancer Ther* **2009**, *8*, 2861-2871.

[8] S. E. Gratton, P. A. Ropp, P. D. Pohlhaus, J. C. Luft, V. J. Madden, M. E. Napier, J. M. DeSimone, *P Natl Acad Sci USA* **2008**, *105*, 11613-11618.

[9] J. M. Lehn, *Chem Soc Rev* **2007**, *36*, 151-160.

[10] aC. D. Meyer, C. S. Joiner, J. F. Stoddart, *Chemical Society Reviews* **2007**, *36*, 1705-1723; bI. Hwang, W. S. Jeon, H. J. Kim, D. Kim, H. Kim, N. Selvapalam, N. Fujita, S. Shinkai, K. Kim, *Angewandte Chemie-International Edition* **2007**, *46*, 210-213; cM. J. W. Ludden, D. N. Reinhoudt, J. Huskens, *Chemical Society Reviews* **2006**, *35*, 1122-1134; dS. Y. Park, A. K. R. Lytton-Jean, B. Lee, S. Weigand, G. C. Schatz, C. A. Mirkin, *Nature* **2008**, *451*, 553-556; eJ. F. Stoddart, H. R. Tseng, *Proc Natl Acad Sci U S A* **2002**, *99*, 4797-4800; fY. Liu, H. Wang, P. Liang, H. Y. Zhang, *Angewandte Chemie (International ed* **2004**, *43*, 2690-2694.

[11] V. P. Torchilin, *Nat Rev Drug Discov* **2005**, *4*, 145-160.

[12] L. Zhang, J. M. Chan, F. X. Gu, J. W. Rhee, A. Z. Wang, A. F. Radovic-Moreno, F. Alexis, R. Langer, O. C. Farokhzad, *Acs Nano* **2008**, *2*, 1696-1702.

[13] P. Ngweniform, G. Abbineni, B. Cao, C. Mao, *Small* **2009**, *5*, 1963-1969.

[14] P. Tanner, P. Baumann, R. Enea, O. Onaca, C. Palivan, W. Meier, *Accounts Chem Res* **2011**, *44*, 1039-1049.

[15] X. Yang, J. J. Grailer, I. J. Rowland, A. Javadi, S. A. Hurley, V. Z. Matson, D. A. Steeber, S. Gong, *Acs Nano* **2010**, *4*, 6805-6817.

[16] D. E. Discher, A. Eisenberg, *Science* **2002**, *297*, 967-973.

[17] aS. Pavlukhina, S. Sukhishvili, *Adv Drug Deliver Rev* **2011**, *63*, 822-836; bC. Oerlemans, W. Bult, M. Bos, G. Storm, J. F. Nijsen, W. E. Hennink, *Pharm Res-Dordr* **2010**, *27*, 2569-2589.

[18] T. K. Endres, M. Beck-Broichsitter, O. Samsonova, T. Renette, T. H. Kissel, *Biomaterials* **2011**, *32*, 7721-7731.

[19] J. Zhou, J. Wu, N. Hafdi, J. P. Behr, P. Erbacher, L. Peng, *Chem Commun (Camb)* **2006**, 2362-2364.

[20] J. Khandare, M. Calderon, N. M. Dagia, R. Haag, *Chem Soc Rev*, *41*, 2824-2848.

[21] T. Terada, M. Mizobata, S. Kawakami, Y. Yabe, F. Yamashita, M. Hashida, *J Drug Target* **2006**, *14*, 536-545.

[22] S. Prabha, W. Z. Zhou, J. Panyam, V. Labhasetwar, *Int J Pharmaceut* **2002**, *244*, 105-115.

[23] M. Sarikaya, C. Tamerler, A. K. Jen, K. Schulten, F. Baneyx, *Nat Mater* **2003**, *2*, 577-585.

[24] S. Angelos, Y. W. Yang, K. Patel, J. F. Stoddart, J. I. Zink, *Angew Chem Int Ed Engl* **2008**, *47*, 2222-2226.

[25] C. Park, K. Oh, S. C. Lee, C. Kim, *Angew Chem Int Ed Engl* **2007**, *46*, 1455-1457.

[26] O. Hayashida, M. Uchiyama, *J Org Chem* **2007**, *72*, 610-616.

[27] F. Sansone, M. Dudic, G. Donofrio, C. Rivetti, L. Baldini, A. Casnati, S. Cellai, R. Ungaro, *J Am Chem Soc* **2006**, *128*, 14528-14536.

[28] D. P. Weimann, H. D. Winkler, J. A. Falenski, B. Koksch, C. A. Schalley, *Nat Chem* **2009**, *1*, 573-577.
[29] Y. Kim, H. Kim, Y. H. Ko, N. Selvapalam, M. V. Rekharsky, Y. Inoue, K. Kim, *Chemistry* **2009**, *15*, 6143-6151.
[30] S. Liu, C. Ruspic, P. Mukhopadhyay, S. Chakrabarti, P. Y. Zavalij, L. Isaacs, *J Am Chem Soc* **2005**, *127*, 15959-15967.
[31] aH. Fan, Q. D. Hu, F. J. Xu, W. Q. Liang, G. P. Tang, W. T. Yang, *Biomaterials* **2012**, *33*, 1428-1436; bM. E. Davis, J. E. Zuckerman, C. H. Choi, D. Seligson, A. Tolcher, C. A. Alabi, Y. Yen, J. D. Heidel, A. Ribas, *Nature* **2010**, *464*, 1067-1070.
[32] S. S. Agasti, M. Liong, C. Tassa, H. J. Chung, S. Y. Shaw, H. Lee, R. Weissleder, *Angew Chem Int Ed Engl* **2012**, *51*, 450-454.
[33] aY. Ping, C. Liu, Z. Zhang, K. L. Liu, J. Chen, J. Li, *Biomaterials* **2011**, *32*, 8328-8341; bX. Lu, Y. Ping, F. J. Xu, Z. H. Li, Q. Q. Wang, J. H. Chen, W. T. Yang, G. P. Tang, *Bioconjugate Chem* **2010**, *21*, 1855-1863.
[34] Q. D. Hu, H. Fan, Y. Ping, W. Q. Liang, G. P. Tang, J. Li, *Chem Commun* **2011**, *47*, 5572-5574.
[35] R. Dong, L. Zhou, J. Wu, C. Tu, Y. Su, B. Zhu, H. Gu, D. Yan, X. Zhu, *Chem Commun* **2011**, *47*, 5473-5475.
[36] aJ. Zhang, P. X. Ma, *Angew Chem Int Ed Engl* **2009**, *48*, 964-968; bA. L. Laza-Knoerr, R. Gref, P. Couvreur, *J Drug Target* **2010**, *18*, 645-656.
[37] A. Schroeder, D. A. Heller, M. M. Winslow, J. E. Dahlman, G. W. Pratt, R. Langer, T. Jacks, D. G. Anderson, *Nat Rev Cancer* **2012**, *12*, 39-50.
[38] P. K. Jain, X. Huang, I. H. El-Sayed, M. A. El-Sayed, *Acc Chem Res* **2008**, *41*, 1578-1586.
[39] H. S. Choi, W. Liu, F. Liu, K. Nasr, P. Misra, M. G. Bawendi, J. V. Frangioni, *Nat Nanotechnol* **2009**, *5*, 42-47.
[40] J. H. Lee, K. Lee, S. H. Moon, Y. Lee, T. G. Park, J. Cheon, *Angew Chem Int Ed Engl* **2009**, *48*, 4174-4179.
[41] aM. E. Davis, Z. G. Chen, D. M. Shin, *Nature reviews. Drug discovery* **2008**, *7*, 771-782; bJ. J. Green, R. Langer, D. G. Anderson, *Accounts Chem Res* **2008**.
[42] J. S. Choi, J. C. Park, H. Nah, S. Woo, J. Oh, K. M. Kim, G. J. Cheon, Y. Chang, J. Yoo, J. Cheon, *Angew Chem Int Ed Engl* **2008**, *47*, 6259-6262.
[43] H. Wang, S. Wang, H. Su, K. J. Chen, A. L. Armijo, W. Y. Lin, Y. Wang, J. Sun, K. Kamei, J. Czernin, C. G. Radu, H. R. Tseng, *Angew Chem Int Ed Engl* **2009**, *48*, 4344-4348.
[44] aJ. Xu, G. Sun, R. Rossin, A. Hagooly, Z. Li, K. I. Fukukawa, B. W. Messmore, D. A. Moore, M. J. Welch, C. J. Hawker, K. L. Wooley, *Macromolecules* **2007**, *40*, 2971-2973; bP. A. Bertin, J. M. Gibbs, C. K. Shen, C. S. Thaxton, W. A. Russin, C. A. Mirkin, S. T. Nguyen, *J Am Chem Soc* **2006**, *128*, 4168-4169.
[45] M. E. Davis, M. E. Brewster, *Nature reviews. Drug discovery* **2004**, *3*, 1023-1035.
[46] N. Erathodiyil, J. Y. Ying, *Accounts Chem Res* **2011**, *44*, 925-935.
[47] aE. Boisselier, D. Astruc, *Chem Soc Rev* **2009**, *38*, 1759-1782; bC. M. Cobley, J. Chen, E. C. Cho, L. V. Wang, Y. Xia, *Chem Soc Rev* **2011**, *40*, 44-56.
[48] aJ. W. Kim, E. I. Galanzha, E. V. Shashkov, H. M. Moon, V. P. Zharov, *Nat Nanotechnol* **2009**, *4*, 688-694; bP. K. Jain, X. Huang, I. H. El-Sayed, M. A. El-Sayed, *Accounts Chem Res* **2008**, *41*, 1578-1586.
[49] aJ. T. Jang, H. Nah, J. H. Lee, S. H. Moon, M. G. Kim, J. Cheon, *Angew Chem Int Ed Engl* **2009**, *48*, 1234-1238; bV. I. Shubayev, T. R. Pisanic, 2nd, S. Jin, *Adv Drug Deliver Rev* **2009**, *61*, 467-477.
[50] aS. E. Skrabalak, J. Chen, Y. Sun, X. Lu, L. Au, C. M. Cobley, Y. Xia, *Accounts Chem Res* **2008**, *41*, 1587-1595; bJ. Park, J. Joo, S. G. Kwon, Y. Jang, T. Hyeon, *Angew Chem Int Ed Engl* **2007**, *46*, 4630-4660.
[51] A. M. Gobin, E. M. Watkins, E. Quevedo, V. L. Colvin, J. L. West, *Small* **2010**, *6*, 745-752.
[52] S. Lal, S. E. Clare, N. J. Halas, *Accounts Chem Res* **2008**, *41*, 1842-1851.

[53] A. Shiotani, Y. Akiyama, T. Kawano, Y. Niidome, T. Mori, Y. Katayama, T. Niidome, *Bioconjugate Chem* **2010**, *21*, 2049-2054.
[54] aY. Xia, W. Li, C. M. Cobley, J. Chen, X. Xia, Q. Zhang, M. Yang, E. C. Cho, P. K. Brown, *Accounts Chem Res* **2011**, *44*, 914-924; bJ. Chen, C. Glaus, R. Laforest, Q. Zhang, M. Yang, M. Gidding, M. J. Welch, Y. Xia, *Small* **2010**, *6*, 811-817.
[55] X. Huang, P. K. Jain, I. H. El-Sayed, M. A. El-Sayed, *Laser Med Sci* **2008**, *23*, 217-228.
[56] A. R. Lowery, A. M. Gobin, E. S. Day, K. Y. Shah, N. J. Halas, J. L. West, *Clin Cancer Res* **2005**, *11*, 9097S-9097S.
[57] aS. Mitragotri, J. Lahann, *Nat Mater* **2009**, *8*, 15-23; bA. E. Nel, L. Madler, D. Velegol, T. Xia, E. M. Hoek, P. Somasundaran, F. Klaessig, V. Castranova, M. Thompson, *Nat Mater* **2009**, *8*, 543-557.
[58] aB. Khlebtsov, V. Zharov, A. Melnikov, V. Tuchin, N. Khlebtsov, *Nanotechnology* **2006**, *17*, 5167-5179; bD. J. Maxwell, J. R. Taylor, S. Nie, *J Am Chem Soc* **2002**, *124*, 9606-9612.
[59] D. Lapotko, E. Lukianova, M. Potapnev, O. Aleinikova, A. Oraevsky, *Cancer Lett* **2006**, *239*, 36-45.
[60] H. H. Richardson, M. T. Carlson, P. J. Tandler, P. Hernandez, A. O. Govorov, *Nano Lett* **2009**, *9*, 1139-1146.
[61] H. Wang, K. J. Chen, S. Wang, M. Ohashi, K. Kamei, J. Sun, J. H. Ha, K. Liu, H. R. Tseng, *Chem Commun* **2010**, *46*, 1851-1853.
[62] J. M. Harris, R. B. Chess, *Nature reviews. Drug discovery* **2003**, *2*, 214-221.
[63] M. V. Rekharsky, Y. Inoue, *Chem Rev* **1998**, *98*, 1875-1918.
[64] V. Kotaidis, C. Dahmen, G. von Plessen, F. Springer, A. Plech, *The Journal of chemical physics* **2006**, *124*, 184702.
[65] aD. O. Lapotko, E. Lukianova, A. A. Oraevsky, *Laser Surg Med* **2006**, *38*, 631-642; bY. F. Huang, K. Sefah, S. Bamrungsap, H. T. Chang, W. Tan, *Langmuir : the ACS journal of surfaces and colloids* **2008**, *24*, 11860-11865; cC. Wang, J. Chen, T. Talavage, J. Irudayaraj, *Angew Chem Int Ed Engl* **2009**, *48*, 2759-2763.
[66] H. Mok, D. J. Palmer, P. Ng, M. A. Barry, *Molecular therapy : the journal of the American Society of Gene Therapy* **2005**, *11*, 66-79.
[67] H. B. Na, I. C. Song, T. Hyeon, *Adv Mater* **2009**, *21*, 2133-2148.
[68] E. A. Waters, S. A. Wickline, *Basic Res Cardiol* **2008**, *103*, 114-121.
[69] W. A. Gibby, *Radiol Clin North Am* **1988**, *26*, 1047-1058.
[70] J. S. Ananta, B. Godin, R. Sethi, L. Moriggi, X. Liu, R. E. Serda, R. Krishnamurthy, R. Muthupillai, R. D. Bolskar, L. Helm, M. Ferrari, L. J. Wilson, P. Decuzzi, *Nat Nanotechnol* **2010**, *5*, 815-821.
[71] M. V. Yigit, A. Moore, Z. Medarova, *Pharm Res-Dordr* **2012**.
[72] aZ. R. Stephen, F. M. Kievit, M. Zhang, *Mater Today (Kidlington)* **2011**, *14*, 330-338; bJ. Xie, G. Liu, H. S. Eden, H. Ai, X. Chen, *Accounts Chem Res* **2011**, *44*, 883-892.
[73] A. Demortiere, P. Panissod, B. P. Pichon, G. Pourroy, D. Guillon, B. Donnio, S. Begin-Colin, *Nanoscale* **2011**, *3*, 225-232.
[74] Y. W. Jun, Y. M. Huh, J. S. Choi, J. H. Lee, H. T. Song, S. Kim, S. Yoon, K. S. Kim, J. S. Shin, J. S. Suh, J. Cheon, *J Am Chem Soc* **2005**, *127*, 5732-5733.
[75] S. Wang, K. J. Chen, T. H. Wu, H. Wang, W. Y. Lin, M. Ohashi, P. Y. Chiou, H. R. Tseng, *Angew Chem Int Ed Engl* **2010**, *49*, 3777-3781.
[76] aR. Weissleder, M. J. Pittet, *Nature* **2008**, *452*, 580-589; bT. F. Massoud, S. S. Gambhir, *Genes Dev* **2003**, *17*, 545-580.
[77] aK. Chen, P. S. Conti, *Adv Drug Deliver Rev* **2010**, *62*, 1005-1022; bS. S. Gambhir, *Nat Rev Cancer* **2002**, *2*, 683-693; cR. Weissleder, *Science* **2006**, *312*, 1168-1171.
[78] aK. Kikuchi, *Chem Soc Rev* **2010**, *39*, 2048-2053; bK. Chen, X. Chen, *Curr Top Med Chem* **2010**, *10*, 1227-1236; cY. W. Jun, J. H. Lee, J. Cheon, *Angew Chem Int Ed Engl* **2008**, *47*, 5122-5135.

[79] J. Cheon, J. H. Lee, *Accounts Chem Res* **2008**, *41*, 1630-1640.
[80] D. Yoo, J. H. Lee, T. H. Shin, J. Cheon, *Accounts Chem Res* **2011**, *44*, 863-874.
[81] aM. E. Phelps, *Proc. Nat. Acad. Sci.* **2000**, *97*, 9226-9233; bJ. Czernin, M. E. Phelps, *Annual Review of Medicine* **2002**, *53*, 89-112; cM. E. Phelps, *PET : molecular imaging and its biological applications*, Springer, New York, **2004**.
[82] Y. Matsumura, H. Maeda, *Cancer Res* **1986**, *46*, 6387-6392.
[83] H. Maeda, *Adv Enzyme Regul* **2001**, *41*, 189-207.
[84] aM. J. Welch, C. J. Hawker, K. L. Wooley, *J. Nucl. Med.* **2009**, *50*, 1743-1746; bM. E. Davis, T. Schluep, J. Hwang, I. J. Hildebrandt, J. Czernin, C. H. J. Choi, C. A. Alabi, B. C. Mack, *Proc. Natl. Acad. Sci. U. S. A.* **2009**, *106*, 11394-11399.
[85] T. Schluep, J. Hwang, I. J. Hildebrandt, J. Czernin, C. H. Choi, C. A. Alabi, B. C. Mack, M. E. Davis, *P Natl Acad Sci USA* **2009**, *106*, 11394-11399.
[86] L. J. Peek, C. R. Middaugh, C. Berkland, *Adv Drug Deliver Rev* **2008**, *60*, 915-928.
[87] aD. A. Benaron, *Cancer Metastasis Rev* **2002**, *21*, 45-78; bA. G. Hays, M. Schar, S. Kelle, *Curr Cardiol Rev* **2009**, *5*, 237-242.
[88] P. Caravan, J. J. Ellison, T. J. McMurry, R. B. Lauffer, *Chem Rev* **1999**, *99*, 2293-2352.
[89] H. Kobayashi, M. W. Brechbiel, *Adv Drug Deliver Rev* **2005**, *57*, 2271-2286.
[90] S. E. Plush, M. Woods, Y. F. Zhou, S. B. Kadali, M. S. Wong, A. D. Sherry, *J Am Chem Soc* **2009**, *131*, 15918-15923.
[91] aD. T. Schuhle, P. van Rijn, S. Laurent, L. Vander Elst, R. N. Muller, M. C. Stuart, J. Schatz, J. A. Peters, *Chem Commun* **2010**, *46*, 4399-4401; bK. E. Lokling, R. Skurtveit, A. Bjornerud, S. L. Fossheim, *Magn Reson Med* **2004**, *51*, 688-696.
[92] aK. Luo, J. Tian, G. Liu, J. Sun, C. Xia, H. Tang, L. Lin, T. Miao, X. Zhao, F. Gao, Q. Gong, B. Song, X. Shuai, H. Ai, Z. Gu, *J Nanosci Nanotechno* **2010**, *10*, 540-548; bW. J. Rieter, J. S. Kim, K. M. Taylor, H. An, W. Lin, T. Tarrant, *Angew Chem Int Ed Engl* **2007**, *46*, 3680-3682.
[93] C. Tilcock, E. Unger, P. Cullis, P. MacDougall, *Radiology* **1989**, *171*, 77-80.
[94] Z. L. Cheng, D. L. J. Thorek, A. Tsourkas, *Adv Funct Mater* **2009**, *19*, 3753-3759.
[95] E. Nakamura, K. Makino, T. Okano, T. Yamamoto, M. Yokoyama, *Journal of controlled release : official journal of the Controlled Release Society* **2006**, *114*, 325-333.
[96] K. J. Chen, S. M. Wolahan, H. Wang, C. H. Hsu, H. W. Chang, A. Durazo, L. P. Hwang, M. A. Garcia, Z. K. Jiang, L. Wu, Y. Y. Lin, H. R. Tseng, *Biomaterials* **2011**, *32*, 2160-2165.
[97] aK. Alitalo, T. Tammela, T. V. Petrova, *Nature* **2005**, *438*, 946-953; bG. Ravizzini, B. Turkbey, T. Barrett, H. Kobayashi, P. L. Choyke, *Wiley Interdiscip Rev Nanomed Nanobiotechnol* **2009**, *1*, 610-623; cT. Barrett, P. L. Choyke, H. Kobayashi, *Contrast Media Mol Imaging* **2006**, *1*, 230-245.
[98] aN. L. Rosi, D. A. Giljohann, C. S. Thaxton, A. K. Lytton-Jean, M. S. Han, C. A. Mirkin, *Science* **2006**, *312*, 1027-1030; bD. Peer, J. Lieberman, *Gene Ther* **2011**, *18*, 1127-1133.
[99] aM. Yan, J. Du, Z. Gu, M. Liang, Y. Hu, W. Zhang, S. Priceman, L. Wu, Z. H. Zhou, Z. Liu, T. Segura, Y. Tang, Y. Lu, *Nat Nanotechnol* **2010**, *5*, 48-53; bT. Nochi, Y. Yuki, H. Takahashi, S. Sawada, M. Mejima, T. Kohda, N. Harada, I. G. Kong, A. Sato, N. Kataoka, D. Tokuhara, S. Kurokawa, Y. Takahashi, H. Tsukada, S. Kozaki, K. Akiyoshi, H. Kiyono, *Nat Mater* **2010**, *9*, 572-578; cY. Lee, T. Ishii, H. J. Kim, N. Nishiyama, Y. Hayakawa, K. Itaka, K. Kataoka, *Angew Chem Int Edit* **2010**, *49*, 2552-2555.
[100] P. Chakravarty, W. Qian, M. A. El-Sayed, M. R. Prausnitz, *Nat Nanotechnol* **2010**, *5*, 607-611.
[101] B. Kim, G. Han, B. J. Toley, C. K. Kim, V. M. Rotello, N. S. Forbes, *Nat Nanotechnol* **2010**, *5*, 465-472.
[102] aR. A. Petros, J. M. DeSimone, *Nature reviews. Drug discovery* **2010**, *9*, 615-627; bS. S. Agasti, S. Rana, M. H. Park, C. K. Kim, C. C. You, V. M. Rotello, *Adv Drug Deliver Rev* **2010**, *62*, 316-328.

[103] Y. Namiki, T. Namiki, H. Yoshida, Y. Ishii, A. Tsubota, S. Koido, K. Nariai, M. Mitsunaga, S. Yanagisawa, H. Kashiwagi, Y. Mabashi, Y. Yumoto, S. Hoshina, K. Fujise, N. Tada, *Nat Nanotechnol* **2009**, *4*, 598-606.
[104] P. Horcajada, T. Chalati, C. Serre, B. Gillet, C. Sebrie, T. Baati, J. F. Eubank, D. Heurtaux, P. Clayette, C. Kreuz, J. S. Chang, Y. K. Hwang, V. Marsaud, P. N. Bories, L. Cynober, S. Gil, G. Ferey, P. Couvreur, R. Gref, *Nat Mater* **2010**, *9*, 172-178.
[105] aS. Nie, Y. Xing, G. J. Kim, J. W. Simons, *Annu Rev Biomed Eng* **2007**, *9*, 257-288; bH. Yu, E. Wagner, *Curr Opin Mol Ther* **2009**, *11*, 165-178.
[106] D. H. Kim, J. J. Rossi, *Nat Rev Genet* **2007**, *8*, 173-184.
[107] aT. Niidome, L. Huang, *Gene Ther* **2002**, *9*, 1647-1652; bK. A. Woodrow, Y. Cu, C. J. Booth, J. K. Saucier-Sawyer, M. J. Wood, W. M. Saltzman, *Nat Mater* **2009**, *8*, 526-533; cV. P. Torchilin, T. S. Levchenko, R. Rammohan, N. Volodina, B. Papahadjopoulos-Sternberg, G. G. D'Souza, *P Natl Acad Sci USA* **2003**, *100*, 1972-1977.
[108] aH. Liang, D. Harries, G. C. Wong, *P Natl Acad Sci USA* **2005**, *102*, 11173-11178; bA. Pathak, P. Kumar, K. Chuttani, S. Jain, A. K. Mishra, S. P. Vyas, K. C. Gupta, *Acs Nano* **2009**, *3*, 1493-1505.
[109] Z. Liu, W. Cai, L. He, N. Nakayama, K. Chen, X. Sun, X. Chen, H. Dai, *Nat Nanotechnol* **2007**, *2*, 47-52.
[110] G. T. Zugates, D. G. Anderson, S. R. Little, I. E. Lawhorn, R. Langer, *J Am Chem Soc* **2006**, *128*, 12726-12734.
[111] M. Meyer, A. Philipp, R. Oskuee, C. Schmidt, E. Wagner, *J Am Chem Soc* **2008**, *130*, 3272-3273.
[112] Q. K. Ng, M. K. Sutton, P. Soonsawad, L. Xing, H. Cheng, T. Segura, *Molecular therapy : the journal of the American Society of Gene Therapy* **2009**, *17*, 828-836.
[113] J. Xie, K. Chen, H. Y. Lee, C. Xu, A. R. Hsu, S. Peng, X. Chen, S. Sun, *J Am Chem Soc* **2008**, *130*, 7542-7543.
[114] S. Fukushima, K. Miyata, N. Nishiyama, N. Kanayama, Y. Yamasaki, K. Kataoka, *J Am Chem Soc* **2005**, *127*, 2810-2811.
[115] L. Bazin, M. Gressier, P. L. Taberna, M. J. Menu, P. Simon, *Chem Commun* **2008**, 5004-5006.
[116] P. Erbacher, J. S. Remy, J. P. Behr, *Gene Ther* **1999**, *6*, 138-145.
[117] aW. Y. Lin, Y. Wang, S. Wang, H. R. Tseng, *Nano Today* **2009**, *4*, 470-481; bY. Wang, W. Y. Lin, K. Liu, R. J. Lin, M. Selke, H. C. Kolb, N. Zhang, X. Z. Zhao, M. E. Phelps, C. K. Shen, K. F. Faull, H. R. Tseng, *Lab Chip* **2009**, *9*, 2281-2285.
[118] aZ. Cao, R. Tong, A. Mishra, W. Xu, G. C. Wong, J. Cheng, Y. Lu, *Angew Chem Int Ed Engl* **2009**, *48*, 6494-6498; bB. C. Cross, I. Sinning, J. Luirink, S. High, *Nat Rev Mol Cell Biol* **2009**, *10*, 255-264; cB. Leader, Q. J. Baca, D. E. Golan, *Nature reviews. Drug discovery* **2008**, *7*, 21-39; dJ. E. Galan, H. Wolf-Watz, *Nature* **2006**, *444*, 567-573; eT. A. Kost, J. P. Condreay, D. L. Jarvis, *Nat Biotechnol* **2005**, *23*, 567-575.
[119] aN. Tokuriki, D. S. Tawfik, *Science* **2009**, *324*, 203-207; bS. Frokjaer, D. E. Otzen, *Nature reviews. Drug discovery* **2005**, *4*, 298-306; cZ. S. Haidar, R. C. Hamdy, M. Tabrizian, *Biomaterials* **2008**, *29*, 1207-1215.
[120] aI. Cheong, X. Huang, C. Bettegowda, L. A. Diaz, Jr., K. W. Kinzler, S. Zhou, B. Vogelstein, *Science* **2006**, *314*, 1308-1311; bV. P. Torchilin, *Nature reviews. Drug discovery* **2005**, *4*, 145-160.
[121] aY. Lee, T. Ishii, H. J. Kim, N. Nishiyama, Y. Hayakawa, K. Itaka, K. Kataoka, *Angew Chem Int Ed Engl* **2010**, *49*, 2552-2555; bL. J. De Cock, S. De Koker, B. G. De Geest, J. Grooten, C. Vervaet, J. P. Remon, G. B. Sukhorukov, M. N. Antipina, *Angew Chem Int Ed Engl* **2010**, *49*, 6954-6973; cS. F. van Dongen, W. P. Verdurmen, R. J. Peters, R. J. Nolte, R. Brock, J. C. van Hest, *Angew Chem Int Ed Engl* **2010**, *49*, 7213-7216.
[122] aP. Ghosh, X. Yang, R. Arvizo, Z. J. Zhu, S. S. Agasti, Z. Mo, V. M. Rotello, *J Am Chem Soc* **2010**, *132*, 2642-2645; bH. Li, Y. Ma, Y. Chen, Y. Sang, T. Zhou, M. Qiu, X. Huang, C. Zhou, Z. Su, *Angew Chem Int Ed Engl* **2010**, *49*, 4930-4933; cD. A. Giljohann, D. S. Seferos, W. L.

Daniel, M. D. Massich, P. C. Patel, C. A. Mirkin, *Angew Chem Int Ed Engl* **2010**, *49*, 3280-3294; dJ. Liu, A. Stace-Naughton, X. Jiang, C. J. Brinker, *J Am Chem Soc* **2009**, *131*, 1354-1355.
[123] B. F. Canine, A. Hatefi, *Adv Drug Deliver Rev* **2010**, *62*, 1524-1529.
[124] aS. Asoh, S. Ohta, *Adv Drug Deliver Rev* **2008**, *60*, 499-516; bS. Console, C. Marty, C. Garcia-Echeverria, R. Schwendener, K. Ballmer-Hofer, *The Journal of biological chemistry* **2003**, *278*, 35109-35114; cJ. S. Wadia, S. F. Dowdy, *Adv Drug Deliver Rev* **2005**, *57*, 579-596.
[125] Y. Kumagai, D. Sumi, *Annu Rev Pharmacol Toxicol* **2007**, *47*, 243-262.
[126] D. Kim, C. H. Kim, J. I. Moon, Y. G. Chung, M. Y. Chang, B. S. Han, S. Ko, E. Yang, K. Y. Cha, R. Lanza, K. S. Kim, *Cell Stem Cell* **2009**, *4*, 472-476.
[127] aN. Maherali, K. Hochedlinger, *Cell Stem Cell* **2008**, *3*, 595-605; bK. Takahashi, K. Tanabe, M. Ohnuki, M. Narita, T. Ichisaka, K. Tomoda, S. Yamanaka, *Cell* **2007**, *131*, 861-872.
[128] Y. Liu, H. Wang, K. Kamei, M. Yan, K. J. Chen, Q. Yuan, L. Shi, Y. Lu, H. R. Tseng, *Angew Chem Int Ed Engl* **2011**, *50*, 3058-3062.
[129] H. Wang, K. Liu, K. J. Chen, Y. J. Lu, S. T. Wang, W. Y. Lin, F. Guo, K. I. Kamei, Y. C. Chen, M. Ohashi, M. W. Wang, M. A. Garcia, X. Z. Zhao, C. K. F. Shen, H. R. Tseng, *Acs Nano* **2010**, *4*, 6235-6243.
[130] aK. Kamei, S. Guo, Z. T. Yu, H. Takahashi, E. Gschweng, C. Suh, X. Wang, J. Tang, J. McLaughlin, O. N. Witte, K. B. Lee, H. R. Tseng, *Lab Chip* **2009**, *9*, 555-563; bK. Kamei, M. Ohashi, E. Gschweng, Q. Ho, J. Suh, J. Tang, Z. T. For Yu, A. T. Clark, A. D. Pyle, M. A. Teitell, K. B. Lee, O. N. Witte, H. R. Tseng, *Lab Chip* **2010**, *10*, 1113-1119.
[131] aD. H. Kim, J. J. Rossi, *Nature Reviews Genetics* **2007**, *8*, 173-184; bD. J. Glover, H. J. Lipps, D. A. Jans, *Nat Rev Genet* **2005**, *6*, 299-310.
[132] aC. M. Niemeyer, M. Adler, S. Lenhert, S. Gao, H. Fuchs, L. Chi, *Chembiochem : a European journal of chemical biology* **2001**, *2*, 260-264; bM. Ferrari, *Nat Rev Cancer* **2005**, *5*, 161-171.
[133] Y. C. Tseng, S. Mozumdar, L. Huang, *Adv Drug Deliver Rev* **2009**, *61*, 721-731.
[134] W. D. Jang, K. M. K. Selim, C. H. Lee, I. K. Kang, *Prog Polym Sci* **2009**, *34*, 1-23.
[135] W. Jiang, B. Y. S. Kim, J. T. Rutka, W. C. W. Chan, *Nat Nanotechnol* **2008**, *3*, 145-150.
[136] H. Wang, K. Liu, K. J. Chen, Y. Lu, S. Wang, W. Y. Lin, F. Guo, K. Kamei, Y. C. Chen, M. Ohashi, M. Wang, M. A. Garcia, X. Z. Zhao, C. K. Shen, H. R. Tseng, *Acs Nano* **2010**, *4*, 6235-6243.
[137] R. Klajn, M. A. Olson, P. J. Wesson, L. Fang, A. Coskun, A. Trabolsi, S. Soh, J. F. Stoddart, B. A. Grzybowski, *Nat Chem* **2009**, *1*, 733-738.
[138] C. C. Lee, G. D. Sui, A. Elizarov, C. Y. J. Shu, Y. S. Shin, A. N. Dooley, J. Huang, A. Daridon, P. Wyatt, D. Stout, H. C. Kolb, O. N. Witte, N. Satyamurthy, J. R. Heath, M. E. Phelps, S. R. Quake, H. R. Tseng, *Science* **2005**, *310*, 1793-1796.
[139] A. Akinc, A. Zumbuehl, M. Goldberg, E. S. Leshchiner, V. Busini, N. Hossain, S. A. Bacallado, D. N. Nguyen, J. Fuller, R. Alvarez, A. Borodovsky, T. Borland, R. Constien, A. de Fougerolles, J. R. Dorkin, K. Narayanannair Jayaprakash, M. Jayaraman, M. John, V. Koteliansky, M. Manoharan, L. Nechev, J. Qin, T. Racie, D. Raitcheva, K. G. Rajeev, D. W. Sah, J. Soutschek, I. Toudjarska, H. P. Vornlocher, T. S. Zimmermann, R. Langer, D. G. Anderson, *Nat Biotechnol* **2008**, *26*, 561-569.
[140] aG. M. Whitesides, *Nature* **2006**, *442*, 368-373; bT. Thorsen, S. J. Maerkl, S. R. Quake, *Science* **2002**, *298*, 580-584; cS. Marre, K. F. Jensen, *Chem Soc Rev* **2010**, *39*, 1183-1202.
[141] C. C. Overly, K. D. Lee, E. Berthiaume, P. J. Hollenbeck, *P Natl Acad Sci USA* **1995**, *92*, 3156-3160.
[142] aS. W. Bae, W. Tan, J. I. Hong, *Chem Commun* **2012**, *48*, 2270-2282; bY. S. Yim, J. S. Choi, G. T. Kim, C. H. Kim, T. H. Shin, D. G. Kim, J. Cheon, *Chem Commun* **2012**, *48*, 61-63.
[143] aM. E. Davis, Z. Chen, D. M. Shin, *Nat Rev Drug Discov* **2008**, *7*, 771-782; bR. A. Petros, J. M. DeSimone, *Nat Rev Drug Discov* **2010**, *9*, 615-627; cG. W. Doorley, C. K. Payne, *Chem Commun* **2012**, *48*, 2961-2963; dA. Curcio, R. Marotta, A. Riedinger, D. Palumberi, A. Falqui, T. Pellegrino, *Chem Commun* **2012**, *48*, 2400-2402; eS. Rana, A. Bajaj, R. Mout, V. M. Rotello, *Adv*

Drug Deliver Rev **2012**, *64*, 200-216; fC. Tassa, S. Y. Shaw, R. Weissleder, *Accounts Chem Res* **2011**, *44*, 842-852.
[144] aV. P. Torchilin, A. N. Lukyanov, Z. G. Gao, B. Papahadjopoulos-Sternberg, *P Natl Acad Sci USA* **2003**, *100*, 6039-6044; bY. Bae, K. Kataoka, *Adv Drug Deliver Rev* **2009**, *61*, 768-784; cN. T. Zaman, Y. Y. Yang, J. Y. Ying, *Nano Today* **2010**, *5*, 9-14.
[145] G. Pasut, F. M. Veronese, *Prog Polym Sci* **2007**, *32*, 933-961.
[146] M. T. Morgan, Y. Nakanishi, D. J. Kroll, A. P. Griset, M. A. Carnahan, M. Wathier, N. H. Oberlies, G. Manikumar, M. C. Wani, M. W. Grinstaff, *Cancer Res* **2006**, *66*, 11913-11921.
[147] S. K. Das, M. K. Bhunia, D. Chakraborty, A. R. Khuda-Bukhsh, A. Bhaumik, *Chem Commun* **2012**, *48*, 2891-2893.
[148] D. Wang, Y. Su, C. Jin, B. Zhu, Y. Pang, L. Zhu, J. Liu, C. Tu, D. Yan, X. Zhu, *Biomacromolecules* **2011**, *12*, 1370-1379.
[149] C. Yang, A. B. Attia, J. P. Tan, X. Ke, S. Gao, J. L. Hedrick, Y. Y. Yang, *Biomaterials* **2012**, *33*, 2971-2979.
[150] H. Wang, S. Wang, H. Su, K. J. Chen, A. L. Armijo, W. Y. Lin, Y. Wang, J. Sun, K. Kamei, J. Czernin, C. G. Radu, H. R. Tseng, *Angew. Chem. Int. Ed.* **2009**, *48*, 4344-4348.
[151] H. Ali-Boucetta, K. T. Al-Jamal, D. McCarthy, M. Prato, A. Bianco, K. Kostarelos, *Chem Commun* **2008**, 459-461.
[152] J. Sun, M. D. Masterman-Smith, N. A. Graham, J. Jiao, J. Mottahedeh, D. R. Laks, M. Ohashi, J. DeJesus, K. Kamei, K. B. Lee, H. Wang, Z. T. Yu, Y. T. Lu, S. Hou, K. Li, M. Liu, N. Zhang, S. Wang, B. Angenieux, E. Panosyan, E. R. Samuels, J. Park, D. Williams, V. Konkankit, D. Nathanson, R. M. van Dam, M. E. Phelps, H. Wu, L. M. Liau, P. S. Mischel, J. A. Lazareff, H. I. Kornblum, W. H. Yong, T. G. Graeber, H. R. Tseng, *Cancer Res* **2010**, *70*, 6128-6138.
[153] E. Hayakawa, K. Furuya, H. Ueno, T. Kuroda, M. Moriyama, A. Kondo, *Chem Pharm Bull* **1991**, *39*, 1009-1012.
[154] V. Y. Erukova, O. O. Krylova, Y. N. Antonenko, N. S. Melik-Nubarov, *Biochim Biophys Acta* **2000**, *1468*, 73-86.
[155] E. Ruoslahti, *Annu Rev Cell Dev Biol* **1996**, *12*, 697-715.
[156] J. Shi, Z. Xiao, N. Kamaly, O. C. Farokhzad, *Accounts Chem Res* **2011**, *44*, 1123-1134.
[157] aY. Namiki, T. Fuchigami, N. Tada, R. Kawamura, S. Matsunuma, Y. Kitamoto, M. Nakagawa, *Accounts Chem Res* **2011**, *44*, 1080-1093; bE. K. Chow, X. Q. Zhang, M. Chen, R. Lam, E. Robinson, H. Huang, D. Schaffer, E. Osawa, A. Goga, D. Ho, *Sci Transl Med* **2011**, *3*, 73ra21; cS. P. Sherlock, S. M. Tabakman, L. Xie, H. Dai, *Acs Nano* **2011**, *5*, 1505-1512; dH. Meng, M. Liong, T. Xia, Z. Li, Z. Ji, J. I. Zink, A. E. Nel, *Acs Nano* **2010**, *4*, 4539-4550.
[158] D. Peer, J. M. Karp, S. Hong, O. C. Farokhzad, R. Margalit, R. Langer, *Nat Nanotechnol* **2007**, *2*, 751-760.
[159] J. R. Heath, M. E. Davis, *Annu Rev Med* **2008**, *59*, 251-265.
[160] S. D. Perrault, C. Walkey, T. Jennings, H. C. Fischer, W. C. Chan, *Nano Lett* **2009**, *9*, 1909-1915.
[161] S. D. Li, L. Huang, *Mol Pharmaceut* **2008**, *5*, 496-504.
[162] aS. Bai, C. Thomas, A. Rawat, F. Ahsan, *Crit Rev Ther Drug* **2006**, *23*, 437-495; bW. C. Zamboni, *Oncologist* **2008**, *13*, 248-260.
[163] M. Gaumet, A. Vargas, R. Gurny, F. Delie, *European journal of pharmaceutics and biopharmaceutics : official journal of Arbeitsgemeinschaft fur Pharmazeutische Verfahrenstechnik e.V* **2008**, *69*, 1-9.
[164] K. J. Chen, L. Tang, M. A. Garcia, H. Wang, H. Lu, W. Y. Lin, S. Hou, Q. Yin, C. K. Shen, J. Cheng, H. R. Tseng, *Biomaterials* **2012**, *33*, 1162-1169.
[165] J. Fang, H. Nakamura, H. Maeda, *Adv Drug Deliver Rev* **2011**, *63*, 136-151.
[166] H. Lu, J. Cheng, *J Am Chem Soc* **2007**, *129*, 14114-14115.
[167] R. Bhatt, P. de Vries, J. Tulinsky, G. Bellamy, B. Baker, J. W. Singer, P. Klein, *J Med Chem* **2003**, *46*, 190-193.

[168] P. Decuzzi, B. Godin, T. Tanaka, S. Y. Lee, C. Chiappini, X. Liu, M. Ferrari, *Journal of controlled release : official journal of the Controlled Release Society* **2010**, *141*, 320-327.
[169] H. Maeda, J. Wu, T. Sawa, Y. Matsumura, K. Hori, *Journal of controlled release : official journal of the Controlled Release Society* **2000**, *65*, 271-284.
[170] J. Cheng, K. T. Khin, M. E. Davis, *Mol Pharmaceut* **2004**, *1*, 183-193.
[171] H. Koo, M. S. Huh, I. C. Sun, S. H. Yuk, K. Choi, K. Kim, I. C. Kwon, *Accounts Chem Res* **2011**, *44*, 1018-1028.
[172] X. Ma, Y. Zhao, X. J. Liang, *Accounts Chem Res* **2011**, *44*, 1114-1122.
[173] K. C. Petkar, S. S. Chavhan, S. Agatonovik-Kustrin, K. K. Sawant, *Crit Rev Ther Drug* **2011**, *28*, 101-164.
[174] aJ. L. Perry, K. P. Herlihy, M. E. Napier, J. M. Desimone, *Accounts Chem Res* **2011**, *44*, 990-998; bA. Puri, R. Blumenthal, *Accounts Chem Res* **2011**, *44*, 1071-1079.
[175] M. E. Caldorera-Moore, W. B. Liechty, N. A. Peppas, *Accounts Chem Res* **2011**, *44*, 1061-1070.
[176] aA. Agarwal, M. A. Mackey, M. A. El-Sayed, R. V. Bellamkonda, *Acs Nano* **2011**, *5*, 4919-4926; bW. Zhang, Z. Guo, D. Huang, Z. Liu, X. Guo, H. Zhong, *Biomaterials* **2011**, *32*, 8555-8561; cZ. Liu, A. C. Fan, K. Rakhra, S. Sherlock, A. Goodwin, X. Chen, Q. Yang, D. W. Felsher, H. Dai, *Angew Chem Int Ed Engl* **2009**, *48*, 7668-7672; dM. K. Yu, Y. Y. Jeong, J. Park, S. Park, J. W. Kim, J. J. Min, K. Kim, S. Jon, *Angew Chem Int Ed Engl* **2008**, *47*, 5362-5365.